

**VOID FRACTION, PRESSURE DROP, AND HEAT TRANSFER IN
HIGH PRESSURE CONDENSING FLOWS THROUGH
MICROCHANNELS**

A Dissertation
Presented to
The Academic Faculty

by

Brendon Keinath

In Partial Fulfillment
of the Requirements for the Degree
Doctor of Philosophy in the
School of Mechanical Engineering

Georgia Institute of Technology
December 2012

**VOID FRACTION, PRESSURE DROP, AND HEAT TRANSFER IN
HIGH PRESSURE CONDENSING FLOWS THROUGH
MICROCHANNELS**

Approved by:

Dr. Srinivas Garimella, Advisor
George W. Woodruff School of
Mechanical Engineering
Georgia Institute of Technology

Dr. S. Mostafa Ghiaasiaan
George W. Woodruff School of
Mechanical Engineering
Georgia Institute of Technology

Dr. Satish Kumar
George W. Woodruff School of
Mechanical Engineering
Georgia Institute of Technology

Dr. Thomas Fuller
School of Chemical and Biomolecular
Engineering
Georgia Institute of Technology

Dr. Michael Bergin
School of Civil and Environmental
Engineering
Georgia Institute of Technology

Date Approved: August 23, 2012

To my wife, Sarah.

ACKNOWLEDGEMENTS

First and foremost, I would like to express my deepest gratitude to my advisor, Dr. Srinivas Garimella, for his support and guidance throughout my PhD studies. His mentorship over the years has proven invaluable to my development as an engineer and individual.

I would like to thank the past and present members of STSL for their consistent support, feedback, and encouragement. The journey would not have been possible or as rewarding without their efforts and kindness. I would especially like to thank Anand Nagavarapu, Jeff Milkie, and Brian Fronk for their friendship and technical guidance over the years.

I would also like to thank my committee members for contributing their time and expertise to the review of my work.

TABLE OF CONTENTS

	Page
ACKNOWLEDGEMENTS	iv
LIST OF TABLES	vii
LIST OF FIGURES	x
LIST OF SYMBOLS AND ABBREVIATIONS	xv
SUMMARY	xxi
<u>CHAPTER</u>	
1 Introduction	1
2 Literature Review	5
2.1 Flow Regime Maps	5
2.2 Void Fraction	27
2.3 Pressure Drop	38
2.4 Heat Transfer	43
2.5 Specific Research Needs	55
2.6 Objectives and Tasks	56
3 Experimental Methods	58
3.1 Phase-Change Tests	59
3.2 High-Speed Camera Setup	76
3.3 Charging Refrigerant Loop with R404A	77
3.4 Test Procedures	78
4 Data Analysis	80
4.1 Large Diameter Tube Condensation Analysis	80
4.2 Small Diameter Tube Condensation Analysis	98

5	Image Analysis	103
5.1	Image Processing	103
5.2	Analysis and Interpretation of Processed Images	106
5.3	Accuracy of Analysis	120
6	Results and Comparisons	126
6.1	Results	126
6.2	Comparison with Literature	150
7	Model Development	203
7.1	Void Fraction Model	204
7.2	Pressure Drop Model	214
7.3	Heat Transfer Model	228
8	Conclusions and Recommendations	244
	APPENDIX A: Uncertainty Propagation	249
	APPENDIX B: Sample Data Point Calculations	257
	APPENDIX C: Primary Loop Pump Heat Addition Calculation	290
	APPENDIX D: Intermittent Pressure Drop Model	293
	APPENDIX E: Void Fraction Model	307
	APPENDIX F: Condensation Heat Transfer and Pressure Drop Models	312
	REFERENCES	324

LIST OF TABLES

	Page
Table 2.1: Summary of Flow Regime Literature Review	25
Table 2.2: Summary of Void Fraction Literature Review	36
Table 2.3: Summary of Pressure Drop Literature Review	44
Table 2.4: Summary of Heat Transfer Literature Review	54
Table 3.1: Pre- and Post-Condenser Dimensions	57
Table 3.2: Primary Loop Dimensions	64
Table 3.3: Secondary Loop Heat Exchanger Dimensions	65
Table 3.4: Data Acquisition System	65
Table 3.5: Large Diameter Tube Facility Pressure Transducers	65
Table 3.6: Temperature Measurements	67
Table 3.7: Large Diameter Tube Facility Flowmeter Specifications	67
Table 3.8: Large Diameter Tube Facility High-Speed Video Equipment	67
Table 3.9: Pre- and Post-Heater Dimensions	70
Table 3.10: Small Diameter Tube Facility Pressure Transducers	71
Table 3.11: Small Diameter Tube Facility Mass Flow Meters and Watt Transducers	71
Table 3.12: Small Diameter Tube Facility High-Speed Video Equipment	72
Table 3.13: Visualization Test Section Dimensions	74
Table 3.14: Heat Transfer Test Section Dimensions	75
Table 4.1: Refrigerant Temperatures and Pressures	81
Table 4.2: Cooling Water Temperatures and Flow Rates	81
Table 4.3: Condenser and Saturation Temperature Comparison	81
Table 4.4: Summary of Heat Losses	88

Table 4.5: Comparison of Measured Thermocouple and Pressure-Based Temperature Measurements	91
Table 4.6: Refrigerant Temperatures and Pressures	99
Table 4.7: Pre- and Post-Heater Inputs	100
Table 4.8: Heater and Saturation Temperature Comparison	100
Table 4.9: Summary of Heat Losses	101
Table 5.1: Representative Image Analysis Calibration Values	106
Table 5.2: Summary of Sensitivity Analysis	121
Table 5.3: Measured Void Fraction and Standard Deviation of Results for the First Frame of the Representative Data Point, $T_{\text{sat}} = 29.85^{\circ}\text{C}$, $G = 206.6 \text{ kg m}^{-2} \text{ s}^{-1}$, and $x = 0.20$	122
Table 6.1: Flow Regimes and Patterns Observed in Condensing R404A Through 3.00 mm Diameter Tubes	127
Table 6.2: Annular-to-Intermittent Transitions at Different Tube Diameters	130
Table 6.3: Summary of Observed Flow Regimes	131
Table 6.4: Properties of R404A at Various Saturation Temperatures	134
Table 6.5: Average Quality Changes, Uncertainties in Void Fraction due to Measurement of Quality, Repeatability and Total Average Uncertainty in Void Fraction Data	138
Table 6.6: Relative Pressure Drop Contributions and Uncertainties	143
Table 6.7: Average Resistance Ratio, Quality Change and Uncertainty in h_t	148
Table 6.8: Comparison of Observed Flow Regime to Flow Regimes Predicted by the Taitel and Dukler (1976) Flow Regime Map	152
Table 6.9: Comparison of Observed Flow Regime to Flow Regimes Predicted by the Tandon <i>et al.</i> (1982) Flow Regime Map	155
Table 6.10: Comparison of Observed Flow Regime to Flow Regimes Predicted by the Cavallini <i>et al.</i> (2002) Flow Regime Map	157
Table 6.11: Comparison of Observed Flow Regime to Predicted Flow Regime by the Nema. (2007) Flow Regime Map	160
Table 6.12: Comparison of Experimental α with Models in Literature	171

Table 6.13: Predictive Capabilities of Models in the Literature for Data from the Present Study Categorized by Tube Diameter	183
Table 6.14: Predictive Capabilities of Models in the Literature for Data from the Present Study Categorized by Saturation Temperature	184
Table 6.15: Predictive Capabilities of Various Models in the Literature for Data from the Present Study Categorized by Tube Diameter	199
Table 6.16: Predictive Capabilities of Various Models in the Literature for Data from the Present Study Categorized by Saturation Temperature	200
Table 7.1: Flow Regimes Predicted by Nema (2007) for R404A Data from the Present Study	203
Table 7.2: Void Fraction Model Predictions	209
Table 7.3: Empirical Constants for Predicting Pressure Drop During Annular and Wavy Flow with Laminar and Turbulent Liquid Phases	217
Table 7.4: Summary of Equations for Predicting Pressure Drop in the Intermittent Flow Regime	221
Table 7.5: Pressure Drop Model Predictions by Tube Diameter	225
Table 7.6: Pressure Drop Model Predictions by Saturation Temperature	225
Table 7.7: Pressure Drop Model Predictions by Flow Regime	225
Table 7.8: Heat Transfer Model Predictions by Tube Diameter	238
Table 7.9: Heat Transfer Model Predictions by Saturation Temperature	239
Table 7.10: Heat Transfer Model Predictions by Flow Regime	239
Table B.1: Sample Test Calculation for $D = 3.05$ mm	258
Table B.2: Sample Test Calculation for $D = 1.55$ mm	275
Table D.1: Pressure Drop Model Predictions by Flow Regime	307
Table E.1: Void Fraction Model	310
Table F.1: Condensation Heat Transfer and Pressure Drop Models	314

LIST OF FIGURES

	Page
Figure 3.1: Photograph of Large Diameter Tube Facility	59
Figure 3.2: Schematic of Large Diameter Tube Test Facility	60
Figure 3.3: Schematic of System for Thermal Amplification Technique	63
Figure 3.4: Photograph of Small Diameter Tube Test Facility	68
Figure 3.5: Schematic of Small Diameter Tube Test Facility	69
Figure 3.6: Refrigerant Heater Schematic for Pre- and Post-Heater in Small Diameter Tube Facility	70
Figure 3.7: Tube-in-Tube Test Section Schematic	72
Figure 3.8: Photograph of Visualization Test Section	73
Figure 3.9: Visualization Test Section Schematic	73
Figure 3.10: Photograph of Heat Transfer Test Sections	75
Figure 3.11: High Speed Video Camera and Lighting Setup	76
Figure 4.1: Schematic of Pre-Condenser Thermal Resistance Network	84
Figure 4.2: Schematic of Test Section Thermal Resistance Network	91
Figure 5.1: Observed Planes: Longitudinal, Overhead, and Cross-Section	103
Figure 5.2: Geometric Graphic User Interface for Video Frame Analysis	105
Figure 5.3: Schematic of Video Frame Analysis	107
Figure 5.4: Schematic of Vapor Bubble Velocity Measurement	109
Figure 5.5: Example of (a) Vapor Bubble Velocity and (b) Coalescence Tracking	109
Figure 5.6: Segmental Analysis of Void Fraction	112
Figure 5.7: Cross-Sectional Areas of Partial-Cylinder and Cylindrical Vapor Phase Cases	112

Figure 5.8: Comparison of (a) High Speed Video Frames to (b) Discretized Analysis and (c) Probability Density Function (PDF) of Film Thickness for $T_{\text{sat}} = 29.85^{\circ}\text{C}$, $G = 206.6 \text{ kg m}^{-2} \text{ s}^{-1}$, and $x = 0.20$	113
Figure 5.9: Void Fraction as a Function of Time for the Center Point of Each Frame (blue), Volume (red) and Average Over Volume and Time (black) for Three Representative Cases	119
Figure 5.10: Sensitivity Analysis: Number and Frequency of Frames Analyzed per Data Point	121
Figure 5.11: Repeatability Regions for Example Data Points; green - $\sigma_{\alpha} < 0.01$, yellow - $\sigma_{\alpha} < 0.02$, red - intractable	123
Figure 5.12: Total Void Fraction Uncertainty and Component Contributions	125
Figure 6.1: Void Fraction versus Quality	132
Figure 6.2: Experimental Void Fraction versus Quality for (a) Increasing Saturation Temperature, (b) Increasing Mass Flux, (c) Increasing Diameter, and (d) Different Flow Regimes	134
Figure 6.3: Comparison of Vapor-Liquid Distribution on a (a) Frame and (b) Local Basis for $T_{\text{sat}} = 30^{\circ}\text{C}$, $G = 200 \text{ kg m}^{-2} \text{ s}^{-1}$	136
Figure 6.4:(a) Quality Change, and (b) Uncertainties in Void Fraction Measurement	138
Figure 6.5: Frictional Pressure Drop versus Quality	140
Figure 6.6: Experimental Pressure Drop versus Quality for (a) Increasing Mass Flux, (b) Increasing Saturation Temperature, and (c) Increasing Diameter	141
Figure 6.7: (a) Quality Change and (b) Ratio of Friction Pressure Drop to Measured Pressure Drop	144
Figure 6.8: Heat Transfer Coefficient versus Quality	146
Figure 6.9: Experimental Heat Transfer Coefficient versus Quality for (a) Increasing Mass Flux, (b) Increasing Saturation Temperature, and (c) Increasing Diameter	147
Figure 6.10: (a) Resistance Ratio, (b) Test Section Heat Duty, and (c) Uncertainty in h_r , for Heat Transfer Experiments versus Mass Flux	149
Figure 6.11: Data from the Present Study Plotted on the Taitel and Dukler (1976) Flow Regime Map	152

Figure 6.12: Data from the Present Study Plotted on the Tandon <i>et al.</i> (1982) Flow Regime Map	155
Figure 6.13: Data from the Present Study Plotted on the Cavallini <i>et al.</i> (2002) Flow Regime Map	157
Figure 6.14: Data from the Present Study Plotted on the Nema (2007) Flow Regime Map	161
Figure 6.15: Comparison of Experimental α with Models in the Literature up to 2000	166
Figure 6.16: Comparison of Experimental α with Models in the Literature from 2000 to the Present	170
Figure 6.17: Comparison of Experimental $(dP/dz)_f$ with Models in the Literature up to 2000	175
Figure 6.18: Comparison of Experimental $(dP/dz)_f$ with Models in the Literature from 2000 to the Present	181
Figure 6.19: Comparison of Experimental h_r from the Present Study with Annular Regime Heat Transfer Models in the Literature	189
Figure 6.20: Comparison of Experimental h_r from the Present Study with Multi-Regime Heat Transfer Models in the Literature	198
Figure 7.1: Schematic of Perimeters and Shear Stresses for Void Fraction Model Development	204
Figure 7.2: Overall Void Fraction Prediction	208
Figure 7.3: Void Fraction Predictions for $T_{\text{sat}} = 30, 40, 50, \text{ and } 60^\circ\text{C}$	209
Figure 7.4: Illustration of Void Fraction Model Trends for Different (a) Saturation Temperatures and (b) Mass Fluxes	211
Figure 7.5: Prediction of Void Fraction Data of Winkler <i>et al.</i> (2012) for R134a for $2.0 < D_h < 4.91$ mm using the Model from the Present Study	213
Figure 7.6: Illustration of Void Fraction Prediction Trends for Refrigerants R404A and R134a	213
Figure 7.7: Schematic of Vapor-Liquid Distribution as the Basis for the Pressure Drop Model Adapted from Garimella <i>et al.</i> (2005)	214
Figure 7.8: Typical Transition Region For Interpolation Between Laminar and Turbulent Liquid Reynolds Number Values	217

Figure 7.9: Schematic of Unit Cell During Intermittent Flow (Garimella <i>et al.</i> , 2002)	218
Figure 7.10: Frictional Pressure Gradient Predictions Categorized by Tube Diameter	222
Figure 7.11: Frictional Pressure Gradient Predictions Categorized by Flow Regime	223
Figure 7.12: Frictional Pressure Drop for 0.508, 1.00, and 3.048 mm Test Sections	224
Figure 7.13: Illustration of Pressure Drop Model Trends	227
Figure 7.14: Film Profile for Condensing R134a in 1 mm Square Channels from the Computational Study of Wang and Rose (2006)	231
Figure 7.15: Cross-Sectional Schematic of the Wavy Flow Regime	233
Figure 7.16: Heat Transfer Coefficient Predictions for R404A by Tube Diameter	235
Figure 7.17: Heat Transfer Coefficient Predictions for R404A by Flow Regime	236
Figure 7.18: Measured and Predicted Heat Transfer Coefficients for $D = 0.86, 1.55,$ and 3.05 mm Test Sections	237
Figure 7.19: Heat Transfer Coefficient Predictions for R404A, NH_3 (Fronk and Garimella, 2012) and CO_2 (Fronk and Garimella, 2010)	240
Figure 7.20: Illustration of Heat Transfer Model Trends	242
Figure 7.21: Prediction of Heat Transfer Model for R404A, NH_3 , and CO_2	243
Figure 8.1: Observed Flow Maldistribution in Condensing R404A Through 1.00 mm Tubes	248
Figure D.1: Schematic of Idealized Unit Cell During Intermittent Flow with Relevant Dimensions Adapted from Garimella <i>et al.</i> (2002)	294
Figure D.2: Plot of Measured Vapor Bubble Velocity, U_{bubble} as Compared to Volumetric Flux, j	297
Figure D.3: Bond Number versus U_{bubble}	298
Figure D.4: Photographs and Schematic of Vapor Bubble and Liquid Slug Interactions in the Small Diameter Tubes ($D = 0.508, 1.00$ mm)	300
Figure D.5: Photographs and Schematic of Vapor Bubble and Liquid Slug Interactions in the Small Diameter Tubes ($D = 3.00$ mm)	300
Figure D.6: Liquid Reynolds Number Versus Measured U_{bubble}	301

LIST OF SYMBOLS AND ABBREVIATIONS

Symbols

a		empirical constant, [-]
A		area, [m ²]
AAD		absolute average deviation, [-]
AD		average deviation, [-]
Bo	Bond number, = $(\rho_l - \rho_v) \cdot g \cdot D^2 / \sigma$,	[-]
b		empirical constant, [-]
c		empirical constant, [-]
c_p		specific heat, [J kg ⁻¹ K ⁻¹]
Ca _l	liquid capillary number, = $\mu \cdot j_l / \sigma$,	[-]
d		empirical constant, [-]
D		diameter, [m]
e	surface roughness, [m];	empirical constant, [-]
f		friction factor, [-]
f(,)		function of (,)
Fr	Froude number, = $j_v / \sqrt{D \cdot g}$,	[-]
Fr _{mod}	modified Froude number, = $G \cdot x / \sqrt{D \cdot g \cdot \rho_v \cdot (\rho_l - \rho_v)}$,	[-]
Ft	Froude rate, = $(j_v / \sqrt{D \cdot g}) \cdot \sqrt{x / (1-x)}$,	[-]
G		mass flux, [kg m ⁻² s ⁻¹]
g		gravitational acceleration = 9.81 [m s ⁻²]
Ga	Galilei number, = $g \cdot \rho_l \cdot (\rho_l - \rho_v) \cdot D^3 / \mu_l^2$,	[-]
Gr	Grashof number, = $g \cdot \beta \cdot (T - T_\infty) \cdot \rho^3 \cdot D^3 / \mu^3$,	[-]

h	heat transfer coefficient, [W m ⁻² K ⁻¹]
H	height, [m]
i	enthalpy, [J kg ⁻¹]
$I.D.$	inner diameter, m
j	superficial velocity, [m s ⁻¹]
Ja_l	Jacob Number, = $c_{p,l} (T_{sat} - T_w) / i_{lv}$, [-]
J_G^*	dimensionless vapor velocity, = $x \cdot G / [g \cdot D \cdot \rho_v (\rho_l - \rho_v)]^{0.5}$, [-]
K	loss coefficient, [-]
k	conductivity, [W m ⁻¹ K ⁻¹]
L	length, [m]
$LMTD$	log-mean temperature difference, [K]
\dot{m}	mass flow rate, [kg s ⁻¹]
Nu	Nusselt number, = $h \cdot D / k$, [-]
N_{conf}	confinement number, = $\sqrt{\sigma / [g \cdot (\rho_l - \rho_v)]} / D$, [-]
P	pressure, [kPa]; perimeter, [m]
p_r	reduced pressure, [-]
Pr_l	liquid Prandtl number, = $c_{p,l} \cdot \mu_l / k_l$, [-]
\dot{Q}	heat duty, [W]
R, r	radius, [m]
r^*	ratio of outer and inner radii = r_{outer} / r_{inner} , [-]
Ra	Rayleigh number, = $D^3 \cdot g \cdot \rho_l \cdot (\rho_l - \rho_v) \cdot c_{p,l} / (\mu_l \cdot k_l)$, [-]
Re_l	liquids Reynolds number, = $\rho_l \cdot j_l \cdot D / \mu_l$, [-]
Re_v	vapor Reynolds number, = $\rho_v \cdot j_v \cdot D / \mu_v$, [-]

STD	standard deviation, [-]
T	temperature, [°C]
t	thickness, m
U	uncertainty, [m]; velocity [m s ⁻¹]
\dot{v}	volumetric flow rate, [m ³ s ⁻¹]
\dot{w}	work input, [W]
w	width, [m]
We_v	Vapor Weber number, = $\rho_v \cdot j_v^2 \cdot D / \sigma$, [-]
X	distance, [m]
x	quality, [-]; calibration value [pixel mm ⁻¹]
y	distance, [m]
Y	Chisholm parameter, [-]
z	length, [m]

Greek Symbols

α	void fraction, [-]; thermal diffusivity, [m ² s ⁻¹]
β	homogeneous void fraction, [-]; thermal coefficient of expansion, [K ⁻¹]
ε	emissivity, [-]
μ	dynamic viscosity, [kg m ⁻¹ s ⁻¹]
η	efficiency, [-]
ϕ	two-phase multiplier, [-]
ρ	density, [kg m ⁻³]
σ	Stefan-Boltzmann Constant = 5.67×10^{-8} W m ⁻² K ⁻⁴ ; surface tension, [N m ⁻¹]; standard deviation, [-]
θ	central angle, [rad]
ν	kinematic viscosity, [m ² s ⁻¹]

ξ perimeter ratio, [-]

Ψ flow multiplier, [-]; modified capillary number (Lee and Lee, 2001),
 $= j_1 \cdot \mu_1 / [(1 - \alpha) \cdot \sigma]$, [-]

X Martinelli Parameter, $= \sqrt{-(dp/dz)_{f,l} / -(dp/dz)_{f,v}}$, [-]

Subscripts and Superscripts

ambient surroundings

annulus annulus side

avg average

bottom bottom

bubble bubble

bulk bulk

cal calibration

crit critical

exp experimental

f friction

f/b film/bubble

film film

flowmeter flowmeter

G gaseous

H homogeneous

h hydraulic

i inner; index; interfacial

inner inner

ideal ideal

in	inlet
ins	insulation
l, L	liquid
laminar	laminar flow
LO	liquid only
measured	measured
nat. conv.	natural convection
nose	nose
o	outer
out	outlet
post	post-condenser; post-heater
pre	pre-condenser; pre-heater
prim	primary loop
pump	pump
r	refrigerant; reduced; relative
ra	Rouhani-Axelsson
rep	repeatability
S	separated flow
s	shell-and-tube
sec	secondary loop
sens	sensitivity
shaft	shaft
SS	stainless steel
strat	stratified flow
t	tube-in-tube

tail	tail
test	test section
tran	transitional
tube	refrigerant or water tube
turbulent	turbulent flow
UC	unit cell
UL	upper limit
v	vapor
w	water
wall	wall

SUMMARY

Flow mechanisms affect transport processes during condensation. Most studies on two-phase flow regimes are qualitative in nature, typically providing only information to guide the identification of the respective regimes and the transitions between them. These studies have, however, not yielded quantitative information to assist the development of pressure drop and heat transfer models. Such qualitative studies have also yielded results with considerable variability between investigators. A comprehensive investigation of flow mechanisms, void fraction, pressure drop and heat transfer during condensation of R404A in microchannels was conducted. In contrast to all prior investigations, high-speed video recordings and image analyses were used to directly measure void fraction, slug frequencies, vapor bubble velocity, vapor bubble dimensions and liquid film thicknesses in tube diameters ranging from 0.508 to 3.00 mm. Experiments were conducted at reduced pressures and mass fluxes ranging from 0.38 to 0.77 and 200 to 800 $\text{kg m}^{-2} \text{s}^{-1}$, respectively, to document their influences on the condensation process at local vapor qualities ranging from 0 to 1. This information was used to develop a model for the void fraction in condensing flows. A complementing set of heat transfer and pressure drop measurements were conducted on the same geometries at similar conditions, and the void fraction model was used in conjunction with these measurements to develop improved heat transfer and pressure drop models. This comprehensive set of experiments and analyses yields a self-consistent and accurate treatment of high-pressure condensation in small hydraulic diameter geometries. Furthermore, the heat transfer model was found to agree well with condensing ammonia and carbon dioxide data that were obtained at significantly different conditions in different tube diameters. The added physical understanding of the condensation process and the models developed will serve as important building blocks for the design of microscale condensers and thermal systems.

CHAPTER 1: INTRODUCTION

Miniaturized heat exchangers that use microchannels have been implemented in many applications. Heat rejection to the ambient is often the limiting case in such applications, and to shrink the envelope of the system, special attention must be given to reducing the condenser size. The use of a microchannel condenser in this and other such applications allows for the reduction in size, working fluid charge, and material requirements due to the increased surface area-to-volume ratios and larger heat transfer coefficients that such geometries offer. Predicting the amount of working fluid charge in a miniaturized system can also be important in reduction of the overall package size, because in the case of a vapor compression system, the accumulator is often one of the largest components. To accurately size the accumulator, one must be able to accurately predict the required fluid charge and the volume change during operation. In such situations, accurate void fraction models in each system component are needed for accurate sizing.

The use of high pressure refrigerants such as R404A is of particular interest in applications such as high-temperature-lift space conditioning because of its low ozone depletion potential. Refrigerant R404A is a replacement for lower pressure refrigerants R22 and R502 which are being phased out in accordance with the Montreal Protocol starting with the freeze of production and consumption in 2013 and complete phase out by 2030. Several other refrigerant blends (e.g., R410A) and natural refrigerants (e.g., CO₂) which are in consideration as more environmentally benign replacements for common refrigerant applications, also operate at high reduced pressures.

There have been various liquid-vapor condensation studies, but most have focused on flow through large tube diameters ($D > 3$ mm,) or are limited in a variety of other ways. For example, many two-phase flow studies have been conducted with either pure

refrigerants at low reduced pressures or air-water mixtures. Heat transfer and friction losses are expected to be substantially different for high pressure refrigerants due to their significantly different fluid properties (e.g., liquid-vapor density and viscosity ratios.) In addition, surface tension at high reduced pressures can be significantly lower than at low reduced pressures, and therefore, findings from investigations at high reduced pressures in larger diameter tubes may not be applicable because they most probably do not capture the influence of surface tension. In small tube diameters, the effects of surface tension forces can be significant. In addition, the models previously developed for heat transfer and pressure drop were not typically based on direct measurements of important parameters such as void fraction, adding to the uncertainties in the models.

For example, in annular flow, Garimella *et al.* (2005) modeled pressure drop by applying a force-momentum balance to compute the shear stress at the vapor-liquid interface. The void fraction in this case can be used for the computation of bulk liquid-phase flow velocities. This can be combined with the overall mass flux information and the vapor-liquid quality to yield the slip ratio. In the absence of void fraction models for condensing refrigerants in small channels, they used a void fraction model developed for two-phase liquid metal flow by Baroczy (1965). Wavy flow heat transfer coefficient correlations often rely on void fraction models to predict tube perimeter in contact with gravity driven film condensate or with convective pool heat transfer. Several models, including that of Cavallini *et al.* (2002), rely on void fraction models like the Zivi (1964) correlation, which was developed for water-steam two-phase flow. While the models available are often capable of predicting the data from which they were developed, most models are unable to accurately predict condensation data under different operating conditions and geometries. While the mechanisms of heat transfer in condensing flows are well known qualitatively, some of the inaccuracies can be attributed to poor predictions of the vapor-liquid distribution.

In the present study, high-speed video recordings are taken over a range of tube diameters, mass fluxes and saturation temperatures for condensing high pressure refrigerant R404A. Flow regimes are observed from the high-speed video recordings and image analyses conducted to measure void fractions, vapor bubble velocities, vapor bubble lengths and slug frequencies. The void fraction data from the present study are used to develop a void fraction model, which is used with the flow regime predictions as a basis for pressure drop and heat transfer models. This approach allows for accurate quantification of the vapor and liquid distribution (e.g., film thicknesses, wetted perimeter ratios) throughout the condensation process. A complementing set of pressure drop and heat transfer experiments are conducted under similar operating conditions for validation and refinement of the pressure drop and heat transfer models. This results in a comprehensive approach to predicting pressure drop and heat transfer coefficients based on a void fraction model developed specifically for high pressure condensing refrigerant through microchannels.

This dissertation is organized as follows. A review of relevant literature on two-phase flow mapping, void fraction and condensation pressure drop and heat transfer is presented and the research needs highlighted in Chapter 2. The experimental approach and test facilities and equipment used are described in Chapter 3. The analysis techniques used to evaluate the two-phase flow conditions, pressure drop, and heat transfer coefficients are presented in Chapter 4, with detailed illustrations of the analyses based on representative data points. The image analysis program used to deduce void fraction is explained in Chapter 5 using a representative data point as the basis. Flow regime maps, and void fraction, pressure drop, and heat transfer results are presented and compared with relevant models from the literature in Chapter 6. Void fraction, pressure drop, and heat transfer models for condensing flows in microchannels are presented in

Chapter 7. Conclusions from this study and recommendations for future investigations are provided in Chapter 8. The appendices detail uncertainty propagation, representative experimental data points, primary loop pump heat addition calculations, a preliminary intermittent pressure drop model and void fraction, pressure drop and heat transfer calculations.

CHAPTER 2: LITERATURE REVIEW

An overview of the literature pertinent to this study is presented here. First, work on flow regime mapping is presented, followed by relevant studies on void fraction, pressure drop, and heat transfer during condensation.

2.1 Flow Regime Maps

Accurate flow regime prediction is often the initial step in the modeling of heat transfer and momentum loss in two-phase flow. A significant number of studies have been conducted on flow regime mapping in two-phase flow. Literature related to this work is presented in this section. The section is divided into adiabatic and condensing flows with an emphasis on the difference between large diameter ($D > 3$ mm) and small diameter ($D < 3$ mm) tube sizes.

2.1.1 Adiabatic Flows: Large Diameter Tubes

Two-phase flow research has been conducted for many years with much of the original focus being on air-water, steam, and oil-gas mixtures. Some of the earliest flow regime mapping was conducted by Baker (1954) based on experiments on adiabatic oil-gas mixtures in tube diameters ranging from 101 to 254 mm. He observed and described several different flow regimes and presented criteria for transition from one regime to another. The flow regimes reported by him included bubble, plug, stratified, wavy, slug, annular and spray. He found a strong dependence of the established flow regime on the gas mass flow rate and the ratio of gas-to-liquid mass flow rate. Correction factors for each of the two terms that served as the axes for a flow regime map were developed. The gas mass flow rate correction factor was a function of phase densities and the correction factor for the ratio of mass flow rates was a function of liquid density, viscosity, and surface tension. The correction factors and mass flow rates were used as x- and y- axes

and transition lines were drawn based on visual observations. The correction factors are empirical in nature and the transitions lines were defined subjectively. Baker was one of the first researchers to realize the importance of the different flow regimes on momentum transfer and developed flow regime specific two-phase multipliers to predict pressure drop.

Similarly, Mandhane *et al.* (1974) developed a flow regime map based on a large database of air-water flows. The database consisted of air-water experiments conducted in tube diameters ranging from 12.7 to 165.1 mm, and superficial gas and liquid velocities varying from 0.043 to 170.7 m s⁻¹ and 0 to 7.315 m s⁻¹ respectively. The data consisted of six observed flow regimes; bubble, stratified, wave, slug, annular-mist, and dispersed bubble. They compared their data with previous maps, including Baker (1954), Hoogendoorn (1959), and Govier and Omer (1962), and concluded that new transition criteria were required to better capture flow regime transitions. They proposed a flow regime map for the air-water data based on superficial phase velocities and empirical property corrections.

Taitel and Dukler (1976) developed a flow regime map based on a theoretical approach to understanding flow regime transitions. They predicted five different flow regimes during two-phase flow in horizontal channels, including annular-dispersed, dispersed-bubble, stratified-wavy, stratified-smooth, and intermittent. The transition from stratified to annular-dispersed or from stratified to intermittent flow was based on an interfacial stability analysis. They suggested that the faster moving vapor core led to surface waves because of a Bernoulli effect and that these surface perturbations were dampened by gravity. Therefore, they proposed using the Kelvin-Helmholtz stability theory to develop their transition criteria. The resulting transition criterion is a density ratio modified Froude number. The transition from annular-dispersed to intermittent was predicted to

occur when the liquid level reaches half of the channel height. They found that for horizontal tubes, this occurred at a constant Martinelli parameter of $X = 1.6$. Taitel and Dukler (1976) hypothesized that the transition from stratified smooth to stratified wavy occurred at the onset of wave generation in the lower liquid film. They used wave theory presented by Jeffreys (1926) as the basis for a transition criterion that was a function of non-dimensional phase areas and a wave sheltering number. They predicted the transition from intermittent to dispersed bubble flow by comparing buoyancy forces to the shear forces acting on the vapor bubbles. They found satisfactory agreement with the map of Mandhane *et al.* (1974). Their flow regime map is cited frequently in many studies, and several other maps use it as a starting point, because of the physical considerations used in its development.

Many of these early studies focused solely on air-water or air-oil fluid pairs at atmospheric pressure where fluid and interfacial properties do not change significantly. Weisman *et al.* (1979) investigated the influence of fluid properties and tube diameter on flow regime transitions. Air-water flows in tube diameters ranging from 11.5 to 51 mm were studied and the flow regimes were categorized based on visual observations and dynamic pressure drop signals. The flow regimes observed included plug/bubble, stratified, wavy, slug, annular and dispersed. The liquid properties were systematically altered such that their influence on flow transition could be investigated. The liquid viscosity was altered by adding glycerol to the liquid, the surface tension by adding a surfactant, and the liquid density by adding potassium carbonate solution. The effect of vapor density on flow regimes was investigated by running closed loop experiments on evaporating Freon 113. This was one of the first experimental investigations on refrigerants and it was noted that much higher gas mass flow rates were needed to transition to annular flow than was the case when air was the gas phase. Weisman *et al.* (1979) found significant deficiencies in models available in literature, for example, those

by Mandhane *et al.* (1974) and Taitel and Dukler (1976), and developed their own flow regime map using property corrections similar to those by Mandhane *et al.* (1974). They found that the most influential parameters for the transition lines were the superficial phase velocities.

While most flow regime maps have been based on observations, there have been efforts to quantitatively assess flow regimes as well. Canière *et al.* (2007) investigated adiabatic air-water flow in 9 mm tubes. In an effort to remove subjectivity from the analysis, they observed flow regimes and simultaneously used capacitance sensors. This allowed for local void fraction measurements and the dynamic signal also allows for quantitative assessment between different regimes using void fraction values and frequencies. The regimes were classified into four major categories; annular, wavy, stratified and intermittent flow. They hypothesized that the signal frequency and amplitude domain would allow for classification of flow regimes through statistical categorization.

2.1.2 Adiabatic Flows: Small Channels

One of the first investigations of capillary effects on two-phase flow was conducted by Suo and Griffith (1964). They investigated gas-liquid flows (air-water, N₂-water, Heptane-He, and Heptane-N₂) in 1-mm diameter tubes. They noted that surface-tension forces dominated at this scale and that capillary slug flow existed regardless of tube orientation. They obtained correlations of transition lines from phase velocity ratios and film thickness using a dimensional analysis. They found that the transition from annular to slug flow could be predicted well when comparing phase velocities to the capillary number. The transition criterion from slug to bubbly slug flow was developed by comparing bubble Reynolds and Weber numbers. It is important to note that in their analysis, they assumed $\rho_l/\rho_v \gg 1$ and $\mu_l/\mu_v > 25$, which is consistent with air as the vapor

phase. The property ratios in condensing refrigerants, specifically at high pressures, do not meet these criteria. For example, the liquid-to-vapor density and viscosity ratios of R404A vary from 18.6 and 8.1 at $T_{\text{sat}} = 30^{\circ}\text{C}$ to 4.8 and 4.2 at $T_{\text{sat}} = 60^{\circ}\text{C}$.

Barnea *et al.* (1983) also investigated the effects of surface tension and decreasing tube diameter on flow regime transitions. They conducted experiments on air-water flows through tube diameters ranging from 4 to 12 mm. The flow regime map presented by (Taitel and Dukler, 1976) predicted all transitions well except for the transition from stratified to slug flow in horizontal tubes. This transition criterion was modified by considering the effects of surface tension. They theorized that surface tension aids in pulling the liquid wave up the tube to allow for a liquid bridge to form while gravity resists this action. From a force balance, a transition criterion was developed by evaluating the minimum vapor height that must exist to prevent intermittent flow from existing. This replaced the Kelvin-Helmholtz stability transition criterion at small tube diameters.

Damianides and Westwater (1988) furthered the understanding of the effects of tube diameter and channel geometries on flow regimes. Visualization experiments were conducted on air-water flows through an offset-fin heat exchanger design and through several round tubes ranging in diameter from 1 to 5 mm. Simultaneous high frequency pressure drop data were obtained to aid in flow regime classification. The observed flow regimes were categorized as bubble, annular, and intermittent. Smooth stratified and wavy stratified flows were not observed in the smallest channels. It was observed that the flow regime at this scale was most influenced by the superficial liquid velocity and that the superficial gas velocity had less of an influence. The flow transitioned directly from annular to intermittent, which was caused by the generation of roll waves because of the absence of the stratified region. They described this transition region as a pseudo-

slug region where both annular and intermittent flow is present. They compared their data to the Taitel and Dukler (1976) map and found reasonable agreement with their largest tube data (5 mm) but as tube diameter decreased, agreement worsened. Damianides and Westwater (1988) attributed these inaccuracies in transitions to different mechanisms that were driving transition in small tubes compared to the theoretical considerations for large tubes used by Taitel and Dukler (1976).

Fukano *et al.* (1989) studied the influence of surface tension forces in adiabatic air-water flows in tube diameters ranging from 1 to 4.9 mm with a focus on transition criteria for intermittent flow. Bubbly, plug, slug and annular flows were observed and were classified based on visual inspection and dynamic pressure drop signals. It was noted that at this length scale, any separated (stratified) flow was nonexistent. Good agreement with their data and the transition criteria presented by Barnea *et al.* (1983) was found assuming that plug and slug flow were both considered intermittent. Fukano *et al.* (1989) found poor agreement with the Mandhane *et al.* (1974) map, which they concluded was a result of the influence of tube diameter. Fukano *et al.* (1989) developed pressure drop correlations for each flow regime and developed vapor bubble velocity and length models as the basis for their intermittent model.

The effect of hydraulic diameter and tube geometry was studied by Coleman and Garimella (1999). Adiabatic air-water flows through circular and rectangular channels were investigated for hydraulic diameters ranging from 1.3 to 5.5 mm. The flow regimes were classified into four major regimes and several flow patterns. The flow regimes observed were classified as either dispersed, intermittent, stratified, or annular flow. The dispersed flow regime was subdivided into bubble and dispersed flow patterns. The flow patterns in the intermittent flow regime were subdivided into elongated bubble and slug flow. The stratified regime was categorized as either stratified smooth or stratified-wavy

flow patterns, and the annular regime consisted of annular-wavy and annular film patterns. The stratified smooth pattern was not observed throughout their experiments. Their data were compared with flow regime maps presented by Taitel and Dukler (1976), Damianides and Westwater (1988), Fukano *et al.* (1989), and Weisman *et al.* (1979). Coleman and Garimella (1999) found poor agreement between their data and the flow regime maps that did not account for decreased tube diameter and surface tension effects; namely the Taitel and Dukler (1976) and Weisman *et al.* (1979) maps. Good agreement between the data obtained in their study and that of Damianides and Westwater (1988) and Fukano *et al.* (1989) was found and it was observed that tube diameter and surface tension were less influential at tube diameters in the range of 10 mm and greater, but at smaller diameters, these parameters become important. Coleman and Garimella (1999) found that channel geometry also had an influence on flow regime transitions. A comparison between their observations from a rectangular channel ($D_h = 5.36$ mm, and $AR = 0.725$) to that of a circular tube with a similar diameter ($D = 5.5$ mm) was made to determine the effects of channel geometry. It was hypothesized that the effect of surface tension in the rectangular channel would be more significant as a result of the liquid getting pulled to the corners. The transition to dispersed flow was observed to occur at a much higher superficial liquid velocity and the transition from intermittent to annular, or intermittent to stratified flows occurred at a much lower superficial vapor velocity. Regardless of tube geometry, it was found that decreasing the hydraulic diameter resulted in annular and intermittent flow regime regions increasing in importance and in the elimination of the wavy flow regime.

Similarly, Triplett *et al.* (1999b) independently investigated circular and semi-triangular channels with hydraulic diameters ranging from 1.09 to 1.49 mm. Superficial gas and liquid velocities were varied from 0.02 to 80 m s^{-1} and 0.02 to 8 m s^{-1} , respectively, and bubbly, churn, slug, slug-annular and annular flow were observed. The stratified flow

regime was absent from both geometries signifying the dominance of surface tension. The data obtained in this study were compared with relevant two-phase flow maps and data. Poor agreement between their data and the transition criteria of Suo and Griffith (1964) was found, but there was satisfactory agreement between their data and Taitel *et al.* (1980). Triplett *et al.* (1999b) stated that this agreement was most probably coincidental, given that the assumptions used in developing the Taitel *et al.* (1980) map are not applicable in microchannels. They found good agreement between their data and that of air-water studies conducted under similar conditions and tube diameters (Damianides and Westwater, 1988; Fukano and Kariyasaki, 1993). The only difference was in the naming and description of similar flow regimes in the two studies.

While air-water studies provide insights into two-phase phenomena, their properties can vary significantly from those of refrigerants. Yang and Shieh (2001) conducted an experimental investigation of adiabatic two-phase flow of air-water and R134a in tubes ranging from 1 to 3 mm in diameter. The R134a experiments were conducted under adiabatic conditions at a saturation temperature of 30°C ($p_r = 0.19$.) Like several previous studies, they noted the increased importance of surface tension forces at smaller tube diameters. Six flow regimes were observed in their study; bubble, slug, plug, wavy stratified, dispersed and annular flow. It was noted that it was difficult to obtain clear transition lines from one flow regime to another, specifically slug-to-annular in air-water experiments but that the transitions in R134a experiments were more defined and sharp. Good agreement was found between their air-water data and those of Damianides and Westwater (1988). Yang and Shieh (2001) observed a shift in the transition from annular to slug flow for R134a, which was found to occur at much lower superficial vapor velocities as compared to air-water data. It was also noted that there were significant deviations in transition lines from bubble to plug and slug flow. They attributed this to differences in fluid properties and suggested that the large difference in surface tension

had the biggest impact. It was hypothesized that surface tension acted to minimize interfacial surface area which allows for bubbles to maintain their circular shapes and delayed the transition to annular flow. It was found that none of the existing flow pattern maps were able to predict both air-water and refrigerant data well because of the significantly different fluid properties. Therefore, one should be careful extrapolating two-phase flow maps developed for air-water studies to fluids with significantly different properties.

More recent studies have focused on sub-millimeter air-water flows. Serizawa *et al.* (2002) examined hydraulic diameters ranging from 20 to 100 μm for air-water flow and 50 μm for steam-water flow. Several interesting flow patterns were observed including disperse bubbly, gas slug, liquid ring, liquid lump, annular, frothy or wispy annular, rivulet, liquid droplet flow. Void fraction measurements were obtained from the visual data and found good agreement with the Armand (1946) correlation. As a result of the increased importance of surface tension at the microscales, Serizawa *et al.* (2002) hypothesized that surface roughness and cleanliness would influence observed flow regimes and transitions. The 100 μm tubes were systematically cleaned and the same set of visualization tests were conducted for comparison. Different flow regimes were observed following the cleaning, which was attributed to better surface wettability. Their observed data compared well with the Mandhane *et al.* (1974) map, which tended to capture the general flow regime trends despite being constructed from data for tubes with diameters an order of magnitude greater.

Kawahara *et al.* (2002) investigated N_2 -water flow through a silica tube with a diameter of 100 μm . They measured void fraction and pressure drop while simultaneously taking high speed video. The flow regimes observed were intermittent and semi-annular which they categorized further into five flow patterns. The flow patterns observed were liquid

alone (or liquid slug,) gas core with a smooth-thin liquid film, gas core with a ring-shaped liquid film, gas core with a smooth-thick liquid film, and a serpentine-like gas core with a deformed liquid film. During experimentation, it was noted that several different flow regimes occurred under the same operating conditions and a probability analysis was conducted to divide the observed flow regimes into four categories for mapping: slug-ring, ring-slug, multiple, and semi annular. Some discrepancies between their observed results and those reported by Damianides and Westwater (1988), Fukano and Kariyasaki (1993), and Triplett *et al.* (1999b) were observed. While Kawahara *et al.* (2002) noted some differences in the locations of the transition lines, the largest difference compared to previous work was the observation of the "multiple" flow regime and the absence of the bubbly and churn flow regime. The lack of the bubble and churn flow regimes was attributed to the existence of laminar flow throughout their experiments. Due to the subjective nature of flow visualization, it is possible that the "multiple" flow regime observed here may be a result of different observations of the same flow structure. It is also possible that the regime was observed due to the oscillation and inability to operate the tests steadily.

Chung *et al.* (2004) studied the influence of tube geometry by comparing flow regime, pressure drop and void fraction data for air-water flows in circular ($D = 100 \mu\text{m}$) and square ($D_h = 95.6 \mu\text{m}$) channels. As mentioned in their previous work (Kawahara *et al.*, 2002), bubbly or churn flow patterns were not observed and their data were categorized into four patterns; slug-ring, ring-slug, semi-annular and "multiple" flow. In the square channels, the liquid-ring flow regime was not observed, which the authors attributed to surface tension forces from the corners. Slight deviations in transition between circular and square data were found, and different flow regime maps were developed for both geometries.

2.1.3 Condensing Flows: Large Diameter Tubes

There have been a plethora of flow regime studies on air-water adiabatic two-phase flow, but studies on condensing fluids have been limited. The difference in fluid properties between air-water and refrigerants is significant and therefore it is expected that the transition criteria will be different. Also, many of the experimentally based flow regime maps for air-water experiments are presented in terms of superficial velocity plots. This may lead to poor predictions of transitions for other fluids because superficial velocities assume that each phase takes up the entire cross-sectional area of the tube. Studies on flow regimes in phase-change flows have primarily focused on larger tube diameters.

Traviss and Rohsenow (1973) investigated condensation of refrigerant R12 in an 8-mm diameter circular tube. Experiments were conducted with saturation temperatures ranging from 10 to 40°C ($0.10 < p_r < 0.23$) and mass fluxes ranging from 100 to 990 kg m⁻² s⁻¹. They observed dispersed, annular, semi-annular and slug flow. While it was stated that the observed flow regimes could be divided into more detailed flow patterns, it was stated that the observations were complex enough and that the objective of the study did not warrant such description. Their data and the data of Soliman and Azer (1971) were compared to the Baker (1954) and Scott (1963) maps. The Scott (1963) map is a modification of the Baker plot with the addition of transition regions instead of discrete transition lines. Traviss and Rohsenow (1973) found reasonably good agreement with the Scott (1963) map and stated that the effect of condensation on the prevalent flow regime was not substantial for these tube diameters. However, it was noted that the maps did not include the semi-annular (or partially stratified regime) and a transition criterion for this transition using a constant film Froude number of 45 was suggested.

One of the earliest studies on the influence of tube diameter on condensing refrigerants was conducted by Breber *et al.* (1980). The effects of tube diameters ranging from 4.8 to

22, 50.8 mm and properties of several different fluids (R11, R12, R113, steam, n-pentane) during condensation were investigated. The experimental data were taken from a large database that included flow visualization work from 10 different studies. Breber *et al.* (1980) compared these data to the Taitel and Dukler (1976) map and found relatively good agreement for data with tube diameters ranging from 8 to 22 mm. For the small tube data ($D = 4.8$ mm,) the Taitel and Dukler (1976) map predicted all of the wavy and slug flows as annular, which Breber *et al.* (1980) attributed to the lack of consideration of surface tension forces in the formulation of the transition criteria. In an effort to develop a simple and useful design tool, Breber *et al.* (1980) focused on dividing the condensation process into two modes: inertial and gravity driven. They differentiated between the zones using a dimensionless gas velocity, J_G^* , and the Martinelli parameter, X . In addition, they developed a map that predicts flow regimes with transition *regions* instead of abrupt transition *lines*. For each regime, a specific heat transfer coefficient is suggested and when in the transition region, a linear interpolation of the two regimes was suggested.

Tandon *et al.* (1982) developed a flow regime map based on data from previous researchers such as Breber *et al.* (1980) on condensing R12 and R113 in tube diameters ranging from 4.8 to 15.9 mm. Five different flow regimes were observed; spray, annular and semi-annular, wavy, slug and plug. Transition criteria between slug, wavy, annular and spray flow regimes were developed based on the same dimensionless vapor velocity, J_G^* , as Breber *et al.* (1980) and a volumetric liquid to vapor ratio $(1-\alpha)/\alpha$. They estimated the void fraction using the Smith (1969) correlation, which was developed based on boiling and air-water experiments. The flow regimes were categorized using constant values of the two parameters which allowed for simple graphical representations of the transitions.

Many of the early refrigerant studies focused on low pressure refrigerants where fluid properties can be significantly different than those at high pressures. Dobson and Chato (1998) investigated flow regimes and their effect on condensation heat transfer for various refrigerants (R12, R22, R134a, and near azeotropic blends of R32/R125) through 3.14 and 7.04 mm smooth tubes. The saturation temperatures of the experiments ranged from 35 to 60°C ($0.21 < p_r < 0.57$.) Flow regimes observed from the study were stratified, wavy, wavy annular, annular, annular-mist and slug flows. Dobson and Chato (1998) stated that the most dominant influence on observed flow regime was of mass flux and quality. This is similar to air-water work where the superficial phase velocities were found to be the most dominant factors. At the lowest mass flux ($G = 25 \text{ kg m}^{-2} \text{ s}^{-1}$), the smooth-stratified regime was observed during condensation. As the mass flux was increased, interfacial waves were observed, and at low qualities slugging occurred. Only at high mass fluxes ($G > 500 \text{ kg m}^{-2} \text{ s}^{-1}$) was wavy annular, and annular flow observed. The fluid properties and diameter had more subtle influences on the observed flow regime transitions. The range of qualities at which annular flow existed was found to increase with decreasing saturation temperature. It was hypothesized that this was a result of increasing difference in vapor and liquid phase properties and surface tension. Agreement between their data and the Mandhane *et al.* (1974) map was poor, which was attributed to the difference in properties between the refrigerants and air-water mixtures. The Taitel and Dukler (1976) map predicted the transition from stratified to wavy flow well but failed to accurately capture the transition from slug to annular, slug to annular-wavy and slug to wavy flows. The data agreed well with the transition criteria from wavy to annular flow presented by Soliman (1982). Similar to Breber *et al.* (1980), Dobson and Chato (1998) focused on determining the transition between shear and gravity driven flow as a basis for their heat transfer models. Based on their observations, it was concluded that all flows with mass fluxes less than $500 \text{ kg m}^{-2} \text{ s}^{-1}$ should be considered to be in the gravity driven regime. In instances where the mass flux is greater

than $500 \text{ kg m}^{-2} \text{ s}^{-1}$, the modified Froude number presented by Soliman (1982) was used to differentiate between gravity and shear-driven condensation. For $Fr_{So} > 20$ the flow is considered shear driven. These criteria developed by Dobson and Chato (1998) are most applicable to fluids and tube diameters used in their study, and also use dimensional parameters such as mass flux to define the transitions. Also, given the discrete nature of the transition lines, discontinuities in predicted heat transfer coefficients across the transitions can be expected.

Cavallini *et al.* (2002) developed a two-phase flow regime map based on a survey of the literature and applied it to a large heat transfer and pressure drop data base of condensing refrigerants at various pressures. Comparing transition criteria from Breber *et al.* (1980), Sardesai *et al.* (1981), Tandon *et al.* (1982), Dobson and Chato (1998) and Rabas and Arman (2000), they determined that annular flow will always exist when the dimensionless gas velocity, J_G^* , is greater than 2.5. When the dimensionless gas velocity is less than this threshold, a constant turbulent-turbulent Martinelli parameter is used to determine the transition from stratified-annular to intermittent or stratified. Cavallini *et al.* (2002) used these transitions as the basis for the development of multi-regime heat transfer and pressure drop models for several refrigerants (R22, R134a, R125, R32, R236ea, R407C, and R410A) in a circular tube of 8 mm.

Trying to use the similarities in phase-change processes, El Hajal *et al.* (2003) presented a condensation flow regime map that they adapted from the flow boiling map of Kattan *et al.* (1998a). The map was originally based on transition criteria presented by Taitel and Dukler (1976). The major flow regimes predicted by the map are fully-stratified, stratified-wavy, intermittent, annular, mist, and bubble flow. They developed a void fraction correlation based on heat transfer coefficient analysis, which enabled liquid level height predictions to be used for flow transition criteria. It is important to note that the

transition from annular to intermittent flow was suggested to occur at a turbulent-turbulent Martinelli parameter of $X_{tt} = 0.34$. For most refrigerants, this corresponds to a transition quality of about 0.5, which indicates an intermittent flow region much larger than has been reported in the literature for condensing flow. It was stated that their flow regime map agreed reasonably well with maps in literature. The transition lines from wavy to annular agreed with those of Sardesai *et al.* (1981) and Dobson and Chato (1998). What is particularly interesting is that the agreement between the work of the map presented here by El Hajal *et al.* (2003) and that of Cavallini *et al.* (2002) is poor despite having some of the authors being common to both papers. Much of the wavy regime from the Cavallini *et al.* (2002) map overlapped the annular and intermittent regime of El Hajal *et al.* (2003). El Hajal *et al.* (2003) attributed this discrepancy to the vague description of the transition and stratified-wavy regimes. They state that this flow regime map is applicable for $16 < G < 1532 \text{ kg m}^{-2} \text{ s}^{-1}$, $3.14 < D < 21.4 \text{ mm}$, $0.02 < p_r < 0.8$ and $76 (We_l/Fr) < 884$ and for over 20 fluids, although substantiation for the wide applicability range is not provided.

More recently, Jassim *et al.* (2007); Jassim *et al.* (2008b) and Jassim *et al.* (2008b) noted the difficulty in observing specific flow regimes in discrete regions and concluded that taking a probabilistic approach to predicting flow conditions would yield continuous functions when used as the basis for heat transfer and pressure drop models. Visualization experiments were conducted on refrigerant R134a at 25, 35, and 49.7°C ($p_r = 0.16, 0.22, 0.32$) and R410A at 25°C ($p_r = 0.3351$) condensing through tubes ranging in diameter from 1.74 to 8.00 mm. They developed image recognition tools that observed the flow regime in real time and categorized it as either intermittent-liquid, stratified or annular flow. The time fraction for each flow regime within each data point was deduced from this. While this is a unique approach to predict flow regimes for heat transfer and pressure drop modeling because it allows for continuous functions across transitions,

some of the results from these maps appear not to be physically feasible. For example, it is unlikely that annular, stratified and intermittent flow occur simultaneously as predicted by their weighting function. This is either a result of predicting large amplitude waves as liquid slugs as the flow transitions from wavy to annular, or perhaps predicting a thin film as annular flow as the flow transitions from intermittent to annular. The flow regimes could also be misinterpreted if the field of view is not wide enough to observe all the characteristics of the flow. For the examples presented in their work, the field of view was approximately three tube diameters, which may not be sufficient.

2.1.4 Condensing Flows: Small Channels

Coleman and Garimella (2000a, b, 2003) investigated the effects of hydraulic diameter and channel geometry on condensing flows of R134a at saturation temperatures of interest ($T_{\text{sat}} = 52^{\circ}\text{C}$, $T_r = 0.52$, $p_r = 0.34$) for heat rejection in air-conditioning systems to the ambient. Condensing flow was visualized in a 4.91 mm circular tube, 1 to 4 mm hydraulic diameter square channels, and two different orientations for rectangular channels of 4×6 mm and 2×4 mm. Four major flow regimes were observed; intermittent, wavy, annular and dispersed. Several different flow patterns were observed within each major flow regime. It was found that the hydraulic diameter is more significant in determining flow regimes and transitions than shape or aspect ratio. As tube diameter decreased, it was found that the extent of wavy flow on the flow regime map diminished. This was attributed to the decreasing importance of gravity and the increased importance of surface tension forces at the smaller diameters. It was also found that the extent of the intermittent flow regime increased as tube diameter decreased. Their results were compared with the Wang *et al.* (1997) and Weisman *et al.* (1979) flow regime maps with good agreement. The discrepancies that were there were primarily due to different nomenclature and interpretations of the observed regimes. For example, what

Coleman and Garimella referred to as "disperse wave," Wang *et al.* (1997) labeled wavy-annular. Similarly, Weisman *et al.* (1979) designated mist, annular, and dispersed wave as annular flow. Coleman and Garimella also compared their R134a data with observations made in a previous investigation using air-water (Coleman and Garimella, 1999). They concluded that simply using superficial velocity plots for flow regime mapping led to poor predictions for fluids with significantly different phase properties and that the use of non-dimensional numbers, such as the Froude number, would yield more accurate transition criteria. From their observed data, they developed a flow regime map for condensing R134a using mass flux and quality as the axes. In the absence of detailed quantitative information about the cross-sectional areas occupied by the different phases or the distribution of the phases, they decided to use mass flux and quality as the coordinate axes, because these are directly measured parameters and do not require assumptions such as those that would be necessary to obtain superficial velocities and other similar variables.

Nema (2007) used the flow regime data from Coleman and Garimella (2000a, b, 2003) and developed transition criteria for condensation in channels with small hydraulic diameters using dimensionless parameters. Using a systematic dimensional analysis, he found that the two best parameters for developing transition lines were the vapor Weber number, We_v , and the modified Froude number, Fr_{mod} . He incorporated several physical observations from Coleman and Garimella (2000a, b, 2003) into these transition criteria. The first was the absence of wavy flow in small tube diameters. Nema (2007) differentiated between large and small tube diameters using the Bond number, Bo . The critical Bond number was determined based on the force balance introduced by Barnea *et al.* (1983) for two-phase flow through small diameter tubes. If the Bond number is less than this critical value, wavy flow is absent and the flow is predicted to transition directly from annular to intermittent flow. If the Bond number is greater than the critical value,

the flow transitions from intermittent to wavy to annular. Another key feature of the transition criteria presented in this work is the transition to intermittent flow. The original work by Taitel and Dukler (1976) considered this transition to arise due to large amplitude waves overcoming gravity forces to bridge the vapor core to the top of the tube for wavy to intermittent flow and used a constant Martinelli parameter for the transition for annular to intermittent flow. The force balance between gravitational and inertial forces for this transition is also accomplished through the use of a constant modified Froude number by Taitel and Dukler (1976), or in the case of Breber *et al.* (1980), Tandon *et al.* (1982), and Cavallini *et al.* (2002), a non-dimensional vapor velocity, J_G^* , is used. However, both transition criteria result in counter-intuitive trends to what is observed for the transition to intermittent flow as diameter decreases. To capture this trend, i.e., as the diameter decreases, the extent of intermittent flow regime increases, Nema (2007) predicted the transition from wavy or annular flow to intermittent flow using the vapor Weber number.

Jassim and Newell (2006) conducted visualization studies of two-phase flow through a multiport microchannel test section. The test section consisted of six parallel tubes with a diameter of 1.54 mm. Adiabatic experiments were conducted on air-water flows, and condensing refrigerants R134a and R410A were investigated at a saturation temperature of 10°C (R134a, $p_r = 0.10$, R410A, $p_r = 0.22$.) Using the image recognition tools developed in a previous study, they evaluated the flow regimes through each tube for a given data point and developed probabilistic flow regime models. Only intermittent and annular flow was observed.

2.1.5 Summary

There has been extensive work on flow regime determination as seen in this review of the literature and summarized in Table 2.1. From these investigations, it can be seen that there are three different approaches to determine the dominant flow regime under a given

operating condition. The most common approach is through the use of superficial velocities. This approach yields good results for a given fluid combination and tube diameter but cannot be accurately extrapolated to different fluids. A majority of the experimental studies have focused on adiabatic air-water studies, which have drastically different fluid properties than those of refrigerants. As a result, one should use the original flow regime maps developed by Baker (1954) and Mandhane *et al.* (1974) with caution. The inadequacy of transition criteria developed from air-water studies to predict refrigerant transitions was demonstrated by Coleman and Garimella (2003), which they attributed to drastically different properties of the two fluid pairs.

The second approach is through the use of non-dimensional parameters explained through physical interpretations of the transition phenomena. This approach is more fundamentally sound, but can often ignore the effects of some relevant forces and dimensions depending on the assumptions used to formulate the transition mechanism. The most widely used map because of its theoretical basis is the Taitel and Dukler (1976) map. Many researchers have used this as the basis to develop specific maps for specific situations and geometries, and also in an attempt to extend its range of applicability. Researchers in condensation have often simplified the transition criteria and focused solely on the transition from gravity to shear driven flow. Breber *et al.* (1980), Tandon *et al.* (1982), Dobson and Chato (1998), and Cavallini *et al.* (2002) all used some form of a modified Froude number to predict this transition. While this is the most important transition in large tubes, the gravity driven regime is not very prevalent in small tubes and the intermittent regime becomes more likely.

One of the most important properties that affects transitions in small tubes is surface tension, which is not considered in the Taitel and Dukler (1976) map. Several researchers highlighted above have investigated these effects in small tube diameters for

air-water flows, but there has been less emphasis on condensing refrigerants. However, there have been few studies focusing on the increased importance of surface tension in small channels for refrigerants. Nema (2007) used the visualization data from Coleman and Garimella (2000a, b, 2003) to develop dimensionless transition criteria in small tube diameters, and accounts for the influence of surface tension. This approach was based on the physical mechanisms applicable at small diameters, but was based on data from only R134a at one specific operating condition, and needs to be validated with more data.

The methods discussed above result in discrete transition criteria, and using them as the basis for predicting heat and momentum transfer can often lead to unrealistic discontinuities in the prediction of heat transfer coefficients and pressure drops. This is overcome by interpolations in the transition regions between multiple regime-specific correlations. The prediction of flow regimes using a probabilistic approach minimizes such discontinuities without defining specific transition regions. For example, Jassim *et al.* (Jassim and Newell, 2006; Jassim *et al.*, 2007; Jassim *et al.*, 2008a) used probability weighting functions for condensing flows as the basis for void fraction, pressure drop and heat transfer models. While this approach leads to continuous functions throughout, the weighting functions are highly empirical and often result in unduly high overlaps between flow regimes without a corresponding physical basis.

Table 2.1: Summary of Flow Regime Literature

Investigator(s)	Fluid(s)	D_h	p_r	Comments
Adiabatic - Large Diameter Tubes				
Baker (1954)	Oil-gas	101 - 254 mm		<ul style="list-style-type: none"> • Superficial velocity coordinate map with empirical property corrections
Mandhane <i>et al.</i> (1974)	Air-water	12.7-165.1 mm		<ul style="list-style-type: none"> • Superficial velocity coordinate map with empirical property corrections
Taitel and Dukler (1976)	Air-water			<ul style="list-style-type: none"> • Theoretical basis for flow regime transitions
Weisman <i>et al.</i> (1979)	Air - water /glycol /surfactant / potassium carbonate	11.5 - 51 mm		<ul style="list-style-type: none"> • Modified Mandhane <i>et al.</i> (1974) map using property correction terms
Canière <i>et al.</i> (2007)	Air-Water	9 mm		<ul style="list-style-type: none"> • Flow regime assessment using capacitance sensors
Adiabatic - Small Tubes				
Suo and Griffith (1964)	Air-water, N ₂ -water, Heptane-He, Heptane-N ₂	1 mm		<ul style="list-style-type: none"> • Dimensionless transition criteria for flow patterns within intermittent flow • Criteria for surface tension dominated region
Barnea <i>et al.</i> (1983)	Air-water	4 - 12 mm		<ul style="list-style-type: none"> • Modified Taitel and Dukler (1976) to account for surface tension for intermittent flow transition
Damianides and Westwater (1988)	Air-water	1 - 5 mm		<ul style="list-style-type: none"> • Agreement with Taitel and Dukler (1976) worsens with decreasing D (decrease in stratified regime)
Fukano <i>et al.</i> (1989)	Air-water	1 - 4.9 mm		<ul style="list-style-type: none"> • Good agreement with Barnea <i>et al.</i> (1983)
Coleman and Garimella (1999)	Air-water	1.3 - 5.5 mm (circular); 5.35 (AR = 0.725, rectangular)		<ul style="list-style-type: none"> • Hydraulic diameter more influential than geometry • Stratified diminishes and intermittent regime increases as D decreases
Triplett <i>et al.</i> (1999b)	Air-water	1.1, 1.45 mm (circular) 1.09, 1.49 mm (triangular)		<ul style="list-style-type: none"> • No stratified flow observed • Data agreed with Damianides and Westwater (1988), Fukano <i>et al.</i> (1989), and Fukano and Kariyasaki (1993)
Yang and Shieh (2001)	Air-water, R134a	1, 2, 3 mm	0.19	<ul style="list-style-type: none"> • Air-water transitions difficult to decipher and R134a transitions clear/sharp • Properties significantly different and map to capture transitions of both unlikely
Serizawa <i>et al.</i> (2002)	Air-water Steam-water	20-100 μ m 50 μ m		<ul style="list-style-type: none"> • Observed several new regimes at this scale • Investigated surface contamination effects

Table 2.1 continued...

Investigator(s)	Fluid(s)	D_h	p_r	Comments
Kawahara <i>et al.</i> (2002)	N ₂ - water	100 μ m		<ul style="list-style-type: none"> Did not observe stratified or bubbly flow Developed flow regime map based on probability of occurrence
Chung and Kawaji (2004); Chung <i>et al.</i> (2004)	N ₂ -water	100 μ m (circular) 95.6 μ m (square)		<ul style="list-style-type: none"> Investigated effects of channel geometries and found slight deviations
Condensation				
Traviss and Rohsenow (1973)	R12	8 mm	0.10 - 0.23	<ul style="list-style-type: none"> Reasonable agreement with Baker (1954) Semi-annular regime transition defined by Fr
Breber <i>et al.</i> (1980)	R11, R12, R113, steam, n-pentane	4.8 - 22 mm 50.8 mm		<ul style="list-style-type: none"> Large database of visualization data Developed transition criteria using dimensionless gas velocity, J_G^*, and Martinelli parameter, X Transition <i>regions</i> instead of abrupt <i>lines</i>
Tandon <i>et al.</i> (1982)	R12, R113	4.8 - 15.9 mm		<ul style="list-style-type: none"> Developed transition criteria using dimensionless gas velocity, J_G^*, and volumetric liquid/vapor ratio using Smith (1969) α model
Dobson and Chato (1998)	R12, R22, R134a, R32/R125	3.14, 4.57, 7.04 mm	0.21 - 0.57	<ul style="list-style-type: none"> Differentiated between shear and gravity driven condensation using G and Fr_{So}
Coleman and Garimella (2000a,b, 2003)	R134a	4.91 mm (circular) 1-4 mm (square) 4.8, 2.7 mm (rectangular)	0.34	<ul style="list-style-type: none"> D is more influential than AR for transition criteria Intermittent and annular flow increase, stratified decreases as D decreases Transition criteria using $G-x$
Cavallini <i>et al.</i> (2002)				<ul style="list-style-type: none"> Developed transition criteria using Dimensionless gas velocity, J_G^*, and Martinelli parameter, X_{tt}, based on data from several sources
El Hajal <i>et al.</i> (2003)				<ul style="list-style-type: none"> Modified Kattan <i>et al.</i> (1998a) flow boiling map
Jassim and Newell (2006)	R134a R410A	1.54 mm	0.10 0.22	<ul style="list-style-type: none"> Used image recognition program to capture flow regimes in 6 parallel tubes Developed probabilistic flow regime maps for microchannels
Jassim <i>et al.</i> (2007), Jassim <i>et al.</i> (2008b)	R134a R410A	1.74 - 8.0 mm	0.16 - 0.33	<ul style="list-style-type: none"> Developed image recognition tools for flow regime observation Presented probabilistic flow regime maps
Nema (2007)				<ul style="list-style-type: none"> Developed non-dimensional transition criteria based on Coleman and Garimella (2000a, b, 2003) data Bo to determine when wavy flow was present, We_v and Fr_{mod} for regime transitions

2.2 Void Fraction

Similar to the literature on flow regime mapping, there is an abundance of experimental studies on void fraction in adiabatic air-water flows, with the same limitations of extrapolation to condensing refrigerant flows as was seen in flow regime mapping. This review focuses primarily on condensing refrigerant studies and air-water studies at small diameters. The review of the literature on void fraction presented here is divided into two main categories; large and small diameter channel studies.

2.2.1 Large Diameter Channels

One of the earliest studies on void fraction was conducted by Armand (1946) on air-water two-phase flow. He developed empirical correlation in which a constant multiplier of 0.83 was applied to the homogeneous void fraction. Because of the simplicity of this model, it is often used and modified by researchers to estimate void fraction.

Another early void fraction study was conducted by Isbin *et al.* (1959). Void fractions of steam-water flows were measured through a horizontal tube with a diameter of 12.29 mm using a radiation-absorption method. Vapor and liquid phases have significantly different densities, which results in different absorption characteristics of electromagnetic radiation. An electromagnetic wave is passed through the two-phase flow and the intensity of the wave is measured using a scintillator combined with a photomultiplier. The intensity of the signal is calibrated using completely liquid and completely vapor filled tubes to allow for quantification of the void fraction. Pressure drop was also measured simultaneously. A sufficient amount of data to justify a correlation was not obtained but it was possible to evaluate the influence of void fraction on the pressure drop two-phase multiplier. They found that the liquid two-phase multiplier had an inverse relationship with the liquid fraction, or one minus the void fraction.

In many cases, researchers have developed theoretical models to predict void fraction because of the challenges in measuring void fraction. Zivi (1964) developed an analytical slip model to predict void fraction in steam-water flows. His theory was based on the concept that under steady-state conditions, a thermodynamic process will reach a state of minimum entropy generation. With this assumption, he developed a slip ratio model for three cases. The first case was for annular flow with no liquid entrainment in the vapor core, and assuming no wall friction. This yielded the simplest result where the slip ratio was found to be $S = (\rho_l/\rho_v)^{1/3}$. Slip ratio models were also developed that consider the wall shear stress and liquid entrainment. Despite being developed for steam-water flows, the Zivi (1964) void fraction model is often used in refrigerant two-phase flow models. For example, the stratified-wavy heat transfer model presented by Cavallini *et al.* (2002) relies on the Zivi (1964) void fraction to predict the wetted perimeter fraction in contact with the stratified pool.

Baroczy (1965) investigated void fraction in two-phase flow for liquid mercury-nitrogen and air-water flowing through channels. He tabulated liquid hold-up, or $(1-\alpha)$, versus Martinelli parameter. Butterworth (1975) developed a Martinelli parameter based void fraction correlation based on this table which is commonly used in two-phase flow because of its simplicity (Equation 6.23.) It was recommended by Rice (1987) for refrigerants and is used in the pressure drop and heat transfer models developed by Garimella and co-workers (Garimella *et al.*, 2005; Bandhauer *et al.*, 2006).

An early study on void fraction in two-phase flow, which serves as the basis for refrigerant models, is that of Rouhani and Axelsson (1970). They studied void fraction in boiling steam flows through vertical annuli, rod clusters and rectangular channels ranging in hydraulic diameter from 4.4 to 46.5 mm. They proposed a modified version of the Zuber and Findlay (1965) drift-flux model based on their data for vertical flows. They fit

flow regime specific distribution parameters and found excellent agreement with their data in the sub-cooled and saturated boiling regions.

Another theoretical void fraction formulation was developed by Ishii (1977), in which a flow regime specific drift flux model for disperse, churn-turbulent and annular, annular mist flow was developed. Distribution functions and vapor drift velocities were developed for each regime by taking into account specific interfacial geometries, and body-force and shear balances. They found good agreement with a large database of void fraction measurements available from the literature. Channel geometry specific distribution functions were also developed signifying a predicted influence of geometry on void fraction. While theoretically based, the formulations of drift-flux and distribution parameters from this author are often a function of void fraction, which makes the solution iterative, and thus challenging to implement.

The Chexal-Lellouche drift flux correlation (Chexal *et al.*, 1992) was developed using an extensive void fraction database. The data included a wide range of diabatic and adiabatic steam, air-water and refrigerant studies. The refrigerants included in the study were R11, R12, R22, R113, and R114 in tubes ranging in diameter from 30 to 120 mm. The goal of the study was to develop a reliable correlation that could predict void fraction in a wide range of geometries typical of Pressurized Water Reactor and Boiling Water Reactor fuel assemblies. Therefore, efforts were made to develop a correlation that was continuous and did not depend on flow regime or spline fitting. The resulting correlation is highly empirical and iterative but was found by the authors to predict void fraction data well for various fluids over a wide range of operating conditions and tube orientations. However, the smallest hydraulic diameter considered was 5 mm for adiabatic steam-water experiments, and the correlation has not been validated at small tube diameters.

Yashar *et al.* (2001) conducted a series of condensation and evaporation void fraction studies on refrigerants R134a and R410A in smooth and Microfin tubes. The evaporation experiments were conducted on 7.3 and 8.9 mm tubes with 0 and 18 degree helix micro fins, while the condensation experiments were conducted only on the set of 8.9 mm tubes. Experiments were conducted at saturation temperatures of 5 and 35°C (R134a: $p_r = 0.08, 0.22$, R410A: $p_r = 0.18, 0.43$.) A shut-off valve method was used to capture the two-phase flow within the test section during steady state operation. By measuring the amount of trapped refrigerant accurately, the void fraction was deduced with a stated uncertainty of 10%. Void fraction data from smooth tubes ranging from 4.3 to 8.9 mm were included in the analysis. They found that in general, the void fraction results were insensitive to hydraulic diameter but hypothesized that tubes with diameters less than 4.3 mm may be sensitive to diameter given the increased amount of intermittent flow present. They also found that despite the difference in heat transfer characteristics between smooth and enhanced tubes, the void fraction was unaffected during evaporation. However, they found that under the same operating conditions, the measured void fractions in the microfin tube were less than those in smooth tubes. They developed a void fraction correlation as a function of the Froude rate and the turbulent-turbulent Martinelli parameter. It was stated that the Froude rate captures the energy dissipation of gravitational lift and falling waves while the Martinelli parameter addresses the energy dissipation as a result of the vapor-liquid interactions. It was expected that their data would either fall under the gravitational (wavy-stratified) or inertia (annular) regimes, and they stated that this combination of non-dimensional parameters best describes the forces of interest. In small tube geometries, gravitational forces are most likely unimportant so it is expected that this correlation would not predict void fraction in such geometries well. It is also interesting to note that although the authors stated that the void fraction is insensitive to tube diameter, the correlation they suggested is a function of diameter.

Due to the difficulty in obtaining void fraction data, some researchers have attempted to obtain void fraction from heat transfer data. El Hajal *et al.* (2003) developed a void fraction correlation based on the reduction of a large database of condensation heat transfer coefficients. They stated that void fraction was a significant parameter when predicting heat transfer coefficients and developed a flow regime specific frame work which relied on void fraction for film thickness and wetted perimeter values. From the heat transfer database, they deduced the void fraction that would be required for their model to accurately predict their heat transfer results. At low reduced pressures, the Rouhani and Axelsson (1970) correlation predicted their results well despite being developed for evaporating flows. El Hajal *et al.* (2003) hypothesized that as the reduced pressure of the refrigerant approaches unity, the void fraction should approach the homogeneous model. The Rouhani and Axelsson (1970) correlation does not approach the homogeneous model in this range, therefore El Hajal *et al.* (2003) recommended a log mean average of the homogeneous and Rouhani and Axelsson (1970) models. The model developed El Hajal *et al.* (2003) was not experimentally validated directly for condensing flows, and is based on a database of heat transfer data for geometries with diameters greater than 3.14 mm.

Many heat exchanger designs include enhanced features. The effect of Microfins on void fraction in two-phase flow was investigated by Koyama *et al.* (2004). Void fraction was measured using the quick-closing-valve method for adiabatic two-phase flow of refrigerant R134a through a smooth tube with a diameter of 7.52 mm and a Microfin tube with a diameter of 8.86 mm. Experiments were conducted at mass fluxes ranging from 90 to 250 kg m⁻² s⁻¹ and reduced pressures of 0.20 and 0.30. They found good agreement between their smooth tube results and the Baroczy (1965) and Smith (1969) correlations. These two correlations were therefore recommended for smooth tube void fraction

prediction. Poor agreement was found between their data and the Microfin tube model developed by Yashar *et al.* (2001). It was found that the saturation pressure had the largest influence on void fraction and that mass flux did not appreciably affect void fraction. However, it was noted that mass flux did have a larger impact on void fraction in Microfin tubes than in smooth tubes. Void fraction models in the stratified-annular regime and in the purely annular regime were developed for Microfin tubes based on a momentum analysis.

Jassim *et al.* (2008a) developed a void fraction model for evaporating and condensing flow using their probabilistic flow regime approach. A different void fraction correlation was recommended for each flow regime coupled with a weighting function based on the likelihood of appearance of each regime under a given operating condition. For annular flow they suggested the Rouhani and Axelsson (1970) model, for stratified flow the Yashar *et al.* (2001) model, and for intermittent flow, they suggested the Graham *et al.* (1998) model. They chose these models because they were in the best agreement with each flow regime when compared to the large database of refrigerant void fractions. The void fraction database included condensing, evaporating and adiabatic two-phase flow of refrigerants (R11, R12, R22, R134a, R410A) in tube diameters ranging from 4.26 to 9.58 mm and saturation temperatures ranging from 5 to 35°C ($0.086 < p_r < 0.43$.) Agreement between their model and the data was very good with 92.7% of the data predicted within 10%.

2.2.2 Small Channels

Mishima and Hibiki (1996a, b) studied two-phase flow of air-water mixtures in vertical small channels ($1 < D < 4$ mm) and measured bubble velocities, void fraction and pressure drop through aluminum tubes using neutron radiography and an image

processing technique. From their data, they developed flow regime specific drift flux correlations for bubbly, slug, churn, and annular flow.

Triplett *et al.* (1999a) analyzed air-water photographs in circular tubes with diameters of 1.1 mm and 1.45 mm and in semi-triangular channels with hydraulic diameters of 1.1 and 1.49 mm. In bubbly flow, they approximated the bubbles to be spheres or ellipsoids based on the diameter and shape of the bubbles. In slug flow, they idealized the vapor slugs as cylinders with spherical caps. Annular flow was not analyzed in this manner. To determine the uncertainty in this technique, they repeated the calculations several times on the same photograph as well as on other photographs taken during the same test condition. In each case, the results deviated by about 10% and therefore, they estimated their uncertainty to be within 15%. They compared their results with the homogeneous model and other relevant correlations in the literature. It was found that the homogeneous model predicted their data the best in the bubbly and slug flow regime, but that all models from the literature over predicted their data in the annular flow regime.

A similar air-water study on microchannel tubes was conducted by Serizawa *et al.* (2002) on tubes with diameters of 20, 25 and 100 μm using a high-speed flow visualization. A set of experiments for steam flows was also conducted on a 50 μm tube. These images were used to calculate void fraction in the bubbly and slug flow regimes by assuming an axi-symmetric shape of the bubbles. At these very small diameters, they found good agreement between their data and the Armand (1946) correlation.

Kawahara *et al.* (2002) used a technique similar to that of Serizawa *et al.* (2002) to measure void fraction of N_2 -water mixtures through 100 μm diameter tube. They declared the void fraction to be either 1 where a large vapor core appeared with small thin film, or 0 when only liquid was present in the frame. For thicker films, they accounted

for the liquid inventory by using the diameter of the vapor core and the length of the tube to calculate the volume of the vapor. . The stated uncertainties in measured void fraction were -0.05 to -0.01. They found weak momentum coupling between the two phases and found that the void fraction was insensitive to superficial vapor velocity. As a result, typical correlations in the literature did not predict their void fraction data well. Therefore, they developed an empirical correlation that is solely a function of homogeneous void fraction and empirical constants. This approach leads to the surprising predictions of slip ratios that are an order of magnitude higher than those reported for channel diameters greater than ~1 mm.

Jassim and Newell (2006) measured void fraction of refrigerants R134a, R410A, and air-water through a six port microchannel test section of circular tubes with a diameter of 1.54 mm. The void fraction data were obtained in a previous study by Niño (2002) by pneumatically crimping the microchannel tubes and weighing the tube filled with refrigerant. This approach is similar to a quick-closing-valve method where the test section is suddenly isolated from the flow loop. It was stated that this method could achieve uncertainties of 0.7% when the tubes were perfectly sealed. There was significant scatter in the data, specifically for high pressure refrigerant R410A, which might imply that the test sections were leaking. Using their probabilistic flow regime map as a basis, a void fraction model was developed. The Armand (1946) correlation was recommended for the intermittent regime, the Niño (2002) correlation for annular flow, and 0 or 1 where pure vapor or liquid, respectively, were predicted. The model was able to predict only about 70% of the refrigerant data within 20%.

More recently, Winkler *et al.* (2012) developed an image analysis program to obtain void fraction from video frames collected in the flow regime studies of Coleman and Garimella (2000a, b, 2003). First, the area based void fraction was determined for the

camera viewing plane. The volume of the vapor was approximated by a specific shape factor for intermittent flows (circular shape for square and circular, and elliptical shape for rectangular geometries,) or based on the average vapor height for wavy flows. A total of 140 data points were obtained in the intermittent, intermittent-wavy, and wavy flow regimes for condensing R134a in square, rectangular and circular channels with hydraulic diameters ranging from 2 to 4.91 mm. It was found that void fraction in the wavy flow regime depended strongly on quality but showed little sensitivity to hydraulic diameter and mass flux. These trends were not as clearly observed in the intermittent or intermittent-wavy overlap regime. From their data they developed a flow regime specific drift flux model and a slip ratio model for the wavy flow regime. It was difficult to define the distribution parameter and vapor drift flux with relevant two-phase flow parameters, therefore, a best fit using empirical constants was chosen. The model predicted 79% of the data within 20% but predicted 95% of the wavy flow data within 11%.

2.2.3 Summary

The relevant studies on void fraction presented here are summarized in Table 2.2. Few studies have measured void fraction of condensing refrigerants in small diameter channels, and none in tubes with diameters smaller than 1 mm or reduced pressures greater than 0.34. Jassim and Newell (2006) measured void fraction in multiport channels using a crimping technique analogous to the quick-closing-valves method. While the stated uncertainty was low, there were concerns about the validity of the method given that the tubes may not have always sealed correctly. This is most likely the result for their often larger than normally observed void fraction results and large scatter in data. Although Winkler *et al.* (2012) investigated refrigerant flows in small diameter channels, they were only able to analyze wavy, intermittent-wavy, and intermittent flow.

Table 2.2: Summary of Void Fraction Literature

Investigator(s)	Fluid(s)	D_h	p_r	Comments
Large Diameter Tubes				
Armand (1946)	Air-water			<ul style="list-style-type: none"> • Simple multiplier to homogeneous void fraction
Isbin <i>et al.</i> (1959)	Steam-water	12.29		<ul style="list-style-type: none"> • Radiation absorption method • Related α to two-phase multiplier
Zivi (1964)				<ul style="list-style-type: none"> • Theoretical α formulation based on minimum entropy • 3 models developed; simplest was slip ratio
Baroczy (1965)	Mercury-N ₂ Air-water			<ul style="list-style-type: none"> • Tabulated liquid hold-up versus Martinelli Parameter • Butterworth (1975) fit table and developed correlation; Recommended by Rice (1987) for refrigerants
Rouhani and Axelsson (1970)	Steam (boiling)	Annulus, rod bundles, rectangular channels 4.4 - 37.4 mm	0.08 - 0.23	<ul style="list-style-type: none"> • Experiments conducted in vertical orientation • Modified Zuber and Findlay (1965) drift-flux model
Ishii (1977)				<ul style="list-style-type: none"> • Derived distribution functions and vapor drift flux velocities from body-force and shear balances for several flow regimes and geometries
Chexal <i>et al.</i> (1992)				<ul style="list-style-type: none"> • Empirical drift-flux correlation based on large database of experiments • All data $D \geq 5$ mm, Refrigerant data $D \geq 30$ mm
Yashar <i>et al.</i> (2001)	R134a R404a	4.3 - 8.9 mm (smooth) 7.3, 8.9 mm (Microfin)	0.08 - 0.43	<ul style="list-style-type: none"> • Quick-close valve experiments on evaporating and condensing refrigerants • D has no influence on α • Microfin surface only affects condensation α • correlation using F_t, X_{tt}
El Hajal <i>et al.</i> (2003)				<ul style="list-style-type: none"> • Developed void fraction correlation from large database of refrigerant condensation heat transfer data ($D > 3.14$ mm) • Log mean average of β and Rouhani and Axelsson (1970)
Koyama <i>et al.</i> (2004)	R134a	7.52 mm 8.86 mm (Microfin)	0.2, 0.3	<ul style="list-style-type: none"> • Quick-closing-valve experiments • Recommended Baroczy (1965) and (Smith, 1969) for smooth tubes • Influence of mass flux negligible in smooth tubes, more pronounced in Microfin tubes • Presented stratified-annular and annular α model for Microfin tubes

Table 2.2 continued...

Investigator(s)	Fluid(s)	D_h	p_r	Comments
Large Diameter Tubes				
Jassim <i>et al.</i> (2008a)				<ul style="list-style-type: none"> • Used probabilistic flow regime approach and recommended Graham <i>et al.</i> (1998) correlation for intermittent flow, Yashar <i>et al.</i> (2001) correlation for stratified flow, and Rouhani and Axelsson (1970) correlation for annular flow • Compared to large database of α for adiabatic, condensing and evaporating flows ($D > 4.26$ mm, $p_r < 0.43$)
Small Diameter Tubes				
Mishima and Hibiki (1996a, b)	Air-water	1 - 4 mm		<ul style="list-style-type: none"> • neutron radiography and image processing • Drift flux correlation for vertical bubbly, slug, churn and annular regimes
Triplett <i>et al.</i> (1999a)	Air-water	1.1, 1.45 mm (circular) 1.1, 1.49 (semi-triangular)		<ul style="list-style-type: none"> • Image analysis technique • β predicted bubbly, slug data well, over-predicted annular data
Serizawa <i>et al.</i> (2002)	Air-water Steam	20, 25, 100 μ m 50 μ m		<ul style="list-style-type: none"> • Image analysis technique • Good agreement with Armand (1946)
Kawahara <i>et al.</i> (2002)	N ₂ -water	100 μ m		<ul style="list-style-type: none"> • Image analysis technique • α insensitive to superficial vapor velocity • β based empirical model with large slip ratios predicted
Jassim and Newell (2006)	R134a, R410A	1.54 mm	0.10 0.22	<ul style="list-style-type: none"> • Probabilistic flow regime model as basis of prediction; Armand (1946) for intermittent, and Niño (2002) for annular flow
Winkler <i>et al.</i> (2012)	R134a	2-4.91 (circular, square, rectangular)	0.34	<ul style="list-style-type: none"> • Image analysis technique based on viewing plane α measurements and flow regimes • Drift-flux model with empirical constants for intermittent and wavy flow regime • Slip ratio correlation for wavy flow regime

At the combination of hydraulic diameter and fluid properties investigated, wavy flow was still present, indicating that the flows established were not fully characteristic of microchannel flow. The Jassim and Newell (2006) and Winkler *et al.* (2012) studies were both conducted at low reduced pressures ($p_r < 0.34$.) As previously noted, refrigerant

properties and air-water properties can vary significantly. Furthermore, refrigerant properties at low reduced pressures can be quite different from those at high reduced pressures. Therefore, studies such as those by Jassim and Newell (2006) and Winkler *et al.* (2012) that are conducted at a single saturation temperature are unable to definitively provide insights into the effects of fluid property variations on void fraction. While these investigators have studied void fraction for condensing refrigerants in small diameter channels, there have not been any studies that account simultaneously for the increasing influence of surface tension at the small diameters on the one hand, and the decreasing surface tension in refrigerants as the critical point is approached with increasing pressures.

2.3 Pressure Drop

Pressure drop in two-phase flow through large diameter tubes has been extensively investigated. This large body of work has been conducted on several fluids, including refrigerants, for larger tube diameters ($D > 3$ mm.) In smaller tube diameters, however, the focus has mostly been on adiabatic and evaporating flows.

Three classical correlations, Lockhart and Martinelli (1949), Chisholm (1973a), and Friedel (1979), form the basis for many of the correlations in the literature. Of these three, only the Friedel (1979) correlation directly considers surface tension effects, which can be significant at the smaller diameters. Although such correlations are widely used, their predictive abilities are often inadequate. This is primarily due to the use of these correlations outside their originally intended range of applicability, and also because such correlations do not differentiate between the vastly different flow regimes for which they were developed.

Friedel (1979) developed a pressure drop correlation using a database of 25,000 frictional pressure drop measurements. The database was obtained from experiments on horizontal and vertical flow of single and two-phase flow through circular tubes. The fluids used included water, R113, R22, R12, R11, N₂, NH₃, Ne, 1Na99K, 8Na92K, air-water and air-oil. This empirical correlation uses a two-phase multiplier that considers both gravitational and surface tensions forces by using the Froude and Weber number. Friedel (1979) found much better agreement with the data than that of Chisholm (1973a) predicting 83% versus 72% of the data within 30%. This model serves as the basis for many two-phase pressure drop correlations in the literature.

Mishima and Hibiki (1996b) investigated the influence of small tube diameters in two-phase flow. This is the same study that was presented in the flow regime and void fraction sections. They measured pressure drop while simultaneously observing the flow regime in air-water vertical flows in tube diameters ranging from 1.05 to 4.08 mm. Despite capturing several different flow regimes, Mishima and Hibiki (1996b) compared all their data to the two-phase multiplier constant presented by Chisholm (1967). Mishima and Hibiki (1996b) observed that as tube diameter decreased, the Chisholm constant decreased and developed an empirical correlation to account for this. The correlation only considers the tube diameter and no other fluid properties. Their results were compared to horizontal air-water data from Sugawara *et al.* (1967) and ammonia data from Ungar and Cornwell (1992) for circular tubes. Good agreement was found and it was concluded that their correlation was valid for vertical and horizontal tubes. This approach was extended to vertical and horizontal ducts by fitting their empirical constant to air-water data from Sadatomi *et al.* (1982), and R113-N₂ data from Moriyama *et al.* (1992). This approach only took into account hydraulic diameter, but does not account for the effects of aspect ratio. The empirical constant derived for noncircular channels is

only slightly different from that derived for circular channels (-0.333 vs. -0.319) and physical interpretations for these values are not provided.

Zhang and Webb (2001) conducted a study on pressure drop in refrigerants through small channels. They investigated adiabatic single- and two-phase flow of refrigerants R134a, R22, and R404A in a multi-port extruded tube with a hydraulic diameter of 2.13 mm, and circular tubes with diameters of 3.25 and 6.25 mm. Experiments were conducted at various reduced pressures ranging from 0.21 to 0.51. The Friedel (1979) correlation was found to predict data well at low reduced pressures but tended to over-predict data as reduced pressure was increased. To account for the effect of reduced pressure on pressure drop, a modification to the Friedel (1979) correlation was suggested by replacing property ratios with reduced pressure. The We and Fr number dependence was also replaced by the reduced pressure and it was stated that the exponents in the original model were very small and thus the two-phase multiplier dependence was very weak. They found reasonable agreement between their data and the reduced pressure based correlation. It predicted 85% of the data within 20%, and they recommended it for tube diameters between 1 and 7 mm and reduced pressures greater than 0.2. They also compared their model to that of Tran *et al.* (2000) and found that it agreed well at low qualities but that as quality increased, deviation between the two predictions worsened. They attributed this to the difference in properties at higher reduced pressures.

Cavallini *et al.* (2002) developed a correlation for a data bank on refrigerants R22, R134a, R125, R32, R236ea, R407C and R410A flowing through an 8-mm tube. A multi-regime pressure drop model was developed for condensing flow of refrigerants. The transition criteria were discussed in Section 2.1.3. A two-phase multiplier correlation for annular flow was developed by modifying the Friedel (1979) equation. They stated that gravitational effects are insignificant in annular flow and removed the Froude number

term from the correlation. For intermittent and stratified flow, they suggested the original Friedel (1979) correlation.

Some of these correlations based on large databases lead to reasonable predictions; however, they may not accurately account for the underlying physical mechanisms because the corresponding sub models may not model the physical mechanisms well. Garimella and co-workers developed a multi-regime pressure drop model with special attention to the specific vapor-liquid interactions. An intermittent flow pressure drop model was developed for condensing refrigerant R134a in circular (Garimella *et al.*, 2002), and non-circular (Garimella *et al.*, 2003b) tubes for channels with hydraulic diameters ranging from 0.4 to 4.9 mm. These models superimposed the contributions of pressure drop at the vapor-liquid film interface, liquid slug, and the transition regions fore and aft of the bubble to estimate the overall pressure drop. The transitional pressure drop was approximated by the method presented by Dukler and Hubbard (1975). Garimella *et al.* (2002, 2003b) predicted the number of transitions, or the number of unit cells (vapor bubble and liquid slug,) based on measured pressure drop values. An annular flow pressure drop model was also developed by Garimella *et al.* (2003a) based on a shear balance at the vapor-liquid interface. The interface, or film thickness, was approximated using the Baroczy (1965) void fraction correlation. The correlation for interfacial friction factor was developed from their data with the Martinelli parameter, the liquid Reynolds number, and a modified capillary number from Lee and Lee (2001) as parameters. They combined the sub models for these different regimes to develop a multi-regime pressure drop model (Garimella *et al.*, 2005). A transition region between intermittent and annular flow was modeled using transition criteria from Coleman and Garimella (2003) based on mass flux and quality. The resulting model predicted 82% of the data within 20%. While the model presented by Garimella *et al.* (2005) is physically based, the data were all obtained at one nominal saturation temperature and for one fluid. Validation and

refinement of the model with experiments conducted at different saturation temperatures with different fluids is needed.

Garimella and co-workers have also investigated condensation of near-azeotropic refrigerant blends at high reduced pressures. Jiang (2004), Mitra (2005), and Andresen (2007) investigated near critical ($p_r = 0.8, 0.9$) condensation of refrigerant R410A and R404A in single tube test sections with diameters ranging from 3.048 to 9.40 mm. Andresen (2007) also conducted condensation experiments on near-critical R410A in multiport microchannel test sections with circular channels ranging in diameter from 0.76 to 1.52 mm. He developed a pressure drop correlation using the high pressure data from all three studies. A two-phase multiplier was developed based on the correlation of Lockhart and Martinelli (1949) that was later modified by Chisholm (1967). Similar to Mishima and Hibiki (1996b), Andresen (2007) modified the Chisholm constant to account for the effects of tube diameter. The effects of surface tension and tube diameter were addressed by using the confinement number, and inertial effects were addressed by including the liquid Reynolds number. The model was able to predict 85% of the data within 25%. However, the difference in properties between reduced pressures of 0.8 and 0.9 are quite small and while the model was able to capture the pressure drop trends from their experiments, extrapolation of the results to lower reduced pressures should be done with caution. For example, the correlation developed by Andresen (2007) over predicts the R134a pressure drop data and the corresponding model of Garimella *et al.* (2005).

Jassim and Newell (2006) developed a probabilistic pressure drop model based on experiments conducted on R134a and R410A at a saturation temperature of 10°C in a multiport test section with tube diameters of 1.54 mm (p_r (R134a) = 0.10, p_r (R410A) = 0.22.) They developed pressure drop equations for liquid, vapor, intermittent and annular regions and assigned weighting functions to each to calculate the total pressure drop.

This approach results in continuous pressure drop functions; however, it appears from the images of the two-phase flow that they obtained simultaneously, that there may be flow mal-distribution in the channels, which may be the reason for different flow regimes occurring in different channels under the same operating conditions.

2.3.1 Summary

The pressure drop literature reviewed in this section is summarized in Table 2.3. There have been extensive studies on pressure drop of condensing refrigerants. The large database used to develop the Cavallini *et al.* (2002) model addresses to some extent the effects of reduced pressure and properties on condensing flows in large diameter channels. However, in large diameter channels, the influence of surface tension is lower. In addition, as reduced pressure increases, surface tension decreases substantially. Large diameter correlations that do not consider the influence of surface tension on the one hand, and small diameter correlations that do consider surface tension effects on the other, may both be unsuitable to address two-phase pressure drop in small diameter channels as reduced pressure is increased. The investigations of Garimella *et al.* (2002; 2003b; 2005) on several tube diameters and shapes at the small scale are a promising start to predicting pressure drop in condensing flows. However, the effect of increasing reduced pressure on pressure drop in these small diameter channels needs further attention.

2.4 Heat Transfer

Studies on condensation heat transfer in small diameter tubes are more limited than those on large diameter tubes because of the low mass flow rates and heat duties characteristic of flows through microchannels, coupled with high heat transfer coefficients that require accurate measurement at small temperature differences.

Table 2.3: Summary of Pressure Drop Literature

Investigator(s)	Fluid(s)	D_h	p_r	Comments
Lockhart and Martinelli (1949)	Air-water/ benzene/ kerosene/ oils	1.5 - 26 mm		<ul style="list-style-type: none"> • Two-phase multiplier a function of gas and liquid Re • Chisholm (1967) correlated two-phase multiplier from data using X
Chisholm (1973a)	Steam-water			<ul style="list-style-type: none"> • Modified Baroczy (1966) procedure and equation which resulted in more convenient two-phase multiplier correlation
Friedel (1979)	R113, R22, R12, E11, N2, NH3, Ne, 1NA99K, 8Na92K, air-water, air-oil			<ul style="list-style-type: none"> • Empirical fit that incorporated surface tension and gravitational forces into two-phase multiplier • Most commonly used framework for small diameters because of the inclusion of surface tension effects
Mishima and Hibiki (1996b)	Air-water	1.05 - 4.08 mm		<ul style="list-style-type: none"> • Found exponential dependence of Chisholm parameter on diameter • Separate empirical constants for circular and rectangular geometries
Zhang and Webb (2001)	R134a, R22, R404A	2.13, 3.25, 6.25 mm	0.21 - 0.51	<ul style="list-style-type: none"> • Adiabatic study • Friedel (1979) agreed well at low p_r but agreement worsened as p_r increased • Reduced dimensionless property variables with p_r
Cavallini <i>et al.</i> (2002)	R22, R134a, R125, R32, R236ea, R407C, R410A	8 mm		<ul style="list-style-type: none"> • Developed multi-regime pressure drop model based on large database of pressure drop data • Modified Friedel (1979) correlation in annular regime by removing Fr and adjusting empirical constants • For all other regimes, recommended original Friedel (1979)
Garimella <i>et al.</i> (Garimella <i>et al.</i> (2002); Garimella <i>et al.</i> (2003b); Garimella <i>et al.</i> (2005))	R134a	0.4 - 4.9 mm	0.34	<ul style="list-style-type: none"> • Mechanistic, multi-regime pressure drop model for intermittent, discrete wave and annular regimes • Annular correlation relies on interfacial area prediction (Baroczy (1966) α correlation) • Conducted at single saturation condition
Jiang (2004), Mitra (2005), Andresen (2007)	R410A, R404A	0.76 - 9.40 mm	0.8, 0.9	<ul style="list-style-type: none"> • Andresen (2007) developed two-phase multiplier using confinement number and Re_l to predict Chisholm constant
Jassim and Newell (2006)	R134a, R410A	1.54 mm	0.10, 0.22	<ul style="list-style-type: none"> • Multi-regime model using probabilistic flow map • Single phase liquid, vapor, intermittent and annular empirical models

Condensation heat transfer in large diameter tubes is generally considered to be governed by either gravitational or shear forces based on the operating conditions. At smaller tube diameters, the influence of gravity decreases and is therefore unlikely to govern condensation. Shear-driven condensation heat transfer models are based on a few basic approaches. One of the more common approaches is the modification of the single-phase heat transfer coefficient with a two-phase multiplier. Shah (1979) developed a two-phase multiplier for the single-phase heat transfer coefficient based on the vapor quality and reduced pressure of the fluid. The formulation was originally developed for evaporation with an entirely wetted perimeter and was validated using data for various fluids (water, R11, R12, R22, R113, methanol, ethanol, benzene, toluene, trichloroethylene) in horizontal, inclined, and vertical tubes, and annuli with hydraulic diameters ranging from 7 to 40 mm. The reduced pressures of the fluids ranged from 0.002 to 0.44. The correlation was able to predict the large database of condensation data with an average deviation of 17%. Despite its largely empirical form, the Shah (1979) correlation is one of the most commonly used. However, the correlation was developed for low pressure fluids in large tube diameters and its applicability to small diameter channels at high reduced pressures needs validation.

Another approach in modeling shear-driven condensation is through the use of the heat-momentum analogy. Traviss *et al.* (1973) developed a shear-driven model based on this analogy and the von Karman universal velocity distribution in the liquid film. For annular flow to occur in large diameter tubes, the vapor Reynolds number must be very large ($Re_v > 35,000$.) The pressure drop was calculated using a two-phase multiplier correlation and the momentum term was evaluated under the assumption that the film thickness was comparatively very thin. The model showed good agreement with data taken for condensing refrigerants R12 and R22 in an 8-mm tube at reduced pressures ranging from 0.024 to 0.35. The agreement with data was not as good at low qualities (x

< 0.1) where intermittent flow is likely, and at high qualities and mass fluxes where mist flow is most probable. The resulting heat transfer coefficient is heavily dependent on the pressure drop correlation, and many researchers have used the same approach but with modifications to the pressure drop term used as the input.

Considerations of both driving forces are accounted for in predictive techniques for cases where neither gravity nor shear-driven mechanisms dominate. In general this is accomplished by the development of flow-regime-specific correlations. Flow regime maps are used for predicting the applicable regime, and the influence of each mechanism during transition is accounted for by weighted parameters. Cavallini *et al.* (2002) presented a method for predicting heat transfer coefficients based on a large database of refrigerants (R11, R12, R22, R113, R134a, R125, R32, R236ea, R407C and R410A) in tube diameters ranging from 3 to 21.4 mm. They recommended or modified previously available correlations for four major flow regimes (annular, stratified, wavy and slug) and suggested linear interpolation based on transition parameters for the transition regions between these regimes. For the annular regime (or shear driven condensation,) they modified the heat-momentum analogy approach of Kosky and Staub (1971). For the stratified regime (or gravity driven condensation,) a Nusselt falling-film type correlation was used to predict condensation along the upper portion of the tube and a two-phase multiplier term was used for predicting the heat transfer in the stratified pool region of the flow. In the annular-stratified region, they suggested a linear interpolation between the two correlations while in the intermittent regime they suggested a linear interpolation between wavy and single phase flow. The heat transfer database did not include any data in this region; therefore, they were unable to validate this portion of their model. Overall the model predicted their data well with an absolute average deviation of 10.4%.

Using the same database, Thome *et al.* (2003) developed a multi-regime heat transfer model based on the flow regime map developed in previous work by their group (El Hajal *et al.*, 2003). In the annular regime, Thome *et al.* (2003) developed an empirical Nusselt number correlation similar to that of Shah (1979). Thome *et al.* (2003) stated that void fraction is the most important parameter when predicting heat transfer coefficients. Due to the lack of void fraction data and models, specifically at high reduced pressures, void fractions were inferred (El Hajal *et al.*, 2003) from a heat transfer database to develop a void fraction model. The same heat transfer database was also used later to develop their heat transfer coefficient correlation. They used the void fraction model to predict the film thickness of the condensate for annular flow, which they used as the characteristic length in a Nusselt number correlation. The gravity driven correlation used a similar Nusselt falling-film type correlation for the upper portion of the tube but used the same annular shear driven correlation to account for the convective heat transfer in the pool. They approximated the liquid at the bottom of the tube as a film with uniform thickness instead of treating it as a stratified pool. The film thickness is based on their void fraction model, and the annular heat transfer model was used to predict the heat transfer coefficient along this portion of the perimeter. This approach led to a smooth transition from stratified to annular flow without direct interpolation. Their model predicted results very similar to those of Cavallini *et al.* (2002), which is to be expected because it was developed from a similar data base. Cavallini *et al.* (2006a) used the same heat transfer data base with some additional studies which included hydrocarbons (propane, butane, iso-butane, propylene,) carbon dioxide, steam, and ammonia to develop a new heat transfer model. They modified their approach to predicting multi-regime heat transfer coefficients focusing solely on differentiating between condensation regimes that are sensitive to tube wall temperatures and those that are not. This effectively groups intermittent and stratified flow together. The transition criteria are estimated by the dimensionless gas velocity like in their previous work. The transition value is adjusted

based on fluid properties and whether the fluid is a refrigerant or a hydrocarbon. The temperature independent heat transfer model in this newer work is an empirical two-phase multiplier while the temperature dependent model uses the same form from their previous work but with newly derived constants. Good agreement was found with their data with an absolute average deviation of 12%. It is important to point out that this deviation is greater than what was achieved in their previous models, which are most likely the result of newer fluids being added that have much different properties. While the extensive database used to deduce heat transfer models leads to the understanding of fluid properties, all of the experiments under consideration were conducted at tube diameters greater than 3 mm. Therefore, it is unlikely that they were able to accurately account for the influence of surface tension, which is an important parameter at small diameters.

There has been significant effort to understand the effects of small tube diameters on condensation in the literature over the past decade. Typically, either a two-phase multiplier or the shear driven heat-momentum models are developed because of the dominance of the annular flow regime observed in small geometries. Webb and co-workers (Yang and Webb, 1997; Webb and Ermis, 2001; Zhang and Webb, 2001) investigated the effects of hydraulic diameter and Microfin enhancements in extruded aluminum microchannels ranging in hydraulic diameter from 0.44 to 2.64 mm. They conducted their experiments on refrigerants R134a and R12 at a saturation temperature of 65°C (R134a, $p_r = 0.47$, R12, $p_r = 0.41$.) They found that the Shah (1979) correlation over-predicted their smooth channel data and that the Akers *et al.* (1959) correlation was in good agreement. For the Microfin tubes, Yang and Webb (1997) developed a heat transfer correlation that accounted for the effects of surface tension and their interaction with the Microfins. They documented that the heat transfer coefficient increased with

decreasing hydraulic diameter but did not make any conclusions regarding the effects of aspect ratio on rectangular channels.

Garimella and co-workers (Garimella and Bandhauer, 2001; Bandhauer, 2002; Bandhauer *et al.*, 2006) also investigated the influence of hydraulic diameter and channel geometries for condensing R134a through extruded aluminum microchannels. They measured heat transfer coefficients of condensing R134a in hydraulic diameters ranging from 0.424 to 1.524 mm at a single saturation temperature of 52°C ($p_r = 0.34$.) Multiple parallel channels were used for the small hydraulic diameters to overcome the small heat duties associated with low mass flow rates. The effect of channel shape was evaluated by comparing rectangular and triangular results to circular geometries with similar hydraulic diameters. They found that the triangular shaped channels had the highest heat transfer coefficients, while there was not a significant difference between the heat transfer coefficients for other tube shapes. Bandhauer *et al.* (2006) developed a model from the circular geometry data using the model of Traviss and Rohsenow (1973) for shear dominated flow as a starting point. They used the pressure drop model developed by Garimella *et al.* (2005) to determine the shear stress to yield better accuracy, because this model was developed for microchannels and accounts for surface tension effects. The resulting model predicted their data well, with 86% of the data being predicted within 20%. However, all their data were obtained for the same fluid at one nominal saturation temperature. Validation of the model using various fluids is required to evaluate its robustness and applicability. More recently, Andresen (2007) investigated condensation of refrigerants at near-critical conditions (R410A, $p_r = 0.8, 0.9$) through circular extruded aluminum test sections ($D = 0.76, 1.52$) and a single copper tube ($D = 3.048$ mm) and found that models available in literature over-predicted his data. He also used the near-critical data from Jiang (2004) and Mitra (2005) for condensing R404A and R410A in 9.4 and 6.2 mm to developed a multi-regime heat transfer correlation. Andresen (2007) used

the transition criteria from Cavallini *et al.* (2002) to predict whether the flow was annular or wavy. He developed a two-phase multiplier model for annular flow and a Nusselt film and convective pool model for wavy flow. However, the properties of refrigerant R410A do not change significantly over this reduced pressure range and additional results over a larger range of reduced pressures are needed to enhance and validate its range of applicability.

Baird *et al.* (2003) investigated the effects of heat duty on condensing refrigerants R123 and R11 through microchannels ($D = 0.92, 1.95$ mm.) A novel technique for measuring local heat fluxes using thermoelectric coolers was developed. A significant influence of heat flux on heat transfer coefficients was observed, especially at high vapor qualities. Their data showed poor agreement with several models from the literature. Similar to Yang and Webb (1997), Baird *et al.* (2003) found the Shah (1979) correlation consistently over-predicted their data. They developed a shear-driven heat transfer model that utilizes the heat-momentum analogy like several previous researchers including Traviss *et al.* (1973). They found that their model was able to capture the trends of varying saturation temperatures, mass fluxes and qualities, but failed to capture their observed trends of the influence of heat flux. The influence of heat flux during gravity or film condensation has been documented previously but no other study has shown this effect in shear driven condensation. It is thus unclear whether this is a realistic phenomenon or if it is the result of the difficulty and uncertainty in measuring heat transfer in microchannels.

Rose and co-workers (Wang and Rose, 2005, 2006; Su *et al.*, 2009; Wang and Rose, 2011) investigated the effects of surface tension on condensation heat transfer computationally. Wang and Rose (2005) developed a theoretical model for predicting heat transfer coefficients for condensing flows through microchannels. They presented

results for square and triangular channels with hydraulic diameter ranging from 0.5 to 5 mm for refrigerants R134a, R22, and R410A. They conducted a laminar flow analysis with attention to the interfacial characteristics at small scales while accounting for surface tension, interfacial shear stress, and gravity. Their model enables the investigation of the effects of each of these governing forces individually or in coupled fashion. When surface tension and gravity were both neglected, they found that the heat transfer coefficients predicted were significantly lower, especially at high qualities. The importance of gravity was noted when comparing heat transfer coefficients in square channels. Buoyancy forces cause the vapor core to float towards the top of the channel, resulting in a very thin film along the top surface. They stated that their results agreed well in relative magnitude with data in the literature, but needed further validation. Wang and Rose (2006) investigated the effects of channel shape on heat transfer coefficient using their computation model. They evaluated square (1 mm), triangular (1 mm side), rectangular (1 × 1.5 mm, 1.5 × 1 mm) and circular ($D = 1$ mm) geometries at a constant refrigerant mass flux of $500 \text{ kg m}^{-2} \text{ s}^{-1}$ and a nominal saturation temperature of 50°C . They found that the heat transfer coefficients in noncircular channels are greater than those in circular tubes with similar hydraulic diameters, especially at high qualities, where surface tension appears to be most important. This is because of the transverse motion of the liquid film into the corners due to surface tension, which leaves a thin film on the heat transfer surfaces, leading to high heat transfer coefficients. Su *et al.* (2009) compared four different correlations developed for condensing R134a in the literature. Of the models compared, only the Cavallini *et al.* (2005) and Bandhauer *et al.* (2006) correlations directly accounted for surface tension in their formulation. Su *et al.* (2009) found reasonable agreement between the predictions of these correlations and the theoretical model of Wang and Rose (2005) when predicting heat transfer coefficients in R134a, but found different results when predicting heat transfer coefficients for condensing ammonia. They suggested that while these correlations may be valid for

refrigerant fluids similar to R134a, caution must be used when using them outside the stated range of applicability. Wang and Rose (2011) modified their computational model to account for tube inclination and investigated additional condensing fluids including ammonia, R152a, propane and CO₂. They observed a surface tension dominated region where gravity and shear stress were negligible and developed a Nusselt number correlation using a non-dimensional analysis. They stated that the Nusselt number correlation allows for easy implementation for condenser design.

Jassim *et al.* (2008b) examined condensation of R134a at 25°C in 8.915-mm tubes and developed a model based on these data as well as other data from the literature. Similar to the void fraction and pressure drop model developed by them, the heat transfer model used a weighting function for each flow regime (annular, stratified, and intermittent) and used models available in the literature to predict heat transfer characteristics in each region. Application of this approach to small geometries could yield a simpler approach because the only flow regimes in these diameters are intermittent, intermittent-annular and annular.

Recently, Cavallini *et al.* (2011) presented data for condensing refrigerants R32 and R245fa through a single tube with a diameter of 0.96 mm. Experiments were conducted at a saturation temperature of 40°C, which corresponds to a reduced pressure of 0.43 and 0.07 for R32 and R245fa, respectively. Their data was compared with the Moser *et al.* (1998) model modified by Zhang and Webb (2001) and their model developed for shear-driven condensation (Cavallini *et al.*, 2006a) in large diameter tubes. The modified Moser model was found to predict R32 data well but failed to capture the trends in the R245fa data. Cavallini *et al.* (2011) found very good agreement between their shear driven correlation for large diameter tubes and their microchannel data.

A summary of the relevant heat transfer studies reviewed here is presented in Table 2.4. Numerous studies on condensation in large diameter tubes and at low reduced pressures have been conducted. Researchers have assembled large databases of condensation data and developed correlations to address the trends in data based on influences of operating conditions and properties. For large diameter tube data, Shah (1979), Cavallini *et al.* (2002), Thome *et al.* (2003), and Cavallini *et al.* (2006a) have developed such models. However, physical inconsistencies can occur in some situations when using such an approach. For example, the annular correlation of Thome *et al.* (2003) predicts an increase in heat transfer coefficient with increasing saturation temperature, which is counter to what is observed. Similarly, the wavy flow model presented by Cavallini *et al.* (2006a) is similar in form to their previous model (Cavallini *et al.*, 2002), but differs significantly in terms of the empirical constants obtained from the data. While the results are similar for the class of fluids examined, it is unclear which model accurately captures the physical trends of the process.

Recent investigations have focused on smaller tube geometries with several of experiments conducted on refrigerants condensing at low reduced pressure refrigerants. For example, Garimella and co-workers (Garimella and Bandhauer, 2001; Bandhauer, 2002; Bandhauer *et al.*, 2006) have extensively investigated microchannel condensation but for a single operating pressure for a low pressure refrigerant. High pressure fluids have significantly different properties and validation of models developed for low pressure refrigerants at high reduced pressures is needed. The investigation by Andresen (2007) at near critical pressures demonstrated that models in the literature over-predict heat transfer data at high reduced pressures. Additionally, the limited data on high reduced pressures in larger diameter tubes may not be applicable in predicting the corresponding behavior in small tube diameters because of the increased influence of surface tension and the effect of high reduced pressures on surface tension. . Rose and

Table 2.4: Summary of Heat Transfer Literature

Investigator(s)	Fluid(s)	D_h	p_r	Comments
Traviss <i>et al.</i> (1973)	R12, R22	8 mm	0.24 - 0.35	<ul style="list-style-type: none"> • von Karman heat-momentum analogy • Two-phase multiplier pressure drop input • Poor agreement at low qualities where intermittent flow is likely
Shah (1979)	Water, R11, R12, R22, R113, methanol, ethanol, benzene, toluene, tri-chloroethylene	7 - 40 mm	0.002 - 0.44	<ul style="list-style-type: none"> • Large database of condensation data • Empirical two-phase multiplier • Most commonly cited due to simplicity and range
Webb and co-workers (Yang and Webb (1997), Webb and Ermis (2001), Zhang and Webb (2001))	R12, R134a	0.44 - 2.64	0.41, 0.47	<ul style="list-style-type: none"> • Extruded aluminum multi-port rectangular channels • Smooth and Microfin tubes • Akers <i>et al.</i> (1959) in good agreement with smooth data, developed Microfin correlation
Garimella and co-workers (Garimella and Bandhauer (2001), Bandhauer (2002), Bandhauer <i>et al.</i> (2006))	R134a	0.424 - 1.524 mm	0.34	<ul style="list-style-type: none"> • Extruded aluminum multi-port channels • Investigated effects of tube shape • Modified Traviss <i>et al.</i> (1973) model for shear-driven condensation • Triangular insert tubes had highest heat transfer coefficients, no significant difference between circular and rectangular channels
Cavallini <i>et al.</i> (2002)	R11, R12, R22, R113, R134a, R125, R32, R236ea, R407C, R410A	3 to 21.4 mm	< 0.8	<ul style="list-style-type: none"> • Multi-regime heat transfer model • Annular model - modified Kosky and Staub (1971) heat-momentum analogy • Stratified - α weighted Nu film and pool two-phase multiplier
Baird <i>et al.</i> (2003)	R123, R11	0.92, 1.95	0.02 - 0.11	<ul style="list-style-type: none"> • Investigated Q'' effects using novel TEC test sections • Observed increased Q'' as x increased • Modified Traviss <i>et al.</i> (1973) model; did not capture Q'' effects
Thome <i>et al.</i> (2003)				<ul style="list-style-type: none"> • Same database as Cavallini <i>et al.</i> (2002) • Multi-regime model using α and flow map from El Hajal <i>et al.</i> (2003) • Annular- two-phase multiplier, δ used as length scale • Stratified - α weighted Nu film and pool two-phase multiplier same as annular; smooth transition

Table 2.4 continued...

Investigator(s)	Fluid(s)	D_h	p_r	Comments
Jiang (2004), Mitra (2005), Andresen (2007)	R404A, R410A	0.76 - 9.4 mm	0.8. 0.9	<ul style="list-style-type: none"> • Models in literature over-predict data • Andresen (2007) developed multi-regime model (annular, wavy) from data using Cavallini <i>et al.</i> (2002) transition criteria
Rose and co-workers (Wang and Rose, 2005, 2006; Su <i>et al.</i> , 2009; Wang and Rose, 2011)	R134a, R22, R410A, Ammonia, R152a, Propane, CO ₂	0.5 - 5 mm (square, triangular, rectangular, circular)		<ul style="list-style-type: none"> • Computational model that accounts for surface tension, interfacial shear stress and gravity • Investigated effects of geometries • Developed Nusselt number correlation for surface tension dominant region
Cavallini <i>et al.</i> (2006a)	Propane, butane, isobutane, propylene, CO ₂ , steam, NH ₃	3 to 21.4 mm	< 0.8	<ul style="list-style-type: none"> • Same database as Cavallini <i>et al.</i> (2002) but with additional fluids • New map based on T_{wall} independent and dependent • T_{wall} independent (Annular) - two-phase multiplier • T_{wall} dependent (Stratified, intermittent) - Re-fit of empirical constants of Cavallini <i>et al.</i> (2002) stratified model
Jassim <i>et al.</i> (2008b)	R134a	8.915 mm	0.164	<ul style="list-style-type: none"> • Probabilistic flow regime map used for condensation heat transfer model
Cavallini <i>et al.</i> (2011)	R32, R245fa	0.96 mm	0.43, 0.07	<ul style="list-style-type: none"> • Found good agreement with shear driven model from Cavallini <i>et al.</i> (2006a)

co-workers (Wang and Rose, 2005, 2006; Su *et al.*, 2009; Wang and Rose, 2011) have computationally investigated the effect of surface tension on condensation in small channels. The effects of reduced pressures over a wide range on microchannel condensation are not well understood and can be significant given the changes in surface tension over this range and its importance in small geometries.

2.5 Specific Research Needs

The above discussion shows that much of the flow visualization literature is on adiabatic air-water flows in large diameter tubes. While in recent years, attention has shifted to small diameter tubes, the use of air-water mixtures in adiabatic flows precludes the applicability of these studies to phase change in refrigerants. These limitations are particularly important when phase-change phenomena in refrigerant mixtures such as

R404A operating at high pressures are of interest. The refrigerant condensation studies in the literature were generally conducted at lower reduced pressures ($p_r < 0.4$) where there is a much larger difference between liquid and vapor properties. These conditions generally correspond to saturation temperatures too low for ambient heat rejection and outside the design envelope for most practical systems. The effects of reduced pressure on void fraction over a large range of conditions for refrigerants have not been investigated and reported in the literature. The importance and influence of flow phenomena on pressure drop and heat transfer characteristics of two-phase flow has been well noted but the implementation of these mechanisms has been driven by qualitative assessment of the flow. Void fractions, in particular, have not been directly measured for the working fluids, geometries, and operating conditions of interest here. These previous studies have also led to the development of separate models for different flow regimes that require interpolation from one flow regime to the other to ensure a continuous prediction. Several of these deficiencies in the literature are addressed in the present study; in particular, the collection of accurate void fraction data, and pressure drop and heat transfer coefficient measurement at high reduced pressures in small diameter tubes. The void fraction model allows for the prediction of film thicknesses, wetter perimeter ratios, and phase velocities, which will serve as the building blocks for pressure drop and heat transfer models.

2.6 Objectives and Tasks

The objectives of this work are to obtain a clear understanding of two-phase flow in microchannels at high pressures, quantify flow parameters relevant to the modeling of condensation, and use these parameters to refine models for pressure drop and heat transfer. The specific tasks are as follows:

- Visualize condensation of R404A in microchannels ranging in hydraulic diameter from 0.508 to 3.00 mm at saturation temperatures ranging from 30 to 60°C ($0.38 < p_r < 0.77$.)
- Analyze the visualization data to deduce void fraction, slug frequencies, vapor bubble velocities, and vapor bubble dimensions for different flow regimes, as applicable.
- Conduct pressure drop and heat transfer experiments during condensation of R404A at similar experimental conditions.
- Develop flow-mechanism-based void fraction, pressure drop and heat transfer coefficient models based on the above mentioned experiments and analyses.

CHAPTER 3: EXPERIMENTAL METHODS

Condensation experiments were conducted over a wide range of tube diameters, $0.508 < D < 3.05$ mm, reduced pressures, $0.38 < p_r < 0.77$, and mass fluxes, $200 < G < 800$ kg m⁻² s⁻¹ across the vapor-liquid dome. Flow visualization, pressure drop, and heat transfer experiments were conducted for these different diameters under similar conditions. Two separate experimental facilities, one for large diameter ($D = 3.00$ or 3.05 mm) and another for small diameter ($0.508 < D < 1.55$ mm) channels, are used to obtain simultaneous high-speed flow visualization and pressure drop measurements, or pressure drop and heat transfer coefficient measurements for the wide range of tube diameters, mass fluxes and reduced pressures stated above using refrigerant R404A as the working fluid.

The Phase-Change/Supercritical Heat Transfer and Pressure Drop Test Facility (Large Tube Facility) was originally developed for studies of flow regimes, pressure drop and heat transfer during condensation of refrigerant R134a by Coleman and Garimella (2000b, 2003), and Bandhauer *et al.* (2006). The facility was later modified such that condensation and supercritical cooling experiments on R404A and R410A could be conducted on 0.76, 1.52, 3.05 6.22 and 9.40 mm diameter tubes (Jiang, 2004; Mitra, 2005; Andresen, 2007). Modifications and re-calibrations were made to the facility to allow for flow visualization of high-pressure refrigerant blend R404A in 3.00 mm tubes for the present study

The Microchannel Condensation Heat Transfer and Pressure Drop Test Facility (Small Tube Facility) was originally developed by Cavallini *et al.* (2005) for condensing R134a in rectangular channels ranging in hydraulic diameter from 100 to 160 μ m and aspect ratios from 1 to 4. Modifications and re-calibrations were made to the test facility to

enable visualization, pressure drop and heat transfer tests on high-pressure refrigerant blend R404A in circular tube diameters ranging from 0.508 to 1.55 mm.

3.1 Phase-Change Tests

This section provides a detailed description of the two test facilities, followed by a description of the visualization and heat transfer test sections.

3.1.1 Test Facility Details

A schematic of the large diameter tube test facility ($D = 3$ mm) is shown in Figure 3.2. The numbers on the schematic note the different state points within the refrigerant loop. The refrigerant exits a tube-in-tube coiled evaporator in the superheated state [1]. Heat is supplied by steam utilities in the laboratory. The superheated state is verified by

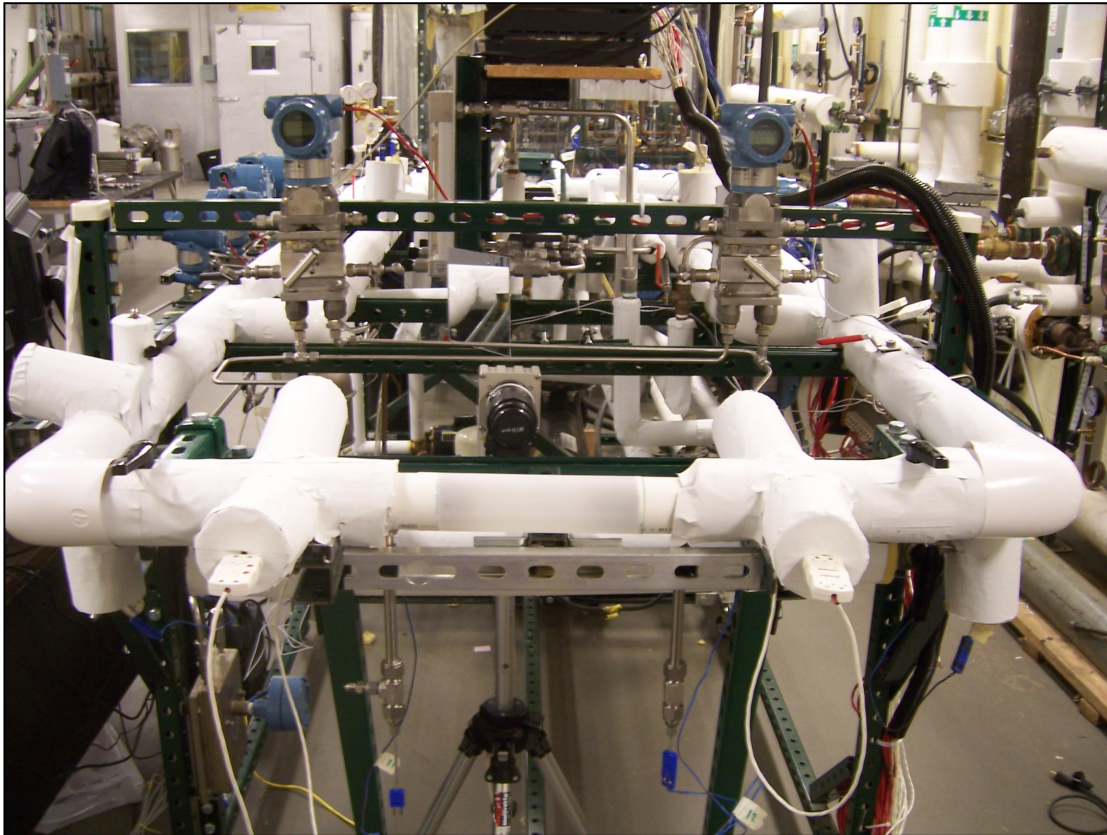


Figure 3.1: Photograph of Large Diameter Tube Facility

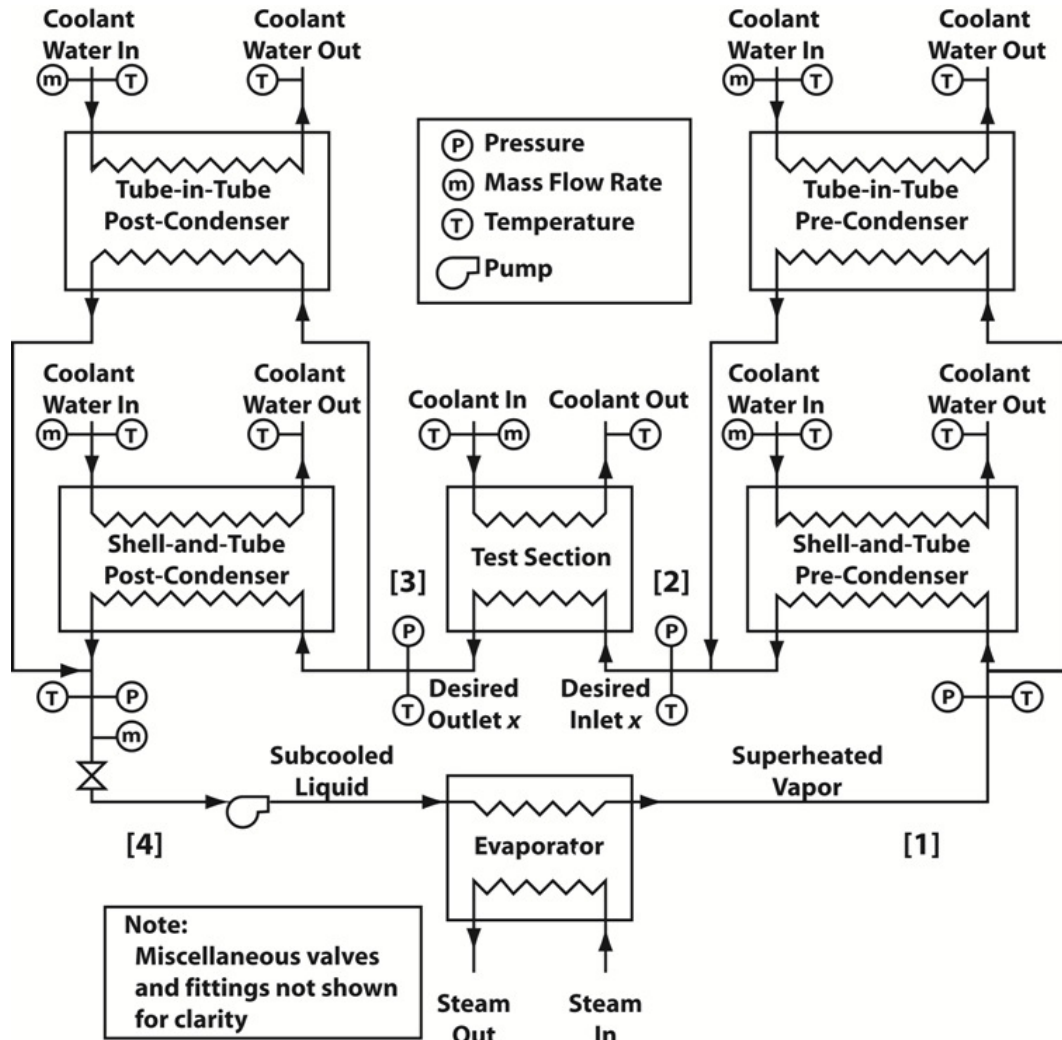


Figure 3.2: Schematic of Large Diameter Tube Test Facility

temperature and pressure measurements at the entrance to the pre-condenser. Either the tube-in-tube or shell-and-tube heat exchanger is chosen for the pre-condenser based on the necessary heat duty to acquire the desired data point. The tube-in-tube condenser has a smaller UA and is used for high quality and low mass flux data where a low heat duty is required to achieve the desired test section inlet state. The shell-and-tube condenser has a larger UA and is used for low quality and high mass flux data where a larger heat duty is required to achieve the desired test section inlet state. A summary of the pre- and post-condenser heat exchanger dimensions are displayed in Table 3.1. The flow rate of the cooling water in the pre-condenser is adjusted to condense the refrigerant to the desired

Table 3.1: Pre- and Post-Condenser Dimensions

Pre-Condenser					
Shell-and-Tube Exergy Inc.: 35 Series Model 00256-1			Tube-in-Tube (in-house)		
Length	$L_{pre,s}$ (mm)	460	Length	$L_{pre,t}$ (mm)	432
Insulation Diameter	$D_{pre,ins,s}$ (mm)	100	Insulation Diameter	$D_{pre,ins,t}$ (mm)	100
Shell, Outer Diameter	$D_{pre,o,s}$ (mm)	38.1	Outer Tube, Outer Diameter	$D_{pre,o,t}$ (mm)	12.7
Shell, Inner Diameter	$D_{pre,i,s}$ (mm)	34.8	Outer Tube, Inner Diameter	$D_{pre,i,t}$ (mm)	10.9
Tube Outer Diameter	(mm)	3.18	Inner Tube, Outer Diameter	(mm)	6.35
Wall Thickness	(mm)	0.32	Inner Tube, Inner Diameter	(mm)	4.57
Heat Transfer Area	(m ²)	0.27			
Tube Length: Condenser to Test Section	$L_{r,pre-to-test}$ (mm)	914	Tube Length: Condenser to Test Section	$L_{r,pre-to-test}$ (mm)	914
Tube/Baffle Count		55/11			
Post-Condenser					
Shell-and-Tube Exergy Inc.: 35 Series Model 00256-1			Tube-in-Tube (in-house)		
Length	$L_{post,s}$ (mm)	206	Length	$L_{post,t}$ (mm)	1295
Insulation Diameter	$D_{post,ins,s}$ (mm)	100	Insulation Diameter	$D_{post,ins,t}$ (mm)	100
Shell, Outer Diameter	$D_{post,o,s}$ (mm)	38.1	Outer Tube, Outer Diameter	$D_{post,o,t}$ (mm)	12.7
Shell, Inner Diameter	$D_{post,i,s}$ (mm)	34.8	Outer Tube, Inner Diameter	$D_{post,i,t}$ (mm)	10.9
Tube Outer Diameter	(mm)	3.18	Inner Tube, Outer Diameter	(mm)	6.35
Wall Thickness	(mm)	0.32	Inner Tube, Inner Diameter	(mm)	4.57
Heat Transfer Area	(m ²)	0.13			
Tube Length: Condenser to Test Section	$L_{r,test-to-post}$ (mm)	914	Tube Length: Condenser to Test Section	$L_{r,test-to-post}$ (mm)	914
Tube/Baffle Count		55/7			

thermodynamic state at the test section inlet [2]. The saturated inlet state (i.e. quality) of the refrigerant is evaluated using the pressure measurement at the test section inlet, energy balances across the pre-condenser, and temperature and pressure measurements at the superheated state. All of the absolute pressure transducers (Rosemount, model 3051) have an uncertainty of $\pm 0.075\%$ of the span. To determine the state at the outlet of the test section [3], a similar method is employed using the temperature and pressure measurements at the subcooled state at the post-condenser outlet [4] and energy balances across the post-condenser. One of the two differential pressure transducers (Rosemount 3051, uncertainty $\pm 0.075\%$ of span) measures the pressure drop across the test section. Whenever possible the low-range differential pressure transducer was used to measure the pressure drop because of its higher accuracy. However, most of the pressure drop measurements were taken using the mid-range differential pressure transducer. The subcooled liquid is then pumped through the evaporator and superheated to complete the closed loop. The active refrigerant inventory in the test loop is accurately controlled using an accumulator (Accumulators Inc. A13100: maximum operating pressure of 21 MPa.)

It is possible to determine the heat duty in the test section using the inlet and outlet conditions measured at the test section. However, uncertainties in measured test section heat duty are unsatisfactory using this method because of the small quality changes desired to obtain data at high quality resolutions. Therefore, the condensation heat duty is also measured in the test section. This loop is cooled by a primary coolant loop. These experiments use the thermal amplification technique developed by Garimella and Bandhauer (2001) to ensure high condensation rate and heat transfer resistance accuracies at small quality increments. The thermal amplification technique uses a closed-loop primary cooling line in the test section, which is in turn coupled to a secondary cooling line with a shell-and-tube heat exchanger. A schematic of the setup is shown in Figure

3.3. The primary cooling loop is operated at a high flow rate, ensuring that the refrigerant side represents the dominant thermal resistance. It is important to maintain the refrigerant side as the dominant thermal resistance in the test section when obtaining the refrigerant heat transfer coefficient from the test section heat duty and LMTD. The high flow rate of the primary loop also results in a very small temperature rise in the coolant that does not permit accurate measurement of the test section heat duty. To address this, the secondary loop is operated at a lower flow rate and the heat transfer from the primary coolant to the secondary coolant results in a large temperature rise in the

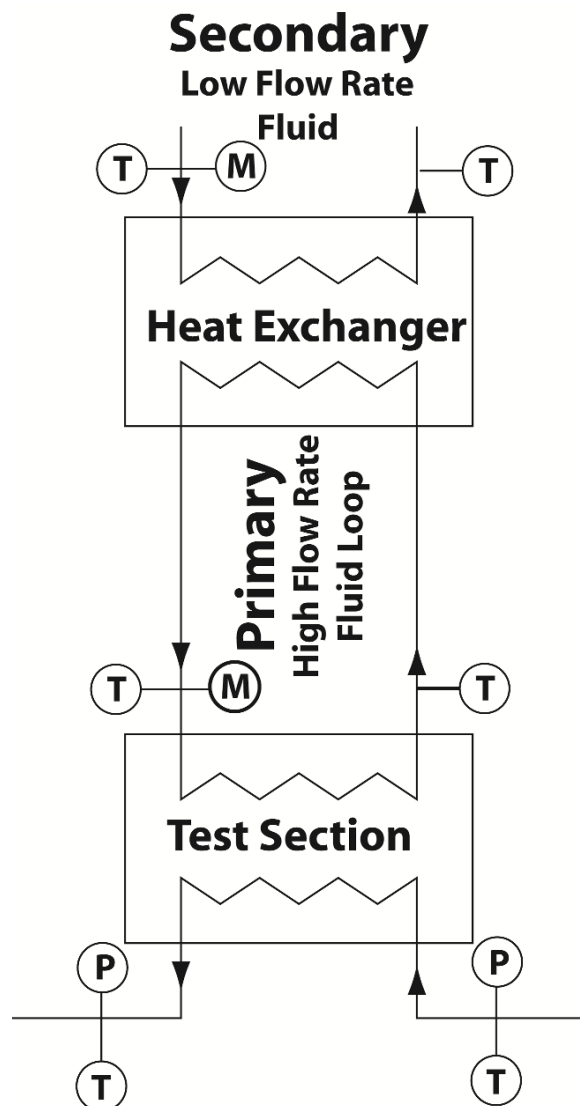


Figure 3.3: Schematic of System for Thermal Amplification Technique

Table 3.2: Primary Loop Dimensions

Primary Loop		
Equivalent Length (for heat loss)	L_{prim} (mm)	4548
Actual Length	$L_{\text{prim,tube}}$ (mm)	2540
Insulation Diameter	$D_{\text{prim,ins}}$ (mm)	76
Outer Diameter	$D_{\text{prim,o}}$ (mm)	12.7
Inner Diameter	$D_{\text{prim,i}}$ (mm)	10.92
Relative surface Roughness	e_{prim} (-)	0.0015

secondary coolant across the shell-and-tube heat exchanger. This large temperature difference enables measurement of test section heat duty with higher accuracy. This technique ensures that the refrigerant side has the dominant resistance while maintaining high accuracies in the measured heat duty, which allows for low uncertainties in refrigerant heat transfer coefficient at small quality increments. The primary cooling loop flow rate is measured using a magnetic flow meter (Rosemount 8711, uncertainty 0.5%) and the secondary cooling loop flow rate is measured using a Coriolis mass flowmeter (Micromotion DS006, uncertainty $\pm 0.15\%$.) The primary cooling loop details are shown in Table 3.2. The equivalent length of the primary cooling loop, L_{prim} , is used for heat loss calculations and is estimated by summing the surface area of all the components within the loop (flow meter, coolant pump, and tubing) and dividing by the inner perimeter. The dimensions of the shell-and-tube secondary loop heat exchanger are shown in Table 3.3.

The large diameter test facility is a closed refrigerant loop constructed mainly of 12.7 mm outer diameter stainless steel tubing with a wall thickness of 1.24 mm and pressure rating of 25 MPa (Swagelok, 2003). A total of 27 resistance temperature detectors (RTDs) and thermocouples, 6 pressure transducers, and 4 flowmeters are used to record the necessary information through a National Instruments data acquisition system (DAQ) and transferred to a Windows-based computer. The equipment details are presented in the

Table 3.3: Secondary Loop Heat Exchanger Dimensions

Shell-and-Tube Exergy Inc.: 23 Series Model 00540-4		
Length	L_{sec} (mm)	173
Insulation Diameter	$D_{sec,ins}$ (mm)	76
Shell, Outer Diameter	$D_{sec,o}$ (mm)	25.4
Shell, Inner Diameter	$D_{sec,i}$ (mm)	22.9
Tube Diameter	(mm)	3.18
Wall Thickness	(mm)	0.32
Heat Transfer Area	(m ²)	0.04
Tube/Baffle Count		19/9

Table 3.4: Data Acquisition System

Instrument	Manufacturer	Model	Description
Measurement Card Chassis	National Instruments	SCXI-1000	4 slots
Thermocouple/ Voltage Card		SCXI-1102	32 Channels
RTD Card		SCXI-1503	16 Channels

Table 3.5: Large Diameter Tube Facility Pressure Transducers

Instrument	Manufacturer	Model	Serial No.	Range	Uncertainty
Absolute Pressure Transducer	Rosemount	3051TA4A2 B21AE5M5	$P_{r,post,out}$:1021623 $P_{r,test,out}$:1019353 $P_{r,test,in}$:1019351 $P_{r,pre,in}$:1019352	0-27580 kPa	± 0.075% of span
Differential Pressure Transducer, $\Delta P_{mid-range}$	Rosemount	3051CD3A2 2A1AB4M5	0687134	0-62 kPa	± 0.075% of span
Differential Pressure Transducer, $\Delta P_{low-range}$		3051CD1A2 2A1AM5	687133	0-6.2 kPa	± 0.075% of span

following tables: DAQ details in Table 3.4, model and serial numbers of the pressure transducers and RTDs/thermocouples in Tables 3.5 and 3.6, respectively, flowmeter specifications in Table 3.7, and high-speed video equipment for large diameter tube experiments in Table 3.8.

Due to the much smaller mass flow rates and condensation heat duties in the smaller diameter tubes investigated in this study and the large thermal mass of the larger test facility, a second, much smaller test facility was used for the 0.508 to 1.55 mm diameter tube experiments. A schematic of the small diameter tube test facility is shown in Figure 3.5. The numbers on the schematic note the different state points of the refrigerant loop. Refrigerant exits the condenser in a subcooled state and is pumped into the test facility pre-heater [1]. The refrigerant mass flow rate is measured using a Coriolis flow meter (Rheonik RHM 015, uncertainty $\pm 0.1\%$ of reading.) The fluid is precisely heated to the desired test section inlet state using a resistance cartridge heater. The dimensions of the cartridge heater and housing are shown in Table 3.9. A schematic of the heater assembly is shown in Figure 3.6. The housing consists of a Swagelok T-fitting and the cartridge heaters are Watlow Firerod Series heaters. The electrical input is accurately measured using an AC Watt Transducer (Ohio Semitronics, uncertainty $\pm 0.2\%$ of reading.) The test section inlet state [2] is evaluated using the pressure measurement at the inlet, and an energy balance across the pre-heater. The heat input to the fluid is obtained from the measured electrical heat input and the heat losses to the environment due to radiation and convection from the heater housing, and the tubing to the test section. All of the absolute pressure transducers (Rosemount, model 3051) have an uncertainty of $\pm 0.075\%$ of the span. The test section outlet state [3] is obtained in a similar manner using the temperature and pressure measurements at the outlet of the post-heater [4], where the refrigerant is in the superheated state, and an energy balance across the post-heater. The refrigerant is then subcooled in the condenser and pumped back through the loop. The

Table 3.6: Temperature Measurements

Instrument	Manufacturer	Model	Range	Uncertainty
Refrigerant & Condenser Loop Thermocouples	Omega	TMQSS-125G-6	Max. Temperature = 220°C	± 0.25°C
Test-Section Thermocouples		5TC-TT-T-36-72	Max. Temperature = 180°C	± 0.25°C
RTDs		PR-13	Max. Temperature = 400°C	± 0.25°C

Table 3.7: Large Diameter Tube Facility Flowmeter Specifications

Instrument	Manufacturer	Model	Serial No.	Range	Uncertainty
Refrigerant Mass Flow Meter	Micromotion	CMF025M319NU	Sensor: 326974	0-3.63 kg/min	± 0.10% of reading
Basic Remote Flow Transmitter		IFT9701R6D3U	IFT: 2114443 Sensor: 366359		
Secondary Loop Water Mass Flow Meter	Micromotion	DS006S100SU	Sensor: 205104	0-0.91 kg/min	± 0.15% of reading
Basic Remote Flow Transmitter		IFT9701R6D3U	IFT: 2114848 Sensor: 366366		
Post- Condenser Rotameter	Gilmont Accucal	GF-4541-1220	XXXXXXXXXX	0-125 mL/min	± 2% of reading
		GF-4541-1240	XXXXXXXXXX	0-2.2 L/min	
		GF-4541-1250	XXXXXXXXXX	0-4.8 L/min	
Primary Loop Volumetric Flow Tube	Rosemount	8711TSE30FS1	80675	0-25.02 L/min	0.5% of reading
Magnetic Flow Transmitter		8712CT12M4	0860087272		
Pre-Condenser Volumetric Flow Tube	Rosemount	8711: RRE15FS1	0071955	0-6.256 L/min	± 0.5% of reading
Magnetic Flow Transmitter		8712CT12M4	63610		

Table 3.8: Large Diameter Tube Facility High-Speed Video Equipment

Instrument	Manufacturer	Model	Serial No.	Specifications
High Speed Video Camera	Photron	Fastcam – ultima 1024	31705025	500 fps at 1024×1024 pixel resolution 16,000 fps at reduced resolution
Camera Lens	Nikon	Micro-Nikkor 105 mm	XXXXXXXXXX	Focuses up to 1:1 52 mm filter thread

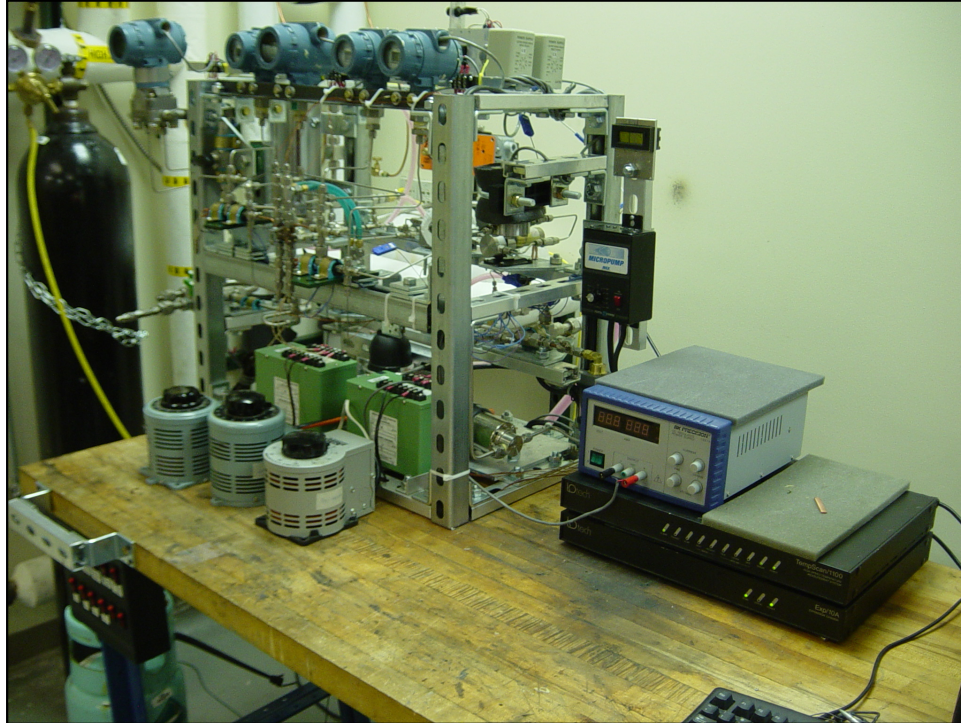


Figure 3.4: Photograph of Small Diameter Tube Test Facility

pressure drop across the test section is measured with a differential pressure transducer (Rosemount, model 3051) that has an uncertainty of $\pm 0.075\%$ of the span. The refrigerant inventory in the small test facility is accurately controlled using an accumulator (Accumulators Inc. AM631003: maximum operating pressure of 21 MPa.)

The test section heat duty is obtained from the energy balances across the pre-heater and post-heater. The coolant flow rate was measured using a rotameter (McMaster-Carr Model 5079K18, uncertainty $\pm 4\%$) and was maintained at the highest flow rate of $4.2 \times 10^{-5} \text{ m}^3 \text{ s}^{-1}$ for almost all experiments. This flow rate was used to determine the coolant-side heat transfer coefficient. The high volumetric flow rate ensured a low coolant side thermal resistance. Heat removed from the test section is rejected to a chilled glycol loop in the laboratory. This chilled glycol loop is used to remove heat from the primary coolant loop and cools the refrigerant at the outlet of the post-heater to a subcooled state before it is pumped back through the system. The chilled glycol loop is

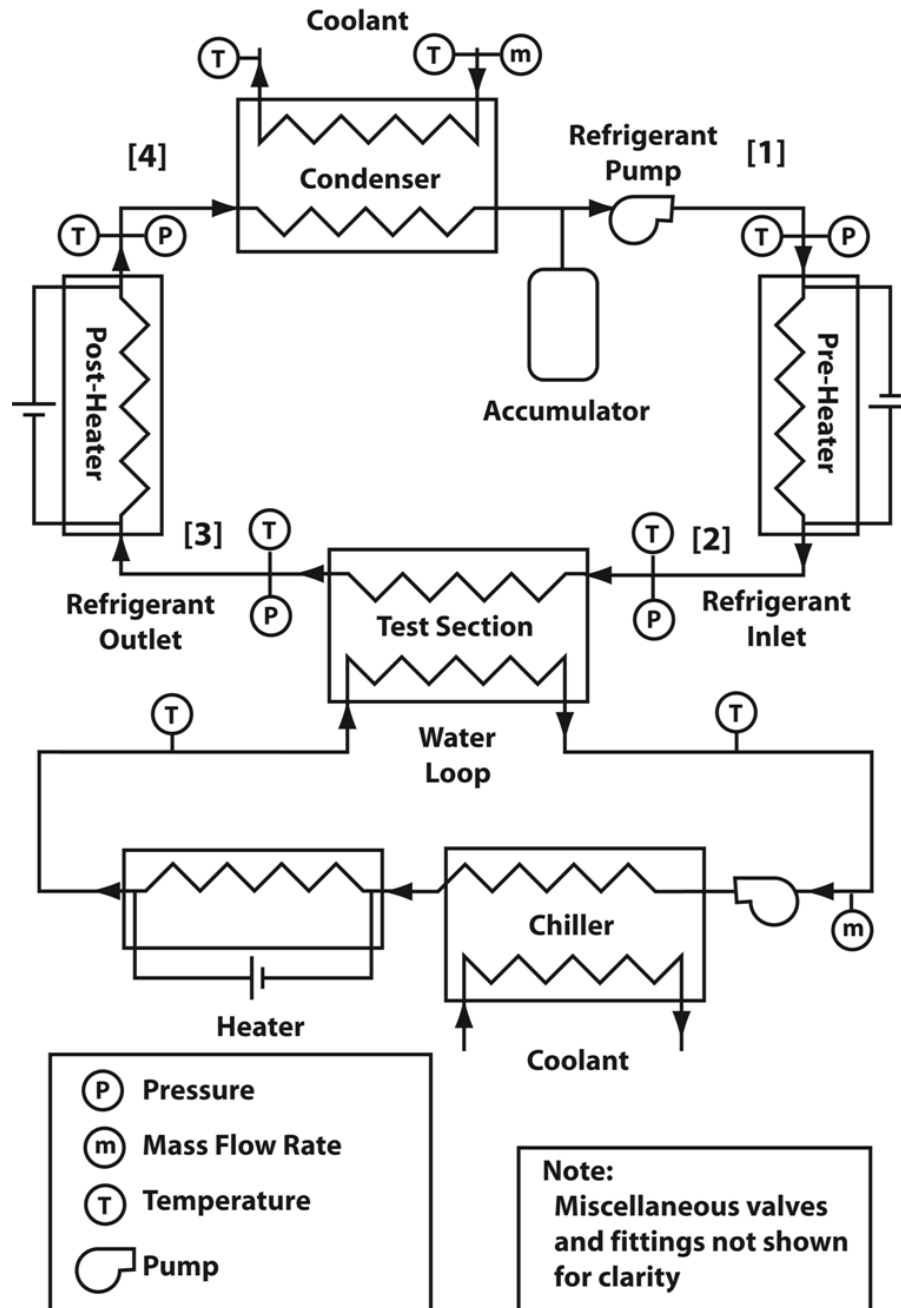


Figure 3.5: Schematic of Small Diameter Tube Test Facility

supplied from a small stand-alone recirculating chiller (Neslab Merlin M75 series (serial number: 109194014) with a capacity of 2225 W and a temperature range of -15 to 35°C.)

The facility is a closed refrigerant loop constructed mainly of 3.2 mm outer diameter stainless steel tubing with a wall thickness of 0.89 mm and pressure rating of 75 MPa

Table 3.9: Pre- and Post-Heater Dimensions

Heater Assembly		
Equivalent Length (for heat loss)	L_{Heater} (mm)	95
Horizontal Length	(mm)	65
Vertical Length	(mm)	30
Heater Fitting, Inner Diameter	$D_{\text{Heatertube,i}}$ (mm)	10.16
Heater Fitting, Outer Diameter	$D_{\text{Heatertube,o}}$ (mm)	15.24
Heater Insulation, Outer Diameter	$D_{\text{heater,ins,o}}$ (mm)	25.4
Cartridge Heater		
Watlow: Firerod Series ModelE2A57		
Heater Rod Diameter	(mm)	6.35
Heater Rod Length	(mm)	50.8

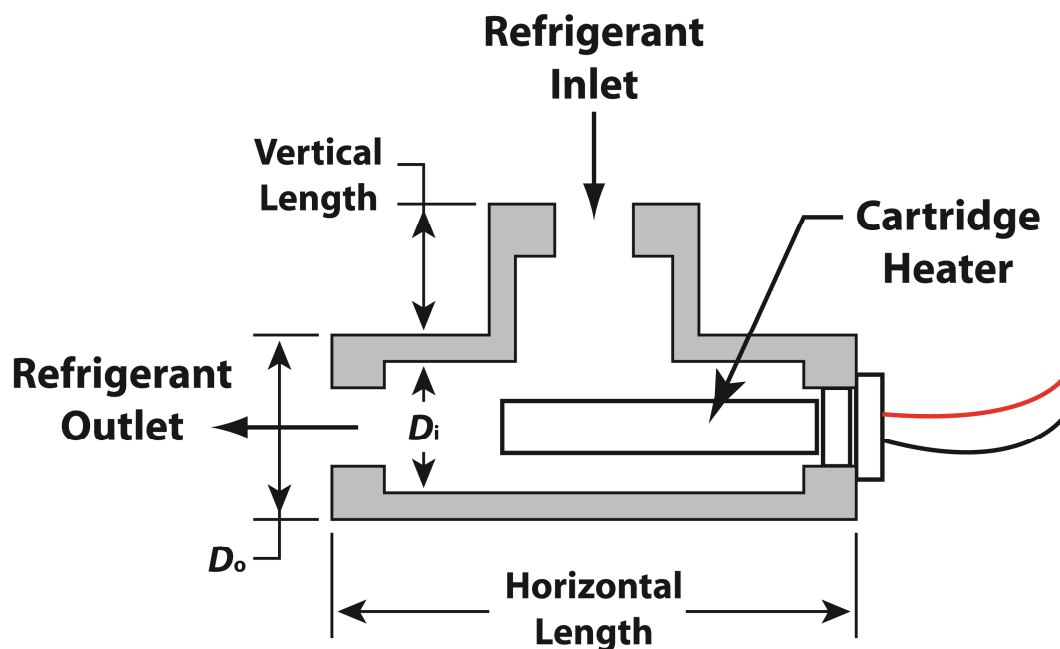


Figure 3.6: Refrigerant Heater Schematic for Pre- and Post-Heater in Small Diameter Tube Facility

(Swagelok, 2003). A total of 10 thermocouples, 5 pressure transducers, 2 flowmeters, and two watt transducers are used to record the necessary information through the same National Instruments data acquisition system (DAQ) and transferred to a Windows-based computer. The equipment details are displayed in the following tables: DAQ details in Table 3.4, model and serial numbers of the pressure transducers in Table 3.10, flow meter and watt transducer specifications in Table 3.11 and the high-speed video equipment used for small tube experiments in Table 3.12.

Table 3.10: Small Diameter Tube Facility Pressure Transducers

Instrument	Manufacturer	Model	Serial No.	Range	Uncertainty
Absolute Pressure Transducer	Rosemount	3051TA5A2 B21AE5M5	$P_{r,pre-heat,out}$:0921022 $P_{r,post-heater,in}$:0921024	0-68948 kPa	$\pm 0.075\%$ of span
		3051CA4A2 2A1AM5	$P_{r,pre-heater,in}$:2036883 $P_{r,post-heater,out}$:2036884	0-27580 kPa	
Differential Pressure Transducer, $\Delta P_{measured}$	Rosemount	3051CD4A2 2A1ADFM5	1719727	0-248 kPa	$\pm 0.075\%$ of span

Table 3.11: Small Diameter Tube Facility Mass Flow Meters and Watt Transducers

Instrument	Manufacturer	Model	Serial No.	Range	Uncertainty
Refrigerant Mass Flow Meter	Rheonik	RHM 015 GNT	RHM-09210	0-0.1 kg/s	$\pm 0.10\%$ of reading
Water Flow Meter	McMaster-Carr	5079k18	X	15.14-151.4 L/hr	$\pm 4\%$ of reading
AC Watt Transducer	Ohio Semitronics	GW5-010E	Pre-heater 11031821	0-1000 Watts	0.2% of reading
			Post-heater 11031822		

Table 3.12: Small Diameter Tube Facility High-Speed Video Equipment

Instrument	Manufacturer	Model	Serial No.	Specifications
High Speed Video Camera	Photron	SA4-500K-M1	31705025	3,600 fps at 1024×1024 pixel resolution 500,000 fps at reduced resolution
Camera Lens	Navitar	12X	464383	0.58-7× Magnification

3.1.2 Test Section

Two different sets of test sections were used, one specifically designed for high-pressure visualization of condensing R404A, and the other for obtaining accurate heat transfer measurements of condensing R404A. Both test sections resemble tube-in-tube heat exchangers. The refrigerant flows through the inner tube, while the coolant flows in a counter-flow orientation in the annulus. A schematic of the test section is shown in Figure 3.7. First the visualization test section design is described, followed by the design of the heat transfer test sections.

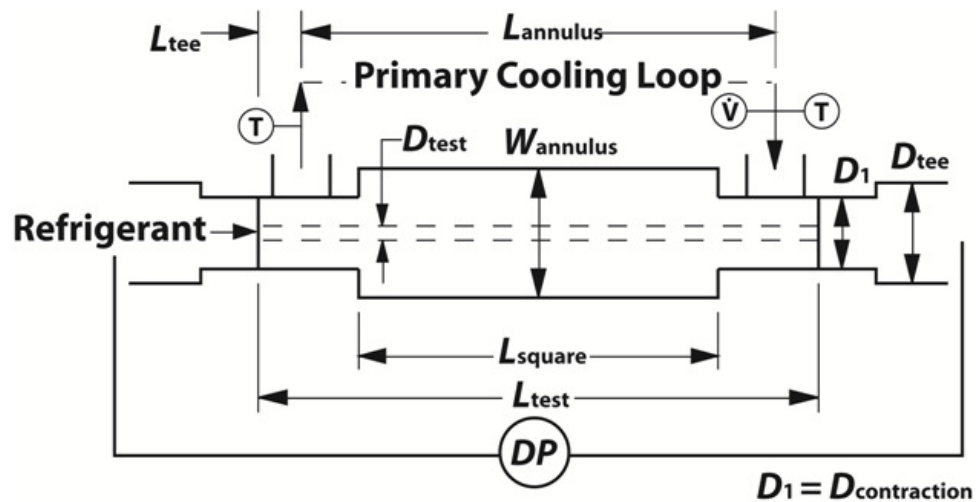


Figure 3.7: Tube-in-Tube Test Section Schematic

The visualization test section resembles a tube-in-tube heat exchanger in which the inner tube is constructed of high strength quartz tubing (Momentive Performance Materials, Strongsville, Ohio) while the annulus is constructed of square acrylic tubing. Square tubing was chosen for the annulus to minimize visual distortion. A photograph of the 3.00 mm visualization test section is shown in Figure 3.8, while a schematic of the test section and its components is displayed in Figure 3.9. A summary of the visualization test section dimensions is presented in Table 3.13. The transparent tubing is coupled to the test facility using intermediate Swagelok tubing and compression fittings. The transparent tubing is secured within these fittings by a method developed in-house as shown in Figure 3.9. The transparent tube is connected to a rubber stopper. The rubber stopper is machined to fit tightly within the Swagelok tubing while securing the inner tube. Both the internal and external mating areas are sealed with epoxy to ensure a leak-free test section. The outer annular tubing is attached with a similar method. However, the rubber stopper in this case is also a transition from circular stock to square stock. The test section was pressure tested and rated to determine maximum saturation temperatures for testing. The inner quartz tubing was shown to withstand elevated pressures (> 2068 kPa) while the outer annular chamber was able to withstand 1379 kPa. The ability to

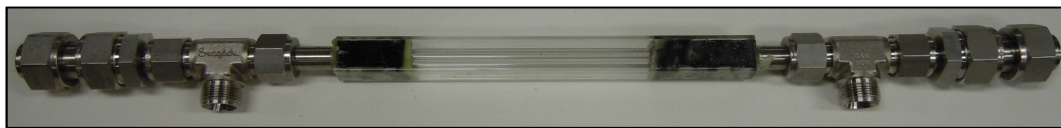


Figure 3.8: Photograph of Visualization Test Section

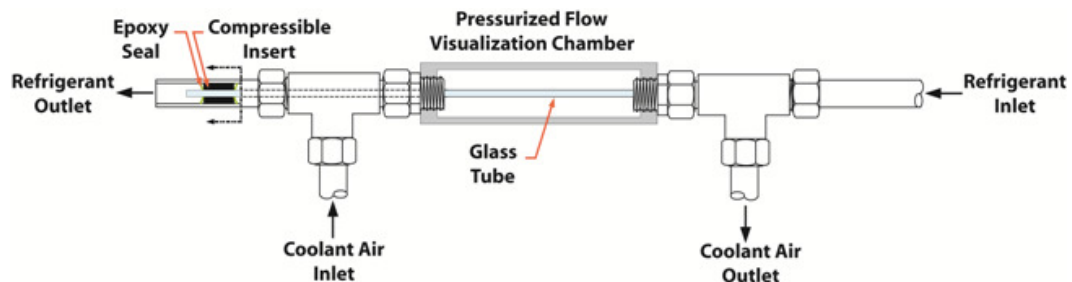


Figure 3.9: Visualization Test Section Schematic

Table 3.13: Visualization Test Section Dimensions

Description	Symbol	Test Section Inner Diameter, mm		
		3.00	1.00	0.508
Length of Annulus	L_{annulus} (mm)	406	155	150
Length of Square	L_{square} (mm)	203	95	95
Length of inner tube	L_{test} (mm)	483	290	285
Length of Tee	L_{tee} (mm)	38.1	26.9	26.9
Insulation diameter	$D_{\text{test, ins}}$ (mm)	100	25.4	25.4
Square tube, outer width	$W_{\text{annulus, o}}$ (mm)	19.1	12.7	12.7
Square tube, inner width	$W_{\text{annulus, i}}$ (mm)	12.7	9.53	9.53
Inner tube, outer diameter	$D_{\text{test, o}}$ (mm)	8.0	3.0	3.0
Inner tube, inner diameter	$D_{\text{test, i}}$ (mm)	3.0	1.0	0.5083
Swagelok Tee-Fitting, inner diameter	D_{tee} (mm)	12.7	4.8	4.8
Swagelok Contraction, inner diameter	$D_{\text{contraction}}$ (mm)	10.2		

hold elevated pressures in both chambers allows for a small pressure difference across the glass tube at high saturation pressures. The flow rate of the air is controlled to achieve a nominal change in quality, Δx , of about 0.05 across the test section. To achieve higher air-side temperatures, a silicon heater wrap (McMaster-Carr, Model 3631K21) was attached to the outside of the air inlet tubing which allowed for an increase in temperature of about 10°C higher than the ambient. At low mass fluxes and high saturation temperatures, the minimum achievable Δx is larger, due to the increased temperature difference from the coolant, the relatively lower heat of vaporization at the higher saturation temperatures, and the low heat duties associated with low mass flow rates.

The heat transfer test sections also resemble tube-in-tube heat exchanges. Refrigerant flows through a copper inner tube housed in an outer seamless stainless tube. Coolant flows through the annulus between the two tubes in a counter-flow configuration. All of

the connections are made with Swagelok components. A photograph of the test sections is shown in Figure 3.10, and a summary of the dimensions is provided in Table 3.14.



Figure 3.10: Photograph of Heat Transfer Test Sections

Table 3.14: Heat Transfer Test Section Dimensions

Description	Symbol	Test Section Inner Diameter, mm		
		3.05	1.55	0.86
Length of Annulus	L_{annulus} (mm)	152	145	85
Length of reducer	L_{reducer} (mm)	22.9	18.5	14.0
Length of inner tube	L_{test} (mm)	324	305	305
Length of Tee	L_{tee} (mm)	13.21	11.5	11.5
Insulation diameter	$D_{\text{test, ins}}$ (mm)	100	100	100
Outer tube, outer diameter	$D_{\text{annulus, o}}$ (mm)	12.7	6.35	6.35
Outer tube, inner diameter	$D_{\text{annulus, i}}$ (mm)	10.2	4.57	4.57
Inner tube, outer diameter	$D_{\text{test, o}}$ (mm)	6.35	3.175	1.57
Inner tube, inner diameter	$D_{\text{test, i}}$ (mm)	3.048	1.549	0.86
Swagelok Tee-Fitting, inner diameter	D_{tee} (mm)	9.25	4.8	4.8
Swagelok Contraction, inner diameter	$D_{\text{contraction}}$ (mm)	4.83	4.57	3.14

3.2 High-Speed Camera Setup

During visualization experiments, the test section was illuminated on the side opposite of the high-speed video receiver as shown in Figure 3.11. Two Lowel Omni-Light light sources were placed approximately one meter from the test section and at an angle of 20° from the test section horizontal centerline. It was important to maintain this angle to ensure that the light sources did not point directly into the camera lens. The light sources were softened using a medium density light diffusion screen. The camera was initially positioned 0.25 m from the test section and the distance and lens adjusted until the desired focus and field of view was achieved. For all tube diameters investigated, a field of view of 10 tube diameters was used. This allows for observation of local liquid films while still viewing the global liquid-vapor dynamics.

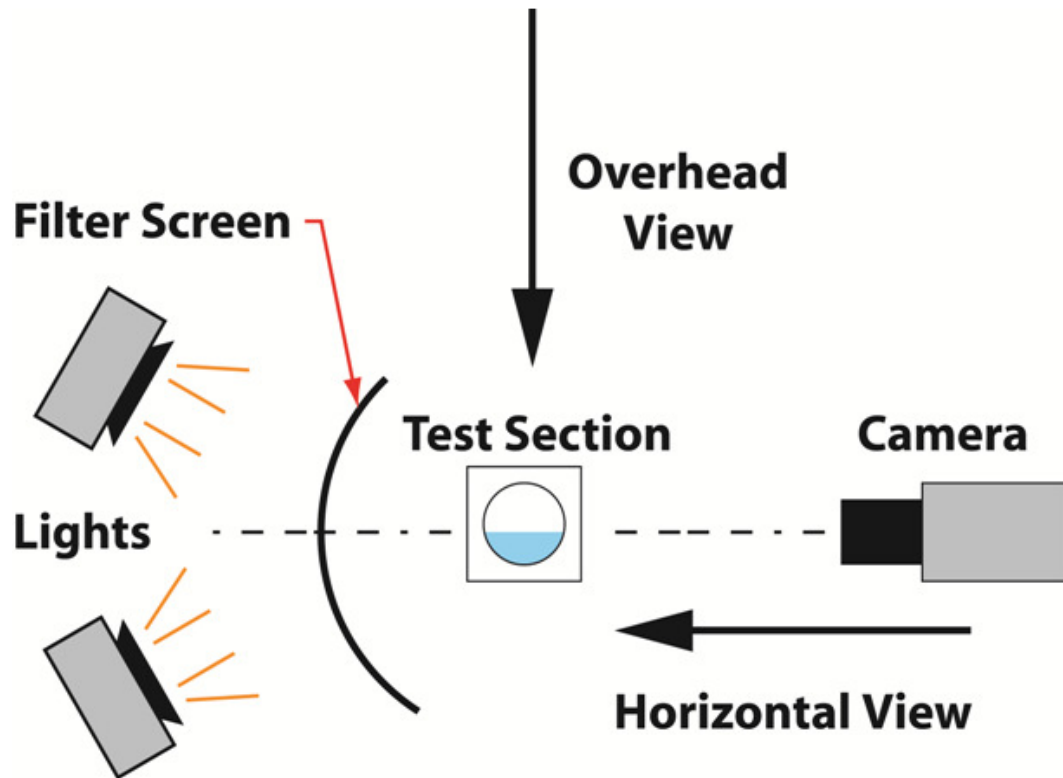


Figure 3.11: High Speed Video Camera and Lighting Setup

The test section was viewed from two different angles at different times using the same camera. When viewing from the side, the camera is placed horizontally, and its placement is verified using a handheld leveling device. Similar verification is used when viewing the test section from an overhead view.

A reference length was required to relate the image captured in pixels to a measureable distance. In each case, the inner tube diameter was used. Details of this process are provided in Sections 5.1 and 5.2.

3.3 Charging Refrigerant Loop with R404A

Before either system was evacuated for charging, leak testing on the refrigerant loop was conducted. The system was initially charged with 1000 kPa of nitrogen, and leaks were detected by an ultrasonic leak detector and by applying a dilute soap mixture to the external surface of the facility. Once all possible leaks were found and corrected using this method, the system was charged with a refrigerant/nitrogen mixture. The system pressure was monitored for 24 hours for slow leaks. The slow leaks were then detected using the Accuprobe UV Leak Detector (United Refrigerants Inc., Model 69336) that is capable of detecting R134a leaks at a rate of 1.7 g yr^{-1} . Once system integrity was established, the test facility (for both facilities) was evacuated using a 3 cfm rotary vane vacuum pump (J.B. Industries, Model: DV-85N) in conjunction with an analog vacuum gage (Thermal Engineering Company, Model: 14571). The facility was monitored for pressure changes after it reached a pressure of 200 microns ($6.9 \text{ kPa} = 5.17 \times 10^4 \text{ microns}$) and the pump turned off. The large tube facility was charged with approximately 3.4 kg, while the small tube facility was charged with approximately 200 g of R404A after confirming that the system was leak-free. Test loop integrity was confirmed by leaving

the system at sub-atmospheric pressure and monitoring the pressure for changes over a period of 24 hours.

3.4 Test Procedures

The refrigerant in the facility is initially at a sub-cooled liquid state, verified by visual observation of the sight glass and the visualization test section. In the large tube test facility, the coolant flow rates for the pre- and post-condensers are set, followed by the flow rate of the refrigerant. The refrigerant flow rate is set to correspond with the desired mass flux at the test section. The steam lines are then opened and the system pressure is closely monitored and adjusted to the necessary operating pressure using a nitrogen cylinder attached to the accumulator. Close attention is also given to the refrigerant mass flow rate and adjustments are made to maintain desirable mass fluxes. In the small diameter tube test facility, the recirculating chiller is turned on and the flow rate of the test section coolant and condenser are set at the desired value. The flow rate of the refrigerant is then set. The post- and pre-heater are slowly adjusted until the desired inlet and outlet test conditions are met.

All measurements are monitored with real-time charting of the refrigerant temperature and pressure in the test section and mass flow rate to determine the approach to steady state. A data point is taken by recording measurements every second over a five minute period after the test reaches steady state. A typical start up time for the large test facility is 2-3 hours, and about 1 hour between data points, depending on mass flux and quality desired. The thermal mass of the small facility is much lower, which results in a faster start-up time (about 1 hour) and shorter time between data points (about 30 minutes.) At the midpoint of recording the data point, the visualization equipment is initialized and high-speed video taken for a duration of 1 second at a speed of 1000 fps. The data are

analyzed immediately to ensure that the desired test conditions are met and necessary energy balances and uncertainties are achieved. These checks include ensuring that energy balances between the thermal amplification technique and pre- and post-condensers energy balances are within acceptable uncertainties, saturation temperatures at the inlets and outlets of the test sections using local thermocouple and pressure measurements are in agreement, and heat transfer coefficient uncertainties are close to the desired 15%. Another data point is taken to ensure that the flow conditions do not change over time. The operating conditions are then altered to obtain the next data point. The data are analyzed using the Engineering Equation Solver (EES) program discussed in the next section.

CHAPTER 4: DATA ANALYSIS

The methods for determining relevant testing states, sample calculations for two-phase tests, heat transfer coefficients, pressure drops, and their associated uncertainties from the measured data are described here. The thermodynamic state and properties of water, air and refrigerants were obtained using Engineering Equation Solver (EES) software (Klein, 2008) coupled with the EES-REFPROP interface to access refrigerant properties from REFPROP Version 7.0 (Lemmon *et al.*, 2002). Uncertainty propagation in EES reported here assume that all measurements are uncorrelated and random (Taylor and Kuyatt, 1994).

4.1 Large Diameter Tube Condensation Analysis

The analysis presented in this section pertains to the test conditions for the large diameter tube test facility. Analyses conducted to obtain the refrigerant pressure drop and heat transfer coefficient from measured data are presented here. All calculation details are also displayed in Appendix B.1. The analyses are illustrated using a representative data point in what follows.

4.1.1 Test Section Quality

A summary of the measured values for the data point is presented in Tables 4.1 and 4.2. Sub-cooled refrigerant enters the evaporator and leaves superheated. The enthalpy of the refrigerant here is calculated using the temperature and pressure measurement at the pre-condenser inlet:

$$i_{r,pre,in} = f(T_{r,pre,in}, P_{r,pre,in}) = f(98.93 \text{ }^\circ\text{C}, 1475 \text{ kPa}) = 453.6 \pm 0.27 \text{ kJ/kg} \quad (4.1)$$

A large difference ($> 10^{\circ}\text{C}$) between the saturation temperature at the respective pressure and the pre-condenser refrigerant inlet temperature is required to ensure a superheated state. Similarly, a large temperature difference is required to ensure the refrigerant is at the sub-cooled state at the exit of the post condenser. These superheated and subcooled states enable calculation of the refrigerant enthalpy using temperature and pressure measurements. It is also important to ensure that sub-cooled liquid enters the pump, thus preventing damage to the pump from the ingress of a two-phase mixture. A summary of these measurements and differences for this example is presented in Table 4.3.

Table 4.1: Refrigerant Temperatures and Pressures

		Temperature ($^{\circ}\text{C}$)		Pressure (kPa)	
Pre – Condenser	Inlet	$T_{r, \text{pre, in}}$	98.93 ± 0.25	$P_{r, \text{pre, in}}$	1475 ± 2.6
	Outlet	$T_{r, \text{pre, out}}$	32.99 ± 0.25		
Test Section	Inlet	$T_{r, \text{test, in}}$	31.49 ± 0.25	$P_{r, \text{test, in}}$	1471 ± 2.6
	Outlet	$T_{r, \text{test, out}}$	30.89 ± 0.25	$P_{r, \text{test, out}}$	1449 ± 2.6
Post - Condenser	Inlet	$T_{r, \text{post, in}}$	30.77 ± 0.25		
	Outlet	$T_{r, \text{post, out}}$	20.75 ± 0.25	$P_{r, \text{post, out}}$	1449 ± 2.6

Table 4.2: Cooling Water Temperatures and Flow Rates

		Temperature ($^{\circ}\text{C}$)		Flow Rate		
Pre – Condenser	Inlet	$T_{w, \text{pre, in}}$	9.2 ± 0.25	$\dot{V}_{w, \text{pre}}$	0.1896 ± 0.001 L/min	$3.16 \pm 0.025 \times 10^{-6}$ m ³ /s
	Outlet	$T_{w, \text{pre, out}}$	46.4 ± 0.25			
Post – Condenser	Inlet	$T_{w, \text{post, in}}$	5.6 ± 0.25	$\dot{V}_{w, \text{post}}$	1.1 ± 0.0106 L/min	$1.83 \pm 0.17 \times 10^{-5}$ m ³ /s
	Outlet	$T_{w, \text{post, out}}$	14.51 ± 0.25			

Table 4.3: Condenser and Saturation Temperature Comparison

	Measured Temperature ($^{\circ}\text{C}$)	Saturation Temperature ($^{\circ}\text{C}$)	Temperature Difference (K)
Pre-Condenser Inlet	98.93 ± 0.25	31.55 ± 0.06	67.38
Post-Condenser Outlet	20.75 ± 0.25	30.46 ± 0.06	9.71

The refrigerant exits the pre-condenser as a two-phase fluid where the enthalpy cannot be deduced from temperature and pressure. The enthalpy of the refrigerant at the test section inlet must therefore be calculated using energy balances in the pre-condenser, Equation 4.3, after calculating the water-side heat duty, Equation 4.2. A more detailed heat loss calculation is presented in a subsequent section 4.1.2. The pre-condenser duty, based on the water-side, after accounting for the heat losses is:

$$\dot{Q}_{pre} = \dot{m}_{w, pre} (i_{w, pre, out} - i_{w, pre, in}) + \dot{Q}_{loss, pre} \quad (4.2)$$

$$\dot{Q}_{pre} = (0.00316 \text{ kg s}^{-1})(194.6 - 39.03) \text{ kJ kg}^{-1} + (0.3552) \text{ W} = 491.9 \pm 5 \text{ W}$$

The intermediate steps, such as water enthalpies and flow rate, can be found in the attached Appendix B.1. The test section inlet enthalpy is calculated using the pre-condenser energy analysis coupled with heat losses from the pre-condenser outlet to test section inlet. The term with the subscript “loss, pre-to-test” accounts for this loss. The enthalpy of the refrigerant entering the test section is a function of the refrigerant enthalpy at the pre-condenser inlet and the heat losses.

$$\dot{Q}_{pre} + \dot{Q}_{loss, pre-to-test} = \dot{m}_r (i_{r, pre, in} - i_{r, test, in}) \quad (4.3)$$

$$491.9 \text{ W} + 0.7649 \text{ W} = (0.005881 \text{ kg s}^{-1})(453 \text{ kJ kg}^{-1} - i_{r, test, in})$$

$$i_{r, test, in} = 369.8 \pm 5.8 \text{ kJ kg}^{-1}$$

The quality at the test section inlet is obtained from the pressure measurement and this refrigerant enthalpy.

$$x_{r, test, in} = f(P_{r, test, in}, i_{r, test, in}) \quad (4.4)$$

$$x_{r, test, in} = f(1471 \text{ kPa}, 369.8 \text{ kJ/kg}) = 0.95 \pm 0.01$$

The same methodology and energy balances are applied to the post-condenser to determine the test section outlet quality. In this example, the test section outlet quality is $x_{r, test, out} = 0.75 \pm 0.04$. The average of the inlet and outlet test section quality is taken for each data point:

$$x_{r, \text{ test, avg}} = \frac{x_{r, \text{ test, in}} + x_{r, \text{ test, out}}}{2} \quad (4.5)$$

$$x_{r, \text{ test, avg}} = \frac{0.95 + 0.75}{2} = 0.85 \pm 0.02$$

Test section heat duties can also be obtained from these quantities. However, due to the small quality difference across the test section, uncertainties in the heat duty are larger than acceptable values. Therefore, the thermal amplification technique method is used, as explained in Section 4.1.4.

4.1.2 Heat Losses to Environment

The entire test loop is covered in fiberglass insulation of low thermal conductivity ($k_{\text{ins}} = 0.043 \text{ W m}^{-1} \text{ K}^{-1}$) to minimize ambient heat losses. Heat losses from the insulation are due to natural convection and radiation. Calculation of the heat losses from the pre-condenser is detailed here. The heat loss calculations for the other elements in the test loop are conducted in a similar manner. All heat loss calculations are detailed in Appendix B.1.

The thermal resistance between the cooling water in the pre-condenser and the tube walls is assumed negligible and the inner wall of the outer shell is equal to the average cooling water temperature of the inlet and outlet of the condenser. This results in the following equation for heat loss to the environment, $\dot{Q}_{\text{loss, pre}}$:

$$\dot{Q}_{\text{loss, pre}} = \frac{(T_{\text{inner wall}} - T_{\text{ambient}})}{R_{\text{wall}} + R_{\text{ins}} + \left(\frac{R_{\text{nat. conv.}} R_{\text{radiation}}}{R_{\text{nat. conv.}} + R_{\text{radiation}}} \right)} \quad (4.6)$$

A schematic of this resistance network is shown in Figure 4.1. Conduction resistances R_{wall} and R_{ins} are determined using Equations 4.7 and 4.8 with all necessary variables provided in Table 3.1. The thermal conductivity of the wall, $k_{\text{pre},s} = 14.9 \text{ W m}^{-1} \text{ K}^{-1}$.

$$R_{\text{wall}} = \frac{\ln\left(\frac{D_{\text{pre},o,s}}{D_{\text{pre},i,s}}\right)}{2\pi k_{\text{pre},s} L_{\text{pre},s}} \quad (4.7)$$

$$R_{\text{wall}} = \frac{\ln\left(\frac{38.1 \text{ mm}}{34.8 \text{ mm}}\right)}{2\pi(14.9 \text{ W/m-K})(0.460 \text{ m})} = 2.104 \times 10^{-3} \text{ K W}^{-1}$$

$$R_{\text{ins}} = \frac{\ln\left(\frac{D_{\text{pre},\text{ins},s}}{D_{\text{pre},o,s}}\right)}{2\pi k_{\text{ins}} L_{\text{pre},s}} \quad (4.8)$$

$$R_{\text{ins}} = \frac{\ln\left(\frac{100 \text{ mm}}{38.1 \text{ mm}}\right)}{2\pi(0.043 \text{ W/m-K})(0.460 \text{ m})} = 7.764 \text{ K W}^{-1}$$

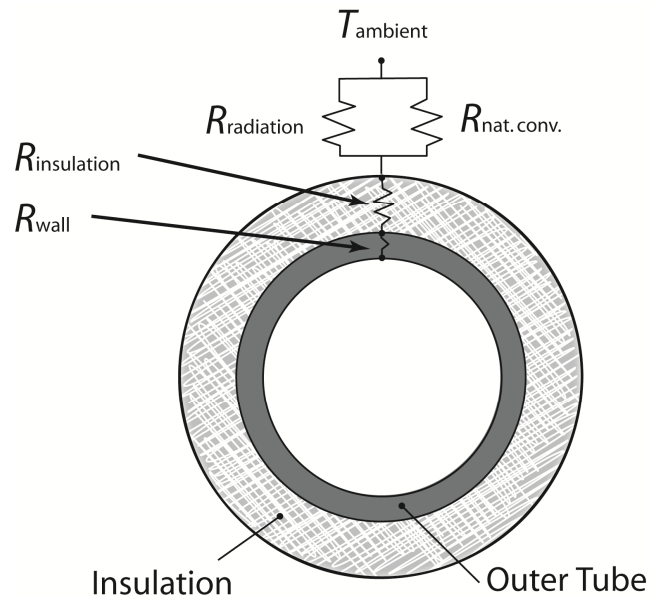


Figure 4.1: Schematic of Pre-Condenser Thermal Resistance Network

The emissivity of the outside surface of the insulation is assumed to be $\epsilon_{\text{ins}} = 0.85$, while the measured temperature of the surroundings is $T_{\text{ambient}} = 24.7^\circ\text{C}$. The radiative resistance is determined using Equation 4.9 where the Stefan-Boltzmann constant is $\sigma = 5.67 \times 10^{-8} \text{ W m}^{-2} \text{ K}^{-4}$. However, the surface temperature of the insulation is unknown and is solved iteratively using Equations 4.6 to 4.12. For this representative data point, the insulation surface temperature is $T_{\text{ins}} = 25.09^\circ\text{C}$.

$$R_{\text{radiation}} = \frac{1}{\epsilon_{\text{ins}} \pi D_{\text{pre, ins, s}} L_{\text{pre, s}} \sigma (T_{\text{ins}}^2 + T_{\text{ambient}}^2) (T_{\text{ins}} + T_{\text{ambient}})} \quad (4.9)$$

$$R_{\text{radiation}} = 1.356 \text{ K W}^{-1}$$

The natural convection heat transfer coefficient is a function of the Raleigh number, Ra . The thermal properties of air are evaluated at the average temperature, $T_{\text{avg}} = (T_{\text{ins}} + T_{\text{amb}})/2 = (25.09 + 24.72)^\circ\text{C} = 24.9^\circ\text{C}$.

$$Ra = \frac{g \beta_{\text{air}} (T_{\text{ins}} - T_{\text{ambient}}) D_{\text{pre, ins, s}}^3}{\nu_{\text{air}} \alpha_{\text{air}}} \quad (4.10)$$

$$Ra = \frac{(9.81 \text{ m s}^{-2})(0.003367 \text{ K}^{-1})(25.09 - 24.72)^\circ\text{C} (0.100 \text{ m})^3}{(1.56 \times 10^{-5} \text{ m}^2 \text{ s}^{-1})(2.206 \times 10^{-5} \text{ m}^2 \text{ s}^{-1})} = 35152$$

The Nusselt number is calculated using the Churchill and Chu (1975) correlation for natural convection around a horizontal cylinder.

$$Nu = \left(0.60 + \frac{0.387 Ra^{1/6}}{\left(1 + \left(\frac{0.559}{\text{Pr}} \right)^{9/16} \right)^{8/27}} \right)^2 \quad (4.11)$$

$$Nu = \left(0.60 + \frac{0.387 (35152)^{1/6}}{\left(1 + \left(\frac{0.559}{0.71} \right)^{9/16} \right)^{8/27}} \right)^2 = 5.94$$

The corresponding heat transfer coefficient is calculated using $h_{\text{nat. conv.}} = \text{Nu } k_{\text{air}}/D_{\text{pre, ins, s}}$, which results in $h_{\text{nat. conv.}} = 1.559 \text{ W m}^{-2} \text{ K}^{-1}$. The heat transfer coefficient in this case is very low because the temperature difference between the insulation and the ambient is very small. The resulting natural convective resistance is given by:

$$R_{\text{nat. conv.}} = \frac{1}{h_{\text{nat. conv.}} \pi D_{\text{pre, ins, s}} L_{\text{pre, ins, s}}} \quad (4.12)$$

$$R_{\text{nat. conv.}} = \frac{1}{(1.599 \text{ W m}^{-2} \text{ K}^{-1}) \pi (0.100 \text{ m}) (0.460 \text{ m})} = 4.438 \text{ K W}^{-1}$$

With all of the necessary terms computed, the heat loss in the pre-condenser is calculated using Equation 4.6, which results in.

$$\dot{Q}_{\text{loss, pre}} = \frac{(27.83 - 24.72)^\circ\text{C}}{\left[(2.104 \times 10^{-3}) + (7.764) + (1.039) \right] \text{K W}^{-1}} = 0.3526 \text{ W}$$

4.1.3 Test Section Heat Loss

The methodology for determining heat loss in the test section is similar to that outlined in the previous section. However, test section heat duties are smaller than those in the pre- and post-condenser, thus, the heat losses are more significant. Therefore, the thermal resistance in the test section includes the thermal resistance due to convection in the annulus, instead of assuming an inner wall temperature based on the coolant average temperature. The thermal resistance in the test section annulus is defined as:

$$R_{\text{annulus,o}} = \frac{1}{h_{\text{annulus}} \pi D_{\text{annulus,o}} L_{\text{test}}} \quad (4.13)$$

The heat transfer coefficient in the annulus, h_{annulus} , is predicted using the curve fit developed by Garimella and Christensen (1995) based on tabular data of Kays and Leung (1963) for laminar and turbulent single phase flows through an annulus. The Nusselt number correlation is a function of Reynolds number, $\text{Re}_{\text{annulus}}$, Prandtl number, Pr , and

diameter ratio, r^* . For the representative data point considered here, the flow is turbulent with $Re_{\text{annulus}} = 9801$, and the corresponding Nusselt number equation is:

$$\begin{aligned} Nu_{\text{turbulent}} &= 0.025 \cdot Re_{\text{annulus}}^{0.78} Pr^{0.48} (r^*)^{-0.14} \\ Nu_{\text{turbulent}} &= 0.025 \cdot (9801)^{0.78} (6.945)^{0.48} (0.6225)^{-0.14} = 87.9 \end{aligned} \quad (4.14)$$

The resulting heat transfer coefficient in the annulus is $h_{\text{annulus}} = 13677 \text{ W m}^{-2} \text{ K}^{-1}$. The thermal resistance in the annulus is calculated using Equation 4.13.

$$R_{\text{annulus,o}} = \frac{1}{(13677 \text{ W m}^{-2} \text{ K}^{-1}) \pi (10.2 \text{ mm}) (152.4 \text{ mm})} = 0.01487 \text{ K W}^{-1}$$

The heat transfer from the test section to the environment is predicted with the added convective thermal resistance in the annulus.

$$\begin{aligned} \dot{Q}_{\text{loss,test}} &= \frac{(T_{w,\text{test,avg}} - T_{\text{ambient}})}{R_{\text{annulus,o}} + R_{\text{wall}} + R_{\text{ins}} + \left(\frac{R_{\text{nat.conv}} R_{\text{radiation}}}{R_{\text{nat.conv}} + R_{\text{radiation}}} \right)} \\ \dot{Q}_{\text{loss,test}} &= \frac{(20.38 - 24.72)^\circ\text{C}}{(0.01497) + (0.01536) + (50.12) + \left(\frac{(14.51)(4.105)}{14.51 + 4.105} \right)} \text{K W}^{-1} = -0.08314 \text{ W} \end{aligned} \quad (4.15)$$

For this example, the coolant temperature is lower than the ambient temperature, and heat is transferred from the surroundings to the coolant. This heat gain only occurs at the lowest saturation temperature ($T_{\text{sat}} = 30^\circ\text{C}$.) A summary of the relevant heat losses in the test loop is displayed in Table 4.4.

For this representative data point, the coolant lines in the primary, secondary and post-condenser are maintained at temperatures lower than the ambient temperature, which results in heat gains.

Table 4.4: Summary of Heat Losses

	Surface Area (m ²)	Radiation Loss $\dot{Q}_{\text{loss, radiation}}$ (W)	Nat. Conv. Loss $\dot{Q}_{\text{loss, nat. conv.}}$ (W)	Total Heat Loss $\dot{Q}_{\text{loss, total}}$ (W)	Heat Duty (W)
Pre-Condenser	0.144	0.27	0.08	0.35	492
Pre-Condenser to Test Section	0.287	0.76	0.25	1.0	
Test Section	0.048	-0.06	-0.02	-0.08	160.5
Test Section to Post-Condenser	0.287	0.59	0.18	0.76	
Post Condenser	0.065	-0.52	-0.23	-0.75	683
Primary Loop	1.086	-2.09	-0.69	-2.79	
Secondary Heat Exchanger	0.054	-0.27	-0.10	-0.37	185.8

4.1.4 Test Section Heat Duty

The test section heat duty is evaluated using the thermal amplification technique with energy balances on the secondary heat exchanger, heat losses in the secondary heat exchanger, test section, and primary loop, and heat additions from the primary loop pump.

$$\dot{Q}_{\text{test}} = \dot{Q}_{\text{sec}} + \dot{Q}_{\text{loss, ambient}} - \dot{Q}_{\text{pump}} \quad (4.16)$$

The primary cooling loop pump heat addition can be significant, and accurate determination of this heat input is required to obtain low uncertainties. A detailed analysis of pump heat addition was conducted in previous work using the test facility by Andresen (2007) and a conservative 50% uncertainty is applied to the predicted value. The methodology and detailed calculations are presented in Appendix C. The pump heat

addition in this example is $\dot{Q}_{\text{pump}} = 22 \pm 11 \text{ W}$. The secondary fluid heat transfer rate is determined by an energy balance using the measured flow rate, and inlet and outlet temperatures. The inlet and outlet temperatures are used to calculate the respective enthalpies for analysis.

$$\dot{Q}_{\text{sec}} = \dot{m}_{\text{w, sec}} (i_{\text{w, sec, out}} - i_{\text{w, sec, in}}) \quad (4.17)$$

$$\dot{Q}_{\text{sec}} = (0.003915 \text{ kg s}^{-1})(78.19 - 30.74) \text{ kJ kg}^{-1} = 185.8 \pm 5.87 \text{ W}$$

It is important to maintain large temperature differences between the heat exchanger inlet and outlet to ensure low uncertainties in secondary heat exchanger heat duties. In this example, $\Delta T_{\text{sec}} = 11.32^\circ\text{C}$, and the temperature difference throughout all experiments conducted in this study was always greater than 10°C . The utility of the thermal amplification technique can be seen in this case by noting that the corresponding temperature difference in the primary loop is only $\Delta T_{\text{prim}} = 0.19^\circ\text{C}$.

The heat losses from the test section, primary loop, and secondary heat exchanger are summed to determine the total heat loss contributions to the test section heat duty. A summary of the heat losses and gains is presented in Table 4.4.

$$\dot{Q}_{\text{loss, ambient}} = \dot{Q}_{\text{loss, test}} + \dot{Q}_{\text{loss, primary}} + \dot{Q}_{\text{loss, sec}} \quad (4.18)$$

$$\dot{Q}_{\text{loss, ambient}} = -0.083 - 2.785 - 0.370 = -3.24 \pm 1.62 \text{ W}$$

In this case, the coolant lines are all at a lower temperature than the ambient temperature, resulting in a heat addition. A conservative 50% uncertainty is applied to the predicted heat gain. The test section heat duty is calculated using Equation 4.16.

$$\dot{Q}_{\text{test}} = 185.8 - 3.2 - 22 \text{ W} = 160.5 \pm 12.6 \text{ W}$$

The largest contribution to uncertainty in measured test section heat duty is the uncertainty in predicted pump heat addition (11 W.) At higher saturation temperatures, the heat loss components increase and the pump heat additions decrease, because the

primary loop velocity required to maintain high resistance ratios is lower, in turn due to the refrigerant heat transfer coefficient being lower with increasing p_r , but it is still the dominant uncertainty.

4.1.5 Refrigerant Heat Transfer Coefficient

To determine the refrigerant heat transfer coefficient, the overall heat transfer conductance, UA , is needed. The overall heat transfer conductance is calculated from the test section heat duty, and the log-mean temperature difference (LMTD) in the test section.

$$\dot{Q}_{\text{test}} = (UA)(\text{LMTD}) \quad (4.19)$$

The test section heat duty is calculated using Equation 4.16, while the LMTD is calculated as follows using measured inlet and outlet temperatures and pressures. The LMTD between the condensing refrigerant and the primary cooling loop is calculated by:

$$\text{LMTD} = \frac{(T_{r, \text{test, in}} - T_{w, \text{test, out}}) - (T_{r, \text{test, out}} - T_{w, \text{test, in}})}{\ln \left[\frac{(T_{r, \text{test, in}} - T_{w, \text{test, out}})}{(T_{r, \text{test, out}} - T_{w, \text{test, in}})} \right]} \quad (4.20)$$

$$\text{LMTD} = \frac{(31.5 - 20.4) - (30.8 - 20.2)}{\ln \left[\frac{(31.5 - 20.4)}{(30.8 - 20.2)} \right]} = 10.87 \pm 0.18 \text{ K}$$

The coolant inlet and outlet temperatures are measured by thermocouples, while the saturation temperatures of the refrigerant are based on measured inlet and outlet pressures. This approach results in a lower predicted uncertainty on saturation temperatures. The measured temperatures are then used as a redundant measurement to ensure accuracy. A summary of measured saturation temperatures is presented in Table 4.5. The difference between the temperatures obtained at the inlet and outlet using these two different methods is an indication of the thermocouple accuracy and also the achievement of steady, desired operating conditions. For this representative case,

Table 4.5: Comparison of Thermocouple and Pressure-Based Temperature Measurements

	Measured $T(^{\circ}\text{C})$	Pressure (kPa)	Enthalpy (kJ kg^{-1})	Saturation $T(^{\circ}\text{C})$	Temperature Difference ($^{\circ}\text{C}$)
Test Section Inlet	31.49 ± 0.25	1471 ± 2.6	370 ± 6	31.55 ± 0.06	0.06
Test Section Outlet	30.89 ± 0.25	1449 ± 2.6	345 ± 5	30.85 ± 0.06	0.04

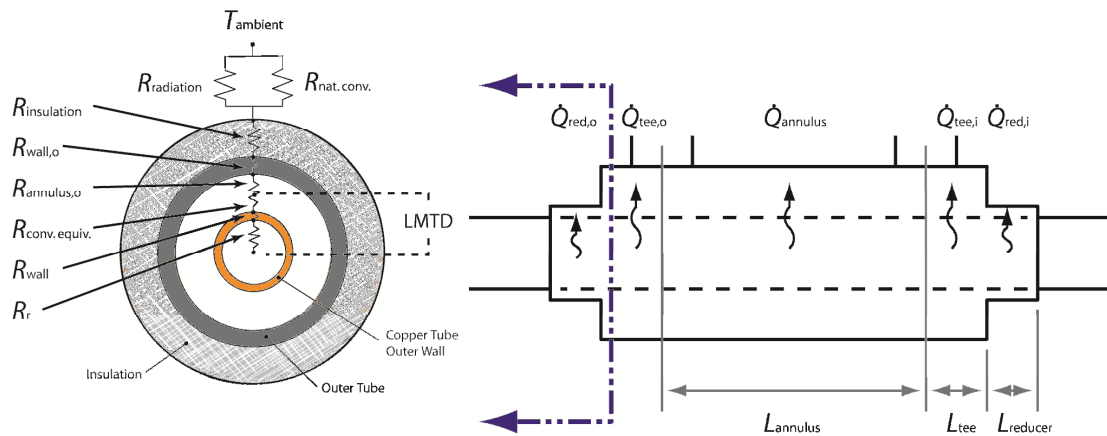


Figure 4.2: Schematic of Test Section Thermal Resistance Network

agreement between the two methods is very good, well within measurement uncertainties.

The overall heat transfer conductance for this example is calculated using Equation 4.19.

$$160.5 \text{ W} = (UA)(10.87 \text{ K}), \quad UA = 14.8 \pm 1.2 \text{ W K}^{-1}$$

The overall heat transfer conductance is based on the thermal resistance from the condensing refrigerant to the test section coolant. A schematic of the different thermal resistances in the test section is shown in Figure 4.2. A major portion of the heat is removed from the refrigerant in the test section annulus between the inlet and outlet ports. A small portion of the heat is removed from the test section in the tee and reducer sections at the inlet and outlet, which allow for the mating of the annulus and refrigerant

tube. An equivalent convective resistance is used to account for the heat removed from these different regions. The thermal resistance network is calculated as follows:

$$UA = \frac{1}{R_r + R_{wall} + R_{conv. equiv.}} \quad (4.21)$$

The conductive resistance in the copper tube is calculated as follows:

$$R_{wall} = \frac{\ln(D_{test,o}/D_{test,i})}{2\pi k_{test} (L_{annulus} + 2(L_{reducer} + L_{tee}))} \quad (4.22)$$

$$R_{wall} = \frac{\ln(6.35 \text{ m}/3.048 \text{ m})}{2\pi(398.3 \text{ W m}^{-1}\text{K}^{-1})(0.1524 \text{ m} + 2(0.02286 \text{ m} + 0.01321 \text{ m}))} = 1.306 \times 10^{-2} \text{ K W}^{-1}$$

The convective resistance of the primary coolant is calculated using a parallel resistance network to the water side, comprised of the main forced convective region between the ports and the relatively stagnant regions of fluid in the inlet and outlet regions.

$$R_{conv. equiv.}^{-1} = R_{annulus,i}^{-1} + 2(R_{tee}^{-1} + R_{reducer}^{-1}) \quad (4.23)$$

The forced convective thermal resistance in the annulus is:

$$R_{annulus,i} = \frac{1}{h_{annulus} \pi D_{test,o} L_{annulus}} \quad (4.24)$$

$$R_{annulus,i} = \frac{1}{(13677 \text{ W m}^{-2}\text{K}^{-1}) \pi (6.35 \text{ mm})(152.4 \text{ mm})} = 0.024 \text{ K W}^{-1}$$

The heat transfer coefficient in the annulus is calculated using Equation 4.14 presented above. The resulting thermal resistance in the annulus region is $R_{annulus,i} = 2.4 \times 10^{-2} \text{ K W}^{-1}$. The thermal resistances in the tee and reducer regions are calculated using an effective thermal conductivity for the relatively stagnant fluid (Incorpera and DeWitt, 1996). The thermal resistance in the tee and reducer are calculated in a similar manner and only the tee resistance is shown here for demonstration purposes. The detailed calculations are presented in Appendix B.1. The thermal resistance is:

$$R_{\text{tee}} = \frac{\ln(D_{\text{tee}}/D_{\text{test, o}})}{2\pi k_{\text{eff}} L_{\text{tee}}} \quad (4.25)$$

The effective conductivity, k_{eff} , is a function of the modified Rayleigh number, Ra^* , Prandtl number, Pr, and the respective tube diameters. The modified Rayleigh number is calculated as follows:

$$Ra_{\text{tee}}^* = \frac{[\ln(D_{\text{tee}}/D_{\text{test, o}})]^4}{(D_{\text{test, o}}^{-3/5} + D_{\text{tee}}^{-3/5})^5} \cdot \frac{g\beta_w(T_{\text{wall, o}} - T_{\text{w, test, avg}})}{v_w \alpha_w} \quad (4.26)$$

$$Ra_{\text{tee}}^* = \frac{[\ln(10.41/6.35)]^4}{((10.41)^{-3/5} + (6.35)^{-3/5})^5} \cdot \frac{(9.81 \text{ m s}^{-2})(2.1 \times 10^{-4} \text{ K}^{-1})(24.1 - 20.3 \text{ K})}{(9.96 \times 10^{-7} \text{ m}^2 \text{ s}^{-1})(1.435 \times 10^{-7} \text{ m}^2 \text{ s}^{-1})} = 52$$

If the modified Rayleigh number is less than 100, the effective thermal conductivity is the same as the conductivity of the fluid. If the modified Rayleigh number is greater than 100, the effective thermal conductivity is calculated using Equation 4.27.

$$\frac{k_{\text{eff}}}{k_{\text{water}}} = 0.386 \left(\frac{\text{Pr}}{0.861 + \text{Pr}} \right)^{1/4} (Ra^*)^{1/4} \quad (4.27)$$

Because the modified Rayleigh number is less than 100 in this case, the effective thermal conductivity is approximated by the thermal conductivity of water, $k_{\text{eff}} = k_{\text{water}} = 0.599 \text{ W m}^{-1} \text{ K}^{-1}$. The thermal resistance in the tee is calculated using Equation 4.25.

$$R_{\text{tee}} = \frac{\ln(10.41/6.35)}{2\pi(0.599 \text{ W m}^{-1} \text{ K}^{-1})(13.21 \text{ mm})} = 9.94 \text{ K W}^{-1}$$

The thermal resistance of the reducer is obtained using the same methodology (Equations 4.25-27), but by replacing the tee dimensions with reducer dimensions. The resulting thermal resistance in the reducer for this representative case is $R_{\text{reducer}} = 4.372 \text{ K W}^{-1}$. The equivalent convective resistance is then determined using Equation 4.23.

$$R_{\text{conv, equiv.}} = \left[(2.4 \times 10^{-2} \text{ K W}^{-1})^{-1} + 2 \left((9.9)^{-1} + (4.4)^{-1} \text{ W K}^{-1} \right) \right]^{-1} = 2.37 \times 10^{-2} \text{ K W}^{-1}$$

The resistance in the annulus is an order of magnitude smaller than that in the reducer and tee, and therefore, a major portion of the heat is transferred in the annulus. In this example the calculated heat transfer through each segment is $\dot{Q}_{\text{reducer}} = 1.74 \text{ W}$, $\dot{Q}_{\text{tee}} = 0.76 \text{ W}$, and $\dot{Q}_{\text{annulus}} = 158.1 \text{ W}$. Despite the ends being insignificant in terms of overall heat transfer, their effects are included here so that the heat transfer area is properly accounted for. With the other resistances now available, the thermal resistance in the condensing refrigerant is obtained from Equation 4.21.

$$14.77 \text{ W K}^{-1} = \frac{1}{R_r + 1.31 \times 10^{-3} \text{ K W}^{-1} + 2.37 \times 10^{-2} \text{ K W}^{-1}}$$

$$R_r = 4.27 \times 10^{-2} \text{ K W}^{-1}$$

The resistance of the condensing refrigerant is used to obtain the refrigerant heat transfer coefficient.

$$R_r = \frac{1}{h_r \pi D_{\text{test, i}} (L_{\text{annulus}} + 2(L_{\text{reducer}} + L_{\text{tee}}))} \quad (4.28)$$

$$4.273 \times 10^{-2} = \frac{1}{h_r \pi (3.048 \text{ mm}) (152.4 + 2(22.9 + 13.2) \text{ mm})}$$

$$h_r = 10884 \pm 2027 \text{ W m}^{-2} \text{K}^{-1}$$

The uncertainty in this measured heat transfer coefficient for this representative case is 18.6%. The resistance ratio for this data point is obtained by comparing the thermal resistance on the refrigerant side to the thermal resistance of the tube wall and annulus.

$$R_{\text{ratio}} = \frac{R_r}{R_{\text{wall}} + R_{\text{conv. equiv.}}} \quad (4.29)$$

The resistance ratio for this example is $R_{\text{ratio}} = 1.711$. High resistance ratios ensure high accuracies in measured heat transfer coefficients. In the present study, the resistance ratios for data taken on the large diameter tube facility ranged from 1.7 to 8.1.

4.1.6 Test Section Pressure Drop

The measured pressure drop, $\Delta P_{\text{measured}}$, is the summation of several pressure loss components, including the frictional pressure drop, ΔP_f , the deceleration (due to condensation) pressure drop, $\Delta P_{\text{deceleration}}$, and the contraction and expansion pressure drops at the inlet and outlet respectively, $\Delta P_{\text{contraction}}$ and $\Delta P_{\text{expansion}}$.

$$\Delta P_{\text{measured}} = \Delta P_f - |\Delta P_{\text{deceleration}}| + \Delta P_{\text{contraction}} - \Delta P_{\text{expansion}} \quad (4.30)$$

Contraction pressure drops were calculated based on the approach suggested by Hewitt *et al.* (1994) where the pressure drop due to contraction is a result of the reducing area as well as frictional losses.

$$\Delta P_{\text{contraction}} = \frac{G^2}{2\rho_1} \left(\underbrace{1 - A_{\text{ratio}}^2}_{\text{Kinetic Energy Change}} + \underbrace{\left(\frac{1}{C_C} - 1 \right)^2}_{\text{Frictional Pressure Loss}} \right) \psi_H \quad (4.31)$$

The ratio of the test section cross-sectional area to the corresponding area of the refrigerant tubing is given by:

$$A_{\text{ratio}} = \frac{A_{\text{test}}}{A_r} \quad (4.32)$$

There are two sequential contractions at the inlet that lead to the total contraction pressure drop as shown in Figure 3.7. They are due to the reduction in flow area from the tee fitting to the refrigerant tubing, and the refrigerant tubing to the test section. The ratios for the respective cross-sectional area changes are calculated using Equation 4.32, as follows.

$$A_{\text{ratio},1} = \frac{A_{\text{contraction}}}{A_{\text{tee}}} = \left(\frac{D_{\text{contraction}}}{D_{\text{tee}}} \right)^2 = 0.6834$$

$$A_{\text{ratio},2} = \frac{A_{\text{test}}}{A_{\text{contraction}}} = \left(\frac{D_{\text{test},i}}{D_{\text{contraction}}} \right)^2 = 0.444$$

The coefficient of contraction term is given by Chisholm (1983):

$$C_c = \frac{1}{0.639[1-(A_{\text{ratio}})]^{1/2} + 1} \quad (4.33)$$

$$\psi_H = 1 + \left(\frac{\rho_{l, \text{test, in}}}{\rho_{v, \text{test, in}}} - 1 \right) x_{r, \text{test, in}} \quad (4.34)$$

The homogeneous flow multiplier is used based on the recommendation of Hewitt *et al.* (1994). For this case, the homogeneous flow multiplier is $\psi_H = 12.18$ at a test section inlet quality $x_{r, \text{test, in}} = 0.9456$. Because it is only a function of phase densities and local quality, the multiplier is the same for both contractions. The coefficient of contraction is different for each component and is calculated using Equation 4.33 as follows:

$$C_{c,1} = \frac{1}{0.639[1-(0.6834)]^{1/2} + 1} = 0.6774$$

$$C_{c,2} = \frac{1}{0.639[1-(0.444)]^{1/2} + 1} = 0.6928$$

The contraction pressure drop for each area reduction is calculated using Equation 4.31. The mass flux in the equation is determined by the mass flow rate in the smaller cross-sectional area of the contraction.

$$\Delta P_{\text{contraction,1}} = \frac{(G \cdot A_{\text{ratio,2}})^2}{2\rho_{l,\text{in}}} \left(1 - A_{\text{ratio,1}}^2 + \left(\frac{1}{C_{c,1}} - 1 \right)^2 \right) \psi_H$$

$$\Delta P_{\text{contraction,1}} = \frac{(803 \cdot 0.444 \text{ kg m}^{-2} \text{ s}^{-1})^2}{2(1014 \text{ kg m}^{-3})} \left(1 - 0.68 + \left(\frac{1}{0.68} - 1 \right)^2 \right) 12.2 = 0.715 \text{ kPa}$$

$$\Delta P_{\text{contraction,2}} = \frac{G^2}{2\rho_{l,\text{in}}} \left(1 - A_{\text{ratio,2}}^2 + \left(\frac{1}{C_{c,2}} - 1 \right)^2 \right) \psi_H$$

$$\Delta P_{\text{contraction,2}} = \frac{(803 \text{ kg m}^{-2} \text{ s}^{-1})^2}{2(1014 \text{ kg m}^{-3})} \left(1 - 0.44 + \left(\frac{1}{0.69} - 1 \right)^2 \right) 12.2 = 4.02 \text{ kPa}$$

The total contraction pressure drop for this representative data point is the sum of the two components and is $\Delta P_{\text{contraction}} = 4.731$ kPa. The total contraction pressure drop is 78% kinetic energy change ($\Delta P_{\text{contraction, kinetic-energy}} = 3.696$ kPa) and 22% frictional losses ($\Delta P_{\text{contraction, friction}} = 3.696$ kPa.) The expansion pressure drop is computed using the following equation suggested by Hewitt *et al.* (1994) is:

$$\Delta P_{\text{expansion}} = \frac{G^2}{2\rho_1} \left(\underbrace{(1 - A_{\text{ratio}}^2)}_{\text{Kinetic Energy Change}} - \underbrace{(1 - A_{\text{ratio}})^2}_{\text{Frictional Loss}} \right) \psi_S = \frac{G^2 A_{\text{ratio}} (1 - A_{\text{ratio}}) \psi_S}{\rho_1} \quad (4.35)$$

Two sequential expansion pressure drop terms are included to account for the test section connections at the outlet as shown in Figure 3.7. The contributions of the two expansions are similar to those presented above for contraction pressure losses. The sum of the two components is presented here, and the contributions of each expansion are detailed in Appendix B.1. The ratio of areas is the same as that presented above, and the separated flow multiplier is given by:

$$\psi_S = 1 + \left(\frac{\rho_{1, \text{test, out}}}{\rho_{v, \text{test, out}}} - 1 \right) \left[B x_{r, \text{test, out}} (1 - x_{r, \text{test, out}}) + x_{r, \text{test, out}}^2 \right] \quad (4.36)$$

The coefficient value given by Chisholm (1983) is $B = 0.25$. As the coefficient approaches unity, the separated flow multiplier reduces to the homogeneous multiplier.

For the representative case under consideration here, $x_{r, \text{test, out}} = 0.7586$, $\psi_S = 8.506$, and the resulting combined expansion drop is:

$$\begin{aligned} \Delta P_{\text{expansion}} &= \Delta P_{\text{expansion, kinetic-energy}} - \Delta P_{\text{expansion, friction}} \\ &= (2.575 - 0.964) \text{ kPa} = 1.61 \text{ kPa} \end{aligned}$$

The component of pressure drop associated with decreasing velocities from condensation is represented in the deceleration pressure drop derived from an axial momentum balance as found in Carey (1992):

$$|\Delta P_{deceleration}| = \left| G^2 \left[\frac{x^2}{\rho_{v, out} \alpha} + \frac{(1-x)^2}{\rho_{l, out} (1-\alpha)} \right]_{\substack{\alpha=\alpha_{r, test, out} \\ x=x_{r, test, out}}} - G^2 \left[\frac{x^2}{\rho_{v, in} \alpha} + \frac{(1-x)^2}{\rho_{l, in} (1-\alpha)} \right]_{\substack{\alpha=\alpha_{r, test, in} \\ x=x_{r, test, in}}} \right| \quad (4.37)$$

The void fraction, α , is a function of the refrigerant quality and refrigerant properties. The void fraction is calculated using the following correlation developed by Baroczy (1965).

$$\alpha = \left[1 + \left(\frac{1-x}{x} \right)^{0.74} \left(\frac{\rho_v}{\rho_l} \right)^{0.65} \left(\frac{\mu_l}{\mu_v} \right)^{0.13} \right]^{-1} \quad (4.38)$$

The calculated void fractions for the representative data point are $\alpha_{in} = 0.9708$ and $\alpha_{out} = 0.9046$, respectively, which results in a deceleration pressure rise of 1921 Pa. The frictional pressure drop is now obtained using Equation 4.30:

$$15.658 \text{ kPa} = \Delta P_f - 1921 \text{ kPa} + 4.731 \text{ kPa} - 1.61 \text{ kPa}$$

$$\Delta P_f = 14.46 \text{ kPa}$$

With a test section length of $L_{test} = 0.4572 \text{ m}$, the resulting pressure gradient is $\nabla P_f = 31.62 \text{ kPa m}^{-1}$. The ratio of the deceleration pressure drop to the measured pressure drop is 12%. The contraction, expansion and frictional pressure drops are 30%, 10% and 92% of the measured pressure drop, respectively.

4.2 Small Diameter Tube Condensation Analysis

Due to the much smaller mass flow rates and condensation heat duties in the smaller diameter tubes in this study, and the large thermal mass of the larger test facility, a

second, much smaller test facility was used for small tube ($D < 2$ mm) experiments. The primary difference between the large tube diameter facility and the small tube diameter facility is in the pre- and post-conditioning of the refrigerant upstream and downstream of the test section. The analysis of data from this test facility is presented here.

4.2.1 Test Section Quality

A summary of measured values for a representative data point is presented in Tables 4.6 and 4.7. Refrigerant is sub-cooled in the condenser and pumped to the pre-heater. The enthalpy of the refrigerant here is calculated using temperature and pressure measurements at the pre-heater inlet.

$$i_{r,\text{pre-heat,in}} = f(T_{r,\text{pre-heat,in}}, P_{r,\text{pre-heat,in}}) \quad (4.39)$$

$$i_{r,\text{pre-heat,in}} = f(23.8^\circ\text{C}, 1810 \text{ kPa}) = 232.7 \pm 0.38 \text{ kJ kg}^{-1}$$

Large temperature differences between the pre-heater inlet temperature and the saturation temperature at the inlet pressure were maintained to ensure that the fluid was completely sub-cooled. Similarly, a large temperature difference at the outlet of the post-heater compared to the saturation temperature at the measured pressure was maintained to ensure that the refrigerant is completely super-heated. A summary of these measurements and their comparison with saturation temperatures is displayed in Table 4.8.

The refrigerant exits the pre-heater as a two-phase fluid, and temperature and pressure

Table 4.6: Refrigerant Temperatures and Pressures

	Temperature ($^\circ\text{C}$)		Pressure (kPa)	
Pre-Heater Inlet	$T_{r,\text{pre-heat,in}}$	23.8 ± 0.25	$P_{r,\text{pre-heat,in}}$	1810 ± 5.2
Test Section Inlet	$T_{r,\text{test,in}}$	39.6 ± 0.25	$P_{r,\text{test,in}}$	1810 ± 5.2
Test Section Outlet	$T_{r,\text{test,out}}$	39.5 ± 0.25	$P_{r,\text{test,out}}$	1780 ± 5.2
Post-Heater Outlet	$T_{r,\text{post-heat,out}}$	51.0 ± 0.25	$P_{r,\text{post-heat,out}}$	1778 ± 5.2

Table 4.7: Pre- and Post-Heater Inputs

	Heater Input (W)	
Pre-Heater	$\dot{Q}_{\text{pre-heat}}$	147.4 ± 0.29
Post-Heater	$\dot{Q}_{\text{post-heat}}$	73.7 ± 0.15

Table 4.8: Heater and Saturation Temperature Comparison

	Measured Temperature (°C)	Saturation Temperature (°C)	Temperature Difference (°C)
Pre-Heater Inlet	23.8 ± 0.25	39.85 ± 0.09	16.05
Post-Heater Outlet	51.0 ± 0.25	39.84 ± 0.09	11.16

measurements are made upon entering the test section. The test section inlet state is calculated from an energy balance across the pre-heater.

$$\begin{aligned} \dot{Q}_{\text{pre-heater}} &= \dot{m}_r (i_{r, \text{test, in}} - i_{r, \text{pre-heat, in}}) + \dot{Q}_{\text{loss, pre-heater}} \quad (4.40) \\ \dot{Q}_{\text{pre-heater}} &= (1.125 \times 10^{-3} \text{ kg s}^{-1}) (i_{r, \text{test, in}} - 232.7 \text{ kJ kg}^{-1}) + 0.524 \text{ W} \\ i_{r, \text{test, in}} &= 363.4 \pm 0.46 \text{ kJ kg}^{-1} \end{aligned}$$

The heat loss in the pre-heater assembly was calculated using the approach outlined in Equations 4.6 to 4.12 and is detailed in Appendix B.2. The quality at the test section inlet is deduced using the pressure measurement and refrigerant enthalpy.

$$\begin{aligned} x_{r, \text{test, in}} &= f(P_{r, \text{test, in}}, i_{r, \text{test, in}}) \quad (4.41) \\ x_{r, \text{test, in}} &= f(1810 \text{ kPa}, 363.4 \text{ kJ kg}^{-1}) = 0.872 \pm 0.0038 \end{aligned}$$

A similar method is used to obtain the test section outlet quality. For this representative data point, the outlet quality is $x_{r, \text{test, out}} = 0.592 \pm 0.006$. The average quality for this representative data point is $x_{r, \text{test, avg}} = 0.7328 \pm 0.0025$.

4.2.2 Heat Losses To Environment

The small tube test facility is covered in insulation ($k_{\text{ins}} = 0.043 \text{ W m}^{-1} \text{ K}^{-1}$) to minimize ambient heat losses. Due to the much lower flow rates and heat duties, losses to the environment constitute a more significant portion of the measured heat duties throughout

the system. Heat loss calculations for this facility are very similar to those for the large tube diameter test facility (Equations 4.6 to 4.15.) A summary of heat losses for the representative data point for the small tube diameter facility is presented in Table 4.9. The detailed calculations are presented in Appendix B.2.

Table 4.9: Summary of Heat Losses

	Surface Area ($\times 10^3 \text{ m}^2$)	Radiation Loss $\dot{Q}_{\text{loss, radiation}}$ (W)	Nat. Conv. Loss $\dot{Q}_{\text{loss, nat. conv.}}$ (W)	Total Heat Loss $\dot{Q}_{\text{loss, total}}$ (W)	Heat Duty (W)
Pre-Heater	3.03	0.14	0.11	0.26	147.4
Pre-Heater to Test Section	0.7964	0.15	0.12	0.27	X
Test Section Annulus	2.08	0.12	0.09	0.21	38.15
Test Section Non-annulus	0.485	0.11	0.08	0.18	
Test Section to Post-Heater	0.7964	0.15	0.12	0.27	X
Post-Heater	3.03	0.35	0.33	0.68	73.7

4.2.3 Test Section Heat Duty

The test section heat duty in the small diameter tube test facility is obtained based on the conditions at the inlet to the pre-heater, at the outlet to the post-heater and energy balances across the refrigerant loop. The condensation heat duty is calculated as follows:

$$\dot{Q}_{\text{test}} = \dot{m}_r (i_{r, \text{post-heat, out}} - i_{r, \text{pre-heat, in}}) - \dot{Q}_{\text{pre-heater}} - \dot{Q}_{\text{post-heater}} + \dot{Q}_{\text{loss}} \quad (4.42)$$

$$\dot{Q}_{\text{test}} = (1.125 \times 10^{-3} \text{ kg s}^{-1}) (363.4 - 329.4 \text{ kJ kg}^{-1}) - 147.4 \text{ W} - 73.7 \text{ W} + 1.88 \text{ W}$$

$$\dot{Q}_{\text{test}} = 38.15 \pm 1.4 \text{ W}$$

The largest contribution to the uncertainty in heat duty is the heat losses to the ambient (0.94 W.) As saturation temperature increases, this component becomes more significant.

4.2.4 Test Section Refrigerant Heat Transfer Coefficient and Pressure Drop

The refrigerant heat transfer coefficient in the small diameter tube test facility was calculated in the same manner as for the large tube facility (Equations 4.19 to 4.28). Detailed calculations are presented in Appendix B.2. For this representative data point, $LMTD = 7.15 \text{ K}$, $UA = 5.34 \text{ W K}^{-1}$, and $R_r = 0.1558 \text{ K W}^{-1}$, which results in a measured heat transfer coefficient of $h_r = 6194 \pm 568.9 \text{ W m}^{-2} \text{ K}^{-1}$ (9.2%.) The resistance ratio for this example was $R_{ratio} = 6.328$. In the present study, the resistance ratios for data taken on the small diameter tube facility ranged from 3.0 to 16.7.

The test section pressure drop in the small diameter tube facility was also calculated using the methodology presented in Equations 4.30 to 4.38 for the large diameter tube facility. The detailed calculations are presented in Appendix B.2. The measured pressure drop in this example was $\Delta P_{measured} = 29.5 \text{ kPa}$. The expansion, contraction, deceleration and frictional components were $\Delta P_{expansion} = 0.711 \text{ kPa}$ (2.4%), $\Delta P_{contraction} = 3.54 \text{ kPa}$ (12%), $\Delta P_{deceleration} = 1.11 \text{ kPa}$ (4%), and $\Delta P_f = 27.75 \text{ kPa}$ (94%). The frictional pressure gradient for this example is $\nabla P_f = 91.04 \text{ kPa m}^{-1}$.

CHAPTER 5: IMAGE ANALYSIS

The methodology for obtaining quantitative information from high speed video images of the two-phase flows taken in this study is detailed in this chapter.

5.1 Image Processing

Previous investigations by Coleman and Garimella (2003) used flow visualization to classify flow regimes and transitions for condensing R134a. While it was possible to obtain qualitative information from the videos, a mathematical image analysis tool is necessary to derive quantitative parameters from such video frames. In the present study, images of the longitudinal section of the tube defined in Figure 5.1 are taken. To obtain three-dimensional information from the two-dimensional images obtained in the video recordings, several geometric assumptions must be made. A second image perpendicular to the longitudinal section (i.e., the overhead section) was also taken in the experiments for representative cases to validate these assumptions.

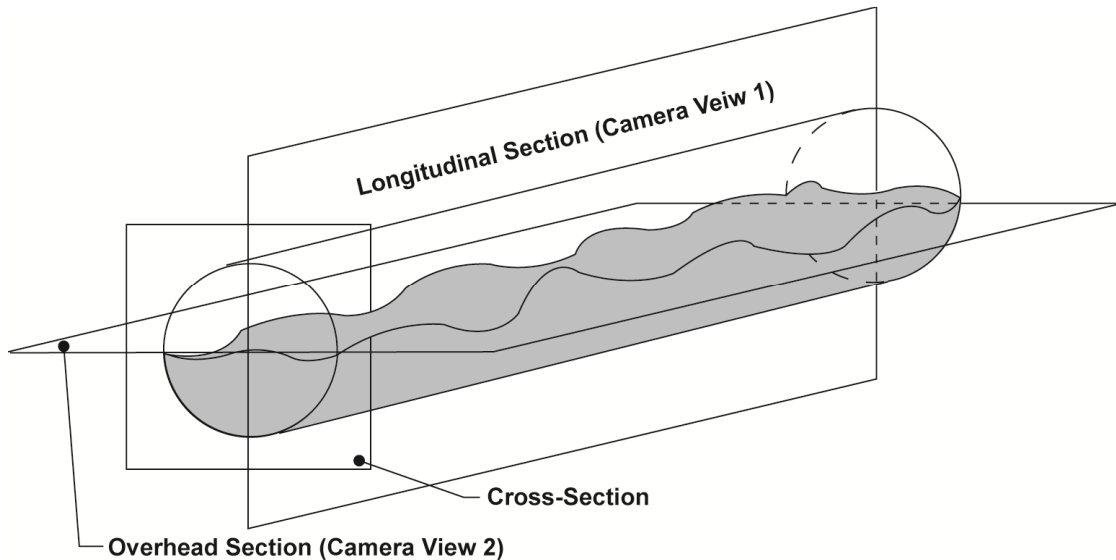


Figure 5.1: Observed Planes: Longitudinal, Overhead, and Cross-Section

An image analysis tool was developed using edge-detection capabilities available in the MATLAB (The MathWorks Inc., 2004c) platform. The tool was originally developed for analyzing falling films and droplets flowing around tube banks. In the present study, this

original tool was modified to quantify vapor slug parameters and void fractions. A detailed description of the development of this image-analysis tool is provided in Killion and Garimella (2004). The basic operation of this image analysis tool, and the main modifications made for the present study are described here.

The image analysis program uses a graphical user interface (GUI) as its input platform. A schematic of the GUI is shown in Figure 5.2. This allows for the video recordings to be uploaded and analyzed in a frame-by-frame manner. Initially, the user defines a region of interest (ROI) by clicking each frame near the vapor-liquid interface. The program automatically detects the edge of the vapor-liquid interface within the ROI, sets points along the path of the detected edges, and fits a smoothing spline through these points. The program uses the Canny edge-detection algorithm from the MATLAB Image Processing Toolbox (The MathWorks Inc., 2004a) combined with the cubic smoothing spline function SPAPS from the MATLAB Spline Toolbox (The MathWorks Inc., 2004b). This process is illustrated in Figure 5.3(a-c). Figure 5.3(a) displays the points detected (blue circles) at the vapor liquid interface. Figure 5.3(b) shows the spline (light blue line) and the ROI (un-shaded area) for the example frame. A schematic of the process is shown in Figure 5.3(c).

The Canny edge-detection algorithm (The MathWorks Inc., 2004a) is a multi-step procedure. First, noise and undesirable textures are removed by a Gaussian smoothing filter. Next, the regions with high first spatial derivatives are highlighted using the gradient-based Sobel operator. Upper and lower threshold values are initially set by the user and any value larger than the upper threshold is considered as an edge pixel. The neighboring pixels are then examined to definitively establish the edge: if the gradient is larger than the lower threshold, it confirms the existence of an edge. All edge pixels are

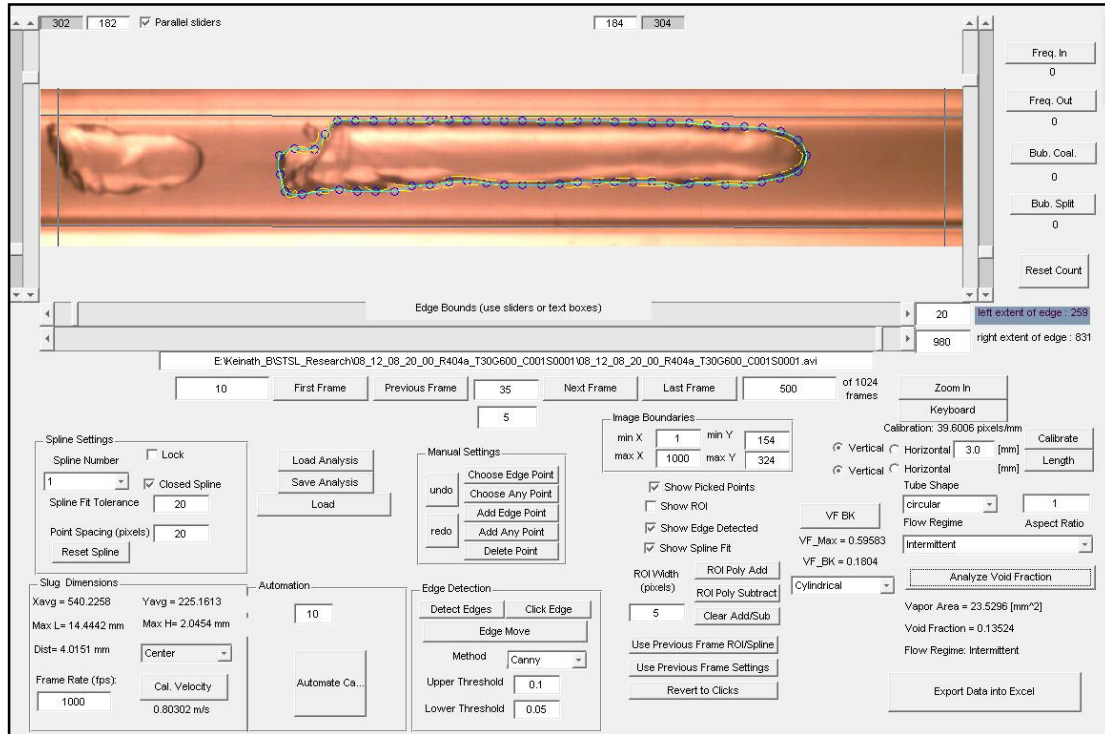


Figure 5.2 Geometric Graphic User Interface for Video Frame Analysis

connected following completion. The Canny edge-detection algorithm was used because of its flexibility in adjusting to different lighting conditions. If necessary, it is possible for the user to manually input edge points based on visual interpretation, but this was rarely necessary for the present study.

The vapor-liquid interface is approximated by a spline, which is a smooth piecewise polynomial function using a set of control points and a non-decreasing knot sequence. The control points are established using a multi-step edge-detection procedure. The user must first set the point spacing value. After applying the aforementioned Canny detection algorithm, the edge points along the interface are automatically selected with a distance between each edge point specified by the point spacing value. The user has the ability to decrease the point spacing value to allow for tracking of intricate shapes. The vertices of the spline's control polygon are the control points, which are then fit by a cubic smoothing spline using the MATLAB (The MathWorks Inc., 2004b) built-in spline

function SPAPS. This function creates the smoothest spline that exists within the user specified tolerance of the control points, which is appropriate given the discrete nature of the location of the edge points.

5.2 Analysis and Interpretation of Processed Images

The methods for measuring void fraction, vapor bubble parameters, and their associated uncertainties from the data are described here. In addition, sample calculations for a representative data point are presented.

5.2.1 Identification of Flow Characteristics

The vapor slug parameters and void fraction are calculated based on the spline fit to the vapor-liquid interface described above and the boundaries of the tube, which are user inputs. The schematic of a frame is shown in Figure 5.3(c), with the pixel coordinate system origin in the upper left corner. This coordinate system is used to define the outline of the tube diameter, D , using the upper and lower lines, and also the tube length, L_{tube} , using the left and right boundary lines. The boundary lines are fully adjustable and are set by the user. The number of pixels per millimeter, x_{cal} , is calibrated to the known tube diameter. This user input procedure is carried out only in the first frame and then used throughout the analysis. For a tube diameter of $D = 3.00$ mm, the length of the tube captured in the image was generally $L_{\text{tube}} = 22$ mm, and a calibration value of $x_{\text{cal}} = 45$ pixels/mm was used. Representative calibration values for each tube diameter are shown in Table 5.1.

Table 5.1: Representative Image Analysis Calibration Values

Diameter (mm)	x_{cal} (pixels/mm)
3.00	45
1.00	125
0.508	220

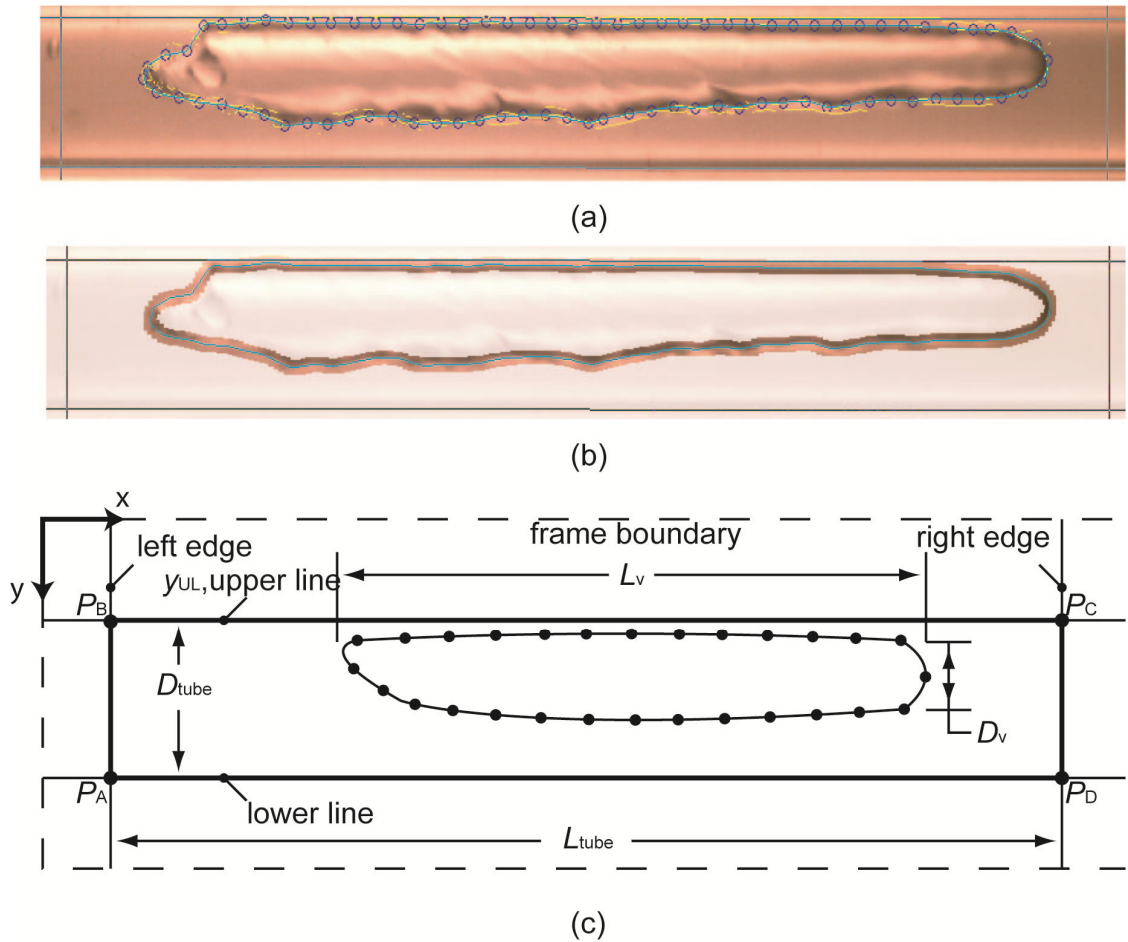


Figure 5.3: Schematic of Video Frame Analysis

5.2.2 Flow Regime Recognition

The condensation flow regime for each data point was categorized into one of four major flow regimes, with several flow patterns within each flow regime. A detailed description of each flow regime is presented in the Results and Discussion, Section 6.1.1. The four major flow regimes identified in this study were Annular, Wavy, Intermittent, and Dispersed. Representative images corresponding to each flow regime are provided in Table 6.1. Recognition of the flow regime is important for classifying the flow as well as for selecting the three dimensional geometry assumptions for calculation of void fraction.

5.2.3 Vapor Bubble Parameters

The vapor bubble parameters can be calculated following the detection of the vapor-liquid interface in a given frame. The maximum diameter of the bubble is calculated by the maximum vertical difference in spline location at a given axial position. The length of the vapor bubble is measured from the minimum horizontal pixel of the spline to the maximum horizontal pixel of the spline. In both cases, the resulting difference is measured in pixels and is converted to millimeters using the known tube diameter as a reference (Figure 5.3(c).) The velocity of the vapor bubble is measured from frame to frame using either the maximum horizontal pixel (the nose,) or the minimum horizontal pixel (the tail.) The change in the minimum and maximum pixel location on the image from one frame to the next is the pixel distance traveled by the tail, X_{tail} , and the nose, X_{nose} , respectively. A schematic of this measurement is shown in Figure 5.4. The nose point is highlighted in red and the tail point highlighted in blue. Using the known capture rate, $Rate_{frame} = 1,000$ fps, the velocity of the vapor bubble can be measured at the nose or the tail:

$$U_{bubble} = X_{nose} Rate_{frame} \vee X_{tail} Rate_{frame} \quad (5.1)$$

Measuring the velocity at the nose is preferred because it yields a more consistent result. The tail of the vapor slug under high mass flux conditions often fluctuates as a result of potential recirculation patterns in the liquid, adding uncertainties to the measurement. However, in some cases the nose of the vapor slug has passed through the frame, in which case, measurement of the velocity at the tail is required. If the entire slug is in the frame, the nose and tail velocity can both be measured to enhance accuracy. The velocity measured at the tail of the vapor slug is typically within 5% of the measured velocity at the nose. An example of vapor bubble velocity tracking is presented in Figure 5.5(a). The time elapsed between frames is shown in the left column. From the first frame, to

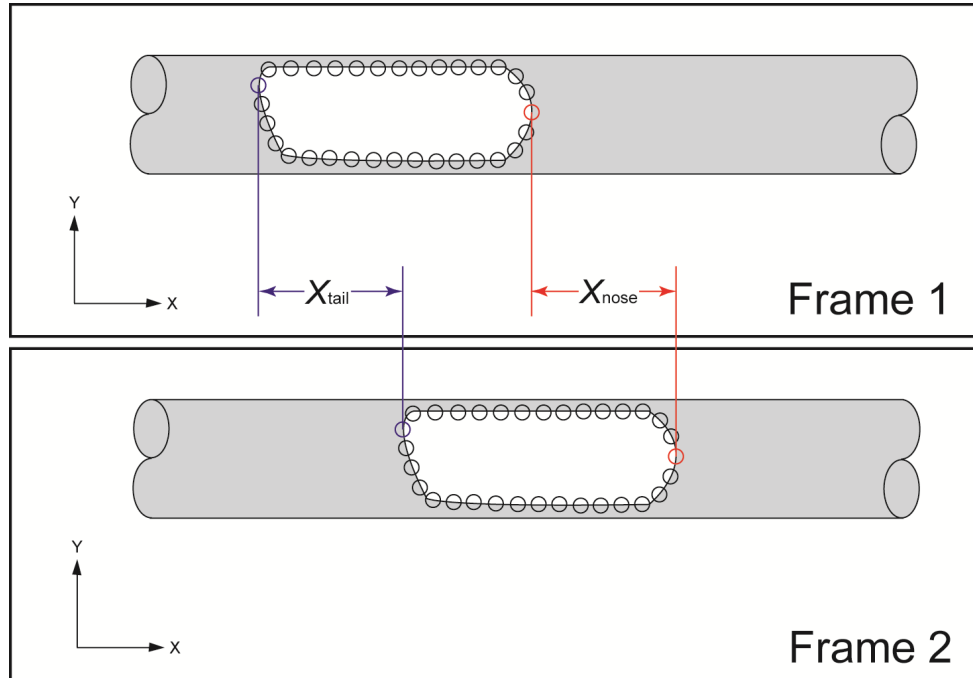


Figure 5.4: Schematic of Vapor Bubble Velocity Measurement

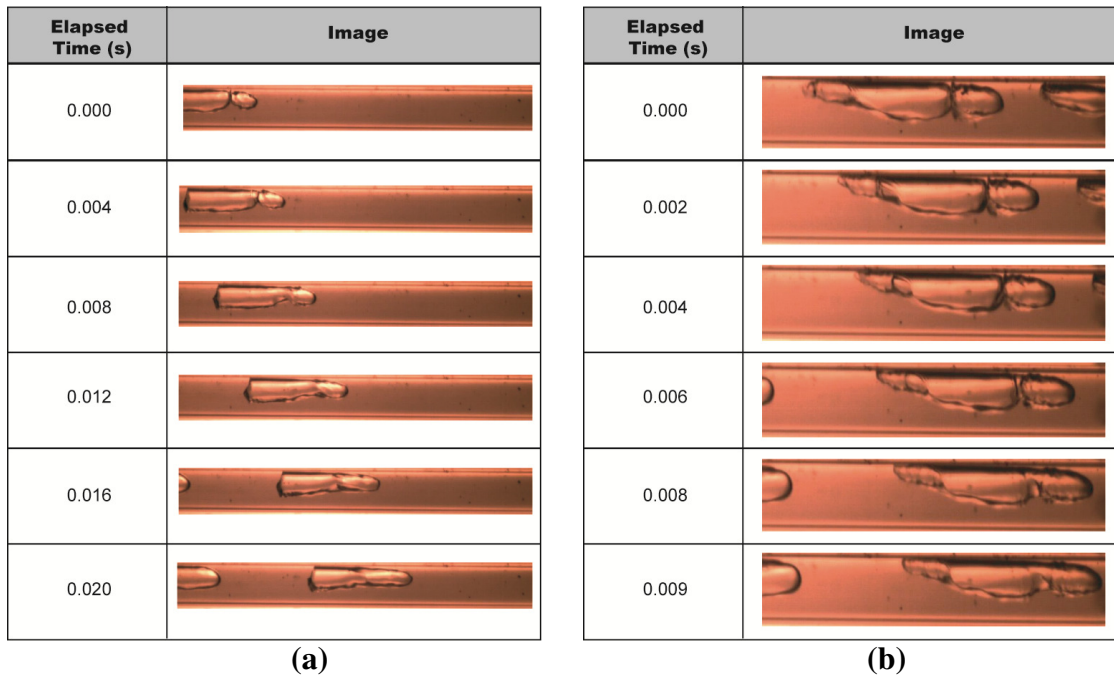


Figure 5.5: Example of (a) Vapor Bubble Velocity, and (b) Coalescence Tracking

the second frame, the nose of the vapor bubble travels $X_{\text{nose}} = 2.40$ mm over a period of 4 ms. The vapor bubble velocity is calculated using Equation 5.1.

$$U_{\text{bubble}} = (2.4 \text{ mm}) \left(\frac{1}{0.004 \text{ s}} \right) = 0.6 \text{ m s}^{-1}$$

The distance traveled by the vapor bubble nose from 0.016 to 0.020 s is $X_{\text{nose}} = 2.46$ mm, which yields a vapor bubble velocity of $U_{\text{bubble}} = 0.615 \text{ m s}^{-1}$. The difference between the measured vapor bubble velocity and the one computed in the first two frames is 2.5%, which is indicative of the relative steadiness and consistency of measured vapor bubble velocity.

Figure 5.5(b) is an example of observed bubble coalescence. The larger vapor bubble in this case approaches the smaller vapor bubble and makes contact at time 0 s. From time 0.002 to 0.006 s, the two vapor bubbles interact as separate entities until a vapor bridge between the two bubbles is formed at time 0.008 s. The bridge is most prominent in the upper portion of the tube at that time. The two bubbles continue to coalesce in the following frame (0.009 s) but the neck where the two bubbles initially made contact is still present. Vapor bubble interactions such as coalescence and splitting can be identified in this manner; however, modeling their effects on heat transfer and pressure drop can be challenging. This is further complicated by the stochastic nature of such processes.

5.2.4 Void Fraction

The two-dimensional image obtained from the procedures described above is used to calculate the void fraction based on the liquid-vapor interface geometry. Two different calculation methodologies are used, as described below. The vapor inventory in each frame is captured in two dimensions using the aforementioned image detection program. If more than one continuous vapor slug is present in a frame, the vapor volume in each

vapor bubble or slug is calculated separately and then summed to determine the volumetric void fraction for each frame.

The procedure for calculating the void fraction is dependent on the closed spline that defines the vapor-liquid interface. The polynomial function that approximates the shape of the curve is represented as a matrix of x- and y-coordinate pixel locations starting at some point along the interface based on the defined region of interest. Initially, the program searches for the tail of the vapor phase, which is defined by the minimum value in the x-coordinate. In the case of wavy or annular flow, the tail corresponds to the left edge of the frame image. The vapor inventory is then subdivided into finite elements along the x-axis to be analyzed, as depicted in Figure 5.6. The thickness of each segment, t_{segment} , is initially varied to check for insensitivity to segment thickness. It was found that a thickness of $t_{\text{segment}} = 5$ pixels yields accurate results without large computational expense. This is equivalent to dividing the vapor inventory in a frame into $10 \mu\text{m}$ segments for the representative tube with a diameter $D = 3.00 \text{ mm}$. As tube diameter decreases, the segment thickness also decreases. For tube diameters of 1.00 and 0.508 mm, these segments are typically 4 and $2.3 \mu\text{m}$ thick, respectively. Within each segment, due to the variation in bubble height, there are several coordinates corresponding to points along the upper and the lower liquid-vapor interface. The upper and lower edges for the given segment are defined as the average of the corresponding upper and lower y-axis coordinates, $y_{\text{avg,upper},i}$ and, $y_{\text{avg,lower},i}$. The difference between these two values is the vapor diameter, $D_{v,i}$ used to calculate the cross-sectional area of each segment element, i , based on the geometric assumptions shown in Figure 5.7, which are in turn validated from images obtained at alternate orientations. An example of the discretization of the upper film, lower film and vapor core is shown in Figure 5.8(a-c) for $T_{\text{sat}} = 29.85^\circ\text{C}$, $G = 206.6 \text{ kg m}^{-2} \text{ s}^{-1}$, and $x = 0.20$. Four successive high speed video frames are shown in Figure 5.8(a) and the discretization of each frame is shown in Figure

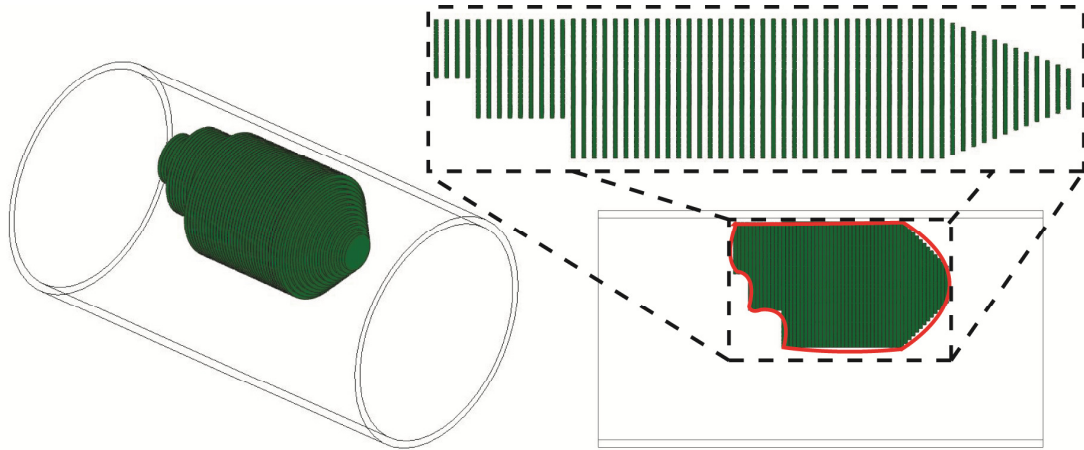


Figure 5.6: Segmental Analysis of Void Fraction

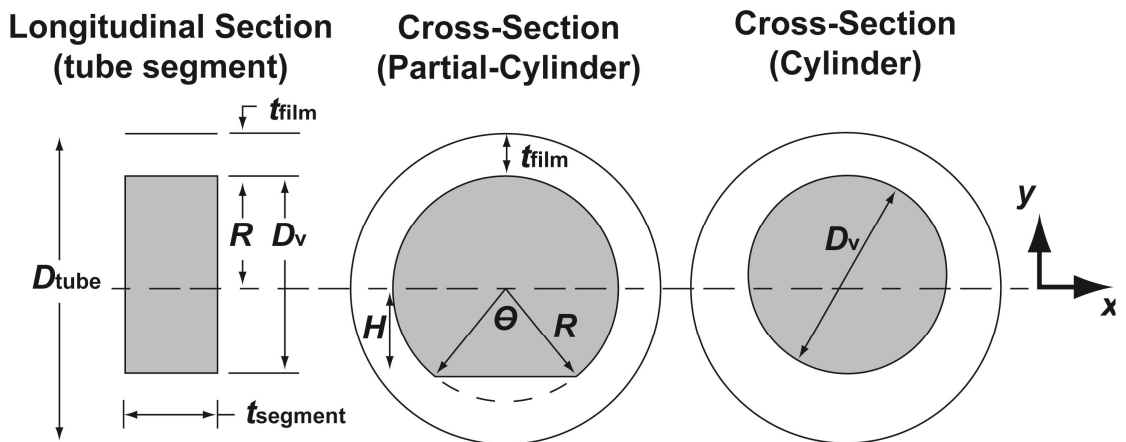


Figure 5.7: Cross-Sectional Areas of Partial-Cylinder and Cylindrical Vapor Phase Cases

5.8(b). The analysis is able to track the local interfacial shape despite averaging the thickness over each segment, t_{segment} . The average lower and upper film thickness for each frame is plotted as a dotted yellow line (Figure 5.8(b).) Local lower film measurements can deviate significantly from the average value and demonstrates the importance of obtaining local measurements. The Probability Density Function (PDF) of the film thicknesses and vapor core are shown in Figure 5.8(c). The PDF is calculated using Equation 5.2.

$$PDF(y) = \lim_{\Delta y \rightarrow 0} \frac{\text{Prob}\{y - \Delta y < y < y + \Delta y\}}{\Delta y} \quad (5.2)$$

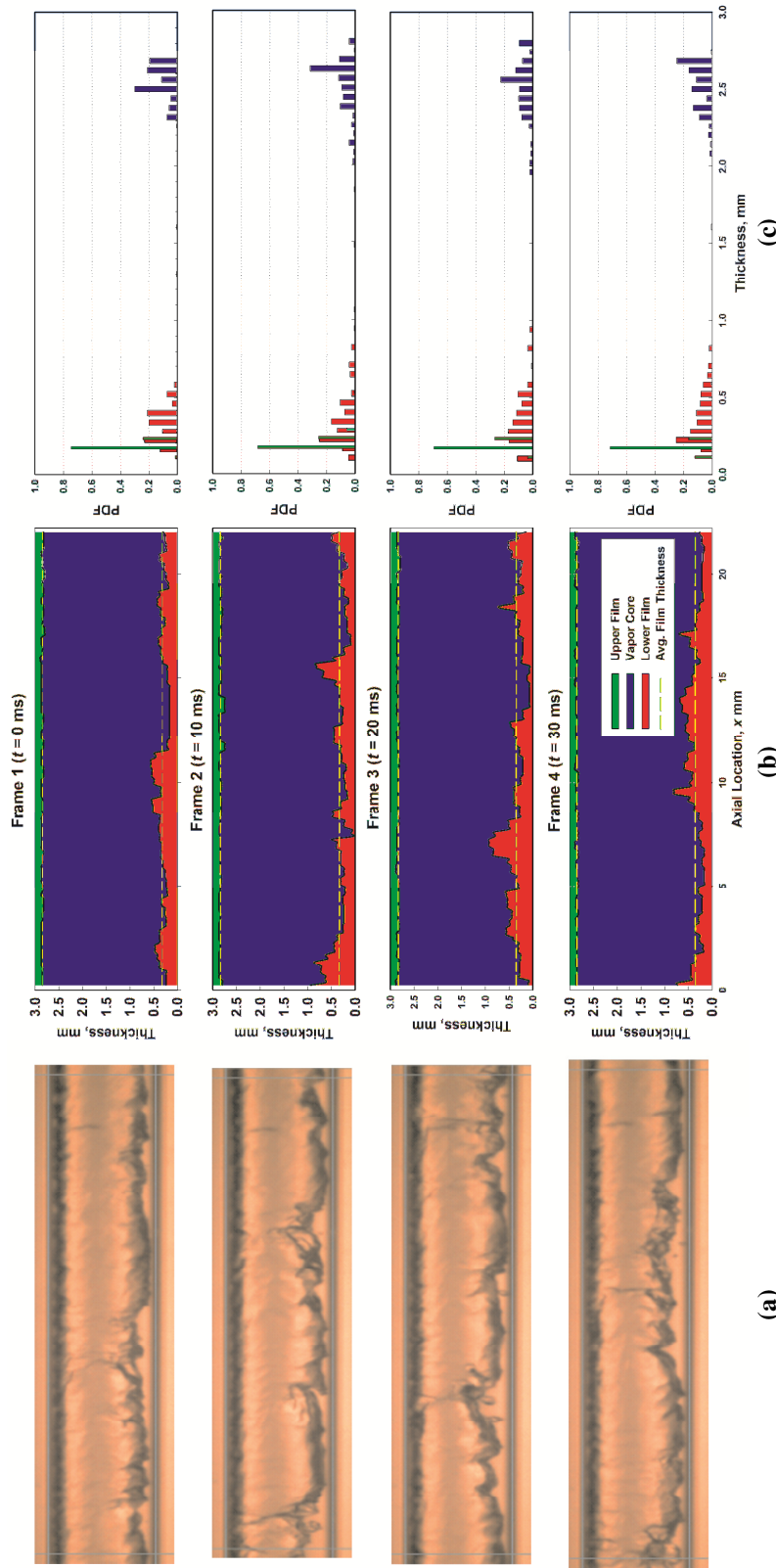


Figure 5.8: Comparison of (a) High Speed Video Frames to (b) Discretized Analysis and (c) Probability Density Function (PDF) of Film Thicknesses for $T_{sat} = 29.85^{\circ}\text{C}$, $G = 206.6 \text{ kg m}^{-2} \text{ s}^{-1}$, and $x = 0.20$

There are only small perturbations in the upper film thickness (capillary waves) and 70% of the upper film thickness values (green) measured are within 0.21 to 0.24 mm. Therefore, the upper film thickness is approximately constant and the lower film thickness (red,) and vapor core (blue) indicate the intensity of the interfacial surface roughness and the PDF of the measured void fraction. While the two dimensional image analysis allows for measurement of film thicknesses and bubble parameters, void fraction measurements would ideally require volumetric measurement.

In the present study, idealizations are made to obtain void fractions from 2-D analyses. Therefore, the resulting void fraction is a function of the geometric assumptions made about the shape of the vapor-liquid interface in the depth dimension. These assumptions are validated using representative alternate viewing angles for some of the experimental conditions. For example, the Overhead Section view (Figure 5.1) provided a view of the condensing fluid from the top, which enabled a realistic construction of the three-dimensional shape of the vapor and liquid features. The cross sectional geometry is either assumed to be a circle, or a partial circle. Analysis of the different vapor phase geometries is described below followed by the methodology for calculating local, volumetric, and time averaged void fraction.

Cylindrical Vapor Geometry

The cylindrical vapor geometry assumption assumes that the vapor inventory flowing through the tube has a circular cross-section. Therefore, the average vapor diameter, $D_{v,i}$, for each segment is used to calculate the cross-sectional area, $A_{cs,i}$.

$$A_{cs,i} = \frac{\pi}{4} D_{v,i}^2 \quad (5.3)$$

The cylindrical geometry assumption is typically valid for small tube diameters where gravitational influences are relatively small. The vapor bubble is modeled as a finite number of cylinders adjacent to each other. This assumption was used for intermittent and annular flows.

Partial Cylinder Geometry

In the wavy flow regime, the effects of an increased liquid inventory at the bottom of the tube must be considered to obtain the volumetric void fraction from the two-dimensional image. This deviation from a symmetrical, circular cross section is accounted for by assuming partial-cylinder geometry (Figure 5.7.) In this case, the thickness of the film located at the top of the tube is calculated using the upper line, y_{UL} , that defines the tube diameter (Figure 5.3(c)) and the average upper edge, $y_{avg,upper,i}$ for each segment:

$$t_{film,i} = y_{UL} - y_{avg,upper,i} \quad (5.4)$$

The film thickness at the center point of the representative data point under consideration is $t_{film,i} = 0.27$ mm. In the case of completely stratified flow, the film thickness at the top would be zero. The radius, R , of the partial-cylinder shape is defined as:

$$R = \frac{D_{tube}}{2} - t_{film} \quad (5.5)$$

$$R = 1.5 - 0.27 = 1.23 \text{ mm}$$

This radius of the vapor core is shown in Figure 5.7. Defining the radius this way may slightly over predict the actual vapor inventory as the region represented by the shaded partial circle in Figure 5.7 is probably not centered on the tube axis, leading to a variation of the film thickness around the circumference. However, that this approach does account well for the more significant issue of the thicker pool of liquid in the stratified region at the bottom. The liquid inventory in the stratified pool is accounted for by

subtracting a portion of the area from the representative vapor circle with radius R at the observed liquid height. The methodology for calculating this area is discussed below.

There are three different cases for the calculation of the cross-sectional area of the vapor inventory, determined by the vertical distance of the bottom liquid-vapor interface, H , from the tube centerline. Thus, H is given by:

$$H = \frac{D_{\text{tube}}}{2} - t_{\text{film}} - D_v \quad (5.6)$$

$$H = 1.5 - 0.27 - 1.46 = -0.23 \text{ mm}$$

Case I (At center-line, $H = 0$)

If the vertical distance, $H = 0$, then the cross-sectional area of the vapor inventory is simply a semi-circle and the resulting cross-sectional area is:

$$A_{\text{cs,i}} = \frac{\pi R^2}{2} \quad (5.7)$$

In general, the vertical distance, H , is usually of some non-zero value and is typically less than 0 like in the representative data point under discussion. This means that the liquid pool is below the tube center-line. The angle, θ , is needed to determine the arc length of the perimeter where the liquid is stratified.

$$\theta = 2 \arccos(H/R) \quad (5.8)$$

$$\theta = 2 \arccos(0.23/1.23) = 2.765 \text{ rad}$$

Case II (Above center-line, $H > 0$)

If the vertical distance, $H > 0$, then the bottom edge of the liquid-vapor interface is located above the tube centerline. In this case, the cross-sectional area is calculated by:

$$A_{\text{cs,i}} = \frac{1}{2} R^2 (\theta - \sin \theta) \quad (5.9)$$

This situation usually occurs at the tail end of a vapor bubble, a large amplitude wave, and in the transition region where wavy flow is transitioning to intermittent flow and a large vapor core is pinching and separating.

Case III (Below center-line, $H < 0$)

If the vertical distance, $H < 0$, then the bottom edge of the liquid-vapor interface is located below the tube centerline, as seen in the representative case in Figure 5.7. In this case, the cross-sectional area of the vapor inventory is calculated as follows:

$$A_{cs,i} = \frac{1}{2} R^2 (2\pi - \theta + 2 \sin \theta) \quad (5.10)$$

$$A_{cs,i} = \frac{1}{2} (1.23 \text{ mm})^2 (2\pi - 2.765 + 2 \sin(2.765)) = 2.94 \text{ mm}^2$$

This occurs mainly during wavy flow, low-mass flux intermittent flows, and during wave-packet annular flow.

Void Fraction Measurement

Once the cross-sectional area for the segment is computed, the volume of the vapor inventory for one segment, $V_{v,i}$, can be calculated as follows:

$$V_{v,i} = A_{cs,i} t_{\text{segment}} \quad (5.11)$$

A sample calculation for the center point of the top frame in Figure 5.8 is discussed here.

The **local void fraction** is a function of axial position. The local void fraction, $\langle \alpha \rangle$, is calculated by dividing the local vapor volume by the tube volume within each segment.

$$\langle \alpha \rangle = \frac{V_{v,i}}{V_{\text{tube},i}} = \frac{A_{cs,i} t_{\text{segment}}}{(\pi/4) D_{\text{tube}}^2 t_{\text{segment}}} = \frac{A_{cs,i}}{(\pi/4) D_{\text{tube}}^2} \quad (5.12)$$

$$\langle \alpha \rangle = \frac{2.94 \text{ mm}^2}{7.07 \text{ mm}^2} = 0.4159$$

The **volumetric void fraction**, $\langle\langle\alpha\rangle\rangle$ (void fraction for 1 frame,) is measured by summing all of the local vapor volumes along the tube and dividing by the tube volume.

$$\langle\langle\alpha\rangle\rangle = \frac{V_v}{V_{\text{tube}}} = \frac{\sum_{i=1} V_{v,i}}{(\pi/4) D_{\text{tube}}^2 L_{\text{tube}}} \quad (5.13)$$

$$\langle\langle\alpha\rangle\rangle = \frac{83.07}{157.6} = 0.527$$

This volumetric void fraction is calculated on a frame-by-frame basis.

The **bulk average void fraction** is obtained by averaging the volumetric void fraction over time.

$$\alpha = \langle\langle\bar{\alpha}\rangle\rangle = \frac{\sum_{j=1}^N \langle\langle\alpha\rangle\rangle_j}{N} \quad (5.14)$$

$$\alpha = \langle\langle\bar{\alpha}\rangle\rangle = \frac{28.05}{50} = 0.561$$

The local, $\langle\alpha\rangle$ (blue,) volumetric, $\langle\langle\alpha\rangle\rangle$ (red,) and volume and time averaged, α (black,) void fraction for three representative cases are shown in Figure 5.9. The top and middle plot demonstrate the difference in dynamic signal as a function of flow regime in the same tube diameter ($D = 3.00$ mm.) The local and volumetric values for the wavy flow example do not deviate significantly from the average value. It is difficult to differentiate between the volume and volume-time average values. The intermittent signal varies significantly from the average value due to the nature of the flow regime. The vapor bubbles are intermittently separated by liquid slugs, which result in a local measured void fraction of 0. The slug frequency can be inferred from this plot. The void fraction measures 0 at 6 different discrete times over the 0.5 s period, resulting in a measured slug frequency of $\omega = 12 \text{ s}^{-1}$. The bottom plot demonstrates the influence of tube diameter ($D = 1$ mm) on measured void fraction for the same flow regime. The bulk averages for the

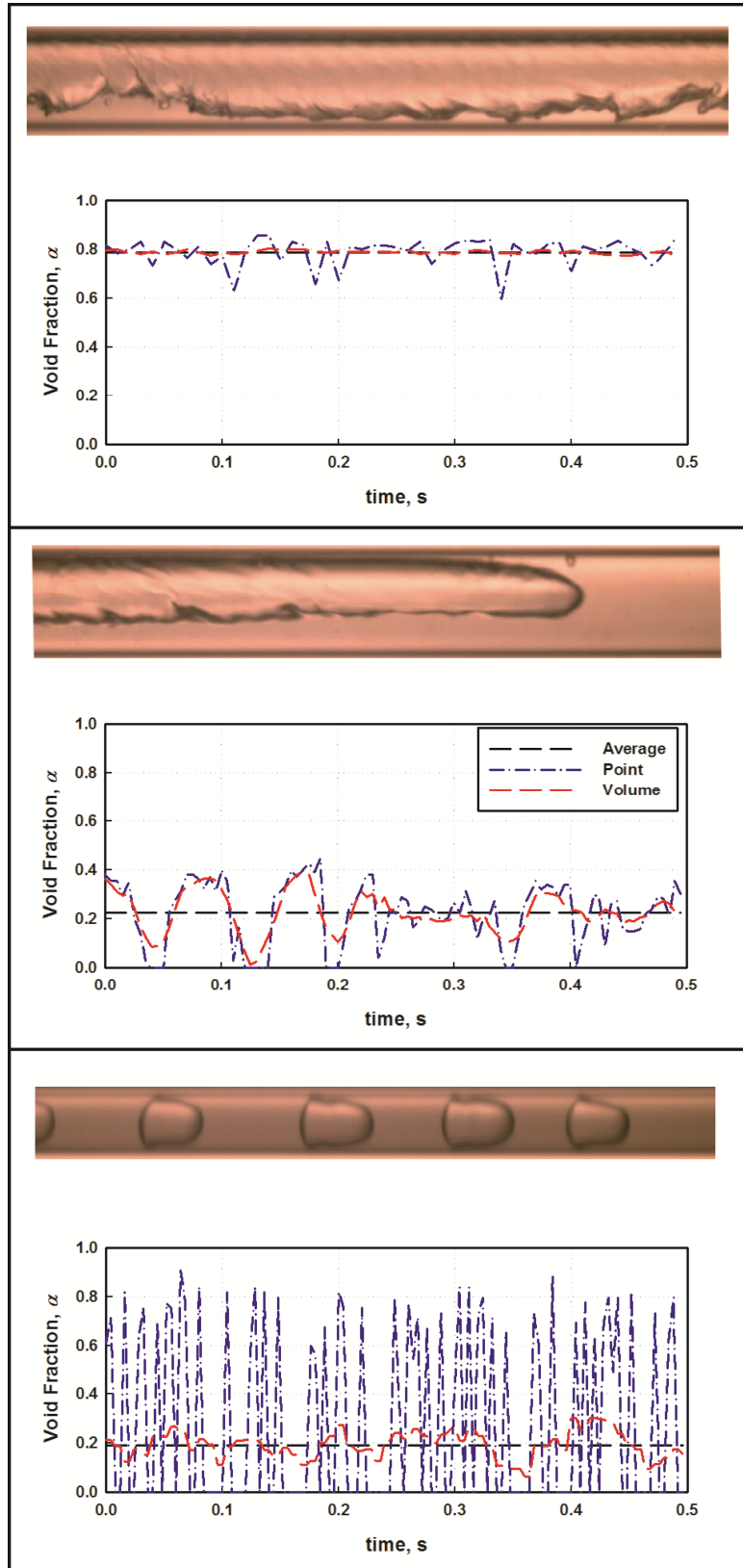


Figure 5.9: Void Fraction as a Function of Time for the Center Point of Each Frame (blue), Volume (red) and Average Over Volume and Time (black) for Three Representative Cases

middle and bottom plot are similar, $\alpha = 0.21$, but the dynamic signals are quite different. The decreased tube diameter results in a substantial increase in vapor bubble velocity and frequency.

5.3 Accuracy of the Analysis

A detailed quantification of the uncertainties in the measured void fractions from the above approach is presented here. First, a sensitivity analysis was performed on the number of frames needed to analyze one data point accurately. As part of this, analyses were also conducted to ensure that the procedure was independent of user input, because the technique is semi-automated. The uncertainties corresponding to these sources, as well as the relevant experimental uncertainties are combined to determine the overall uncertainty in the void fraction. The methods for calculating each of the constituent uncertainties are discussed below.

5.3.1 Sensitivity to Number of Frames

A sensitivity analysis was performed to determine the number of frames required for each data point in each different flow regime. It was desired to achieve accurate results without excessive computational times. Attempts to fully automate the image analysis program were unsuccessful due to variations in wave/interface propagation and perturbations. Therefore, the analysis required user oversight which increased computational time. Every frame from a wavy and annular flow data point was analyzed and the effect of the number and frequency of frames analyzed was investigated. An example of this analysis for wavy flow is shown in Figure 5.10. A summary of these results is shown in Table 5.2. It is clear that there is little deviation ($< 1\%$) beyond 500 frames. It was also found that analyzing every 50th frame in this example led to 5%

deviation as compared to an analysis of every frame. Similarly, analyzing every 10th slide led to a deviation of 0.83%. Therefore, it was determined that analyzing every 10th frame for 500 frames per data point yielded high accuracies while substantially reducing computation time for wavy and annular flows. This corresponds to a total of 50 frames per void fraction data point. A similar analysis was conducted for intermittent flow, which was found to be more sensitive to the frame frequency because of the intermittent nature of the flow. Based on these considerations, 500 frames at a frequency of 5 frames were analyzed for this flow regime, which yielded a deviation of 0.63%.

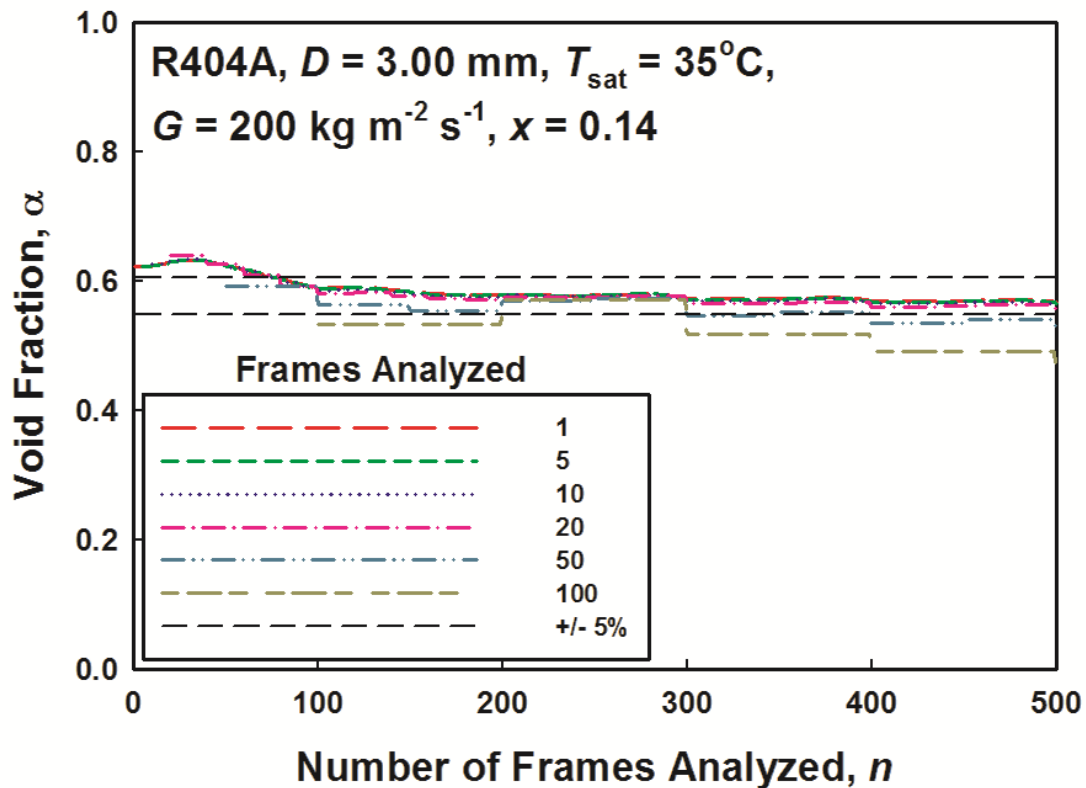


Figure 5.10: Sensitivity Analysis: Number and Frequency of Frames Analyzed per Data Point

Table 5.2: Summary of Sensitivity Analysis

Flow Regime	Total Frames	Frame Frequency	Frames Analyzed	Accuracy (%)
Annular/Wavy	500	10	50	0.83
Intermittent	500	5	100	0.67

5.3.2 Repeatability

A repeatability analysis was also conducted to ensure that the analysis was insensitive to the choice of the tube edge location and the calibration of the frame envelope to the physical dimensions by the user. Thus, for every data point analyzed, the first frame is set-up and analyzed five times. Set-up procedure requires the user to enter the location of the tube diameter, and the calibration of pixels to millimeters. The standard deviation between five measured void fractions was calculated to quantify the repeatability of the process. For the example data point, the five measured void fractions from the first frame are presented in Table 5.3. The standard deviation of the five measured values is 0.008834. The repeatability of the process was used as an indicator of the ability to obtain void fractions from the high speed video data. There were several flow regimes where the vapor-liquid interface was intractable. Any flow regime where there is liquid entrainment in the vapor core was not possible to analyze using this approach. A specific example of flow regimes where analysis was not possible is the mist and disperse flow regime. These conditions typically occur at high mass fluxes and high qualities. Figure 5.11 shows the regions where the standard deviation is less than 0.01 (green,) less than 0.02 (yellow,) and where the vapor-liquid interface is intractable. Therefore, if it was possible for the program to decipher the vapor liquid interface, it was capable of doing it with high repeatability.

Table 5.3: Measured Void Fraction and Standard Deviation of Results for the First Frame of the Representative Data Point, $T_{\text{sat}} = 29.85^{\circ}\text{C}$, $G = 206.6 \text{ kg m}^{-2} \text{ s}^{-1}$, and $x = 0.1995$

	Analysis					Std. Dev.
	1	2	3	4	5	
α	0.69971	0.70245	0.71098	0.69968	0.72003	0.008834

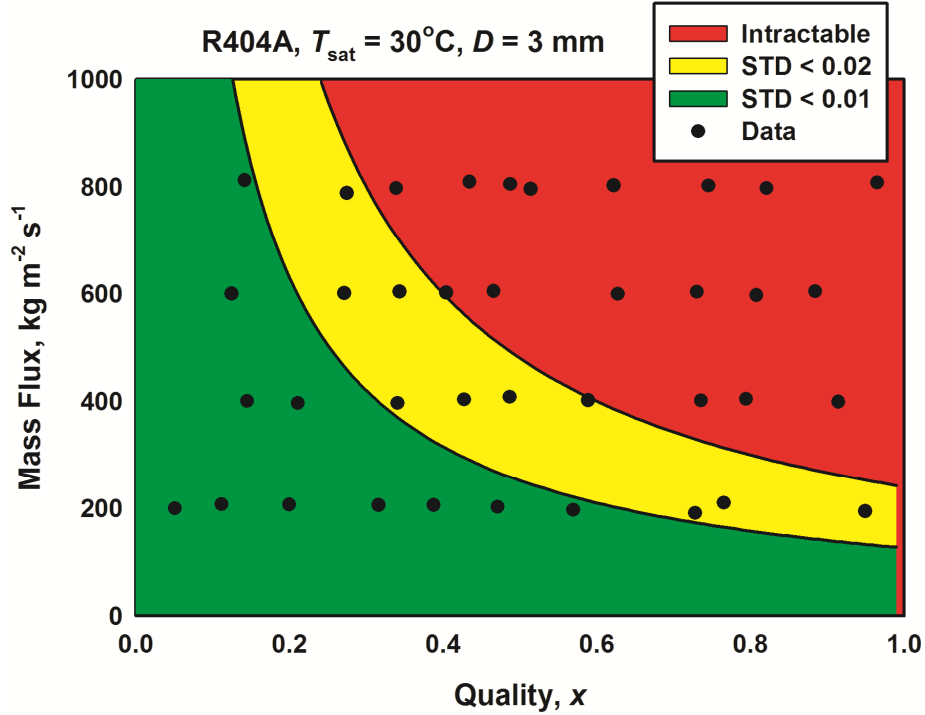


Figure 5.11: Repeatability Regions for Example Data Points; green: $\sigma_u < 0.01$, yellow: $\sigma_u < 0.02$, red: intractable

5.3.3 Total Uncertainty

The total uncertainty in the void fraction was estimated using a root mean square of all of the major uncertainties in the measurements and analyses. The total uncertainty accounts for the uncertainty of the average test section quality from experiments, $U_{x,\text{exp}}$, deviations introduced by the selection of the number and frequency of frames analyzed, U_{sens} , and the repeatability of the process, U_{rep} .

$$U_{\text{tot}} = \sqrt{U_{x,\text{exp}}^2 + U_{\text{sens}}^2 + U_{\text{rep}}^2} \quad (5.15)$$

The uncertainty value from the error propagation analysis (U_{sens}) is taken from Table 5.2, while the repeatability uncertainty (U_{rep}) is taken as 3 times the measured standard deviation. Three times the standard deviation was chosen because this results in a confidence level is 99.7%. The uncertainty from the sensitivity analysis is $U_{\text{sens}} =$

0.0561, and from the repeatability analysis is $U_{\text{rep}} = 0.0265$ for the representative data point under consideration.

The experimental uncertainty for the average test section quality has an effect on the uncertainty in measured void fraction. At high qualities, this effect is small, because the void fraction tends to be a weak function of quality. At low qualities, this can be significant because the void fraction is strongly dependent on quality. To account for this in the void fraction uncertainty, the homogeneous void fraction model is used. The homogeneous void fraction is calculated using the upper ($\beta_+(x_{\text{avg}}+\Delta x_{\text{unc}})$) and lower ($\beta_-(x_{\text{avg}}-\Delta x_{\text{unc}})$) limit of the average test section quality. These values are compared with the homogeneous void fraction evaluated using the average test section quality and the maximum difference is used as the uncertainty.

$$U_{x,\text{exp}} = \text{MAX} \left[\beta(x + U_{x,\text{avg}}) - \beta(x), \beta(x) - \beta(x - U_{x,\text{avg}}) \right] \quad (5.16)$$

$$U_{x,\text{exp}} = \text{MAX} \left[\beta(0.199 + 0.015) - \beta(0.199), \beta(0.199) - \beta(0.199 - 0.015) \right]$$

$$U_{x,\text{exp}} = \text{MAX} \left[(0.7873 - 0.7716), (0.7716 - 0.754) \right] = 0.01574$$

The total uncertainty is calculated using Equation 5.14.

$$U_{\text{tot}} = \sqrt{(0.0157)^2 + (0.0265)^2 + (0.0056)^2} = 0.0313$$

The percent uncertainty for this case is 5.6%. The total uncertainty for the measured void fraction and its components for several different data points at different qualities is displayed in Figure 5.12.

At low qualities, the experimental uncertainty component dominates the total uncertainty. This is a result of the large dependence of void fraction on quality at low vapor qualities. At high vapor qualities, the repeatability component dominates the total uncertainty. This is a result of the thin liquid films formed around the tube that are more sensitive to the

calibration. The average percent uncertainty in void fraction over the entire range of qualities for which the tests were conducted was found to be 10.3%, with the minimum uncertainty of 2% occurring at $\alpha = 0.86$ ($x = 0.57$), and the maximum uncertainty of 30.6% occurring at $\alpha = 0.27$ ($x = 0.051$.)

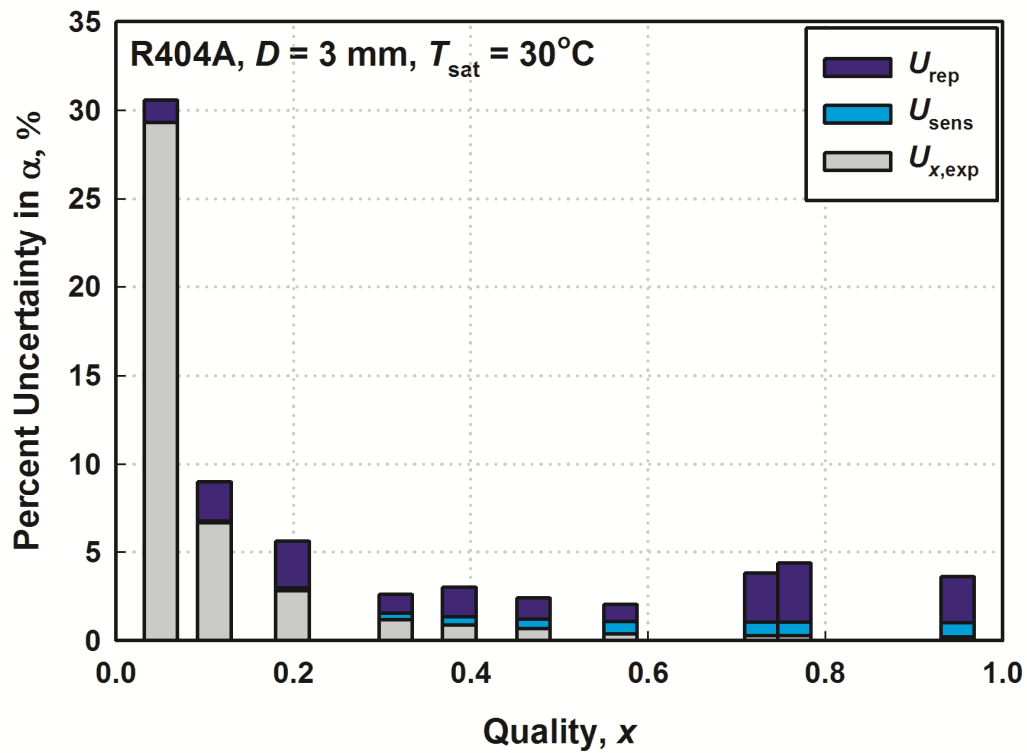


Figure 5.12: Total Void Fraction Uncertainty and Component Contributions

CHAPTER 6: RESULTS AND DISCUSSION

This chapter details the experimental results from this study and compares them to relevant models from the literature. The observed flow regimes are presented first, followed by void fraction results, pressure drop, and heat transfer data.

6.1 Results

6.1.1 Flow Regime

A summary of flow regimes observed is presented in this section. First, a detailed description of the observed flow regimes is presented, followed by a discussion of the effects of tube diameter on the observed phenomena.
















Flow Regimes

Each data point was categorized as belonging to one of four major flow regimes, with several flow patterns within each regime. The four major flow regimes observed in this study were annular, wavy, intermittent, and dispersed. Representative images corresponding to each flow regime are provided in Table 6.1. The flow regimes observed in this study are similar to those reported by Coleman and Garimella (2003) for R134a in small hydraulic channels. A description of the different flow regimes is presented here.

Annular Regime

Annular flow is characterized by a vapor core surrounded by a liquid annulus. At high mass fluxes, liquid droplets can become entrained within the vapor core and vapor bubbles entrained in the liquid film. The flow patterns observed within this regime are

Table 6.1: Flow Regimes and Patterns Observed in Condensing R404A Through 3.00 mm Diameter Tubes

		FLOW REGIMES				
Annular		Wavy	Intermittent	Dispersed		
FLOW PATTERNS	Mist Flow	 Mist Flow	 Discrete Wave (0)	 Slug Flow	 Bubbly Flow	
	Annular Ring	 Annular Ring	 Discrete Wave (1)	 Slug Flow	 Bubbly Flow	
	Wave Ring	 Wave Ring	 Discrete Wave (2)	 Plug Flow		
	Annular Film	 Annular Film	 Disperse Wave (3)	 Plug Flow		
			Note: Numbers above denote intensity of secondary waves	 Plug Flow		

mist flow, annular ring, wave ring, wave packet, and annular film. The mist flow pattern is described as a uniform mist with small droplets entrained in the vapor core. A thin liquid annulus can still exist. Mist flow generally occurs at high mass fluxes and high vapor qualities. The annular ring pattern is described as similar to mist flow except with a periodic liquid film build-up along the tube which resemble rings. The wave ring pattern is similar to the annular ring pattern; however, the liquid shows some settling toward the bottom due to gravity giving the bottom portion of the liquid a wave-like appearance. The annular film pattern is described as having a continuous vapor core surrounded by a wavy liquid annulus. At high velocities, the liquid waves increase in frequency.

Wavy Regime

Although condensing flows are expected to have a coating of liquid around the entire circumference, the distinction between wavy and annular flow highlights the influence of gravity in (stratified) wavy flows. The wavy flow regime is further subdivided into flow patterns of increasing wave intensity. For very low mass flux laminar vapor and liquid flows, a smooth interface between the liquid and vapor phases is expected. The completely stratified regime is observed in large tube diameters but was not observed in this study. As vapor and liquid velocities increase, the interfacial waves increase in frequency and amplitude. The major distinction between discrete and dispersed wave patterns is due to the characteristics of the secondary waves. The discrete wave pattern has waves of large amplitude and very few dominant frequencies. The disperse wave pattern consists of a large number of secondary waves with no dominant frequency or amplitude, and typically occurs at high mass fluxes and higher qualities. In Table 6.1, these flow patterns are categorized according to the intensity of these small amplitude, high frequency waves. This flow regime is seen only in situations where gravity is

influential and is therefore absent in very small diameter tubes due to the dominant influence of surface tension.

Intermittent Regime

The intermittent flow regime exists at low qualities during condensation and is typified by the alternating passage of liquid and vapor “slugs” and “plugs” through the tube. The slug flow pattern is classified as vapor “slugs” traveling through the liquid, which are often trailed by small vapor bubbles. The vapor-liquid interface is observed as wavy and the importance of gravity is present as the “slugs” are located toward the top of the tube. Plug flow consists of rigid vapor “slugs” that are typically non-stratified and axisymmetric. Vapor plugs are very similar to Taylor bubbles and have bullet-like shapes with rounded fronts and blunt tails.










Dispersed Regime

At even lower qualities and high mass fluxes, the vapor plugs become small and the bubbly flow pattern is observed. The transition to the disperse flow happens when the aspect ratio of the vapor bubbles, $L_{\text{bubble}}/D_{\text{bubble}}$ is less than 2. This regime was not observed in the experiments conducted for the present study.

Effects of Tube Diameter

As tube diameter decreases, the influence of gravity decreases and the importance of surface tension increases. As a result, the wavy flow regime is not observed in the 1.00 and 0.508 mm diameter tubes, and the flow transitions directly from annular to intermittent flow or vice versa. A summary of these transitions is shown in Table 6.2. For the large 3.00 mm diameter tube, the transitional region between annular and intermittent flow exhibits wavy flow characteristics. The transitional regime for small

Table 6.2: Annular-to-Intermittent Transitions at Different Tube Diameters

D , mm	FLOW REGIMES		
	Annular	Transitional	Intermittent
3.00			
1.00			
0.508			

tube diameters has a continuous vapor core surrounded by a liquid film that begins to neck and pinch the vapor core until vapor bubbles are formed. The two mechanisms for which transition from annular to intermittent flow or wavy to intermittent flow occurs are very different. Therefore, the forces that govern this transition are most probably different as well. For example, in large tubes, the waves must overcome gravitational forces to reach the top of the tube and bridge the vapor core. Taitel and Dukler (1976) use this rationale to model the transition to intermittent flow. For the small diameter tubes ($D = 0.508, 1.00$ mm) investigated in the present study, inertial forces compete with surface tension, and the ratio of these forces determines transition from annular flow to intermittent flow. A summary of the flow regimes observed for each tube diameter is shown in Table 6.3. A majority of the flow visualization data in the 3.00 mm tube were in wavy flow (50.5%,) while the majority of data for the 1.00 and 0.508 mm tubes were in the annular regime (62.7, 67.1%,) respectively.

Table 6.3: Summary of Observed Flow Regimes

Regime Observed	Diameter, mm			Total
	3.00	1.00	0.508	
Intermittent	13	21	12	46
Transitional	NA	29	13	42
Wavy	98	NA	NA	98
Annular	83	84	51	218
Total	194	134	76	424

6.1.2 Void Fraction

Condensation void fraction and pressure drop data were obtained for tube diameters of 0.508, 1.00, and 3.00 mm at mass fluxes and saturation temperatures ranging from 200 to 800 kg m⁻² s⁻¹ and 30 to 60°C, respectively, for a total of 142 void fraction and 424 pressure drop data points. The smaller set of void fraction data is because of the high uncertainties in void fraction determination at some of the conditions tested, for example,

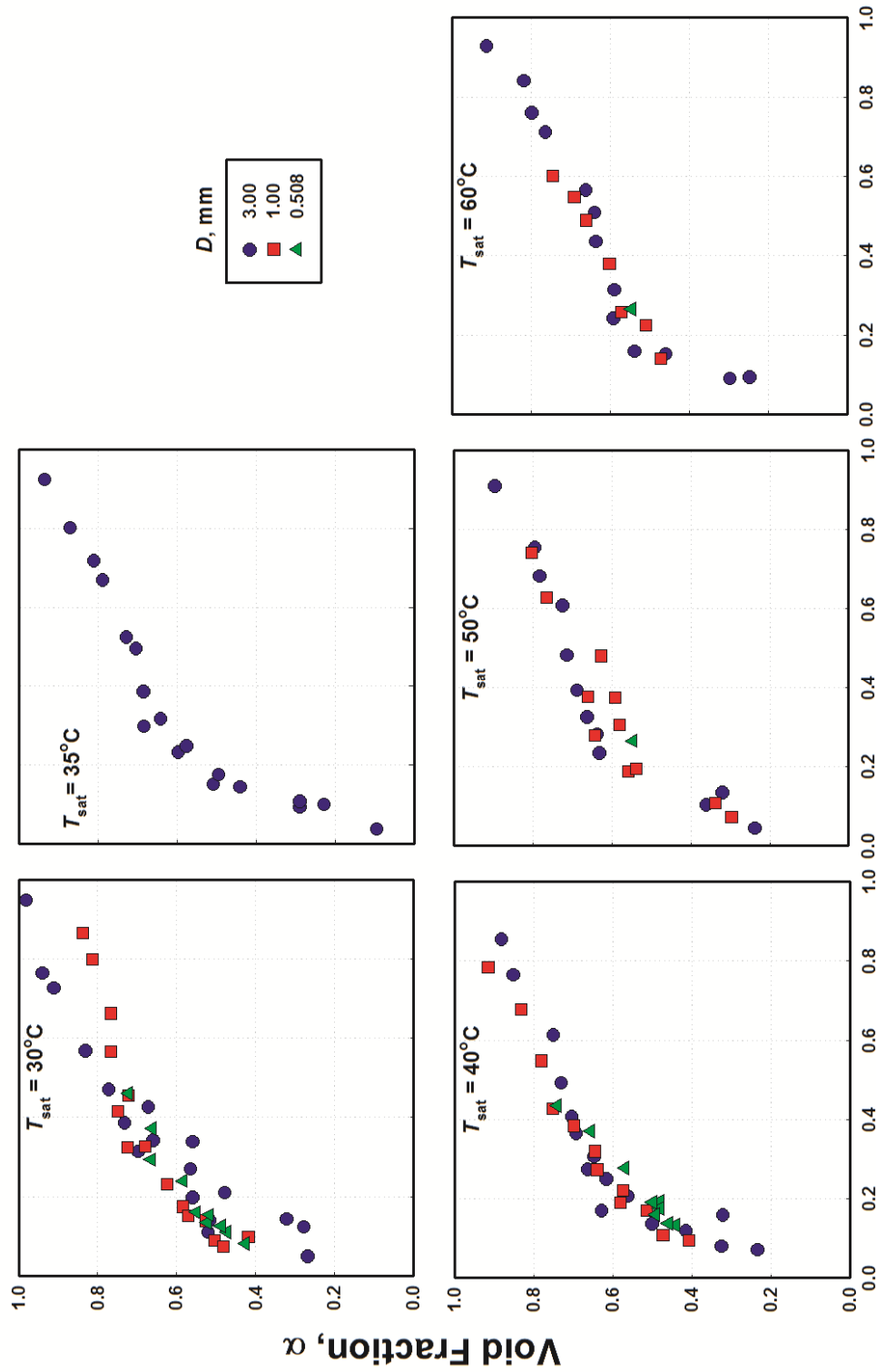


Figure 6.1: Void Fraction versus Quality

at high mass fluxes and qualities, where accurate identification of the interface is difficult. The void fraction results are presented in Figure 6.1. The influences of parameters such as mass flux, saturation temperature and hydraulic diameter on void fraction and pressure drop are discussed below, followed by comparisons of these results with the predictions of the relevant models from the literature.

Figure 6.2(a) shows void fraction as a function of quality for varying saturation temperatures for $D = 3.00$ mm and $G = 200$ kg m⁻² s⁻¹. As saturation temperature increases, the void fraction decreases. For all saturation temperatures, the void fraction approaches unity as the flow becomes completely vapor and approaches 0 as the flow becomes completely liquid. At both extremes, the measured results approach the homogeneous flow model. The influence of saturation temperature on void fraction is most pronounced in the quality range $0.25 < x < 0.75$. As the saturation temperature increases, the vapor-liquid density ratio decreases, increasing the vapor volume at a given quality. Relevant property ratios at several saturation temperatures are presented in Table 6.4 at several saturation temperatures. The difference in density ratio from 30 to 60°C is almost 3.5, while the difference in measured void fraction, for example, at a quality of 0.57, is 20%. However, if the void fraction were predicted for both saturation temperatures using the homogeneous model, the void fraction decreases from $\beta = 0.948$ at $T_{\text{sat}} = 30^\circ\text{C}$ to $\beta = 0.862$ at $T_{\text{sat}} = 60^\circ\text{C}$, i.e., a 10% decrease. It appears from these results that for the tube diameters under consideration here, the void fraction is influenced to a larger extent by phase density ratios than is expected in homogeneous flow.

Figure 6.2(b) for a representative case with $D = 3.00$ mm and $T_{\text{sat}} = 35^\circ\text{C}$ shows that mass flux does not influence void fraction, especially at low qualities. The influence of mass flux on void fraction was found to be negligible for all saturation temperatures and tube diameters investigated in this study.

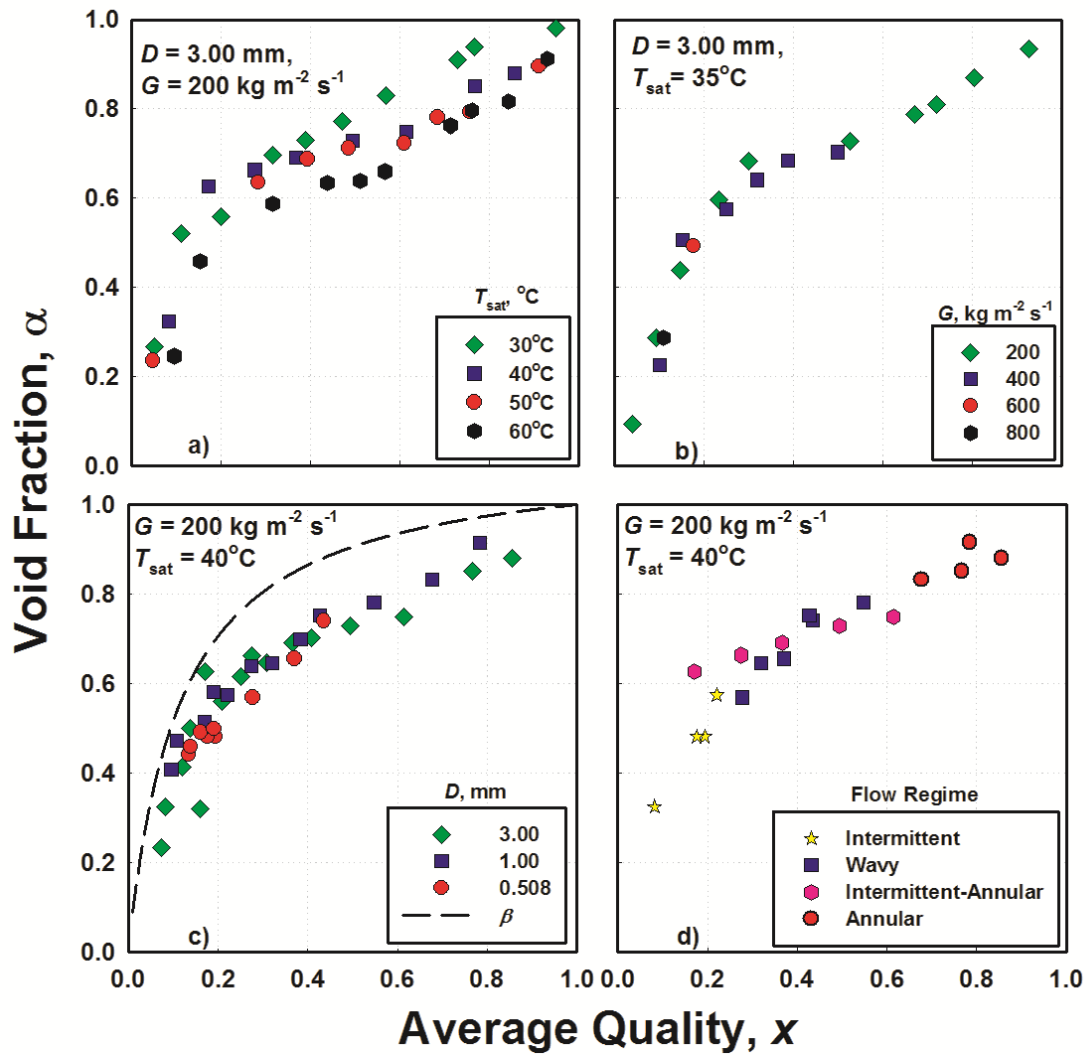


Figure 6.2: Experimental Void Fraction Versus Quality for (a) Increasing Saturation Temperature, (b) Increasing Mass Flux, (c) Increasing Diameter, and (d) Different Flow Regimes

Table 6.4: Properties of R404A at Various Saturation Temperatures

$T_{sat}, ^\circ\text{C}$	p_r	$\rho_l \rho_v^{-1}$	$\mu_l \mu_v^{-1}$	$\sigma, \text{N m}^{-1} (\times 10^3)$
30	0.38	18.6	8.1	3.5
40	0.49	9.4	6.5	2.5
50	0.62	6.6	5.2	1.6
60	0.77	4.8	4.2	1

Figure 6.2(c) shows a plot of void fraction versus quality at $T_{\text{sat}} = 40^\circ\text{C}$ for $D = 0.508$, 1.00, and 3.00 mm. It can be seen that throughout the condensation process, the measured void fraction is over predicted by the homogeneous flow void fraction expression, and also that the void fraction is insensitive to hydraulic diameter. This was found to be the case for all saturation temperatures. Figure 6.2(d) shows the effects of flow regime on bulk measured void fraction. There is little measureable difference in bulk void fraction based on flow regime. For example, at $x = 0.4$, the measured void fraction for the intermittent-annular data point is $\alpha = 0.65$, while under the same operating conditions, the void fraction for the wavy data point is $\alpha = 0.66$. However, even though the vapor-to-liquid volume ratio appears unaffected by tube diameter and flow regime, the location and distribution of this vapor volume and the interfacial area can be quite different. For the 3.00 mm tubes, the vapor phase was located near the top of the tube, leaving a thicker stratified film at the bottom, indicating the relevance of buoyancy forces. For the 1.00 and 0.508 mm tubes, the vapor core is located at the center of the tube, with a uniform liquid film surrounding it. This signifies the importance of surface tension and gravitational forces. As the tube diameter decreases, surface tension forces overcome the counteracting gravity forces which results in a more axi-symmetric distribution of vapor and liquid within the tube. Therefore, even at relatively similar liquid or vapor volume ratios, as the hydraulic diameter changes, surface tension may affect the *distribution* of the vapor-liquid inventory. Figure 6.3(a) shows the effects of tube diameter on vapor-liquid distribution under similar conditions. For both cases, $T_{\text{sat}} = 30^\circ\text{C}$ and $G = 200 \text{ kg m}^{-2} \text{ s}^{-1}$, and the resulting void fractions are 0.527 and 0.523. For $D = 3.00$ mm, there is stratified liquid inventory near the bottom of the tube corresponding to the wavy flow regime. The film thickness in this case varies azimuthally. The interfacial area, A_i , to wetted tube area, $A_w = \pi DL$, ratio is 0.744. For $D = 1.00$ mm, the flow is in the intermittent regime and the interfacial area is the vapor bubble surface. The ratio of A_i to A_w for this distribution is 0.708. While the resulting area ratios are similar,

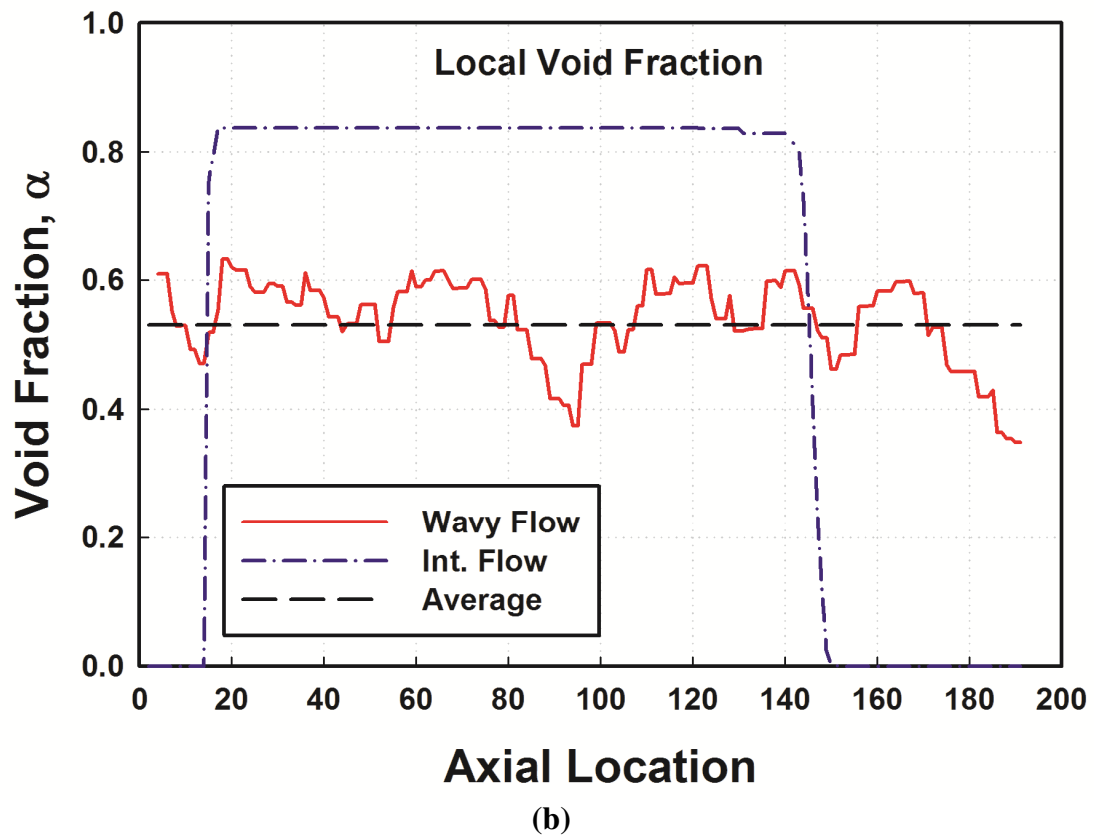
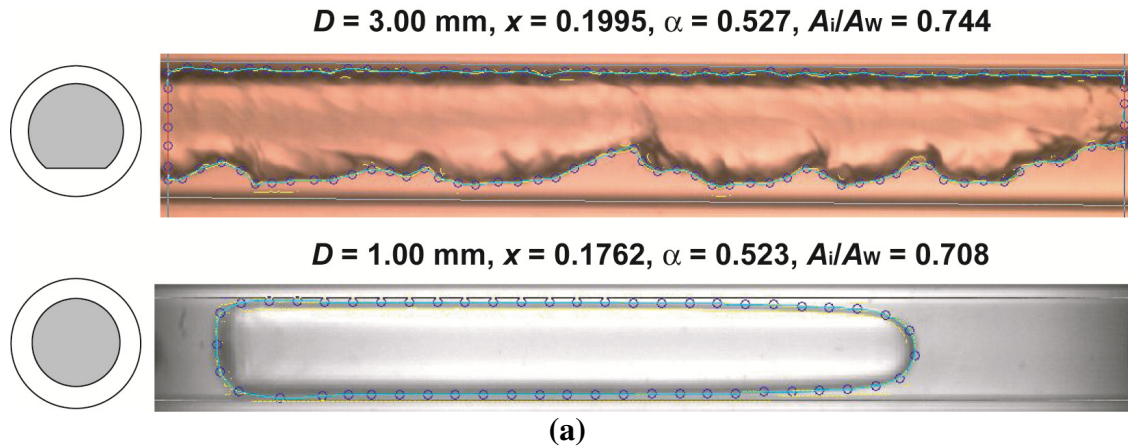


Figure 6.3: Comparison of Vapor-Liquid Distribution on a (a) Frame and (b) Local Basis for $T_{\text{sat}} = 30^\circ\text{C}, G = 200 \text{ kg m}^{-2} \text{ s}^{-1}$

the area of the vapor-liquid interface along the tube varies significantly. The vapor core in the wavy flow case extends the entire length of the tube $L_i/L = 1$, whereas in the intermittent flow case, this ratio is $L_i/L = 0.7$. Some of the interfacial area in the intermittent case is located on the nose and tail of the vapor bubble. The different interfacial area ratios in these cases, in conjunction with the respective phase velocities,

determine pressure drop and heat transfer. The local void fraction for each of these frames is shown in Figure 6.3(b). Despite the bulk void fraction averages being approximately the same, it is clear that the local void fraction distribution differs substantially. These different distributions correspond to different vapor-liquid transport mechanisms and also different velocity profiles within each phase. Combinations of liquid film thickness (thin in the case of intermittent flow, thick in the case of stratified flow), the velocities within these phases, and the interfacial shear determine the respective pressure drop and heat transfer phenomena. While thick films typically indicate larger resistances, the velocity field and the local interfacial shear, and the changing film thickness could induce additional mixing in the film, affecting local pressure drop and heat transfer. In intermittent flows, even at the same overall void fraction, the pressure drop and heat transfer would be determined by the low resistances in the thin-film bubble regions, combined with the higher resistances in the liquid slug region. Knowledge of these phase distributions based on the detailed void fraction measurements presented here assists in the accounting of the locally varying transport processes and their respective resistances.

A summary of the quality change, uncertainty associated with experimentally measured quality (Equation 5.15), repeatability of the analysis (Section 5.3.2) and total void fraction uncertainty is displayed in Table 6.5. The average uncertainty of all measured void fraction data is 10.3%. In general, quality changes increase with increasing saturation temperature because of the decrease in latent heat, i_{fg} , and the increase in heat losses. This is shown in Figure 6.4(a). The total average uncertainty for each data point is plotted in Figure 6.4(b). The uncertainty in measured void fraction is highest at low qualities. This is a result of the large effect that experimental uncertainty in quality has on void fraction measurement (Equation 5.15.) The uncertainty in measured void fraction also increases at high qualities. At high qualities, the liquid film becomes thinner

Table 6.5: Average Quality Changes, Uncertainties in Void Fraction due to Measurement of Quality, Repeatability and Total Average Uncertainty in Void Fraction Data

D , mm	Δx	$U_{x,exp}$ (%)	U_{rep} (%)	U_{tot} (%)
3.00	0.08	9.0	4.5	11.2
1.00	0.20	1.0	9.2	9.4
0.508	0.21	2.0	8.7	9.0
Total	0.14	5.5	6.6	10.3

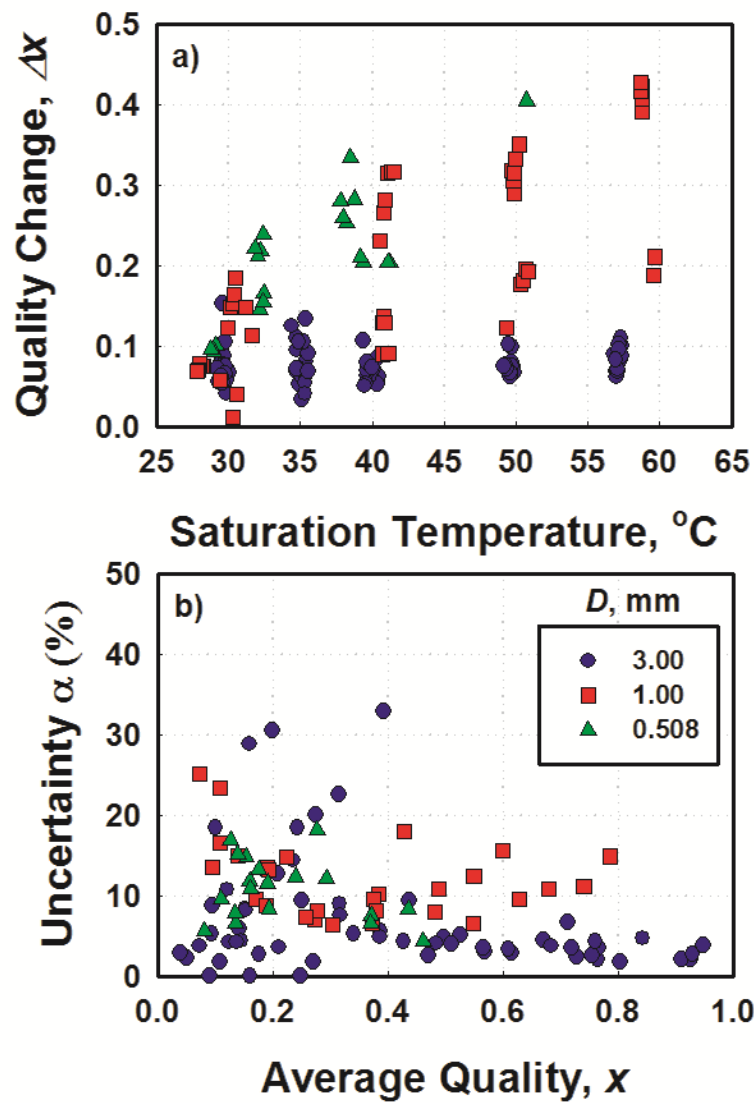


Figure 6.4: (a) Quality Change, and (b) Uncertainties in Void Fraction Measurements

and the repeatability analysis discussed in Section 5.3.2 increases in importance. The standard deviation at high qualities increases, resulting in an increase in overall uncertainty.

6.1.3 Pressure Drop

Condensation pressure drop data were obtained during visualization for tube diameters 0.508, 1.00 and 3.00 mm. However, uncertainties in pressure drop measurements for the 3.00 mm diameter tubes were unsatisfactory due to large pressure losses at the inlets and outlets of the test section headers. Therefore, the pressure drop measurements from the heat transfer experiments conducted on the 3.05 mm diameter tube are presented here. The pressure drop results from this study are displayed in Figure 6.5. Following a discussion of the trends in the data, a summary of the contributions of each pressure drop component to the total pressure drop is presented.

The influence of mass flux on pressure drop is shown in Figure 6.6(a) for a representative case with $D = 1.00$ mm and $T_{\text{sat}} = 30^\circ\text{C}$. As expected, increasing mass flux increases the pressure drop. At $x = 0.45$, for example, the pressure drop increases almost eight-fold for a four-fold increase in mass flux from $200 \text{ kg m}^{-2} \text{ s}^{-1}$ to $800 \text{ kg m}^{-2} \text{ s}^{-1}$. The frictional pressure drop also increases with increasing quality. The effect of quality on pressure drop is greater at the higher mass fluxes. At $G = 800 \text{ kg m}^{-2} \text{ s}^{-1}$, as x changes from 0.10 to 0.8, the pressure drop increases by almost a factor of four, while at $G = 200 \text{ kg m}^{-2} \text{ s}^{-1}$, the increase is less than a factor of two. For reference, the void fraction for $G = 200 \text{ kg m}^{-2} \text{ s}^{-1}$ at $x = 0.0897$ is 0.503, and increases to 0.812 at $x = 0.7985$. For $G = 800 \text{ kg m}^{-2} \text{ s}^{-1}$ and $x = 0.098$, the void fraction is 0.42, while at $x = 0.811$ at this mass flux, it was not possible to measure the void fraction due to the flow being in the mist flow regime. The larger increase in pressure drop at the higher mass flux is due to a combination of the

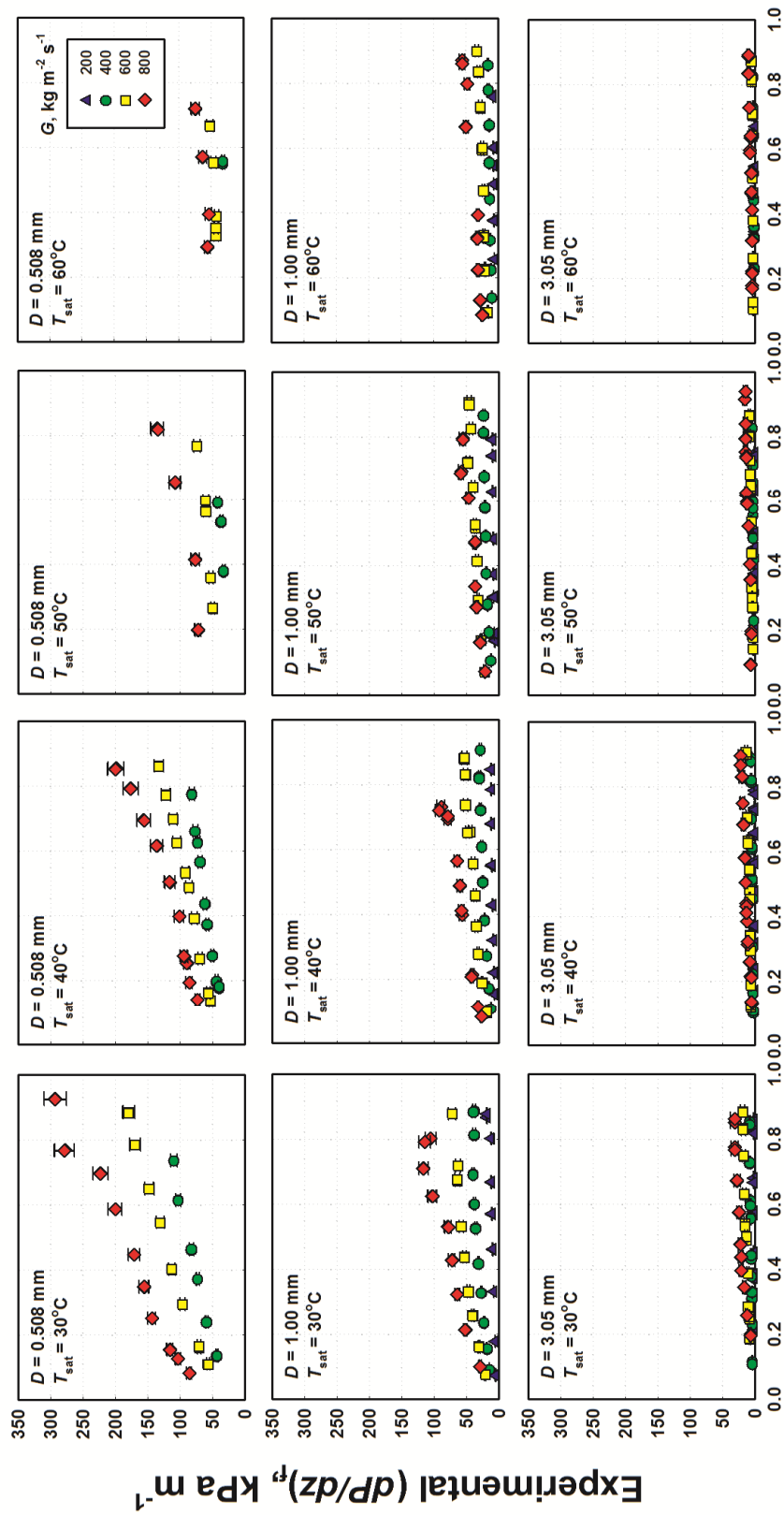


Figure 6.5: Frictional Pressure Drop versus Quality, x

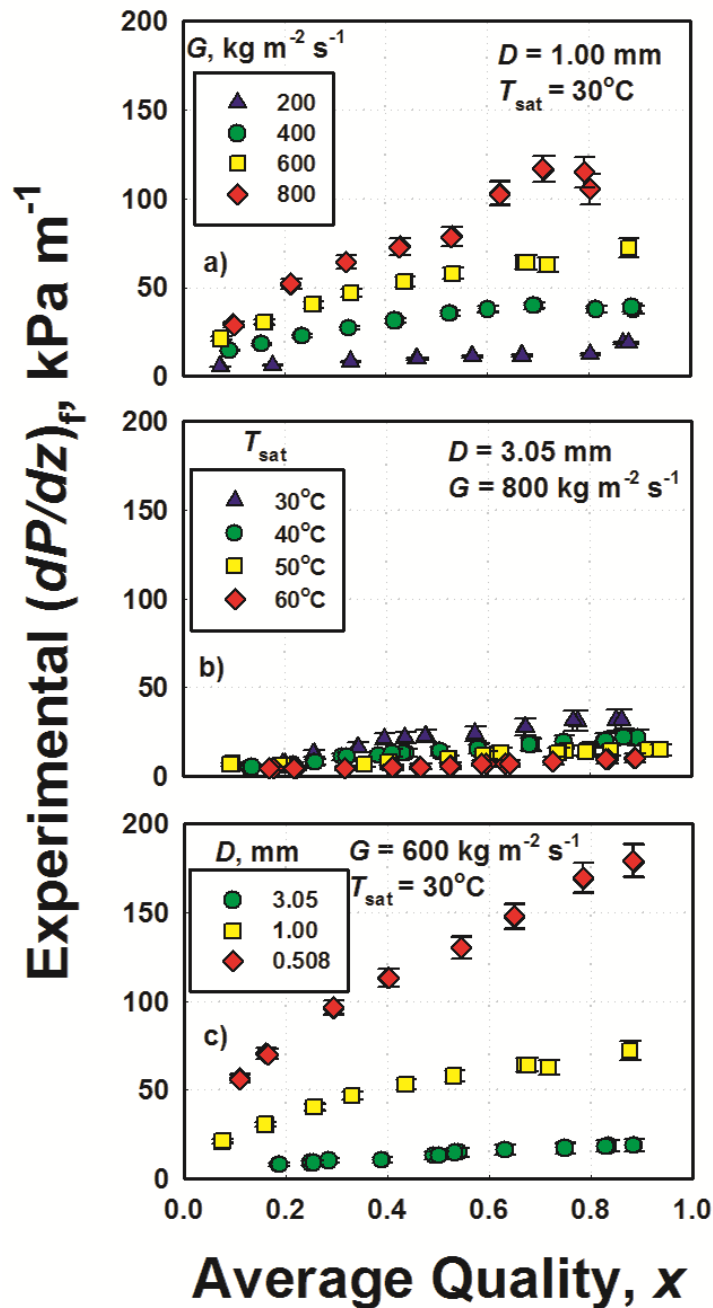


Figure 6.6: Experimental Pressure Drop versus Quality for (a) Increasing Mass Flux, (b) Increasing Saturation Temperature, and (c) Increasing Diameter

higher overall velocities, the increased shear between the two phases, and the drag induced by the droplets in the mist flow mode at the higher quality.

Figure 6.6(b) shows the influence of saturation temperature on pressure drop for a representative case with $D = 3.05$ mm and $G = 800$ kg m⁻² s⁻¹. As the saturation temperature increases, the pressure drop decreases at the same mass flux and quality. For example, as saturation temperature increases from 30 to 60°C at $x = 0.6$, the pressure drop decreases from 25 to 8 kPa m⁻¹. The decrease in pressure drop is a result of a decrease in the difference between individual phase properties, which in turn leads to lower shear. Figure 6.6(c) shows the effects of hydraulic diameter on pressure drop for a representative case with $T_{\text{sat}} = 30^\circ\text{C}$ and $G = 600$ kg m⁻² s⁻¹. As expected, the pressure drop increases as hydraulic diameter decreases, keeping mass flux constant. As tube diameter decreases from 3.05 to 0.508 mm at $x = 0.4$, the pressure gradient increases from 10 to 109 kPa m⁻¹.

A summary of the individual pressure drop contributions of the frictional, deceleration, and end effects ($\Delta P_{\text{endeffects}} = \Delta P_{\text{contraction}} - \Delta P_{\text{expansion}}$) to the measured pressure drop is presented in Table 6.6. The values are presented as averages over all mass fluxes and qualities for a given tube diameter and saturation temperature. In general, the contributions of deceleration and end effects increase with decreasing mass flux and decreasing quality. The deceleration component increases with decreasing quality because higher quality changes, Δx , must be achieved to maintain reasonable heat duties. The change in quality versus test saturation temperature is plotted in Figure 6.7(a) to display this trend. The significance of the end effects increases as a result of lower frictional pressure drops experienced in the test section at low mass fluxes and qualities. It was important to maintain high percentages of the frictional contributions to maintain acceptable accuracies. A conservative 50% uncertainty is applied to the predictions of $\Delta P_{\text{deceleration}}$, $\Delta P_{\text{contraction}}$, and $\Delta P_{\text{expansion}}$ when estimating the uncertainty in the frictional pressure drop. These components become more substantial as saturation temperature is increased because the frictional pressure drop decreases. This is presented in Figure

Table 6.6 Relative Pressure Drop Contributions and Uncertainties

D , mm	T_{sat} (°C)	p_r	$\frac{\Delta P_f}{\Delta P_{\text{measured}}} (\%)$	$\frac{\Delta P_{\text{deceleration}}}{\Delta P_{\text{measured}}} (\%)$	$\frac{\Delta P_{\text{endeffects}}}{\Delta P_{\text{measured}}} (\%)$	$\frac{U_{\Delta P_f}}{\Delta P_{\text{measured}}} (\%)$
3.05	30	0.38	92.4	13.1	20.7	16.6
	40	0.49	88.7	9.8	21.1	18.0
	50	0.62	87.9	13.5	25.5	22.4
	60	0.77	86.6	16.7	30.1	27.5
1.00	30	0.38	92.8	1.5	8.7	4.9
	40	0.49	93.0	2.2	9.2	5.3
	50	0.62	93.4	2.9	9.5	5.5
	60	0.77	92.0	3.8	11.8	7.0
0.508	30	0.38	94.8	1.7	6.9	4.5
	40	0.49	94.2	2.7	8.5	5.5
	50	0.62	94.2	4.6	10.4	6.8
	60	0.77	93.5	6.3	12.8	8.5
Average	All		91.5	7.1	23.8	12.0

6.7(b), where the contribution of the frictional pressure drop to the measured pressure drop decreases with increasing saturation temperature. As a result, the uncertainty in frictional component of the measured pressure drop increases. Overall, the average uncertainty in ΔP_f for all tube diameters is 12.0% and ranged from 2.69 to 39.48%. The highest uncertainty is in the 3.05 mm test section, where the frictional pressure drop component is the lowest. Uncertainties in the smaller test sections are much lower as a result of increased frictional pressure gradient with decreasing tube diameter.

6.1.4 Heat Transfer

The local heat transfer measurements for each data point are shown in Figure 6.8. The major trends in the data are presented first, followed by discussion of the measured heat transfer coefficients.

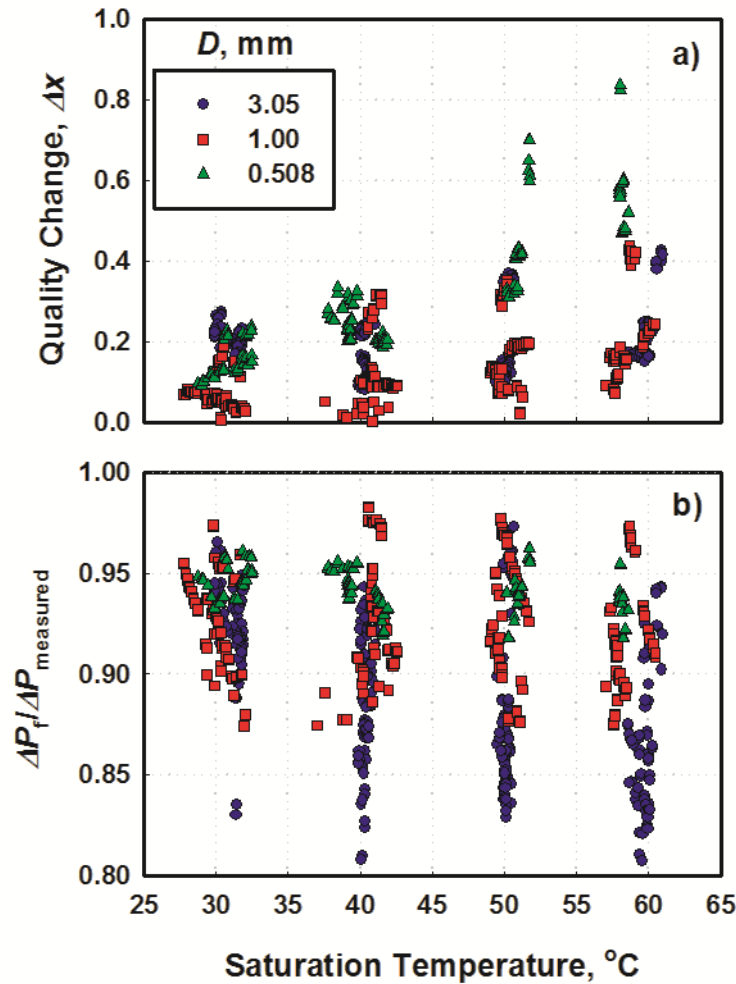
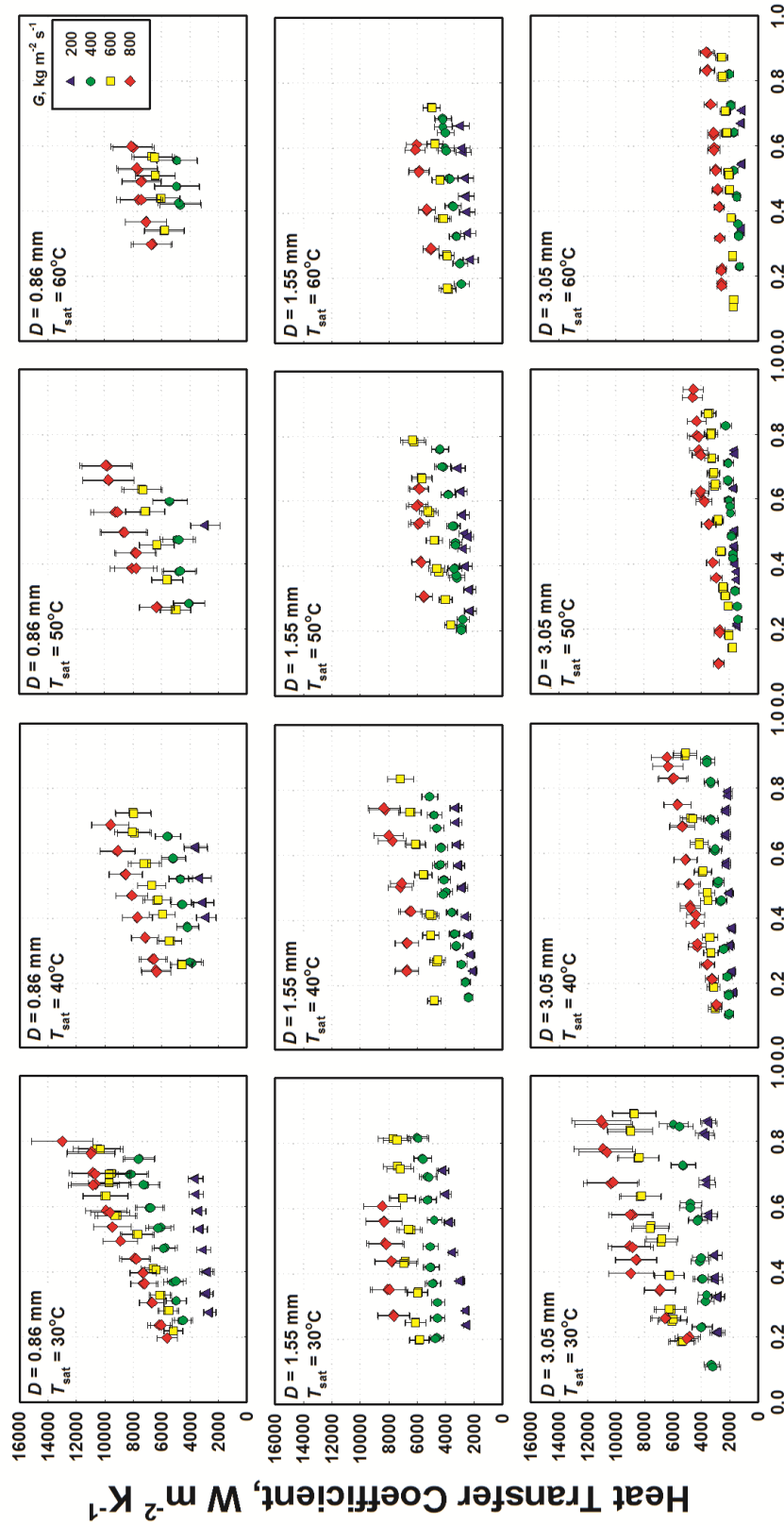


Figure 6.7: (a) Quality Change , and (b) Ratio of Friction Pressure Drop to Measured Pressure Drop

The heat transfer data follow trends similar to those observed in the pressure drop data. An increase in mass flux, G , and quality, x , results in an increase in heat transfer coefficient. This is displayed in Figure 6.9(a). For example, a four-fold increase in mass flux at $x = 0.53$ from 201 to 824 kg m⁻² s⁻¹ results in a measured heat transfer coefficient increase from 3300 to 9460 W m⁻² K⁻¹. Measured heat transfer coefficient also increases with decreasing tube diameter, as shown in Figure 6.9(c). At this high mass flux, annular flow is expected through most of the condensation process and the difference in measured heat transfer coefficient is less pronounced because the film thickness does not

change significantly. For example, the predicted film thickness for $D = 1.55$ mm, $T_{\text{sat}} = 40^\circ\text{C}$, $x = 0.70$, and $G = 600$ kg m⁻² s⁻¹ is $\delta = 0.0809$ mm, while the film thickness for the same T_{sat} and x at $G = 800$ kg m⁻² s⁻¹ is $\delta = 0.0817$ mm. As saturation temperature is increased, the measured heat transfer coefficient decreases as displayed in Figure 6.9(b). As saturation temperatures increase, the critical pressure is approached, resulting in a decrease in property differences between the phases and the latent heat. For example, the ratio of densities and latent heat at $T_{\text{sat}} = 30^\circ\text{C}$ is 18.6 and 132.9 kJ kg⁻¹, and decreases to 4.8 and 80.19 kJ kg⁻¹, respectively, at $T_{\text{sat}} = 60^\circ\text{C}$ for R404A. The difference in vapor and liquid velocities therefore decreases, reducing the interfacial shear, which results in lower heat transfer coefficients in the shear driven region. Similarly, as saturation temperature increases, the surface tension decreases significantly. The surface tension at $T_{\text{sat}} = 30^\circ\text{C}$ is $\sigma = 3.5 \times 10^{-3}$ N m⁻¹ and decreases to 1×10^{-3} N m⁻¹ at $T_{\text{sat}} = 60^\circ\text{C}$. Surface tension can influence flow regime and the corresponding phase distributions. For example, in Figure 6.9(b), there is a significant decrease in measured heat transfer coefficient from $T_{\text{sat}} = 30$ to 60°C . At a quality of $x = 0.63$, the measured heat transfer coefficient at $T_{\text{sat}} = 30^\circ\text{C}$ is $h = 8304$ W m⁻² K⁻¹, which is double the heat transfer coefficient at $T_{\text{sat}} = 60^\circ\text{C}$, $h = 4132$ W m⁻² K⁻¹. Such a large increase in heat transfer coefficient is not only explained by the change in transport properties, but also based on the flow regime expected under such conditions. At $T_{\text{sat}} = 30^\circ\text{C}$, the flow is in the annular regime and at $T_{\text{sat}} = 60^\circ\text{C}$, it is in the wavy regime based on the transition criteria of Nema (2007) where heat transfer coefficients are expected to be lower. In the wavy flow regime, the latent heat, i_{fg} , and specific heats of the respective phases are important in determining heat transfer. As saturation temperature increases, the latent heat decreases from 132.9 kJ kg⁻¹ at $T_{\text{sat}} = 30^\circ\text{C}$ to 80.19 kJ kg⁻¹ at $T_{\text{sat}} = 60^\circ\text{C}$. The specific heats of the two phases both increase from $c_{\text{p,l}} = 1.601$ kJ kg⁻¹ K⁻¹ and $c_{\text{p,v}} = 1.307$ kJ kg⁻¹ K⁻¹ at $T_{\text{sat}} = 30^\circ\text{C}$ to $c_{\text{p,l}} = 2.584$ kJ kg⁻¹ K⁻¹ and $c_{\text{p,v}} = 2.853$ kJ kg⁻¹ K⁻¹ at $T_{\text{sat}} = 60^\circ\text{C}$. At lower reduced pressures, the change in saturation temperature has a large effect on heat



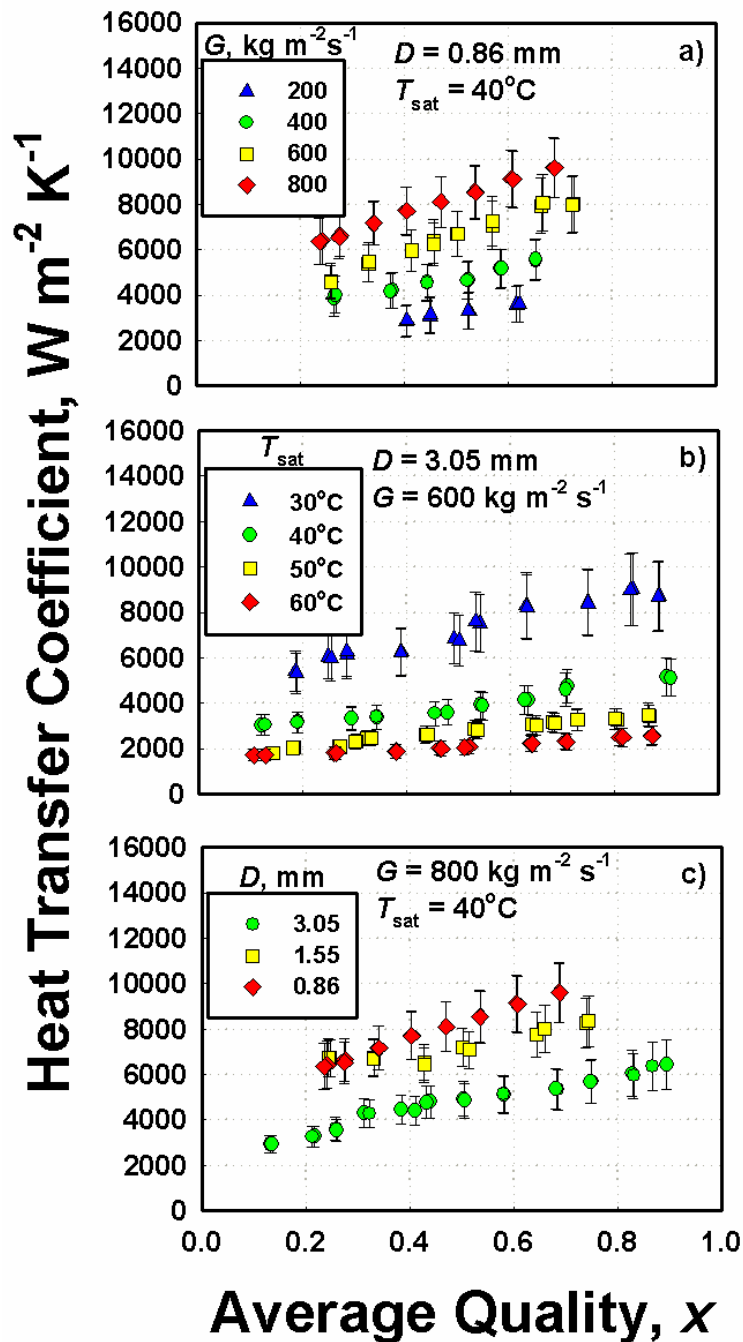


Figure 6.9: Experimental Heat Transfer Coefficient versus Quality for (a) Increasing Mass Flux, (b) Increasing Saturation Temperature, and (c) Increasing Diameter

transfer coefficient signifying that the decrease in latent heat is more important. At high reduced pressures, the same change in saturation temperature results in very small changes in measured heat transfer coefficient signifying that the decrease in latent heat is

offset by the increase in specific heat. Shear forces and surface tension are expected to have lower influences on condensation in the wavy flow regime, thereby decreasing the effect of changes in phase densities and surface tension as reduced pressure is changed.

A summary of the averages and standard deviations of resistance ratios, quality changes and uncertainties in measured heat transfer coefficients is presented in Table 6.7. The average values are based on the data for all qualities and mass fluxes. In general, resistance ratio and uncertainty increase with decreasing mass flux and quality. Quality change increases with decreasing mass flux and tube diameter to maintain test section heat duties large enough for accurate heat transfer coefficient measurements. This trend is shown in Figure 6.10(a). While it was desirable to take data at quality changes less than 0.20, it was not possible to achieve acceptable uncertainties in heat transfer coefficient measurements with the lower test section heat duties at these small

Table 6.7: Average Resistance Ratio, Quality Change and Uncertainty in h_r

D , mm	T_{sat}	p_r	$R_{ratio} \pm STD$	$\Delta x \pm STD$	$\frac{U_{h_r}}{h_r} \pm STD$
3.05	30	0.38	2.8 ± 0.6	0.20 ± 0.03	16.7 ± 0.8
	40	0.49	3.7 ± 0.9	0.14 ± 0.05	14.6 ± 1.2
	50	0.62	5.0 ± 1.6	0.17 ± 0.09	14.2 ± 1.6
	60	0.77	5.0 ± 1.6	0.21 ± 0.08	14.4 ± 1.0
1.55	30	0.38	5.8 ± 2.4	0.30 ± 0.05	11.6 ± 2.0
	40	0.49	8.0 ± 3.0	0.30 ± 0.05	11.7 ± 1.0
	50	0.62	8.8 ± 2.9	0.35 ± 0.04	13.7 ± 2.3
	60	0.77	9.5 ± 2.9	0.42 ± 0.06	16.0 ± 3.9
0.86	30	0.38	7.5 ± 3.5	0.34 ± 0.07	14.3 ± 1.2
	40	0.49	8.4 ± 3.1	0.44 ± 0.08	16.8 ± 3.5
	50	0.62	8.2 ± 3.0	0.50 ± 0.08	21.3 ± 4.4
	60	0.77	7.9 ± 1.5	0.63 ± 0.05	23.0 ± 4.8
All	Average		6.4 ± 3.2	0.30 ± 0.14	15.0 ± 3.5
	Range		1.7-16.8	0.08-0.74	8.3-35.1

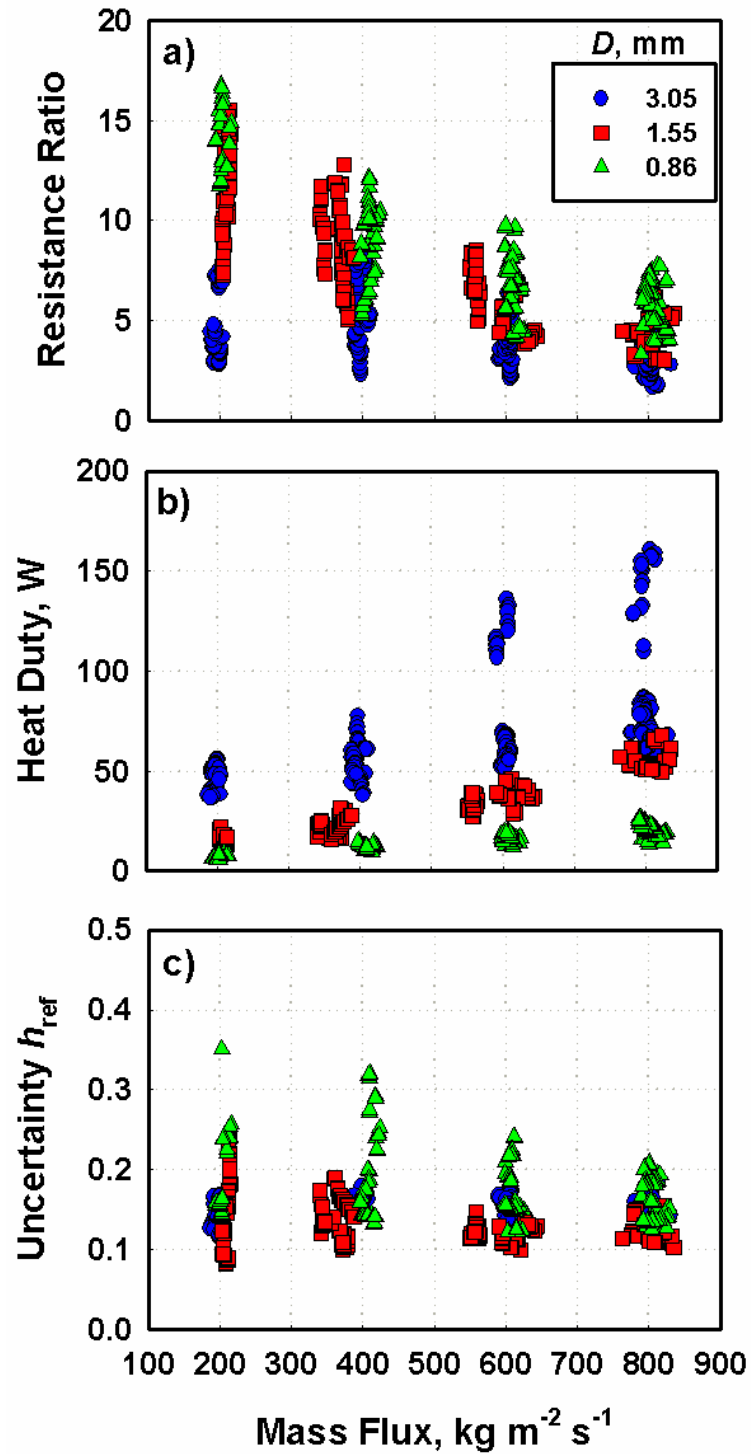


Figure 6.10: (a) Resistance Ratio, (b) Test Section Heat Duty, and (c) Uncertainty in h_r , for Heat Transfer Experiments versus Mass Flux

condensation rates. Similarly, at higher saturation temperatures, the latent heat decreases, requiring larger quality changes to maintain desired heat duties. The only exception to this trend is for the data taken at $T_{\text{sat}} = 30^{\circ}\text{C}$ and $D = 3.05$ mm. Resistance ratios in this range were low because of high refrigerant heat transfer coefficients. Higher resistance ratios were achieved by increasing the primary coolant loop velocity. This resulted in an increase in heat addition from the pump. The test section heat duty was increased in an effort to minimize the sensitivity to pump heat additions. This led to increased accuracy in measured heat transfer coefficient at the cost of larger test section quality changes.

The average uncertainty for all measured heat transfer coefficients is 15.0%. Test section heat duties and heat transfer coefficient uncertainties as a function of mass flux are displayed in Figures 6.10(b-c). The largest uncertainties are at the highest saturation temperatures for the smallest tube diameter particularly at the low mass fluxes and low qualities. Heat duties for these experiments are smaller as a result of decreased mass flow rate, and therefore, heat losses from the facility can become significant.

6.2 Comparison with Literature

The results from this study on flow regime transitions, void fraction, pressure drop and heat transfer coefficients are compared with relevant models from the literature here. There are currently no flow regime maps or void fraction models for refrigerants at the high reduced pressures and small channel diameters under consideration here. Therefore, results from the literature for fluids, operating conditions, and channel diameters closet to those studied here were used as the basis for comparison. The comparisons are made using the average deviation (AD,) and absolute average deviation (AAD,) which are defined as:

$$AD = \frac{1}{n} \sum_{i=1}^n \left(\frac{X_{\text{model}} - X_{\text{exp}}}{X_{\text{exp}}} \times 100 \right) \quad (6.1)$$

$$AAD = \frac{1}{n} \sum_{i=1}^n \left(\frac{|X_{\text{model}} - X_{\text{exp}}|}{X_{\text{exp}}} \times 100 \right) \quad (6.2)$$

The AD provides an indication of whether the model under-predicts or over-predicts the data. The AAD indicates the deviations of the data from the model.

6.2.1 Flow Regimes

A comparison of the flow regimes observed in this study with several relevant flow regime maps from the literature is presented in this section. Agreement of the observed flow regimes from the present study with the transitions from the literature is shown graphically, and the percentage of data predicted correctly by a particular flow regime map is also reported.

Taitel and Dukler (1976) developed a comprehensive flow regime map based on physical interpretations of the transition phenomena. They developed non-dimensional transitional criteria for annular-dispersed, stratified wavy, stratified smooth, intermittent and dispersed bubble flow. The only transition criterion applicable for data obtained in this study is that for the transition from annular to intermittent flow. They found that the transition from annular to intermittent flow occurred for a constant Martinelli Parameter, $X = 1.6$. This corresponds to a constant quality value for each saturation temperature and is independent of tube diameter and mass flux. On the other hand, in the present study, the transition to intermittent flow was observed to be influenced by both mass flux and tube diameter. This is most likely a result of the increased significance of surface tension forces whereas the basis of the Taitel and Dukler (1976) criterion was the stratified liquid level increasing to the point where liquid waves could overcome gravity and bridge the

Table 6.8: Comparison of Observed Flow Regimes and Flow Regimes Predicted by the Taitel and Dukler (1976) Flow Regime Map

Observed Regime	Predicted Regime				
	Dispersed Bubble	Intermittent	Stratified-Smooth	Stratified-Wavy	Annular-Dispersed
Intermittent	0.0%	80.4%	0.0%	0.0%	19.6%
Transitional	0.0%	14.3%	0.0%	0.0%	85.7%
Wavy	0.0%	18.4%	0.0%	0.0%	81.6%
Annular	0.0%	0.0%	0.0%	0.0%	100.0%
Mist	0.0%	0.0%	0.0%	0.0%	100.0%

Note: The table summarizes the amount of data predicted by the flow regime map for each observed flow regime. Each row sums to 100% for the observed regime. Green cells signify correct predictions and white cells are incorrectly predicted regimes.

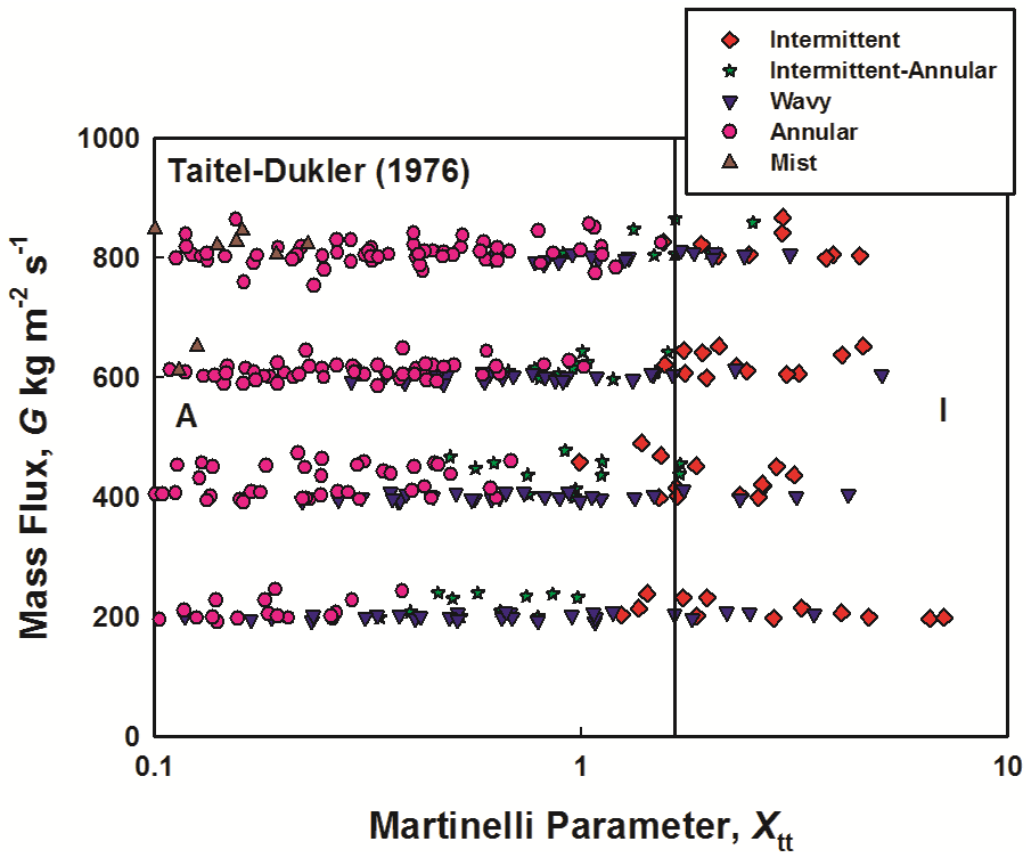


Figure 6.11: Data from the Present Study Plotted on the Taitel and Dukler (1976) Flow Regime Map

vapor gap. While this idealization may describe the phenomena in large diameter tubes, it is clear that it does not provide a physical representation of what is observed in microchannels. Therefore, several intermittent data are predicted by their criteria as annular and vice versa. A summary of the comparison between the regimes predicted by their criteria and the data from the present study is presented in Table 6.8. For these data, the only flow regimes predicted by the Taitel and Dukler (1976) map are the intermittent or annular disperse regimes as shown in Figure 6.11. While the criterion for transition to intermittent flow does a reasonable job (80.4%) of predicting the intermittent regime, it is not physically consistent with the observations on the influence of diameter and mass flux in the present study. At small tube diameters, the transition is most likely due to a balance between inertial and surface tension forces rather than gravity forces as was theorized by Taitel and Dukler (1976). The transitional (85.7%), wavy (81.6%), and mist (100%) flow regime data from this study are mostly predicted to be in the annular-disperse region. This is most probably a result of some subjectivity in visually evaluating the images. Perhaps the annular-disperse regime could be further classified into the regimes such as mist flow observed here, which would increase the accuracy of the flow map.

Tandon *et al.* (1982) developed a flow regime map based on data from previous researchers on condensing R12 and R113 in tube diameters ranging from 4.8 to 15.9 mm. They observed five different flow regimes: spray (S), annular and semi-annular (A), wavy (W), slug (I) and plug (P). They developed transition criteria based on the dimensionless vapor velocity, J_G^* , and a volumetric liquid-to-vapor ratio $(1-\alpha)/\alpha$. They approximated the void fraction using the Smith (1969) correlation, which was developed based on boiling water and air-water experiments. The flow regimes were divided using constant values of the two parameters and are summarized below.

Spray:

$$\begin{aligned} J_G^* &> 6.0 \\ (1-\alpha)/\alpha &> 0.5 \end{aligned} \quad (6.3)$$

Annular and Semi-annular:

$$\begin{aligned} 1.0 < J_G^* &\leq 6.0 \\ (1-\alpha)/\alpha &< 0.5 \end{aligned} \quad (6.4)$$

Wavy:

$$\begin{aligned} J_G^* &< 1.0 \\ (1-\alpha)/\alpha &< 0.5 \end{aligned} \quad (6.5)$$

Slug:

$$\begin{aligned} 0.1 < J_G^* &\leq 0.5 \\ (1-\alpha)/\alpha &> 0.5 \end{aligned} \quad (6.6)$$

Plug:

$$\begin{aligned} J_G^* &< 0.1 \\ (1-\alpha)/\alpha &> 0.5 \end{aligned} \quad (6.7)$$

The approach by Tandon *et al.* (1982) results in horizontal and vertical transition lines when plotted on a J_G^* vs. $(1-\alpha)/\alpha$ plot. However, there is an undefined region on their flow regime map when $J_G^* > 0.5$ and $(1-\alpha)/\alpha < 0.5$. Tandon *et al.* only observed a few data points in this undefined region, which is most probably because their criteria were developed for large tube diameters. In the present study, there are several data points that were in this undefined region. In large tube diameters, there is no direct transition from annular to intermittent flow, which might explain their not defining this zone. Overall, this flow regime map does not predict the observed flow regimes well, as shown in Figure 6.12 and summarized in Table 6.9. Almost all (87.0%) of the intermittent flow data from the present study are predicted to be in this region that they do not define. Transition to Spray flow is also poorly predicted, which is seen in the prediction of spray

Table 6.9: Comparison of Observed Flow Regimes to Flow Regimes Predicted by the Tandon *et al.* (1982) Flow Regime Map

Observed Regime	Predicted Regime					
	Not Defined	Plug (P)	Slug (I)	Wavy (W)	Annular /Semi-annular (A)	Spray (S)
Intermittent	87.0%	0.0%	10.9%	0.0%	2.2%	0.0%
Transitional	45.2%	0.0%	0.0%	0.0%	31.0%	23.8%
Wavy	37.8%	0.0%	1.0%	0.0%	58.2%	3.1%
Annular	5.4%	0.0%	0.0%	0.0%	19.2%	75.4%
Mist	0.0%	0.0%	0.0%	0.0%	0.0%	100.0%

Note: The table summarizes the amount of data predicted by the flow regime map for each observed flow regime. Each row sums to 100% for the observed regime. Green cells signify correct predictions and white cells are incorrectly predicted regimes.

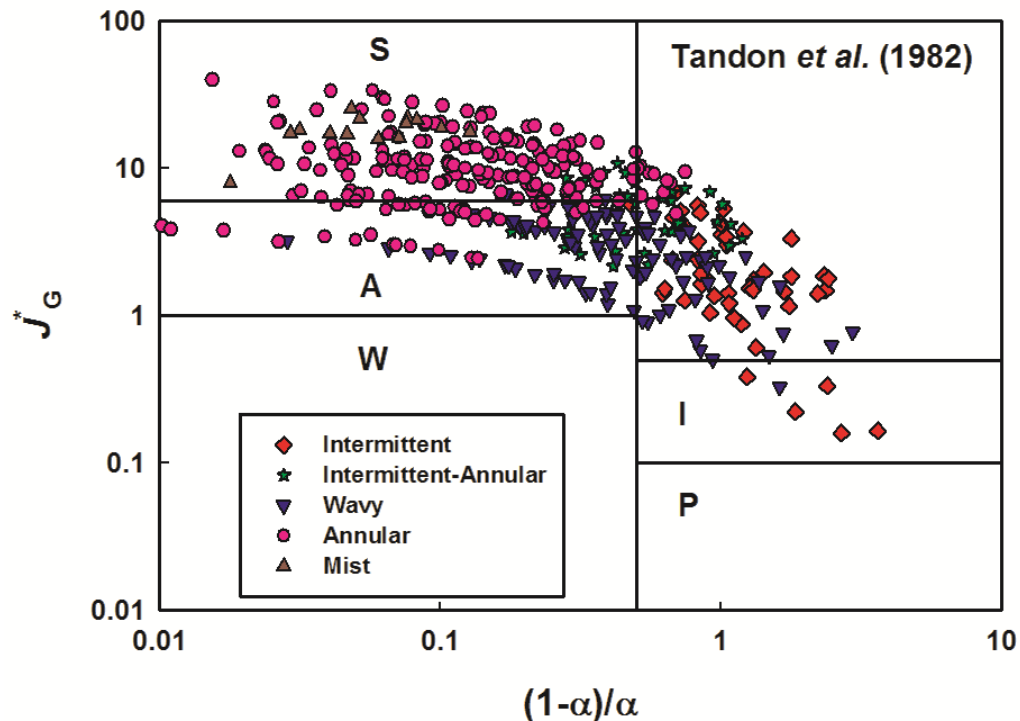


Figure 6.12: Data from the Present Study Plotted on the Tandon *et al.* (1982) Flow Regime Map

flow (75.4%) when the data from the present study are in annular flow.

Cavallini *et al.* (2002) developed a flow regime map based on data from a variety of sources from the literature on condensing flows. They predicted that annular flow should always exist when the dimensionless vapor velocity, $J_G^* = x G [g D \rho_v(\rho_l - \rho_v)]^{-0.5}$, is greater than 2.5. When the dimensionless vapor velocity is less than this value, they stated that the flow is either annular-stratified and stratified when $X_{tt} < 1.6$, or stratified-slug and slug flow when $X_{tt} > 1.6$. The stated applicability of these criteria is for $p_r < 0.75$, and $3 < D < 21$ mm. A comparison between the data from the present study and this transition criterion is shown in Figure 6.13 and summarized in Table 6.10. Agreement between the observed flow regimes and the predictions from this map is reasonable, with excellent prediction of annular flow (99% of annular data observed, and 95.2% of transitional data observed are accurately predicted in the annular regime by this map.) The flow regime map of Cavallini *et al.* (2002) does not explicitly differentiate between mist and annular flow and 100% of mist flow data from this study were predicted to be in annular flow. Their criteria do not predict wavy and intermittent flow regime data from this study well. The annular-stratified regime was only observed in the 3.00 mm tube in this study, and the Cavallini *et al.* (2002) map consistently predicts these data to be in annular flow. The reason for the discrepancy may be associated with the subjectivity in defining the difference between the annular and annular-stratified regime. The transition to intermittent flow is also not predicted well. At large tube diameters, their transition criterion is defined based on the critical Martinelli Parameter, X_{tt} . The transition to intermittent flow was observed in the present study to be influenced by tube diameter and mass flux, whereas the Martinelli Parameter, X_{tt} , is a function of phase densities, viscosities and quality. Therefore, this criterion does not vary with decreasing tube diameter or decreasing mass flux and is constant for a given saturation temperature. As tube diameter decreases, the transition criteria to intermittent flow are increasingly

Table 6.10: Comparison of Observed Flow Regimes to Flow Regimes Predicted by the Cavallini *et al.* (2002) Flow Regime Map

Regime	Predicted Regime		
	Stratified-Slug (SS)	Annular-Stratified (SA)	Annular (A)
Intermittent	58.7%	8.7%	32.6%
Transitional	0.0%	4.8%	95.2%
Wavy	16.3%	30.6%	53.1%
Annular	0.0%	1.0%	99.0%
Mist	0.0%	0.0%	100.0%

Note: The table summarizes the amount of data predicted by the flow regime map for each observed flow regime. Each row sums to 100% for the observed regime. Green cells signify correct predictions and white cells are incorrectly predicted regimes.

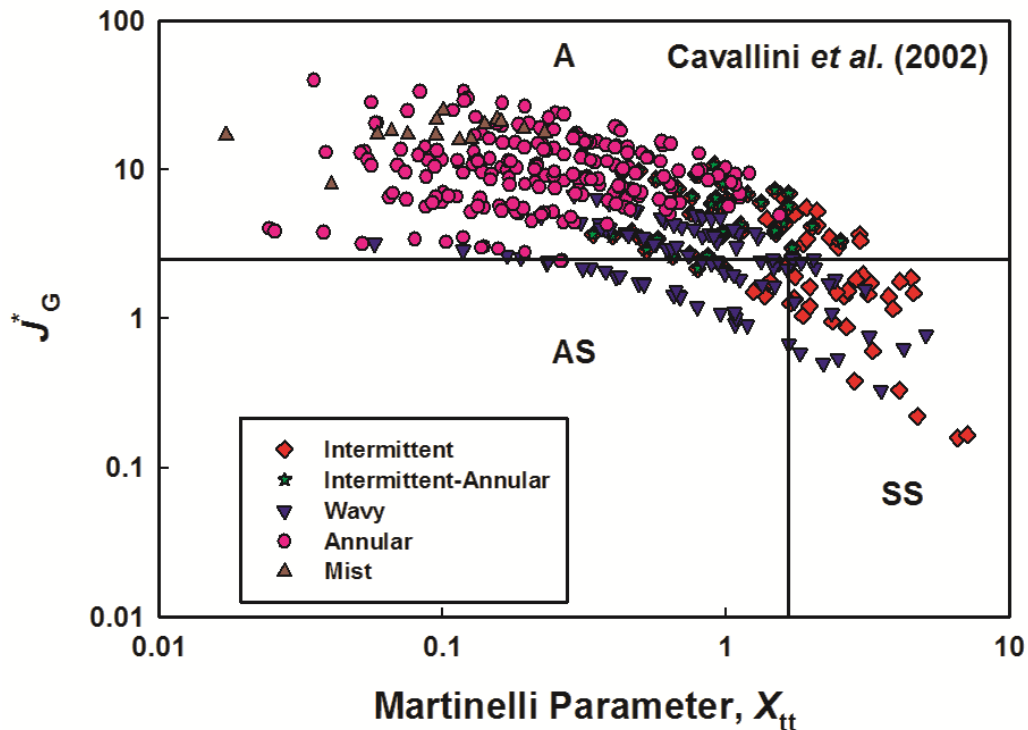


Figure 6.13: Data from the Present Study plotted on Cavallini *et al.* (2002) Flow Regime Map

determined by non-dimensional vapor velocity, J_G^* instead of the Martinelli Parameter, X_{tt} , for R404A. This is observed in Figure 6.13 where the transition from annular to intermittent flow occurs across the constant J_G^* line. Because J_G^* is inversely proportional to $D^{0.5}$, transition to intermittent flow for the same operating parameters but decreased D will be predicted to occur at a lower quality. The trends from the present study are different, however. Griffith and Lee (1964) stated that the ability of surface tension forces to overcome vapor inertial forces and create a liquid bridge within the tube is the physical mechanism for transition to intermittent flow in microchannels. As tube diameter decreases, the surface tension forces increase in importance which results in the increased occurrence of intermittent flow, as seen in the present study. The use of the non-dimensional vapor velocity, J_G^* , does not account for this trend.

Nema (2007) developed non-dimensional transition criteria based on flow visualization work by Coleman and Garimella (2003) on condensing R134a in channel sizes ranging from 1 to 4.91 mm. Nema (2007) developed transition criteria for the intermittent (I), intermittent-annular (IAF), intermittent-discrete wave (IDcW), discrete wave (DcW), disperse wave (DpW), annular (AF), mist (M) and disperse (D) flow regimes. The non-dimensional parameters used for the transition criteria are the vapor Weber number, We_v , the Martinelli Parameter, X_{tt} , the Bond number, Bo , and the modified Froude number, Fr_{mod} . The study differentiated between large diameter tube and microchannel transitions by evaluating the relative magnitudes of the surface tension and gravitational forces. This was accomplished through the use of the Bond number, Bo , as compared to a critical value.

$$Bo = (\rho_l - \rho_v) \cdot g \cdot D^2 \cdot \sigma^{-1} \quad (6.8)$$

$$Bo_{crit} = (\rho_l \cdot [\rho_l - \rho_v]^{-1} - \pi/4) \quad (6.9)$$

For $Bo < Bo_{crit}$, microchannel flow is predicted with only Intermittent, Annular, and Mist flow present. The transition criteria were found to be:

Annular to Intermittent:

$$We_v < 6, X_{tt,slug} < X_{tt} \quad (6.10)$$

where

$$\begin{aligned} We_v &= \rho_v \cdot j_v^2 \cdot D \cdot \sigma^{-1} \\ X_{tt,slug} &= X_{tt0} = 0.3521 \end{aligned} \quad (6.11)$$

Mist to Annular Film

$$We_v > 700, X_{tt} < 0.175 \quad (6.12)$$

For small diameter channel data (1 mm,) it was observed that there was a direct transition from intermittent to annular flow, and no stratified liquid regions. Increased stratification was observed for $Bo > Bo_{crit}$, and additional transitions were required to account for the presence of discrete and disperse wavy flows. The transition criteria to Mist flow remained the same with the following criteria proposed for the existence of a given flow regime.

Intermittent:

$$We_v < 6, X_{tt,slug} < X_{tt} \quad (6.13)$$

where

$$\begin{aligned} X_{tt,slug} &= X_{tt0} + \frac{X_{tt1} \cdot (Bo - Bo_{crit})}{Bo - Bo_{crit} + 5.5} \\ X_{tt1} &= 1.2479 \end{aligned} \quad (6.14)$$

Intermittent/Discrete wave:

$$\begin{aligned} 6 &\leq We_v < 35 \\ X_{tt} &\leq X_{tt,slug} \end{aligned} \quad (6.15)$$

Discrete Wave:

$$\begin{aligned} Fr_{mod} &< 2.75 \\ We_v &\geq 35 \text{ OR } (We_v < 35, X_{tt} \leq X_{tt,slug}) \end{aligned} \quad (6.16)$$

Disperse Wave:

$$Fr_{\text{mod}} \geq 2.75 \quad (6.17)$$

$$We_v \leq 6 + 7 \cdot (Bo - Bo_{\text{crit}})^{1.5}$$

Annular:

$$We_v > 6 + 7 \cdot (Bo - Bo_{\text{crit}})^{1.5} \quad (6.18)$$

The Martinelli Parameter criterion for transition to intermittent flow was modified by Nema (2007) to account for the effects of tube diameter and transitions to the commonly used transition criteria of Taitel and Dukler (1976) in large tubes ($X_{tt} = 1.6$.) The model developed by Nema (2007) predicts flow regime trends the best out of all models considered here. A comparison of this flow regime map with data from the present study is shown in Figure 6.14, with a summary of the agreement with the predictions shown in Table 6.11. The map predicts the Wavy region well, with almost 90% of the data accurately predicted. The transitional regime from intermittent to annular flow in small

Table 6.11: Comparison of Observed Flow Regime to Predicted Flow Regime by the Nema (2007) Flow Regime Map

Observed Regime	Predicted Regime						
	Intermittent (I)	Intermittent-Discrete (ID)	Intermittent-Annular (IAF)	Discrete Wave (DcW)	Disperse Wave (DpW)	Annular (AF)	Mist (M)
Intermittent	17.4%	28.3%	32.6%	13.0%	2.2%	6.5%	0.0%
Transitional	0.0%	2.4%	9.5%	2.4%	4.8%	81.0%	0.0%
Wavy	1.0%	6.1%	0.0%	45.9%	43.9%	3.1%	0.0%
Annular	0.0%	0.0%	0.0%	1.0%	8.9%	68.0%	22.2%
Mist	0.0%	0.0%	0.0%	0.0%	0.0%	13.3%	86.7%

Note: The table summarizes the amount of data predicted by the flow regime map for each observed flow regime. Each row sums to 100% for the observed regime. Green cells signify correct predictions and white cells are incorrectly predicted regimes.

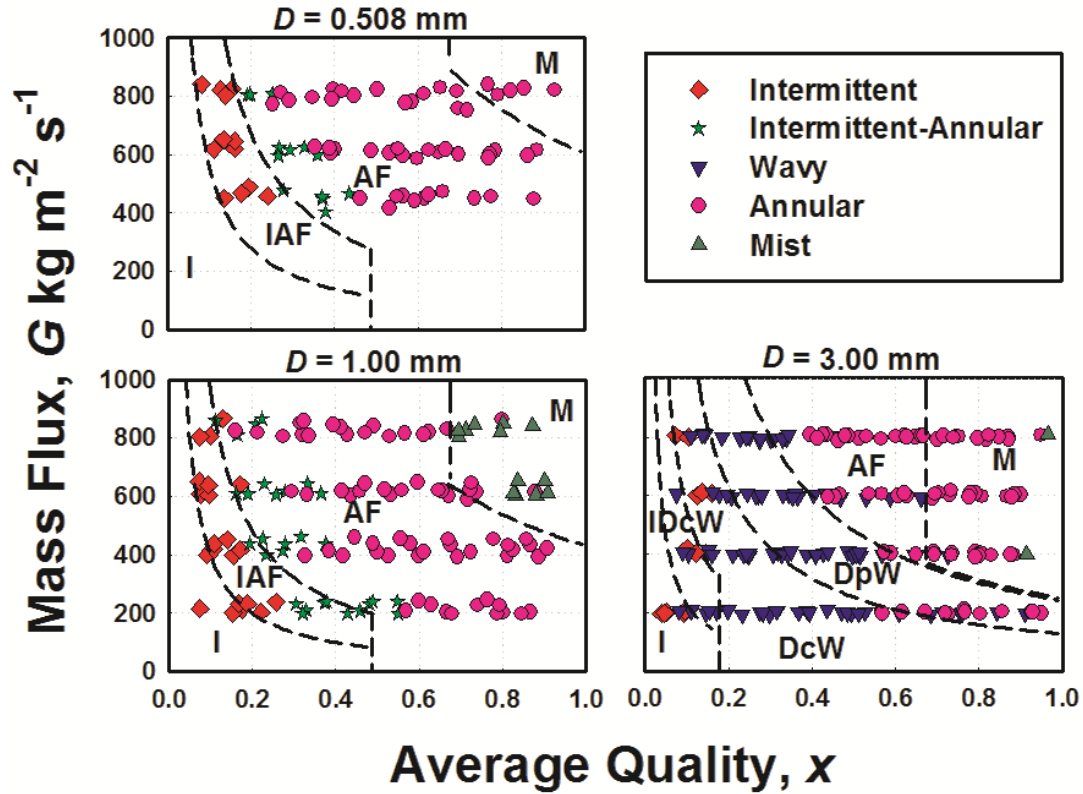


Figure 6.14: Data from the Present Study Plotted on the Nema (2007) Flow Regime Map

channels is predicted to be in the annular regime for 90.5% of the data. The data in mist flow are predicted correctly for 86.7% of the data, but a large percentage (22.2%) of annular flow data is predicted as mist flow. This is attributed to some extent to the difficulty in assigning a flow regime to a data point based on visual interpretation. The transition to intermittent flow using the modified Martinelli parameter, $X_{tt,slug}$, only accounts for the prediction to intermittent flow at very low mass fluxes when $Bo < Bo_{crit}$, and at larger tube diameters where $X_{tt,slug} \rightarrow 1.6$. Prediction of intermittent flow data from the present study by Nema's (2007) model is not very good, with large disagreement for situations in which the flow transitions to the intermittent regime from the annular regime for cases with $Bo < Bo_{crit}$.

6.2.2 Void Fraction

Many void fraction correlations have been developed for large diameter tubes and air-water mixtures flowing through microchannels as discussed in Chapter 2. This section compares the void fraction results obtained in this study with the relevant models from the literature. A summary of these comparisons is presented in Table 6.12. The data are presented by flow regime observed, because of large deviations in the intermittent and transition regions and the negligible effects of tube diameter and mass flux.

The most basic model is the homogeneous void fraction model (Equation 6.19), which assumes that no slip occurs at the interface.

$$\beta = \left[1 + \left(\frac{1-x}{x} \right) \frac{\rho_v}{\rho_l} \right]^{-1} \quad (6.19)$$

The homogeneous void fraction is thus only a function of the quality and phase densities and neglects any interfacial shear effects. As the critical pressure is approached, the relative difference between saturated vapor and liquid properties decreases and better agreement with the homogenous assumptions can be expected. It was recommended by Triplett *et al.* (1999a) that the homogeneous void fraction model be used for microchannels. The homogeneous void fraction model over-predicts all data from the present study with an AAD and AD of 30.2 and 29.9%, respectively. Agreement is best in the annular regime where the void fraction tends to 1. Agreement in the intermittent and intermittent-wavy regime is the worst, despite the approach to a value of 0. The increased deviation in these regimes is perhaps a result of the increased difference in phase velocities.

The Armand (1946) correlation is often used or modified because of its simple form. In these models, constant multiplier is applied to the homogeneous flow model.

$$\alpha = C \cdot \beta \quad (6.20)$$

The constant C was obtained by Armand from air-water experiments at atmospheric pressure and found to be 0.83. He found poor agreement between this modified homogeneous model and his data for $\beta > 0.9$ and recommended it not be applied beyond that range. Overall, there is good agreement with the data from the present study, with an AAD and AD of 12.9% and 8.2%, respectively. The annular regime data are slightly under-predicted and the most accurate, despite some data being outside the range of applicability. All other flow regimes are over predicted. The deviation between measured and predicted void fraction increases at lower values with the largest inaccuracies occurring in the intermittent and intermittent-wavy regime. The deviations between the data from the present study and the values predicted by this model are most likely a result of the use of a single empirical constant C for the entire range of data. Similarly, because the model is based on the homogeneous flow assumption, the only parameters that affect the predicted void fraction are quality and density ratios, which can therefore not account for the changes in properties like surface tension. In this case, the multiplier was developed for air-water mixtures whose properties are drastically different than those of R404A, which also contribute to the lack of agreement with the present data. These differences are lower at high void fraction values because all models tend to 1.

Lockhart and Martinelli (1949) used the shutoff valves technique to measure void fraction. They found that void fraction depended on the Lockhart-Martinelli Parameter X_{tt} . Their data base consisted of experiments conducted on adiabatic flows of air and oil, kerosene, diesel, benzene and water in tubes with diameters of 1.5 to 25.8 mm and pressures ranging from 101.3 to 329 kPa. Butterworth (1975) correlated their graphical results to obtain the following expressions:

$$\alpha = \left[1 + 0.28 \left(\frac{1-x}{x} \right)^{0.64} \left(\frac{\rho_v}{\rho_l} \right)^{0.36} \left(\frac{\mu_l}{\mu_v} \right)^{0.07} \right]^{-1} \quad (6.21)$$

This correlation results in some physical inconsistencies at high reduced pressure. As the critical pressure is approached and the density and viscosity approach each other, the void fraction should approach the homogeneous model. This model does not follow such trends, which may account for the differences from the void fractions measured in the present study. This correlation was found to over predict all data from the present study with an AD of 40.1%. The poorest agreement is in the intermittent and intermittent-wavy regimes with an AD of 76.5% and 78.7%, respectively.

Zivi (1964) derived several analytical models by applying the concept that the flow would orient itself such that the rate of energy dissipation would be minimized. The most simplified case is where there is no liquid entrainment in annular flow, which results in a simplified void fraction model.

$$\alpha = \left[1 + \left(\frac{1-x}{x} \right) \left(\frac{\rho_v}{\rho_l} \right)^{0.67} \right]^{-1} \quad (6.22)$$

This model is similar to the homogeneous flow model with the slip ratio being a function of density ratios, $S = (\rho_l/\rho_v)^{1/3}$. This implies that the phase velocities are not equal; however, it neglects the effects of viscosity. Overall agreement between measured data from this study and predictions of this model is good with an AAD and AD of 13.5% and 3.7%, respectively. Agreement is best in the annular-intermittent and annular regimes, which is to be expected given that the annular regime forms the basis of this model. In addition, this model yields the lowest AAD and AD from among the predictions of all models considered here for the intermittent regime.

Butterworth (1975) developed a correlation from data obtained by Baroczy (1965), which was used to predict pressure drop in two-phase flow by Garimella *et al.* (2005). The correlation was developed for liquid metal flow applications.

$$\alpha = \left[1 + \left(\frac{1-x}{x} \right)^{0.74} \left(\frac{\rho_v}{\rho_l} \right)^{0.65} \left(\frac{\mu_l}{\mu_v} \right)^{0.13} \right]^{-1} \quad (6.23)$$

This correlation accounts for the effects of phase viscosities on void fraction. However, its formulation also leads to inaccuracies at high reduced pressures because of the non-linear dependence on quality ratio. This model yields the best overall agreement with the data from the present study from among those considered here for comparison, with the lowest AAD of 11.2% and an AD of 6.7%. Agreement in the annular, intermittent-annular regimes is excellent, but larger scatter is seen in the intermittent and intermittent-wavy regimes. The accuracy of this model is surprising, given that its development was for liquid metal applications. The deviations in measured versus predicted values in the intermittent regime are most probably due to the different properties of R404A compared to those of liquid metals and the high uncertainties in these measured values.

Steiner (1998) modified the drift-flux model developed by Rouhani and Axelsson (1970), which includes the effects of surface tension and mass flux that are often neglected.

$$\alpha = \frac{x}{\rho_v} \left[(1 + 0.12[1-x]) \left(\frac{x}{\rho_v} + \frac{1-x}{\rho_l} \right) + \frac{1.18(1-x)(g \cdot \sigma \cdot [\rho_l - \rho_v])^{0.25}}{G \cdot \rho_l^{0.5}} \right]^{-1} \quad (6.24)$$

This model was developed for boiling, and was determined to be accurate at low-to-medium pressures by El Hajal *et al.* (2003). However, it does not approach the homogeneous model as the critical pressure is approached. There is reasonable agreement between the data from the present study and the values predicted by the model with an AAD and AD of 17.1% and 14.5%, respectively. The model slightly over

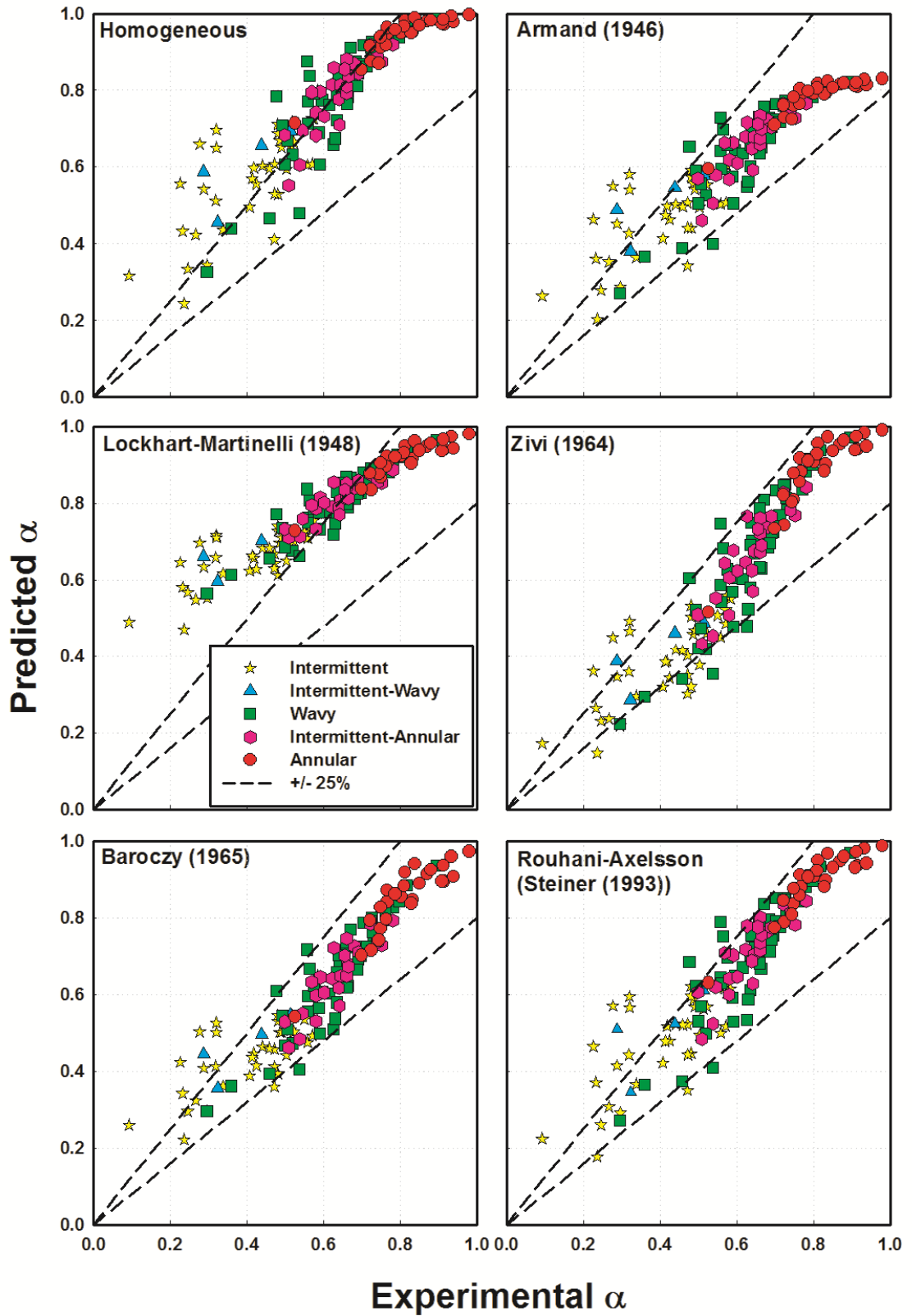


Figure 6.15: Comparison of Experimental α with Models in the Literature up to 2000

predicts the void fractions in the annular flow regime and under predicts all other regimes. The poorest agreement is in the intermittent and intermittent-wavy regimes, with AAD of 36.6% and 30.4%, respectively, which may be because of the difference in fluid properties and the high uncertainties in intermittent data.

Yashar *et al.* (2001) developed an empirical model based on evaporation and condensation experiments on refrigerants R134a and R404A flowing through Microfin tubes. Condensation experiments were conducted at a saturation temperature of $T_{\text{sat}} = 35^{\circ}\text{C}$, while evaporation experiments were conducted at $T_{\text{sat}} = 5^{\circ}\text{C}$. They hypothesized that gravitational drag between the phases was important in the stratified and annular regime, which was typical of the flow regimes present in large diameter tubes. They accounted for stratified regime effects through the use of Froude rate, $Ft = [x/(1-x)]^{0.5} Fr_{jv}$ and annular regime effects through the Martinelli parameter, X_{tt} . They developed a single void fraction model for condensation and evaporation using these terms.

$$\alpha = \frac{1}{(1 + 1/Ft + X_{tt})^{0.321}} \quad (6.25)$$

The inclusion of the Froude rate number is consistent with the mass flux dependency they observed in condensing flows. Similar to this work, they found no effect of diameter on void fraction during evaporation in smooth tubes. Their model over predicts all data with the best agreement being in the annular regime with an AAD of 14.4%. Even with the inclusion of the Froude rate, wavy flow regime void fractions from the present study are not predicted well, with an AAD of 25.5%. These differences are probably due to the low reduced pressures ($p_r(\text{R134a}) = 0.22$, $p_r(\text{R410A}) = 0.43$) at which their experiments were conducted.

Kawahara *et al.* (2002) developed an empirical correlation based on nitrogen-water experiments conducted in a 100 μm diameter tube. They found that the effect of superficial liquid velocity on void fraction was negligible. The model they developed was based on the homogeneous void fraction.

$$\alpha = \frac{0.03\beta^{0.5}}{1-0.97\beta^{0.5}} \quad (6.26)$$

The model is solely based on homogeneous void fraction and does not include the effects of properties other than density. The properties and conditions of the nitrogen-water experiments are drastically different from those of the high pressure refrigerant experiments conducted here. The agreement between data from the present study and predictions of the correlation is poor, with all data being under predicted with an AAD of 61.2%. This is most likely due to the difference in fluid properties.

The void fraction model presented by El Hajal *et al.* (2003) was specifically developed for refrigerants at various reduced pressures. They found that the Steiner (1998) modified Rouhani and Axelsson (1970) model was accurate at low to mid reduced pressures but not accurate at high reduced pressures where they hypothesized that the homogeneous model was applicable. El Hajal *et al.* (2003) found that a logarithmic mean of the two void fraction models yielded the best agreement.

$$\alpha = \frac{\beta - \alpha_{ra}}{\ln\left(\frac{\beta}{\alpha_{ra}}\right)} \quad (6.27)$$

In this equation, the variable α_{ra} is determined using Equation 6.24. They found this expression to be valid from low reduced pressures ($p_r = 0.02$) to high reduced pressures ($p_r = 0.8$) when compared to their heat transfer data. There is reasonably good agreement of the data from the present study with this model, but it over predicts most data, with an

AAD and AD of 23.0% and 22.0%, respectively. It is important to note that this correlation over predicts the void fractions from the present study, while the Steiner (1998) modified Rouhani and Axelsson (1970) also over predicts the data. Therefore, the logarithmic mean of the two models results in an over-prediction of void fraction values from the present study.

A probabilistic void fraction model for refrigerants was developed by Jassim *et al.* (2008b). They observed multiple flow regimes occurring at the same time under the same conditions and obtained weighted parameters for intermittent, stratified and annular flow regimes. Their expression for void fraction is as follows::

$$\alpha = F_{\text{int}} \cdot \alpha_{\text{int}} + F_{\text{strat}} \cdot \alpha_{\text{strat}} + F_{\text{ann}} \cdot \alpha_{\text{ann}} \quad (6.28)$$

where the weighting parameters are a function of:

$$F_{\text{int}} = (1-x)^i, i = 0.0243 \cdot \xi + 8.07$$

$$\xi = (We_{\text{vo}})^{0.4} \cdot \left(\frac{\rho_1}{\rho_v} \right), We_{\text{vo}} = \left(\frac{G^2 \cdot D}{\rho_v \cdot \sigma} \right) \quad (6.29)$$

$$F_{\text{strat}} = \left(1 - x^{\left[\frac{s}{x^{0.5}} \right]^i} \right) - (1-x)^i \quad (6.30)$$

$$s = (0.45 \cdot X_s)^{-1} + (0.025 \cdot X_s^{4.44})^{-1}, X_s = \left(\frac{\rho_v}{\rho_1} \right) Fr_{\text{vo}}$$

$$F_{\text{ann}} = 1 - F_{\text{int}} - F_{\text{strat}} \quad (6.31)$$

They suggested that any void fraction model can be used for any of the regimes using these weighted parameters. They found that using the Steiner (1998) modified Rouhani and Axelsson (1970) model (Equation 6.24) in the annular regime, the Yashar *et al.* (2001) model (Equation 6.25) in the stratified region, and the equation developed by Graham *et al.* (1998) for the intermittent regime yielded the best agreement. There is good agreement between the data from the present study and values of void fraction predicted by their correlation with an AAD and AD of 15.6% and 5.9%, respectively.

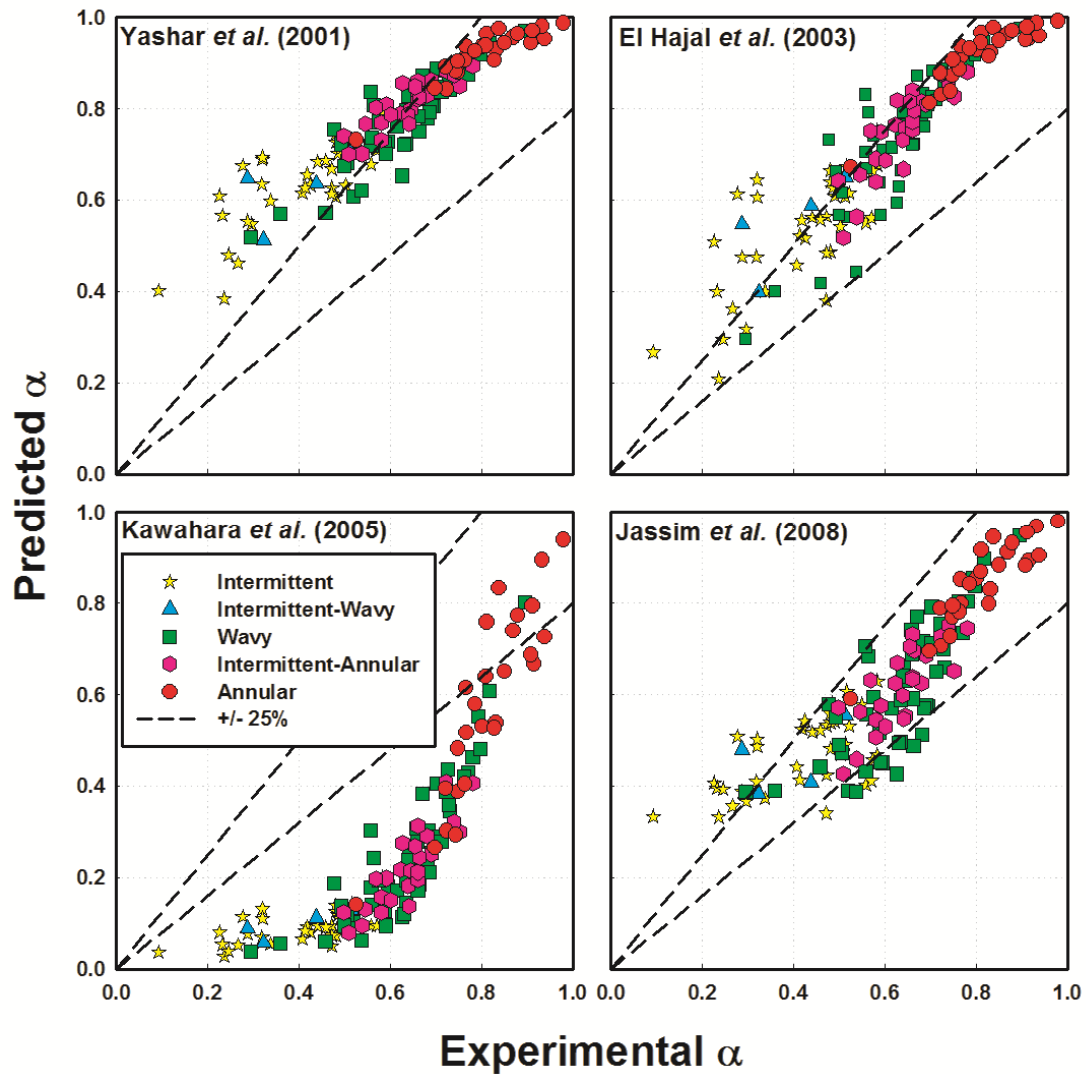


Figure 6.16: Comparison of Experimental α with Models in the Literature from 2000 to the Present

The best agreement is in the annular and intermittent-annular regimes. However, this model has one of the poorest agreements with the data from the present study for the intermittent regime. This is most probably due to the intermittent regime correlation (Graham *et al.*, 1998) used in their model, having been developed for large diameter tubes.

A summary of the AAD and AD for all correlations discussed above is presented in Table 6.12. The Baroczy (1965) model yields the least scatter, or lowest AAD, while the Zivi

Table 6.12: Comparison of Experimental α with Models in Literature

Correlation	AAD %	AD %	Comments
Homogeneous	30.2	29.9	Over-predicts all data with best accuracy in Annular Regime
Armand (1946)	12.9	8.2	Over-predicts all data except for Annular Regime were data are under-predicted
Lockhart-Martinelli (1948)	40.1	40.1	Over-predicts all data
Zivi (1964)	13.5	3.7	Good overall agreement; Large scatter in intermittent regime but small average deviation
Baroczy (1965)	11.1	6.7	Best overall agreement; Poor agreement in intermittent and intermittent/wavy regime
Rouhani-Axelsson (Steiner (1993))	17.1	14.5	Reasonable agreement throughout
Yashar <i>et al.</i> (1998)	36.3	36.3	Over predicts all data
Kawahara <i>et al.</i> (2002)	61.2	-61.2	Largely under-predicts data
El Hajal <i>et al.</i> (2003)	23.0	22.0	Over-predicts most data
Jassim <i>et al.</i> (2008)	22.6	21.6	Good agreement with Annular regime; Under-predicts transition regions and over predicts Intermittent regime

(1964) model yields the lowest AD. The models specifically developed for refrigerants yield reasonable agreement (Rouhani and Axelsson, 1970; Yashar *et al.*, 2001; El Hajal *et al.*, 2003; Jassim *et al.*, 2008b) with differences that can be attributed to the lack of measured void fractions in their studies at high reduced pressures. Their predictive capabilities deteriorate at high reduced pressures, with all of them over predicting the void fractions measured in the present study. It is clear from these comparisons that no model available in literature accurately predicts void fraction in the intermittent regime for the geometries and conditions under consideration in the present study, while agreement in the other regimes is often reasonable. The intermittent regime is the only regime where there is not a continuous vapor core and the axial and radial distribution of

the liquid phase varies considerably. It is also typically has the highest uncertainties in measured values, which may account for some of the discrepancies.

6.2.3 Pressure Drop

The use of a two-phase flow multiplier is a common approach ((Lockhart and Martinelli, 1949; Chisholm, 1973; Friedel, 1979) to predict two-phase pressure drops based on single-phase pressure drops.. These correlations were developed for two-phase flow in large diameter tubes. The Friedel (1979) correlation is the preferred correlation for small diameter tubes because its formulation includes surface tension effects through the Weber number. This section compares the pressure drop data from the present study with the predictions of relevant models from the literature.

One of the original two-phase flow studies was conducted by Lockhart and Martinelli (1949) on adiabatic flow of air and several liquids through pipes ranging in diameter from 1.5 to 26 mm. The liquids investigated were benzene, kerosene, water and various oil mixtures. They found good agreement between several two-phase flow phenomena and a function of the ratio of liquid-to-vapor pressure drop, $X = [(dP/dz)_l/(dP/dz)_v]^{1/2}$. Chisholm (1967) correlated the Martinelli parameter, X , to develop the following two-phase multiplier expression based on the corresponding liquid phase pressure drop:

$$\phi_1^2 = 1 + C \cdot X^{-1} + X^{-2} \quad (6.32)$$

where C depends on whether the liquid and vapor are in turbulent or laminar flow.

$$\begin{aligned} \text{Re}_l > 2000, \text{Re}_v > 2000 : C &= 20 \\ \text{Re}_l < 2000, \text{Re}_v > 2000 : C &= 12 \\ \text{Re}_l > 2000, \text{Re}_v < 2000 : C &= 10 \\ \text{Re}_l < 2000, \text{Re}_v < 2000 : C &= 5 \end{aligned} \quad (6.33)$$

In this study, the vapor phase is almost always turbulent except for a few select cases at low mass fluxes and qualities in 1.00 mm and 0.508 mm tubes. A majority of the data are in the turbulent-turbulent regime, with a corresponding constant of $C = 20$. Agreement between this model and measured pressure drop is extremely poor, with an AAD and AD of 191.2 and 190.2%, respectively. Almost all data are largely over-predicted. These large differences between the data from the present study and the predictions of this model are most probably due to the significantly different properties of the fluids used in this study. This is further substantiated by the increased difference as reduced pressure is increased. At $p_r = 0.38, 0.49, 0.62$ and 0.77 , the AD is 91.3, 148.5, 221.0, and 326%, respectively.

A similar correlation approach was used by Chisholm (1973a) based on work by Baroczy (1966) on water/air, steam, and mercury/nitrogen. He attempted to account for the influence of fluid properties, quality, and mass flux in the formulation of the two-phase multiplier. Similar to the Martinelli parameter, Chisholm (1973a) developed a parameter based on the ratio of vapor-only and liquid-only frictional pressure gradient, $Y = [(dP/dz)_{GO}/(dP/dz)_{LO}]^{1/2}$ and proposed the following expression for the two-phase multiplier.

$$\phi_{LO}^2 = 1 + (CY^2 - 1) \cdot B \cdot x^{(2-n)/2} \cdot (1-x)^{(2-n)/2} + x^{(2-n)} \quad (6.34)$$

Here, n is the turbulent Reynolds number exponent for single-phase pressure drop, C is an empirical constant of unity in this form, and the constant B is a function of the Chisholm parameter and mass flux as follows:

$$\begin{aligned} 0 < Y < 9.5, B &= 55/G^{1/2} \\ 9.5 \leq Y < 28, B &= 520/(Y \cdot G^{1/2}) \\ 28 \leq Y, B &= 15,000/(Y^2 \cdot G^{1/2}) \end{aligned} \quad (6.35)$$

Overall agreement between the data from the present study and pressure drops predicted by this model is reasonable, with an AAD and AD of 34.6 and 29.7%, respectively. The correlation is unable to address the effects of tube diameter on pressure drop. Agreement with the 3.05 mm diameter data is extremely poor (AAD = 60.7%), agreement with 1.00 mm diameter data is good (AAD = 13.8%), and agreement with 0.508 mm tube data is reasonable (AAD = 21.4%.) The correlation does not account for increased reduce pressure accurately and increasingly over-predicts pressure drop as reduced pressure increases. At $p_r = 0.38, 0.49, 0.62$ and 0.77 , the AD is 9.7, 26.7, 32.8, and 49.8%, respectively. The inability to account for these effects is most probably due to the drastically different properties of the fluids for which this correlation was developed, compared to those used in the present study.

Friedel (1979) correlated a two-phase multiplier based on 25,000 data points for horizontal and vertical flow in round tubes. He found a weak inverse dependence on modified Froude and Weber numbers. The Froude and Weber number are calculated using a two-phase mixture density, $\rho_{TP} = [x \rho_G^{-1} + (1-x) \rho_L^{-1}]$.

$$\phi_{LO}^2 = E + 3.24 \cdot F \cdot H \cdot Fr^{-0.045} \cdot We^{-0.035} \quad (6.36)$$

where

$$\begin{aligned} E &= (1-x)^2 + x^2 \left(\frac{\rho_l}{\rho_v} \right) \left(\frac{f_{vo}}{f_{lo}} \right) \\ F &= x^{0.78} \cdot (1-x)^{0.224} \\ H &= \left(\frac{\rho_l}{\rho_v} \right)^{0.91} \left(\frac{\mu_v}{\mu_l} \right)^{0.19} \left(1 - \frac{\mu_v}{\mu_l} \right)^{0.7} \end{aligned} \quad (6.37)$$

The Friedel (1979) correlation over-predicts most of the data from the present study with an AAD and AD of 41.7% and 36.0%, respectively. Despite the inclusion of surface tension effects in the formulation, the correlation is unable to predict the effects of decreasing tube diameter, with an AD of -65.9, 10.1, and 24.6% for the 3.05, 1.00, and

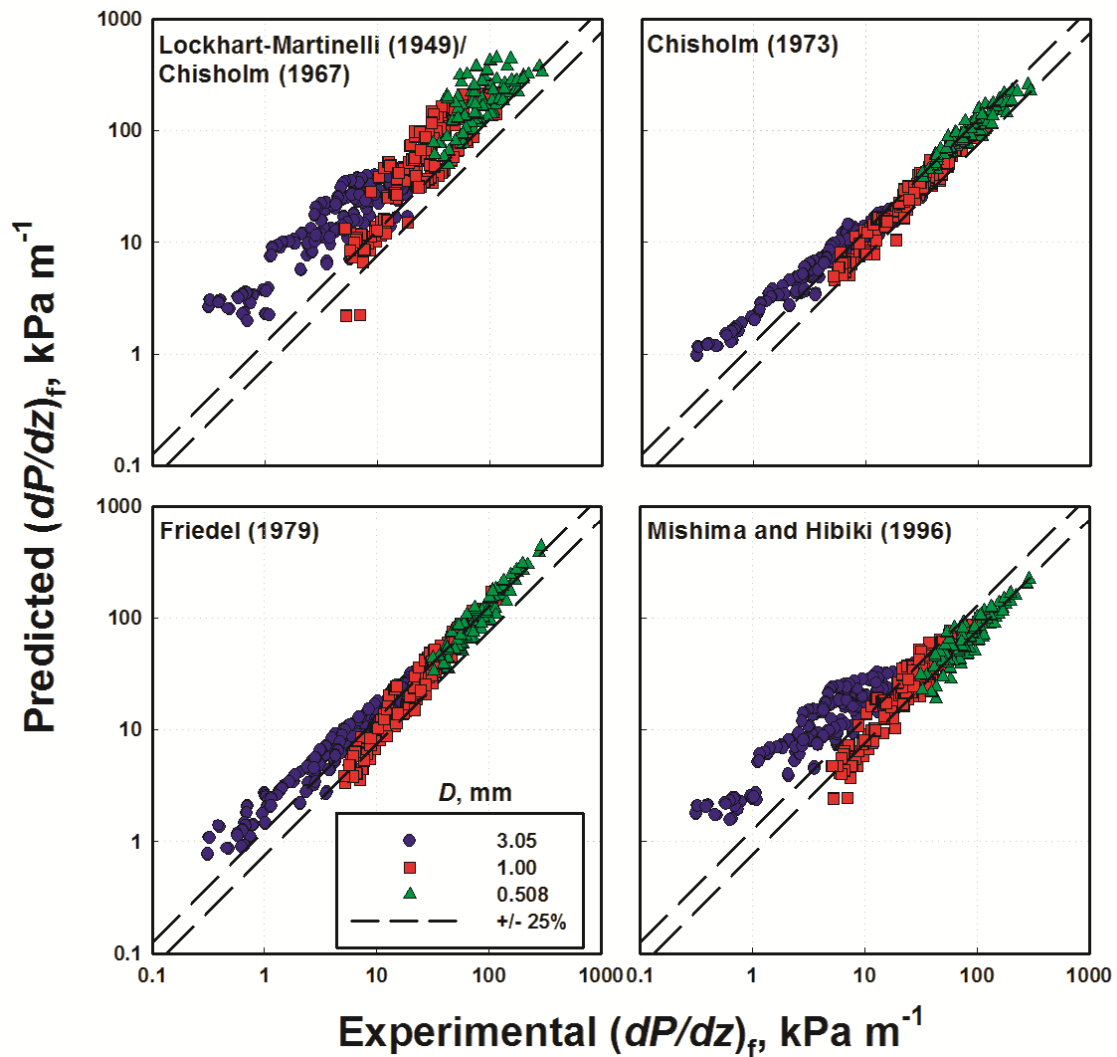


Figure 6.17: Comparison of Experimental $(dP/dz)_f$ with Models in the Literature up to 2000

0.508 mm tubes, respectively. The correlation also does not predict the effects of increased reduced pressure well, with an AD of 14.2, 30.8, 42.2 and 61.4% for $p_r = 0.38$, 0.49, 0.62 and 0.77, respectively.

Mishima and Hibiki (1996b) developed a correlation for a modified C coefficient in the Lockhart-Martinelli correlation (Equation 6.32) for adiabatic air-water flows in tubes ranging in diameter from 1 to 4 mm.

$$C = 21(1 - \exp(-0.319 \cdot D)) \quad (6.38)$$

In the above correlation, diameter is in mm. The overall agreement with the data from the present study is very poor, with an AAD and AD of 82.9% and 63.8%, respectively. The correlation substantially over-predicts pressure drop in the 3.05 mm diameter tube (AD = 170.6%), while the agreement is reasonable for 1.00 and 0.508 mm diameter tube data, for which the correlation slightly under predicts the data from the present study, with ADs of -3.1% and -21.0%, respectively. The reason for the poor agreement, despite being developed for similar tube diameters, is most probably the difference in properties between adiabatic air-water flows and two-phase refrigerant flow. Similarly, the model does not predict the effects of increasing reduced pressure well. As reduced pressure increases, the correlation over-predicts the data from the present study by an increasing amount. For $p_r = 0.38, 0.49, 0.62$ and 0.77 , the AD is 3.3, 38.0, 87.1, and 143.1%, respectively, because of the increased difference in property ratios as saturation temperature increases. At the lowest saturation temperature, density and viscosity ratios are closest to that of air-water, and as saturation temperature rises, the density and viscosity ratios decrease, which may be the reason for the increased over-prediction at the high pressures.

Tran *et al.* (2000) modified the approach of Chisholm (1973a) based on refrigerant phase-change data in small diameter channels ($D_h = 2.46, 2.40,$ and 2.92 mm.) Tran *et al.* (2000) tried to account for the effects of tube diameter and surface tension through the use of the confinement number. The confinement number was used to replace the constant B in Equation 6.34

$$N_{\text{conf}} = \left(\frac{\sigma}{g \cdot (\rho_l - \rho_v)} \right)^{0.5} D^{-1} \quad (6.39)$$

They found the best agreement with their data with a value of constant C equal to 4.3. Overall agreement of the data from the present study with this correlation is reasonable, with an AAD and AD of 33.4% and 9.0%, respectively. This correlation has the lowest AD and the second lowest AAD of all models from the literature that were considered here. There is reasonable agreement with the 3.05 and 1.00 mm diameter tube data, but consistent over-prediction of the 0.508 mm diameter tube data. This is most probably due to the correlation being developed for two-phase flow on channels larger than 2 mm in diameter. The correlation also captures the effects of increased reduced pressure reasonably well, despite being developed based on low reduced pressure conditions. For $p_r = 0.38, 0.49, 0.62$ and 0.77 the AD is -2.4, 6.1, 7.6, and 27.5%, respectively. The increase in over-prediction is most probably due to their model being based on data at lower reduced pressures ($0.03 < p_r < 0.24$) where changes in saturation temperature have a larger effect on properties than at the higher reduced pressures under consideration in the present study ($0.38 < p_r < 0.77$.)

Cavallini *et al.* (2002) modified the Friedel (1979) correlation based on condensation experiments on several refrigerants in an 8 mm diameter tube. They found that the dimensionless vapor velocity, J_G^* , predicted the transition to annular flow well. For non-annular flow, where $J_G^* < 2.5$, they found good agreement between data and the original Friedel (1979) (Equation 6.36). For values of $J_G^* \geq 2.5$ they suggested the following two-phase multiplier:

$$\phi_{lo}^2 = E + 1.262 \cdot F \cdot H \cdot We^{-0.1458} \quad (6.40)$$

where

$$\begin{aligned}
E &= (1-x)^2 + x^2 \cdot \left(\frac{\rho_l}{\rho_v} \right) \left(\frac{f_{vo}}{f_{lo}} \right) \\
F &= x^{0.6978} \\
H &= \left(\frac{\rho_l}{\rho_v} \right)^{0.3278} \left(\frac{\mu_v}{\mu_l} \right)^{-1.181} \left(1 - \frac{\mu_v}{\mu_l} \right)^{3.477} \\
We &= G^2 \cdot D \cdot (\rho_v \cdot \sigma)^{-1}
\end{aligned} \tag{6.41}$$

The form of the Cavallini *et al.* (2002) correlation is almost identical to that of the original Friedel (1979) correlation, but with revised empirical constants. The two major differences are in the exclusion of the Froude number, which is justified by the lack of gravitational effects, and the empirical constant F only being a function of x , and not $(1-x)$ like in the original. Whereas in the original correlation, $F \rightarrow 0$ as $x \rightarrow 1$, resulting in the expression for single-phase vapor pressure drop, the modified version does not. The Cavallini *et al.* (2002) model results in the lowest scatter from the data from the present study, with an AAD of 30.0%, and the second best AD of -10.8% from among the pressure drop correlations considered here. The correlation slightly under-predicts the data from the present study for $D = 0.508$ mm, with an AD = -23.5%, significantly over-predicts the present data at $D = 1.00$ mm, with an AD = 30.4%, and over-predicts the present data for $D = 3.05$ mm, with an AD = 13.2%. These differences can be attributed to the fact that the Cavallini *et al.* (2002) correlation was developed for a single 8 mm diameter tube. The influence of reduced pressure is addressed to some extent by this correlation, as evidenced by a decrease in AD from -21.0% at $p_r = 0.38$ to -3.9% at $p_r = 0.77$. However, the scatter, AAD, increases with increasing reduced pressure.

Garimella *et al.* (2005) developed a multi-regime pressure drop model for condensation in small diameter tubes. The model was experimentally validated for condensing R134a in tube diameters ranging from 0.5 to 4.91 mm. They used transition criteria based on visualization experiments conducted by Coleman and Garimella (1999, 2003) and

developed sub models for pressure drop in different flow regimes. They developed an annular flow regime model to predict the pressure drop in the annular/mist/and dispersed regime. Their correlation can be represented in the form of a two-phase multiplier to the vapor phase pressure drop for ease of comparison with the other models discussed above.

$$\phi_v^2 = A \cdot X^a \cdot \text{Re}_1^b \cdot \psi^c \cdot \alpha^{-2.5} \cdot \left(\frac{f_1}{f_v} \right) \quad (6.42)$$

where ψ is a modified liquid capillary number proposed by Lee and Lee (2001)

$$\psi = \frac{j_1 \cdot \mu_1}{(1 - \alpha) \cdot \sigma} \quad (6.43)$$

They determined the constants from Equation 6.42 using Reynolds numbers defined within the cross section occupied by each phase. They defined their Reynolds numbers in terms of the annular flow area occupied by the phases.

$$\text{Re}_1 = \frac{G \cdot (1 - x) \cdot D}{(1 + \sqrt{\alpha}) \cdot \mu_1} \quad (6.44)$$

$$\text{Re}_v = \frac{G \cdot x \cdot D}{\sqrt{\alpha} \cdot \mu_v}$$

They used the Blasius (1908) friction factor for the corresponding single-phase pressure drop calculations. The empirical constants vary based on liquid Reynolds number as follows.

$$\begin{aligned} \text{Re}_1 < 2100: A = 1.308 \times 10^{-3}, a = 0.427, b = 0.930, c = -0.121 \\ \text{Re}_1 > 3400: A = 25.64, a = 0.532, b = -0.327, c = 0.021 \end{aligned} \quad (6.45)$$

In the transition region between the two limits for Reynolds number, the value of pressure drop at each limit is predicted and a linear interpolation of the two based on quality and mass flux is used. The intermittent and discrete wave flow regimes were modeled by representing the pressure drop as the sum of the pressure drop at the liquid-

vapor interface around the bubble, the liquid slug, and the transition between the slug and film regions.

$$\frac{\Delta P}{L} = \left(\frac{dP}{dz} \right)_{f/b} \left(\frac{L_{\text{bubble}}}{L_{\text{unit cell}}} \right) + \left(\frac{dP}{dz} \right)_{\text{slug}} \left(\frac{L_{\text{slug}}}{L_{\text{unit cell}}} \right) + \Delta P_{\text{one transition}} \left(\frac{N_{\text{unit cells}}}{L} \right) \quad (6.46)$$

The number of unit cells was deduced based on the measured pressured drop across the test section length and was related to the slug Reynolds number.

$$D_h \left(\frac{N_{\text{unit cells}}}{L_{\text{tube}}} \right) = \left(\frac{D_h}{L_{\text{unit cell}}} \right) = \omega \frac{D_h}{U_{\text{bubble}}} = a \text{Re}_{\text{slug}}^b \quad (6.47)$$

The number of unit cells is directly related to the bubble frequency which was not directly measured in their study, but obtained from the data to provide closure to the model. For circular tubes, the empirical constants were found to be $a = 1.573$ and $b = -0.507$. A majority of the data from the present study is over-predicted by the model with an AAD and AD of 37.8% and 23.2%, respectively. The lowest agreement was for $D = 3.05$ mm (AD = 54.0%,) which is most probably due to a majority of the data for this tube being in the wavy flow regime, which was not explicitly modeled as a separate regime by Garimella *et al.* (2005). Agreement is best for $D = 1.00$ and 0.508 mm (AD = -0.6% and 6.6%, respectively,) where annular flow is prominent. For $p_r = 0.38, 0.49, 0.62$ and 0.77, the AD for all the data from the present study is -13.5, 8.3, 34.6, and 73.2%, respectively. The increasing over-prediction demonstrates that the correlation does not accurately account for increasing reduced pressure, because their R134a experiments were conducted at a single nominal reduced pressure of $p_r = 0.34$.

Andresen (2007) investigated condensation of R410A at high reduced pressures ($p_r = 0.8, 0.9$) at tube diameters ($D = 3.05, 1.52$ and 0.76 mm) similar to those in the present study. He modified the Chisholm (1967) correlation (Equation 6.34) by relating the empirical constant C to the liquid Reynolds number, Re_l , and the confinement number, N_{conf} .

$$C = 24 \cdot \text{Re}_1^{-0.3} \cdot N_{\text{conf}}^{-0.4} \quad (6.48)$$

The liquid Reynolds number was used to model the effects of inertia, while the confinement number addresses the relative influence of surface tension and gravitational effects in small diameter tubes. Agreement of the predictions from this model with the data from the present study is reasonable, with an AAD and AD of 31.8% and -11.9%, respectively. The correlation over-predicts data from the present study for $D = 3.05$ mm (AD = 13.5%) and consistently under-predicts data for $D = 1.00$ and 0.508 mm (-30.6 and

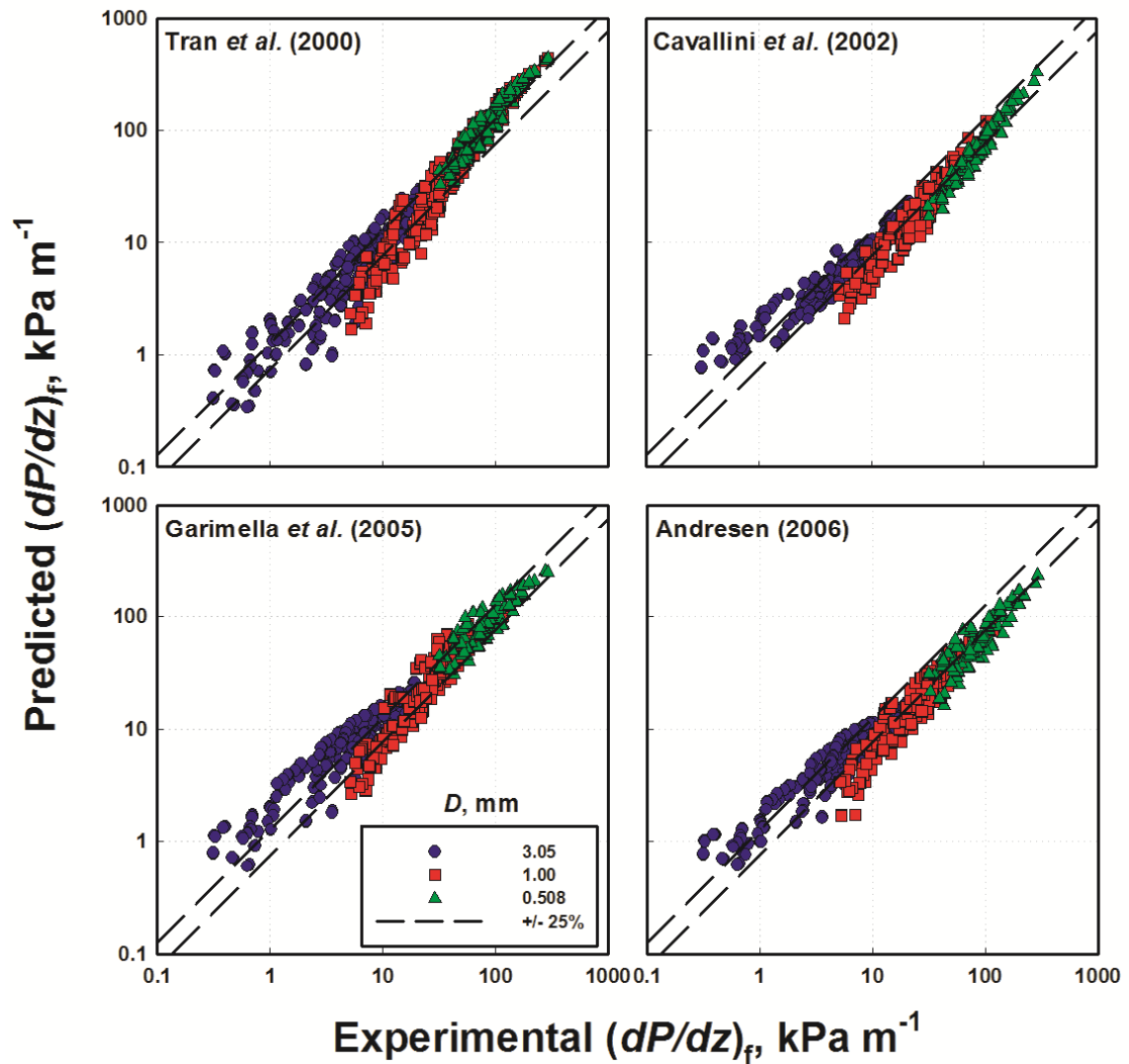


Figure 6.18: Comparison of Experimental $(dP/dz)_f$ with Models in the Literature from 2000 to the Present

-27.2%, respectively.) The consistent under-prediction perhaps signifies that the model is capturing the trends well, albeit without being able to match the magnitudes of the pressure gradient data from the present study. Thus, the confinement number may be accounting for the effects of decreasing tube diameter and the increasing importance of surface tension for the 1.00 and 0.508 mm diameter tubes at the conditions investigated in the present study. The poor agreement for the 3.05 mm diameter tube data may be due to the inability of the confinement number to accurately account for increased gravitational effects at larger tube diameters. The correlation poorly predicts the effects of increases in high reduced pressures. It significantly under predicts pressure drop at the lowest reduced pressure, $p_r = 0.38$, with an AD of -38.5% and trends towards over-predicting pressure drop at $p_r = 0.77$ with an AD of 25.5%. Perhaps the influence of other important properties such as viscosity are not accurately captured for large changes in reduced pressures through the use of only the Martinelli parameter for the correlation. It is also important to note that the reduced pressures studied by Andresen (2007) were over a small span at near critical conditions ($0.8 < p_r < 0.9$.) The present study spans a much larger range of reduced pressures, $0.38 < p_r < 0.77$.

Summary of Comparison

A summary of AAD and AD as a function of tube diameter is provided in Table 6.13, and is presented as a function of saturation temperature (reduced pressure) in Table 6.14. While some of the correlations predict pressure drop from the present study well in narrow ranges of data, it is clear that none accurately capture the trends in pressure drop with decreasing tube diameter and increasing reduced pressure that were observed in the study. The model presented by Garimella *et al.* (2005) predicts data well at the lowest reduced pressure ($p_r = 0.38$), but fails to accurately account for the change in properties as reduced pressure increases. However, while it may not properly account for the

Table 6.13: Predictive Capabilities of Models in the Literature for Data from the Present Study Categorized by Tube Diameter

Study	Diameter, mm						TOT	
	3.05		1.00		0.508		AAD	AD
	AAD %	AD %	AAD %	AD %	AAD %	AD %	%	%
Lockhart-Martinelli (1949)/ Chisholm (1967)	285.0	284.9	122.9	120.5	133.2	133.2	191	190
Chisholm (1973)	60.7	59.1	13.8	4.6	21.4	18.1	34.6	29.7
Friedel (1979)	66.6	65.9	23.0	10.1	27.1	24.6	41.7	36.0
Mishima and Hibiki (1996)	170.6	170.6	21.2	-3.1	24.8	-21.0	82.9	63.8
Tran <i>et al.</i> (2000)	35.4	12.9	30.2	-10.0	35.4	34.5	33.4	9.0
Cavallini <i>et al.</i> (2002)	32.7	13.2	30.4	-29.5	24.2	-23.5	30.0	-10.8
Garimella <i>et al.</i> (2005)	59.0	54.0	24.9	-0.6	20.6	6.6	37.8	23.2
Andresen (2006)	33.5	13.5	31.6	-30.6	28.6	-27.2	31.8	-11.9

change in properties with p_r , the excellent agreement at the lowest reduced pressure may indicate that the model does well in capturing the effects of tube diameter, especially for the small diameters. Overall, the best agreement with data from the present study is for the Cavallini *et al.* (2002) and Andresen (2007) models, although both models consistently under-predict small diameter tube data. No model from the literature was able to accurately account for property changes with changing reduced pressure, while simultaneously accounting for diameter changes at this scale. Therefore, a new model is required for better predictions of data from the present study.

Table 6.14: Predictive Capabilities of Models in the Literature for Data from the Present Study Categorized by Saturation Temperature

Study	$T_{sat}, ^\circ\text{C} (p_r)$							
	30 (0.38)		40 (0.49)		50 (0.62)		60 (0.77)	
	AAD %	AD %	AAD %	AD %	AAD %	AD %	AAD %	AD %
Lockhart-Martinelli (1949)/ Chisholm (1967)	93.2	91.3	150.1	148.5	221.0	221.0	326.6	326.6
Chisholm (1973)	16.4	9.7	32.0	26.7	38.5	32.8	50.5	49.8
Friedel (1979)	20.9	14.2	36.7	30.8	49.8	42.2	63.5	61.4
Mishima and Hibiki (1996)	39.3	3.3	61.3	38.0	99.5	87.1	144.3	143.1
Tran <i>et al.</i> (2000)	25.9	-2.4	32.2	6.1	32.2	7.6	45.4	27.5
Cavallini <i>et al.</i> (2002)	23.2	-21.0	26.6	-8.9	34.8	-8.5	37.1	-3.9
Garimella <i>et al.</i> (2005)	16.8	-13.5	21.8	8.3	44.6	34.6	76.4	73.2
Andresen (2006)	38.5	-38.5	26.9	-22.8	27.2	-4.5	35.5	25.5

6.2.4 Heat Transfer

Internal convective condensation models are commonly divided into gravity dominated, wavy-stratified regime models, or shear dominated, annular regime models. Wavy-stratified regimes are often modeled using the Nusselt (1916) condensation approach. Annular flow is either modeled using a shear driven or two-phase multiplier approach. In this study, the largest percentage of the heat transfer data (186/402) are predicted to be in the annular regime based on the transition criteria of Nema (2007). In this section, a comparison of heat transfer data with annular flow models is presented first, followed by comparison with more comprehensive, multi-regime heat transfer models.

Annular Flow Models

A two-phase multiplier correlation was developed by Cavallini and Zecchin (1974) for condensing refrigerants. Their model was compared with condensing R11, R22, and R114 data in annular flow. The Nusselt number correlation is based on an equivalent Reynolds number, Re_{eq} , which enables treating the flow as single-phase flow.

$$Nu = 0.05 \cdot Re_{eq}^{0.8} Pr_1^{1/3} \quad (6.49)$$

Where

$$Re_{eq} = \frac{GD}{\mu_1} \left[(1-x) + x \left(\frac{\rho_l}{\rho_v} \right)^{1/2} \right] \quad (6.50)$$

This correlation over-predicts most of the data from the present study with an AAD and AD of 38.5 and 33.5%, respectively. It significantly over-predicts the 3.05 mm diameter tube data, which are mostly in wavy flow. It predicts annular flow data extremely well. Their model predicts data from the present study best at the lowest reduced pressure, which is to be expected given the lower pressure refrigerants for which the model was originally developed. Agreement with the present data decreases as reduced pressure is increased, indicating that the model does not accurately account for phase property changes at higher reduced pressures.

Shah (1979) developed a purely empirical correlation for internal flow condensation. The correlation is based on a large database for condensing fluids in horizontal, vertical and inclined pipes. The fluids considered included water, R11, R12, R22, R113, methanol, ethanol, benzene, toluene, and trichloroethylene. The operating conditions ranged from reduced pressures of 0.002 to 0.44. The tube diameters and mass fluxes from the studies ranged from 7 to 40 mm, and 140 to 20740 $kg\ m^{-2}\ s^{-1}$, respectively. From this large database, he developed a two-phase multiplier that is solely a function of quality and reduced pressure.

$$h = h_{D-B} \left[(1-x)^{0.8} + \frac{3.8x^{0.76} (1-x)^{0.04}}{p_r^{0.38}} \right] \quad (6.51)$$

where

$$h_{D-B} = 0.0023 \text{Re}_1^{0.8} \text{Pr}_1^{0.4} \frac{k_1}{D} \quad (6.52)$$

The single-phase heat transfer coefficient recommended is the Dittus and Boelter (1930) correlation, h_{D-B} . This correlation predicts the relative magnitude of the data from the present study reasonably well. The comparison is shown in Figure 6.19, and the overall AAD and AD are 43.6 and 38.3%, respectively. The data are consistently over-predicted with poor agreement with the 3.05 mm diameter tube data, but increasingly better agreement as the diameter decreases. This is probably because the correlation is formulated for the annular flow regime. Similarly, agreement is worst compared to the 3.05 mm diameter tube data from the present study where stratified and wavy flow exist. This correlation also predicts the lowest reduced pressure ($p_r = 0.38$) data from the present study well, but the predictions deviate increasingly as reduced pressure increases.

Moser *et al.* (1998) developed a condensation heat transfer model based on the heat-momentum analogy. They compared their model to a large data base from refrigerant experiments (R12, R22, R113, R134a, R410A) in tube diameters ranging from 4.57 – 12.7 mm, and reduced pressures ranging from 0.02 – 0.7. They based their approach on an equivalent Reynolds number similar to that used by Akers *et al.* (1959). Using the heat-momentum analogy, they obtained the following expression for equivalent Reynolds number.

$$\text{Re}_{\text{eq}} = \phi_{\text{LO}}^{8/7} \text{Re}_{\text{lo}} \quad (6.53)$$

They suggested using the Friedel (1979) two-phase multiplier (ϕ_{LO} from Equation 6.36) in Equation 6.53. They approximated the single-phase heat transfer coefficient using the Petukhov (1970) correlation and modified the results for heat transfer in the liquid annulus using the approach by Traviss and Rohsenow (1973). The resulting two-phase heat transfer correlation becomes:

$$Nu = \frac{hD}{k_1} = \frac{0.0994^{C_1} Re_1^{C_2} Re_{eq}^{1+0.875C_1} Pr_1^{0.815}}{(1.58 \ln(Re_{eq}) - 3.28)(2.58 \ln(Re_{eq}) + 13.7 Pr_1^{2/3} - 19.1)} \quad (6.54)$$

where

$$\begin{aligned} R^+ &= 0.0994 Re_{eq}^{7/8} \\ C_1 &= 0.126 Pr_1^{-0.448} \\ C_2 &= -0.113 Pr_1^{-0.563} \end{aligned} \quad (6.55)$$

Overall, the Moser *et al.* (1998) correlation predicts the heat transfer data from the present study the best as shown in Figure 6.18. The AAD and AD are 25.8 and 10.3%, respectively. Agreement is very good with the data for the small tubes taken in the present study, where the flow is always laminar; the AAD for the 1.55 and 0.86 mm diameter tubes are both 10%. Cavallini *et al.* (2006b) found very good agreement with this model for condensing refrigerants R410A, R134a, and R236ea in hydraulic diameters ranging from 0.4 to 3 mm. Bandhauer *et al.* (2006) also found good agreement with the Moser *et al.* (1998) correlation for condensing R134a in microchannel geometries with hydraulic diameters ranging from 0.506 to 1.524 mm. Despite its accuracy, the correlation is dependent on the two-phase multiplier chosen. Moser *et al.* (1998) used the Friedel (1979) correlation, which increasingly over-predicted pressure drop data from the present study with increasing reduced pressure. The heat transfer predictions of the Moser *et al.* (1998) correlation show a similar trend and increasingly over-predict heat transfer coefficients as reduced pressure increases.

A shear-driven heat transfer model was developed by Bandhauer *et al.* (2006) for condensing R134a in microchannels. Experiments were conducted on multiport test sections with hydraulic diameters ranging from $0.506 < D_h < 1.524$ mm and mass fluxes ranging from 150 to 750 $\text{kg m}^{-2} \text{s}^{-1}$. Their boundary layer modeling approach was based on the work by Traviss *et al.* (1973) for shear-driven flow. They expressed the heat transfer coefficient in terms of a shear velocity, u^* , and dimensionless temperature, T^+ as follows:

$$h = \frac{\rho_l \cdot c_{p,l} \cdot u^*}{T^+} \quad (6.56)$$

The shear velocity, u^* , is related to the predicted pressure drop as follows:

$$u^* = \sqrt{\frac{\tau_i}{\rho_l}} = \sqrt{\left(\frac{dp}{dz}\right)_f \frac{D_i}{4\rho_l}} \quad (6.57)$$

The frictional pressure drop is approximated using the annular flow correlation from the work of Garimella *et al.* (2005) on these same hydraulic diameters. Different expressions for the non-dimensional temperature, T^+ , were developed for different liquid Reynolds number, Re_l , ranges.

For $Re_l < 2100$

$$T^+ = 5 \cdot Pr_l + 5 \cdot \ln \left[Pr_l \left(\frac{\delta^+}{5} - 1 \right) + 1 \right] \quad (6.58)$$

For $Re_l > 2100$

$$T^+ = 5 \cdot Pr_l + 5 \cdot \ln(5 \cdot Pr_l + 1) + \int_{30}^{\delta^+} \frac{dy^+}{\left(\frac{1}{Pr_l} - 1\right) + \frac{y^+}{5} \left(1 - \frac{y^+}{R^+}\right)} \quad (6.59)$$

where

$$\begin{aligned} y^+ &= \frac{y \cdot \rho_l \cdot u^*}{\mu_l} \\ R^+ &= \frac{R \cdot \rho_l \cdot u^*}{\mu_l} \\ \delta^+ &= \frac{\delta \cdot \rho_l \cdot u^*}{\mu_l} \end{aligned} \quad (6.60)$$

The film thickness, δ , is obtained from the Baroczy (1965) void fraction correlation. The model under-predicts most data with an AAD and AD of 27.7 and -11.7%, respectively. This model predicts the data from the present study well, even for the wavy flow regime data points, although its formulation was based on annular flow. While the agreement is reasonable, the pressure drop model of Garimella *et al.* (2005) slightly over-predicts the pressure drop data from the present study, which may not result in the best representation of the heat transfer data from the present study.

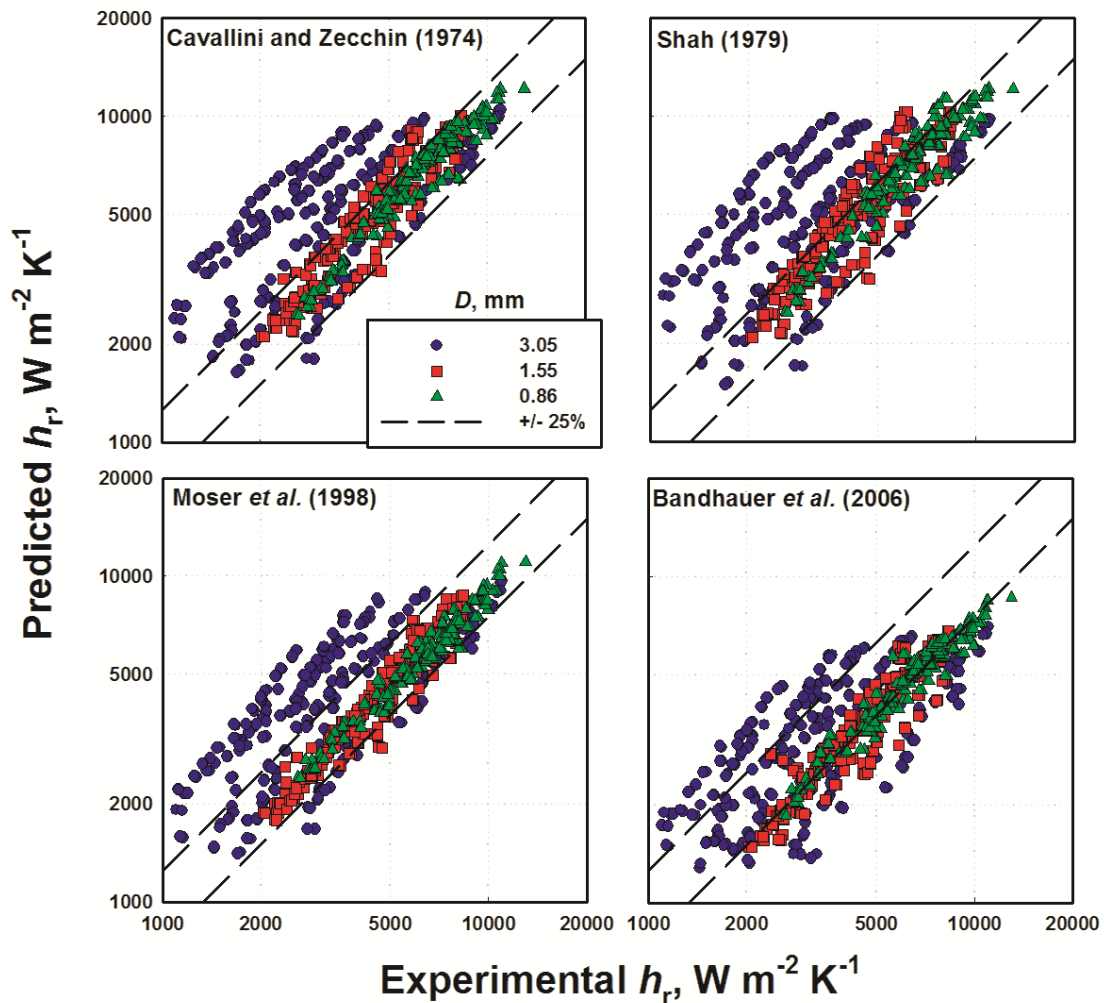


Figure 6.19: Comparison of Experimental h_r from the Present Study with Annular Regime Heat Transfer Models in the Literature

Multi-Regime Models

Dobson and Chato (1998) developed a multi-regime heat transfer model based on data for condensing R12, R22, R134a, and near-azeotropic blends of R32/R125 (50/50 and 60/40) flowing through tube diameters of 3.14 and 7.04 mm. Experimental mass fluxes and reduced pressures ranged from 75 to 800 kg m⁻² s⁻¹, and 0.21 to 0.57, respectively. They observed stratified, wavy, wavy annular, annular mist, and slug flow and developed sub models for gravity and shear dominated flows. For shear driven flow, they developed an empirical two-phase multiplier for the Dittus-Boelter equation for single-phase flow.

$$Nu = 0.023 Re_1^{0.8} Pr_1^{0.4} \left[1 + \frac{2.22}{X_{tt}^{0.89}} \right] \quad (6.61)$$

Here the exponent on the Prandtl number is 0.4, which is recommended for heating, but they found better agreement with their data using this exponent and noted that it had also been used in the Shah (1979) correlation. The two-phase multiplier is a function of the turbulent-turbulent Martinelli parameter, X_{tt} , which approaches infinity as quality approaches zero, resulting in the single-phase heat transfer coefficient. For gravity driven flow, they modeled the upper film and lower film separately and applied these expressions based on wetted perimeter fraction. The upper film condensation was modeled using a film condensation approach.

$$Nu_{film} = \frac{0.23 Re_{vo}^{0.12}}{1 + 1.11 X_{tt}^{0.58}} \left[\frac{Ga Pr_1}{Ja_1} \right]^{0.25} \quad (6.62)$$

where

$$Ga = \frac{g \rho_l (\rho_l - \rho_v) D^3}{\mu_l^2} \quad (6.63)$$
$$Ja_l = \frac{c_{p,l} (T_{sat} - T_{wall})}{i_{lv}}$$

They hypothesized that heat transfer in the lower film would be governed by convective flow and developed a two-phase multiplier for this region.

$$Nu_{\text{pool}} = 0.0195 Re_1^{0.8} Pr_1^{0.4} \left(1.376 + \frac{c_1}{X_{tt}^{c_2}} \right) \quad (6.64)$$

For $0 < Fr_{so} \leq 0.7$,

$$\begin{aligned} c_1 &= 4.172 + 5.48 Fr_1 - 1.564 Fr_1^2 \\ c_2 &= 1.733 - 0.169 Fr_1 \end{aligned} \quad (6.65)$$

For $Fr_{so} > 0.7$,

$$\begin{aligned} c_1 &= 7.242 \\ c_2 &= 1.655 \end{aligned} \quad (6.66)$$

The wetted perimeter in contact with the forced convection component is predicted using the Zivi (1964) void fraction model and the geometric relation:

$$1 - \frac{\theta}{\pi} = \frac{\cos^{-1}(2\alpha - 1)}{\pi} \quad (6.67)$$

The Nusselt number accounting for upper and lower film contributions in wavy flow is then calculated as follows:

$$Nu_{\text{wavy}} = Nu_{\text{film}} + Nu_{\text{pool}} \left(1 - \frac{\theta}{\pi} \right) \quad (6.68)$$

Dobson and Chato recommended that the shear driven correlation should be used for all cases in which mass flux is greater than $500 \text{ kg m}^{-2} \text{ s}^{-1}$, or when the Soliman modified Froude number, Fr_{so} , is greater than 20. For all other cases, the wavy correlation should be used. This model assigns 22% of the data from the present study to the wavy regime and the rest to annular flow. It also predicts some wavy flow for the smallest tube diameter (0.86 mm) tube, which demonstrates that the flow regime determination by Dobson and Chato may not adequately account for diameter effects on flow regime transitions for the present data. The majority of the data from the present study are over-predicted with an AAD and AD of 54.4 and 52.2%, respectively. The over-prediction is primarily for the wavy flow regime, but the shear-driven correlation predicts data better (AAD = 42.7%, AD = 40.1%), with improving agreement with decreasing tube diameter.

The agreement is best at the lowest reduced pressure and decreases with increasing reduced pressure, primarily because such pressures are outside its range of applicability.

Cavallini *et al.* (2002) developed a multi-regime pressure drop and heat transfer model for pure and blended halogenated refrigerants. They compared their model to a large data base of condensing refrigerants R22, R134a, R125, R32, R236ea, R407C and R410A in an 8-mm smooth tube at mass fluxes ranging from 100 to 750 kg m⁻² s⁻¹, and saturation temperatures ranging from 30 to 60°C. For Annular flow ($J_G^* \geq 2.5$.) they adapted the approach of Kosky and Staub (1971), which uses the heat-momentum analogy and used their modification (Cavallini *et al.*, 2002) to the Friedel (1979) correlation as the input for predicting interfacial shear.

$$h = \frac{\rho_l c_{p,l} (\tau / \rho_l)^{0.5}}{T^+} \quad (6.69)$$

where

$$\begin{aligned} T^+ &= \delta^+ Pr_l & \delta^+ &\leq 5 \\ T^+ &= 5 \left\{ Pr_l + \ln \left[1 + Pr_l \left(\delta^+ / 5 - 1 \right) \right] \right\} & 5 < \delta^+ < 30 \\ T^+ &= 5 \left[Pr_l + \ln (1 + 5 Pr_l) + 0.495 \ln (\delta^+ / 30) \right] & \delta^+ \geq 30 \\ \delta^+ &= (Re_l / 2)^{0.5} & \text{for } Re_l \leq 1145 \\ \delta^+ &= 0.0504 Re_l^{7/8} & \text{for } Re_l > 1145 \\ \tau &= (dp/dz)_f D/4 \end{aligned} \quad (6.70)$$

For stratified flow, they hypothesized that heat is transferred through the thin gravity driven layer of condensate on the upper part of the tube and also accounted for heat transfer through the thick layer of liquid in the bottom part of the tube. A Nusselt-type equation was used to predict heat transfer in the upper film, while a two-phase multiplier and single-phase heat transfer coefficient were used to account for heat transfer in the bottom pool. The resulting equation for stratified flow is:

$$h_{\text{strat}} = 0.725 \left[1 + 0.82 \left(\frac{1-x}{x} \right)^{0.268} \right]^{-1} \left[\frac{k_1^3 \rho_1 (\rho_1 - \rho_v) g i_{lv}}{\mu_1 D \Delta T} \right]^{0.25} + h_{1,\text{pool}} \left(1 - \frac{\theta}{\pi} \right) \quad (6.71)$$

where

$$\begin{aligned} h_{1,\text{pool}} &= h_{1o} (1-x)^{0.8} \\ h_{1o} &= 0.023 \text{Re}_{1o}^{0.8} \text{Pr}_1^{0.4} \frac{k_1}{D} = 0.023 \left(\frac{GD}{\mu_1} \right)^{0.8} \left(\frac{c_{p,l} \mu_1}{k_1} \right)^{0.4} \frac{k_1}{D} \\ 1 - \frac{\theta}{\pi} &= \frac{\cos^{-1}(2\alpha - 1)}{\pi} \end{aligned} \quad (6.72)$$

The amount of liquid flowing in the lower film is approximated using the void fraction model presented by Zivi (1964). Cavallini *et al.* recommended using a linear interpolation between the stratified and annular regimes based on the non-dimensional gas velocity, J_G^* .

$$h_{\text{trans}} = \left(h_{\text{ann}, J_G^*} - h_{\text{strat}} \right) \left(\frac{J_G^*}{2.5} \right) + h_{\text{strat}} \quad (6.73)$$

This approach allows for a smooth transition from stratified to annular flow predictions. For slug flow, they again linearly interpolated between stratified flow at the transition ($X_{tt} = 1.6$) and single-phase heat transfer where the mass flow rate is fully in the liquid phase using the Dittus-Boelter equation (Equation 6.52.)

$$\begin{aligned} h_{\text{tran, strat-slug}} &= h_{1o} + \frac{x(h_{\text{strat}, X_{tt}=1.6})}{x_{X_{tt}=1.6}} \\ x_{X_{tt}=1.6} &= \left(\frac{\mu_1}{\mu_v} \right)^{1/9} \left(\frac{\rho_v}{\rho_1} \right)^{5/9} \left[1.686 + \left(\frac{\mu_1}{\mu_v} \right)^{1/9} \left(\frac{\rho_v}{\rho_1} \right)^{5/9} \right]^{-1} \end{aligned} \quad (6.74)$$

The majority of the results from the present study are predicted to be in the annular flow regime (81.7%), with 13.7% predicted to be in the stratified-annular regime, and the remaining 4.6% predicted to be in the stratified slug regime. A majority of the data are under-predicted with an AAD and AD of 28.0 and -16.9%, respectively. The large tube

diameter data are on average slightly over-predicted, which can be attributed to an annular flow model being applied to wavy flow data. The annular flow data in the small tube diameters are under-predicted, which may be due to the inability to accurately predict pressure drop data from the present study as discussed in the previous section in connection with their pressure drop model (Cavallini *et al.*, 2002). The annular flow correlation is a shear driven model and both the pressure drop and heat transfer coefficients consistently under-predict the data from the present study by about -30%.

Thome *et al.* (2003) developed a multi-regime heat transfer model for condensing refrigerants. They used the flow regime map developed by El Hajal *et al.* (2003). Thome *et al.* (2003) combined the intermittent and mist flow regimes with the annular flow regime for modeling purposes, stating that they are all shear driven flows. Their heat transfer model was fit to a large database of refrigerant data that was taken from the previous study of Cavallini *et al.* (2002). They also compared their results to hydrocarbon condensation data. They hypothesized that heat transfer during condensation is either forced convection driven or gravity driven. The convective component is predicted using a two-phase multiplier.

$$h_{\delta} = 0.003 \cdot \text{Re}_{1,\delta}^{0.74} \text{Pr}_1^{0.5} \frac{k_1}{\delta} \phi \quad (6.75)$$

This is a unique approach where the characteristic length scale is not the typically used tube diameter, but the film thickness, δ . The liquid Reynolds number is also defined using the film thickness and the average liquid velocity, U_1 .

$$\text{Re}_{1,\delta} = \frac{4\rho_1 U_1 \delta}{\mu_1} = \frac{4G(1-x)\delta}{(1-\alpha)\mu_1} \quad (6.76)$$

where

$$A_1 = (1-\alpha)\pi \frac{D^2}{4} = \frac{(2\pi-\theta)}{8} [D^2 - (D-2\delta)^2] \quad (6.77)$$

The angle θ is described as the upper angle of the tube wetted by the condensing film. They used the void fraction model from their previous work, El Hajal *et al.* (2003), for Equation 6.77. This approach treats the lower liquid as a uniformly thick liquid film along the bottom of the tube instead of the typical approach, which models the liquid as a stratified pool. The upper film heat transfer coefficient was obtained using Nusselt theory for laminar flows. Instead of integrating from 0 to $\theta/2$, they approximated the contribution of the film by using an averaged solution.

$$h_{\text{film}} = 0.728 \left[\frac{\rho_l (\rho_l - \rho_v) g i_v k_l^3}{\mu_l D (T_{\text{sat}} - T_{\text{wall},i})} \right] \quad (6.78)$$

They combined the effects of both portions by weighting the amount of area in contact with the tube diameter using the angle θ .

$$h = h_{\text{film}} \left(\frac{\theta}{2\pi} \right) + h_\delta \left(1 - \frac{\theta}{2\pi} \right) \quad (6.79)$$

This type of approach allows for smooth transition between stratified, wavy and annular flow regimes. The flow regime map of El Hajal *et al.* (2003) was used to determine the applicable regime, which allows for determination of θ and the two-phase multiplier, ϕ . When mist, annular or intermittent flow are predicted, $\theta = 0$, and the two-phase multiplier is:

$$\phi = 1 + \left(\frac{U_v}{U_l} \right)^{0.5} \left(\frac{(\rho_l - \rho_v) g \delta^2}{\sigma} \right)^{0.25} \quad (6.80)$$

They likened the two-phase multiplier to a surface roughness and theorized that the interfacial roughness should be directly linked to the interfacial slip, $U_v U_l^{-1}$. The second term was adapted from the Taylor instability wavelength of a film. Again, they theorized that surface roughness should decrease with increasing surface tension because surface

tension will dampen out surface waves. The exponents in the above equation were based on the test data. For fully stratified or stratified-wavy flow:

$$\theta = \theta_{\text{strat}} \left[\frac{(G_{\text{wavy}} - G)}{(G_{\text{wavy}} - G_{\text{strat}})} \right]^{0.5} \quad (6.81)$$

Where θ_{strat} can be solved using Equation 6.71 and G_{wavy} and G_{strat} are determined using the flow regime map presented by El Hajal *et al.* (2003).

$$\phi = 1 + \left(\frac{U_v}{U_l} \right)^{0.5} \left(\frac{(\rho_l - \rho_v) g \delta^2}{\sigma} \right)^{0.25} \left(\frac{G}{G_{\text{strat}}} \right) \quad (6.82)$$

Here the two-phase multiplier is similar to that for annular flow, except for the inclusion of the ratio of mass fluxes, which dampens out the enhancement effects at the interface. The flow regime map by El Hajal *et al.* (2003) predicts all of the data from the present study in the shear-driven regime (either intermittent, annular, or mist); therefore, all comparisons with the data from the present study are based on Equation 6.74. The correlation of Thome *et al.* (2003) generally under-predicts heat transfer data from the present study with an AAD and AD of 32.4 and -16.3%, respectively. The model predicts increasing heat transfer coefficients with increasing reduced pressures, which is the opposite of the observed trends. As reduced pressure increases, surface tension significantly decreases, which results in an overall increase in the predicted two-phase multiplier developed by Thome *et al.* (2003) (Equation 6.80) for the fluid and conditions investigated in the present study. Also, it is important to note that their correlation is heavily dependent on the film thickness, which is a function of the void fraction. Thome *et al.* did not measure void fraction in this study, but developed their void fraction model (Equation 6.27) using inferences from heat transfer data. Their void fraction model (El Hajal *et al.*, 2003) was found to consistently over-predict the measured void fraction

values from the present study. As a result, the estimated film thickness, δ , is under-predicted.

Andresen (2007) developed an annular and wavy flow heat transfer model based on data on condensing R410A and R404A at reduced pressures of 0.8 and 0.9. He investigated condensing R410A in channel diameters ranging from 0.76 to 3.05 mm and on 6.22 and 9.40 mm diameter tube R410A data from Mitra (2005) and on 9.40 mm diameter tubes R404A data from Jiang (2004) to develop this model. His annular flow regime Nusselt number correlation was as follows:

$$Nu_{\text{annular}} = 0.0133 \text{Re}_1^{4/5} \text{Pr}_1^{1/3} \left[1 + \left(\frac{x}{1-x} \right)^{0.80} \left(\frac{\rho_1}{\rho_v} \right)^{0.88} \right] \quad (6.83)$$

The term in the brackets resembles the inverse Martinelli parameter, but without the viscosity ratio. For the wavy flow regime, he modeled the upper film surface and the liquid pool at the bottom of the tube separately like the approach used by previous researchers Dobson and Chato (1998) and Cavallini *et al.* (2002). The liquid film was modeled using a Nusselt falling film condensation analysis. The liquid pool contribution was obtained using a two-phase multiplier similar to that of Cavallini and Zecchin (1974). The wetted perimeter in contact with the liquid pool was approximated using the Baroczy (1965) void fraction model. The overall wavy flow regime Nusselt number model he presented is as follows:

$$Nu_{\text{wavy}} = \left(\frac{1.93}{2\pi} \right) \left(Ra \left[\frac{1}{Ja_1} + 1 \right] \right)^{1/4} + 0.018 \text{Re}_1^{0.8} \text{Pr}_1^{1/3} \left[1 + \left(\frac{x}{1-x} \right) \left(\frac{\rho_1}{\rho_v} \right)^{1.24} \right] \left(\frac{D}{9.389} \right)^{0.34} \left(1 - \frac{\theta}{2\pi} \right) \quad (6.84)$$

Here the Jakob number Ja_1 is given by Equation 6.63, while the Rayleigh number, Ra , is the product of the Prandtl and Grashof number. Andresen estimated the transition region

from annular to wavy flow using the non-dimensional vapor velocity, J_G^* , and suggested that the transition most likely occurs at approximately $J_G^* = 2.5$, which was the criterion presented by Cavallini *et al.* (2002). From $J_G^* = 2$ to $J_G^* = 3$ a linear interpolation between the wavy and annular flow regime models based on J_G^* is suggested. This transition criterion predicts 75.4% of the data from the present study in the annular regime, 11.0% of the data in the wavy flow regime, and 13.6% of the data in the transitional flow regime. The model has the best agreement with data from the present study out of all models from the literature considered here, with an AAD and AD of 25.4 and -13.5%, respectively. In general, the model under-predicts all annular data and over-

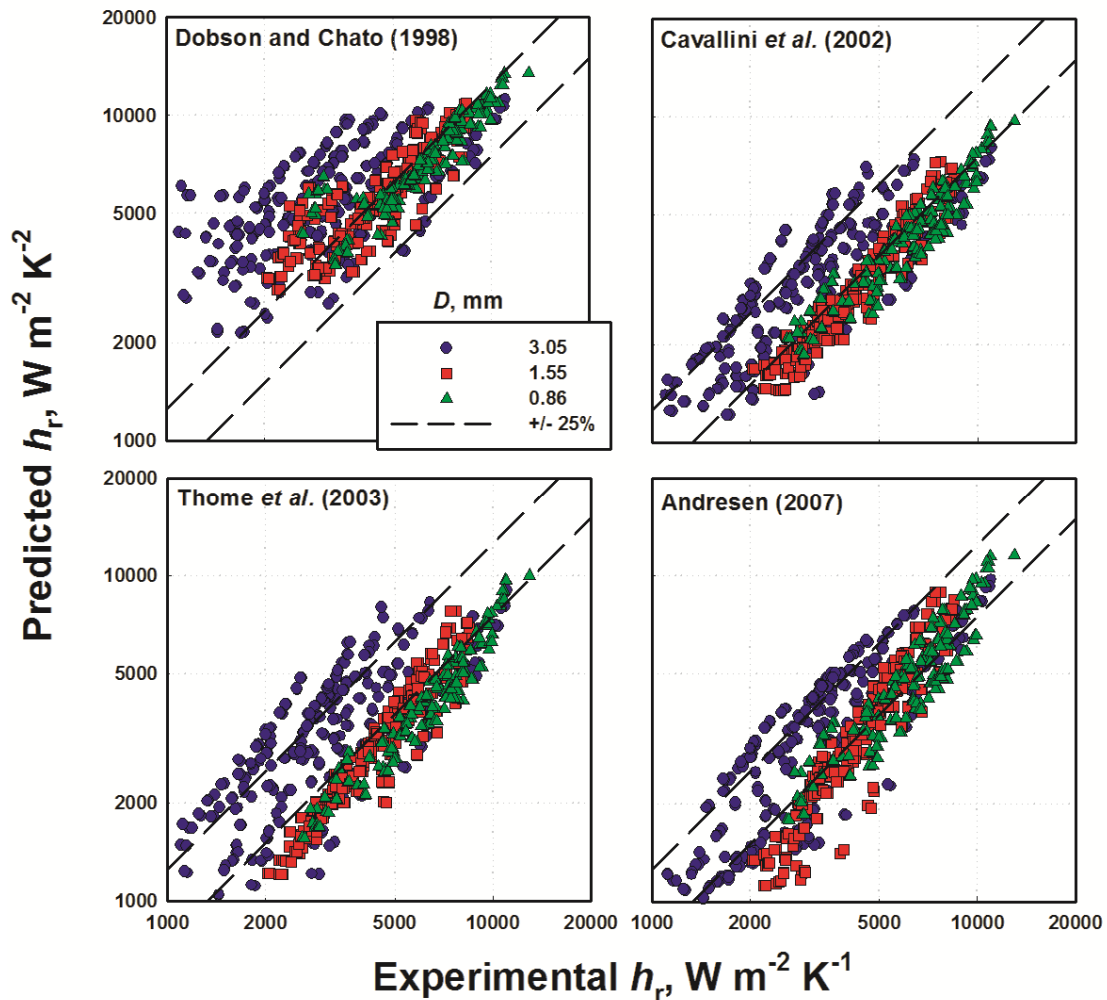


Figure 6.20: Comparison of Experimental h_r from the Present Study with Multi-Regime Heat Transfer Models in the Literature

predicts wavy flow data from the present study. This may be due to wavy flow data points from the present study being inaccurately predicted as being in annular flow. However, this model appears to capture the effects of changes in properties with reduced pressure the best out of all models from literature considered here. The data from the present study are consistently under-predicted with AD of -18.1, -13.4, -9.9, -10.9% for $p_r = 0.38, 0.49, 0.62, \text{ and } 0.77$, respectively. This is perhaps because of the high reduced pressures and large range of tube diameters investigated for R410A and R404A in the studies by Jiang (2004), Mitra (2005), and Andresen (2007).

Table 6.15: Predictive Capabilities of Various Models in the Literature for Data from the Present Study Categorized by Tube Diameter

Study	Diameter, mm						TOT	
	3.05		1.55		0.86		AAD %	AD %
	AAD %	AD %	AAD %	AD %	AAD %	AD %	AAD %	AD %
Annular								
Cavallini and Zechin (1974)	75.3	69.2	16.2	11.2	9.9	6.4	38.5	33.5
Shah (1979)	80.9	73.4	21.2	16.3	14.2	11.9	43.6	38.3
Moser <i>et al.</i> (1998)	48.7	37.6	10.1	-7.1	10.3	-10.0	25.8	-10.3
Bandhauer <i>et al.</i> (2006)	32.7	5.4	23.3	-22.7	24.3	-24.3	27.4	-11.7
Multi-Regime								
Dobson and Chato (1998)	94.0	90.9	33.4	31.1	19.6	19.0	54.4	52.2
Cavallini <i>et al.</i> (2002)	25.7	1.6	29.2	-29.2	30.0	-30.0	28.0	-16.9
Thome <i>et al.</i> (2003)	31.5	8.0	31.5	-31.4	34.8	-34.8	32.4	-16.3
Andresen (2007)	26.3	2.1	26.8	-26.0	22.0	-21.8	25.4	-13.5

Summary of Comparison

A summary of comparisons of the heat transfer data from the present study with the predictions of correlations from the literature is provided in Table 6.15 categorized by tube diameter, and in Table 6.16 by saturation temperature. Some models are able to predict the data from the present study well in some ranges of geometry and operating conditions but in general, do not predict the trends with respect to tube diameter and operating conditions well. The large disagreements are in part due to the fact that the flow regimes observed for some data points in this study do not correspond to the regimes predicted by the correlations, which leads to the inapplicability of the heat transfer models. Several of the heat transfer models are reliant on void fraction correlations to

Table 6.16: Predictive Capabilities of Various Models in the Literature for Data from the Present Study Categorized by Saturation Temperature

	$T_{sat}, ^\circ\text{C} (p_r)$							
	30 (0.38)		40 (0.49)		50 (0.62)		60 (0.77)	
Study	AAD %	AD %	AAD %	AD %	AAD %	AD %	AAD %	AD %
Annular								
Cavallini and Zechin (1974)	11.3	-4.5	24.1	23.0	53.7	53.5	83.3	83.3
Shah (1979)	11.9	-5.1	24.4	23.7	59.7	59.7	101.0	101.0
Moser <i>et al.</i> (1998)	15.0	-14.3	13.9	5.2	34.4	24.3	49.6	38.9
Bandhauer <i>et al.</i> (2002)	33.1	-33.1	18.7	-17.1	23.8	-0.7	35.4	15.9
Multi-Regime								
Dobson and Chato (1998)	19.0	12.1	40.9	40.4	74.4	74.4	104.6	104.6
Cavallini <i>et al.</i> (2002)	29.0	-29.0	20.9	-18.5	28.3	-9.3	36.5	-5.0
Thome <i>et al.</i> (2003)	31.8	-31.8	25.1	-20.3	33.1	-7.8	42.9	3.1
Andresen (2006)	19.2	-18.1	20.9	-13.4	30.7	-9.9	34.9	-10.9

determine the wetted perimeter in contact with different heat transfer regions, or to determine liquid film thicknesses. The void fraction correlations are often taken from literature for significantly different conditions, which may also lead to improper modeling of the hydrodynamics.

6.2.5 Summary

It can be seen from the above discussion that while some models in the literature predict pressure drop and heat transfer coefficients from the present study well under certain conditions, there is no comprehensive model that accurately accounts for the variation of phase properties with saturation temperature and the effects of hydraulic diameter in mini and micro channels. The discrepancies stem from the inability of most flow regime maps to accurately predict flow regimes observed for the geometries and conditions investigated here, which leads to pressure drop and heat transfer models developed based on different physical idealizations being applied incorrectly. Furthermore, pressure drop and heat transfer coefficient models require knowledge of the distribution of vapor and liquid within the tube; however, these models are based on measurements for different fluids or are inferred from other parameters rather than being directly measured. For example, the work by El Hajal *et al.* (2003) and Thome *et al.* (2003) attempted to develop a comprehensive integrated approach to flow regime determination and condensation heat transfer modeling. They identified the importance of predicting film thicknesses, and deduced it from a void fraction model which was in turn inferred from other measured parameters. While their approach was well conceived, it was ultimately based on observations of evaporating flows and a regression analysis of a large database of condensation data. Therefore, the governing mechanisms may not have been adequately modeled, which leads to reasonable agreement with the data base, but may not actually model the underlying flow phenomena. Stratified heat transfer models like that of

Dobson and Chato (1998), and Cavallini *et al.* (2002) rely on void fraction to determine the amount of wetted perimeter in contact with the stratified pool. Both researchers used the Zivi (1964) correlation, which is an analytical model developed for steam flow, and may result in inaccurate predictions of convective contributions. An integrated modeling approach where void fraction, pressure drop and heat transfer coefficients validated over a large range of operating conditions and diameters is required to yield improved predictive capabilities for condensation for the data under consideration in the present study.

CHAPTER 7: MODEL DEVELOPMENT

The results and discussion presented in the previous chapter demonstrate that the void fraction, pressure drop and heat transfer coefficient models and correlations from the literature are unable to adequately predict the data from the present study. Therefore, new models were developed here for void fraction, pressure drop, and heat transfer coefficients. The void fraction model and the predicted flow regimes are used as building blocks for the development of the pressure drop and heat transfer models.

The flow regime map developed by Nema (2007) agreed well with the flow regimes observed in the present study. Therefore, the criteria from that map were used to assign flow regimes to data points. For the 3.05 mm diameter tube data from the present study, the intermittent, wavy, annular and mist flow regimes were predicted by the Nema flow regime map. For the 0.508, 0.86, 1.00, and 1.55 mm diameter tube data from the present study, only intermittent, annular and mist flow were predicted by the Nema flow regime map. The predicted flow regimes were then used as a basis to develop mechanistic models. A summary of flow regimes predicted for the void fraction, pressure drop and heat transfer data from the present study is provided in Table 7.1. The largest portions of

Table 7.1: Flow Regimes Predicted by Nema (2007) for R404A Data from the Present Study

Regime	α	ΔP	h
Intermittent	4	4	0
Intermittent/Annular	22	22	7
Intermittent/Discrete Wave	17	16	10
Discrete Wave	45	45	63
Disperse Wave	21	54	67
Annular	33	178	186
Mist	0	45	69
Total	142	364	402

the pressure drop and heat transfer data are in the annular flow regime. In this section, a void fraction model is presented first, followed by the pressure drop and heat transfer models, which use the void fraction model developed from this work as a basis.

7.1 Void Fraction Model

The vapor drift flux velocity was used here to develop a model for the void fraction. The derivation of the vapor drift flux velocity was conducted based on an approach similar to that presented by Ishii *et al.* (1976). A schematic of the analysis is shown in Figure 7.1.

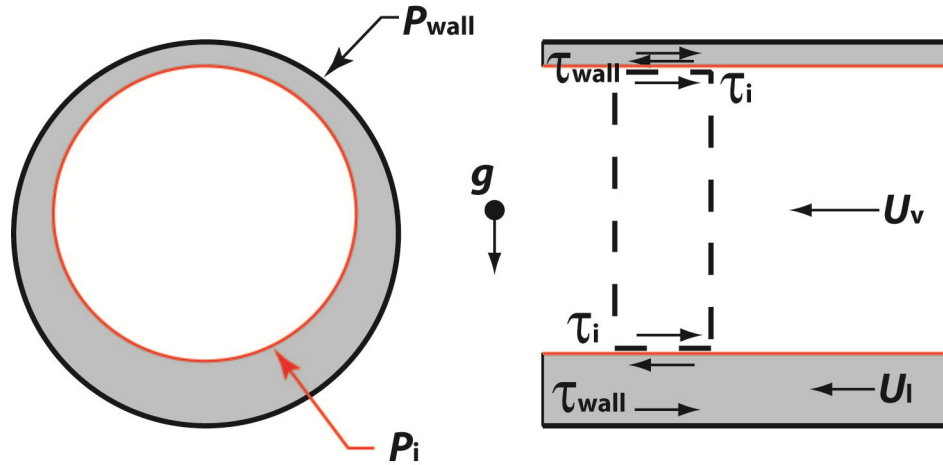


Figure 7.1: Schematic of Perimeters and Shear Stresses for Void Fraction Model Development

The one-dimensional momentum equations for each phase are:

Vapor Phase Momentum

$$-\left(\frac{dP}{dz} + \rho_v g\right) = \frac{\tau_i P_i}{\alpha A} \quad (7.1)$$

Liquid Phase Momentum

$$-\left(\frac{dP}{dz} + \rho_l g\right) = \frac{\tau_{wall} P_{wall}}{A(1-\alpha)} - \frac{\tau_i P_i}{A(1-\alpha)} \quad (7.2)$$

Where P_i is the perimeter of the interface and P_{wall} is the perimeter of the wall. The ratio of the interfacial perimeter to wall perimeter can be represented by the non-dimensional term:

$$\xi = \frac{P_i}{P_{\text{wall}}} \quad (7.3)$$

Subtracting Equation 7.2 from 7.1, the following result is obtained for equal pressure gradients in both phases.

$$0 = \frac{\tau_{\text{wall}} P_{\text{wall}}}{A(1-\alpha)} - \frac{\tau_i P_i}{A} \left[\frac{1}{\alpha} + \frac{1}{1-\alpha} \right] = \frac{\tau_{\text{wall}} P_{\text{wall}}}{A(1-\alpha)} - \frac{\tau_i P_i}{A\alpha(1-\alpha)} \quad (7.4)$$

By rearranging and balancing the interfacial and wall shear forces, the following equation is obtained:

$$\frac{\tau_i P_i}{\alpha} = \tau_{\text{wall}} P_{\text{wall}} \quad (7.5)$$

To obtain a closed form solution, the shear stresses in the liquid film and at the interface need to be defined. The film shear stress is defined as:

$$\tau_{\text{wall}} = \frac{f_i \rho_l U_l |U_l|}{2} \quad (7.6)$$

The interfacial shear stress is defined as:

$$\tau_i = \frac{f_i \rho_v U_r^2}{2} \quad (7.7)$$

Where U_r is the relative velocity between the two phases and can be related to the vapor drift flux velocity using the following relation:

$$\bar{V}_{vj} = U_v - j = (1-\alpha)U_r \quad (7.8)$$

Substituting Equations 7.6 and 7.7 into 7.5, the force balance can be written in terms of velocities and friction factors.

$$\left(\frac{f_i \rho_v U_r^2}{2}\right) \frac{P_i}{\alpha} = \left(\frac{f_i \rho_l U_1 |U_1|}{2}\right) P_{\text{wall}} \quad (7.9)$$

Rearrangement of Equation 7.9 yields the following expression for the relative velocity, U_r , between the two phases

$$U_r^2 = \left(\frac{f_l}{f_i}\right) \left(\frac{\rho_l}{\rho_v}\right) \left(\frac{P_{\text{wall}}}{P_i}\right) U_1 |U_1| \alpha \quad (7.10)$$

The liquid film velocity can be approximated using the relationship:

$$U_1 = j_l / (1 - \alpha) \quad (7.11)$$

Substituting Equation 7.11 and 7.8 into Equation 7.10, the vapor drift flux velocity can be approximated as follows:

$$\bar{V}_{vj}^2 = \left(\frac{f_l}{f_i}\right) \left(\frac{\rho_l}{\rho_v}\right) \left(\frac{P_{\text{wall}}}{P_i}\right) \alpha j_l^2 \quad (7.12)$$

The interfacial friction has been predicted by previous researchers in two-phase flow. Wallis (1969) developed one of the original equations for interfacial friction and more recently, Garimella *et al.* (2005) developed a formulation specific for condensing flow:

$$\frac{f_i}{f_l} = A \cdot X^a \text{Re}_l^b \left(\frac{\text{Ca}_l}{1 - \alpha}\right)^c \quad (7.13)$$

The interfacial friction factor ratio was defined by Garimella *et al.* (2005) as a function of the Martinelli parameter, $X = \sqrt{(dp/dz)_{fl} / (dp/dz)_{fv}}$, the liquid Reynolds number, $\text{Re}_l = (1 - x) \cdot G \cdot D / [\mu_l \cdot (1 + \alpha^{0.5})]$, and the liquid Capillary number, $\text{Ca}_l = \mu_l \cdot j_l / \sigma$. The model in the present study uses the Garimella *et al.* (2005) friction factor ratio while Ishii *et al.* (1976) used the Hewitt and Hall-Taylor (1970) equation for predicting the liquid friction factor and the Wallis (1969) correlation for predicting the interfacial friction factor. Also, the model from the present study differs from the work of Ishii *et al.* (1976) by yielding a modified closed form solution (Equation 7.12) for the vapor drift flux

velocity that uses the non-dimensional terms for the friction factor ratio from Garimella *et al.* (2005) with coefficients and exponents obtained from a regression analysis. The friction factor ratio of Garimella *et al.* (2005) was used here because it was specifically developed for condensing refrigerants in small channels. The resulting vapor drift flux velocity equation can then be interpreted in terms of the parameters:

$$\bar{V}_{vj} = f \left(X, Re_1, Ca_1, \sqrt{\frac{\rho_l}{\rho_v}}, \sqrt{\frac{P_{wall}}{P_i}}, \sqrt{\alpha}, j \right) \quad (7.14)$$

It was observed that the bulk measured void fraction was not strongly dependent on diameter, mass flux, or flow regime as discussed in Section 6.7. Therefore, the Reynolds number, and perimeter ratio are not considered to be particularly significant, and are excluded from the formulation. It was also deemed that any minor gains in accuracy by retaining void fraction as a dependent variable would be offset by the requirement of an iterative solution; therefore, the void fraction was also excluded from the formulation. The vapor drift flux velocity should approach zero resulting in the void fraction approaching the homogeneous model as the critical pressure is approached. To account for this observation, an additional minus one is included in the density ratio term. As a result, as the critical pressure is approached, the density ratio will tend to unity and the drift flux will approach zero. The formulation is simplified based on these idealizations to yield the following vapor drift velocity equation:

$$\bar{V}_{vj} = A \cdot X^b \cdot Ca_1^c \cdot \left(\sqrt{\frac{\rho_l}{\rho_v}} - 1 \right)^d j \quad (7.15)$$

Using this equation as the basis, a regression analysis was conducted only on data in the annular flow regime (23% of data) because the physical considerations are based on this flow mechanism, and the results were extrapolated to the data from the other regimes. The analysis yielded the following expression.

$$\bar{V}_{vj} = 0.336 \cdot X^{0.25} \cdot Ca_1^{0.154} \cdot \left(\sqrt{\frac{\rho_l}{\rho_v}} - 1 \right)^{0.81} j \quad (7.16)$$

The resulting vapor drift flux velocity correlation differs from the Ishii *et al.* (1976) model in several ways. The present model includes the effects of surface tension, while the properties accounted for in the Ishii *et al.* (1976) model are phase densities and viscosities. The present model is also simple to use because it does not need iterative computations, and accounts for the effects of properties at near-critical pressures. As the critical pressure is approached, the drift flux velocity approaches 0 and the void fraction tends to the homogeneous model prediction. The vapor drift flux velocity is related to void fraction as follows:

$$\alpha = \frac{\beta}{C_o + \bar{V}_{vj}/j} \quad (7.17)$$

It is important to note that the drift flux distribution function $C_o = 1$ was found to yield the best agreement over all flow regimes for the data from the present study. The void fraction predictions from this model are shown in Figure 7.2. The model predicts 92.3%

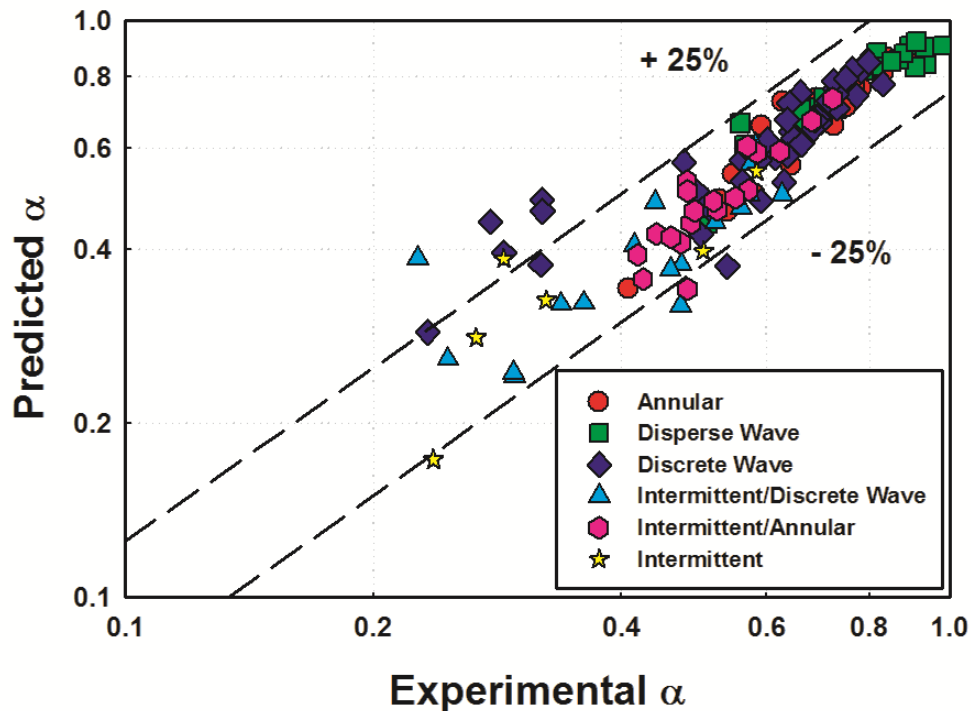


Figure 7.2: Overall Void Fraction Prediction

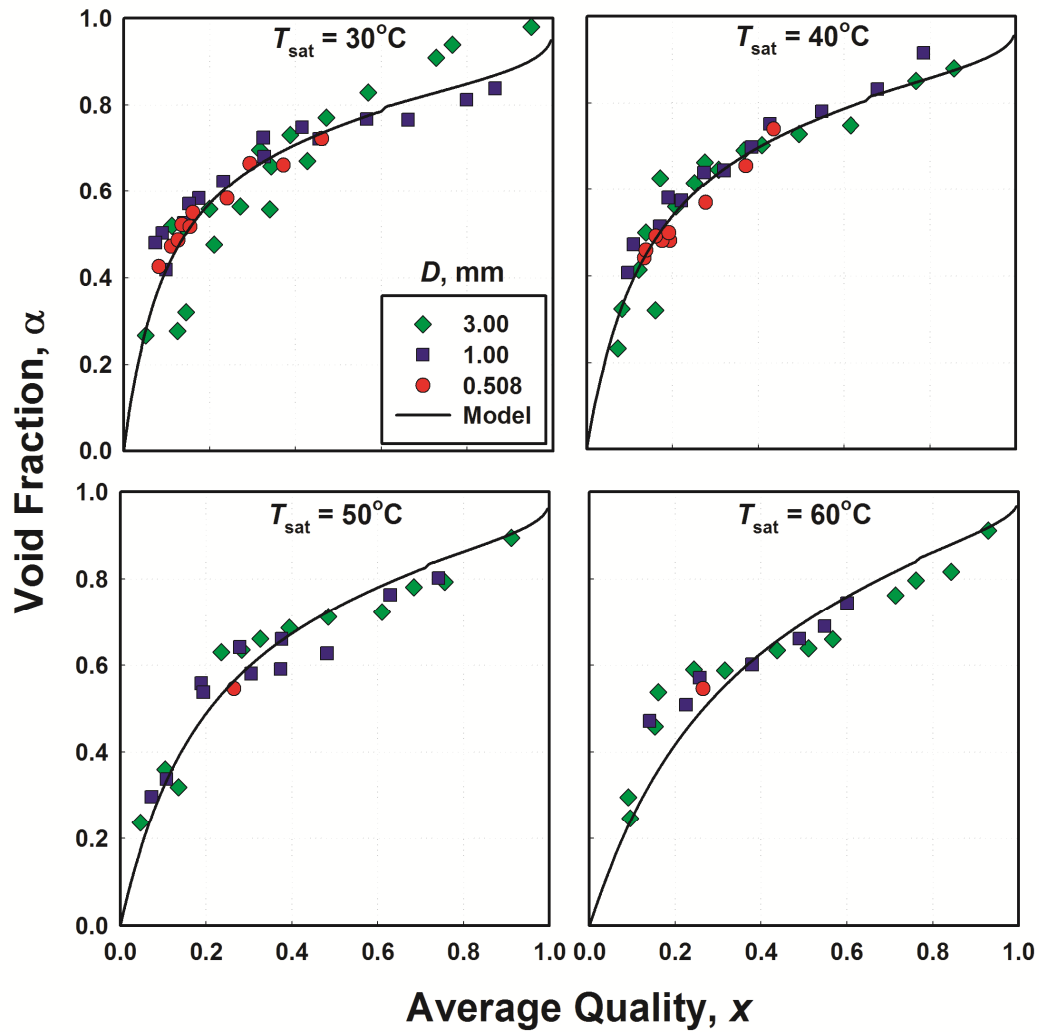


Figure 7.3: Void Fraction Predictions for $T_{sat} = 30, 40, 50$ and 60°C

Table 7.2: Void Fraction Model Predictions

Regime	AAD %	AD %	Data < 25% Deviation
Intermittent	31.4	16.0	57.1
Intermittent/Annular	8.3	-5.8	91.4
Intermittent/Discrete Wave	16.3	-5.8	88.2
Discrete Wave	11.4	4.1	88.9
Disperse Wave	5.1	0.4	100.0
Annular	5.6	-2.2	100.0
Total	10.3	0.2	92.3

of the all the data from the present study within $\pm 25\%$ with an AAD and AD of 10.3 and 0.2%, respectively. The R^2 value of the model is 88.4%. The predictions for each saturation temperature are shown in Figure 7.3. A summary of the average deviations is shown in Table 7.2. The model predicts all data in the annular, disperse wave, and intermittent/annular regime very well. The model predicts these flow regimes well despite being developed using annular flow as the basis. It was observed that other than intermittent flow at low qualities, the flow regime did not have a significant influence on the measured bulk void fraction values. In the present study, a thin film of condensate was always present along the top surface of the tube during wavy flow. Therefore, the differences in shapes between annular and wavy flow interfaces for the conditions for the present study are not substantial, leading to good predictions using the same drift flux model. The model over-predicts 4 data points from the discrete wave, 1 data point intermittent/discrete wave, and 1 data point from the intermittent regime by a substantial margin. These data points were measured at low qualities and have high uncertainties.

The void fraction model is able to represent the trends in data well. The slight discontinuity observed in the model curves is a result of the transition that occurs from laminar to turbulent flow in the liquid phase. Here the Martinelli parameter transitions from $X_{tt} \rightarrow X_{vt}$. As quality approaches unity, the model tends to unity, representing the vapor phase. At high qualities ($x > 0.95$), although the void fraction tends to 1, the inflection in the predicted void fractions is not supported by data, which were generally limited to $x < 0.95$. Therefore, this model is only recommended for qualities ranging from 0.05 to 0.95. As the saturation temperature is increased (Figure 7.3,) void fraction decreases. This is also illustrated in Figure 7.4(a), where increasing saturation temperature results in a diminishing difference between the vapor and liquid properties (e.g., density,) reducing the average velocity differences between the two phases. As the critical temperature is approached, the void fraction model approaches values

corresponding to the homogeneous flow values. This is observed mathematically in Equation 7.16, in which the vapor drift velocity approaches 0 as the density ratio approaches unity. The effects of mass flux on void fraction are shown in Figure 7.4(b), where it can be seen that the mass flux does not appreciably influence the void fraction, as was also the case with the measured data.

The predictions of this void fraction model are also compared with the void fraction data obtained by Winkler *et al.* (2012). A comparison of their data and the predictions of the

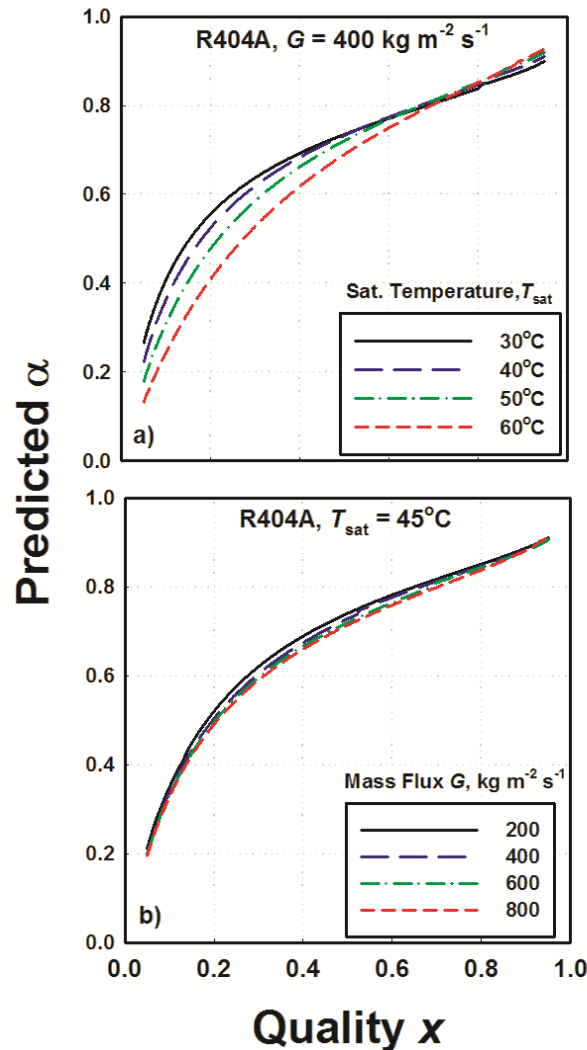


Figure 7.4: Illustration of Void Fraction Prediction Trends for Different (a) Saturation Temperatures and (b) Mass Fluxes

present model is shown in Figure 7.5. The present model predicts 70% of the R134a data of Winkler *et al.* (2012) within 25% with an AAD and AD of 15.6 and -4.0%, respectively. The present model under predicts the data of Winkler *et al.* (2012) in the discrete wave flow regime with an AAD and AD of 9.1 and -8.0%, respectively. This under prediction may be due to their measured void fractions not accounting for the upper liquid film. The present model does not predict the data of Winkler *et al.* (2012) in the intermittent-discrete wave and intermittent flow regimes well. The AAD and AD of the present model when compared to their data in the intermittent flow regime are 30.6 and 8.3%, respectively, while the AAD and AD of the present model when compared to their data in the intermittent-discrete wave region are 21.3 and -5.3%, respectively. In the present study, the highest uncertainties in measured void fraction were at low qualities due to the sensitivity of the void fraction to quality. The difficulty in measuring void fraction in these regions may have led to the low agreement.

A comparison of the predictions of the present model for void fractions of refrigerants R404A and R134a is shown in Figure 7.6. At low qualities, the void fraction of R134a is greater. For example, at $x = 0.2$, the predicted void fraction for R134a is $\alpha = 0.57$, while for R404A, the corresponding value is $\alpha = 0.49$. The predicted void fraction for R134a is 15% larger than that of R404A, and as quality decreases, the deviation in predicted void fraction between R134a and R404A increases. While the model predicts the void fraction of R404A to be greater than that of R134a at high qualities ($x > 0.5$), the resulting predictions are very similar with a maximum deviation between the two of 4.1% at $x = 0.87$ (for R134a, $\alpha = 0.87$, for R404A, $\alpha = 0.90$) indicating that the model is predicting similar film thicknesses for both fluids. As quality increases, the homogeneous void fraction model for both fluids approaches one. The larger difference in phase densities of R134a results in a larger vapor drift flux velocity and therefore, a slightly lower predicted void fraction at higher qualities.

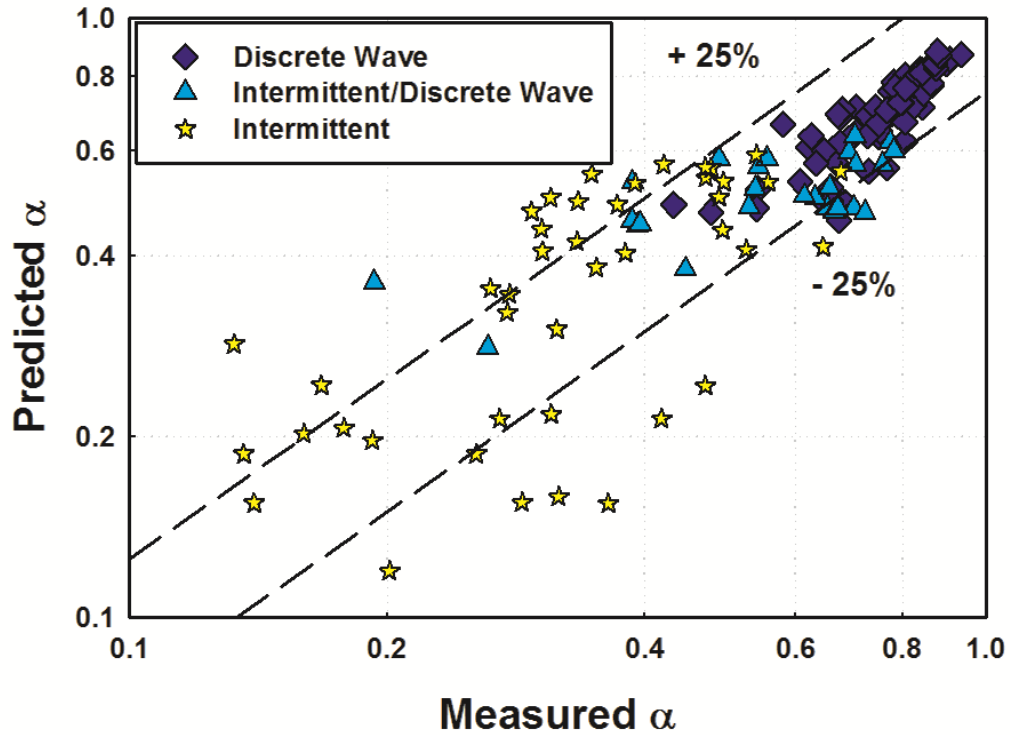


Figure 7.5: Prediction of Void Fraction Data of Winkler *et al.* (2012) for R134a for $2.0 < D_h < 4.91$ mm Using the Model from the Present Study

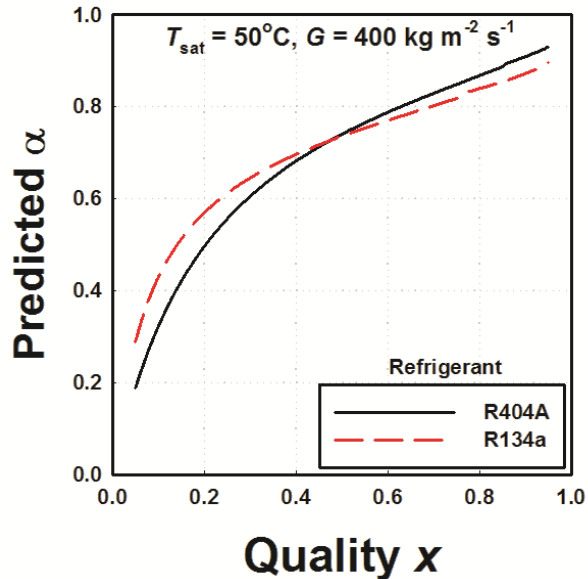


Figure 7.6: Illustration of Void Fraction Prediction Trends for Refrigerants R404A and R134a

7.2 Pressure Drop Model

This section describes the multi-regime pressure drop model for condensing flow developed from the data taken in the present study. The model is divided into an intermittent regime, and a continuous vapor core (CVC) region that encompasses annular and wavy flow. The annular and wavy flow model is presented first, followed by a discussion of the intermittent regime model. The predictions of the resulting model are then compared with the data from this study.

7.2.1 Annular and Wavy Regime

Annular and wavy flow regimes in this study were observed to have a liquid annulus film around the entire circumference of the tube and a fast moving vapor core. A schematic of the vapor and liquid distribution in these regimes is shown in Figure 7.7. The approach is based on the model presented by Garimella *et al.* (2005) and assumes that the flow is steady, that the liquid film is uniform, the pressure gradient across the vapor core and

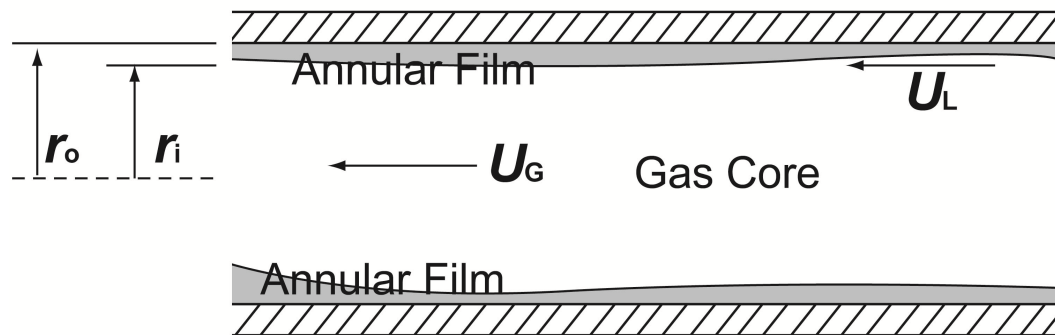


Figure 7.7 Schematic of Vapor-Liquid Distribution as the Basis for the Pressure Drop Model Adapted from Garimella *et al.* (2005)

liquid film are equal and that there is no entrainment of liquid droplets in the vapor core. Applying a force balance on a finite segment of the vapor core results in the equation:

$$-\left(\frac{dP}{dz}\right)_f = \frac{4\tau_i}{D_i} \quad (7.18)$$

The interfacial shear stress can be evaluated in terms of an interfacial friction factor, f_i , and the vapor density and velocity.

$$\tau_i = \frac{1}{2} f_i \rho_v U_v^2 \quad (7.19)$$

Substituting the interfacial shear stress, τ_i , from Equation 7.19 to the numerator of Equation 7.18 results in:

$$-\left(\frac{dP}{dz}\right)_f = \frac{1}{2} f_i \rho_v U_v^2 D_i^{-1} \quad (7.20)$$

The interfacial diameter, D_i , and vapor velocity, U_v , can be written using void fraction, α , hydraulic diameter, D , and superficial gas velocity, j_v .

$$-\left(\frac{dP}{dz}\right)_f = \frac{1}{2} f_i \rho_v j_v^2 \alpha^{-2.5} D^{-1} \quad (7.21)$$

This interfacial friction factor, f_i , is modeled by relating it to the single-phase Churchill (1977) liquid friction factor.

$$f = 8 \cdot \left[\left((8/\text{Re})^{12} + \left(\left(2.457 \cdot \ln \left(\frac{1}{(7/\text{Re})^{0.9} + 0.27 \cdot (\varepsilon/D)} \right) \right)^{16} + (37530/\text{Re})^{16} \right)^{-1.5} \right)^{1/12} \quad (7.22)$$

The interfacial roughness increases with increased liquid momentum, and is dampened out by gravitational, viscous and surface tension forces. Therefore, the interfacial friction factor is approximated by:

$$\frac{f_i}{f_l} = A \cdot X^b \cdot \text{Re}_l^c \cdot \left(\frac{\text{Ca}_l}{1-\alpha} \right)^d \left(\frac{\rho_l}{\rho_v} \right)^e \quad (7.23)$$

where the liquid Reynolds number, $\text{Re}_l = (1-x) \cdot G \cdot D / [\mu_l \cdot (1+\alpha^{0.5})]$, and the liquid

Capillary number, $\text{Ca}_l = [\mu_l \cdot (1-x) \cdot G] / (\rho_l \cdot \sigma)$ The interfacial friction factor for annular

flow is a function of the Martinelli parameter, $X = \sqrt{(dp/dz)_{f,l} / (dp/dz)_{f,v}}$, the liquid Reynolds number, $Re_1 = (1-x) \cdot G \cdot D / [\mu_1 \cdot (1 + \alpha^{0.5})]$, and a modified version of the liquid capillary number, $Ca_1 / (1 - \alpha) = [\mu_1 \cdot j_1] / [\sigma(1 - \alpha)]$ which was first presented by Lee and Lee (2001) to account for surface tension forces. The density ratio term was included to account for the variation in fluid properties for varying saturation temperatures. For the wavy flow regime, in which there is a significant stratified liquid pool, gravitational forces can be considered to be the dominant force for surface wave dampening. The interfacial friction factor then takes the form of:

$$\frac{f_i}{f_1} = A \cdot X^b \cdot Re_1^c \cdot Fr_{mod}^d \left(\frac{\rho_l}{\rho_v} \right)^e \quad (7.24)$$

The modified Froude number, $Fr_{mod} = G \cdot x / \sqrt{D \cdot g \cdot \rho_v \cdot (\rho_l - \rho_v)}$, replaces the capillary number for wavy flows because gravity becomes dominant. For the pressure drop measurements in the present study, vapor core flows were all in the turbulent regime, while liquid film flows were laminar, transitional, or turbulent. The Reynolds number dependence in laminar ($Re_1 < 2100$) and turbulent ($Re_1 > 3400$) film flows is expected to be different. Therefore, a separate regression analysis was conducted for cases with laminar and turbulent flows for the annular and wavy flow regimes. In the transition region, a linear interpolation between the lower limit of the turbulent region and the upper end of the laminar region is used to obtain the interfacial friction factor.

$$f_i = \left(\frac{Re_{crit,turb} - Re_1}{Re_{crit,turb} - Re_{crit,lam}} \right) f_{i,crit,lam} + \left(\frac{Re_1 - Re_{crit,lam}}{Re_{crit,turb} - Re_{crit,lam}} \right) f_{i,crit,turb} \quad (7.25)$$

In this equation, $Re_{crit,turb} = 3400$, and $Re_{crit,lam} = 2100$, and the liquid Reynolds number, Re_1 , is used to interpolate between the two values calculated at the respective limiting Reynolds number values. Figure 7.8 shows the representative transition region between

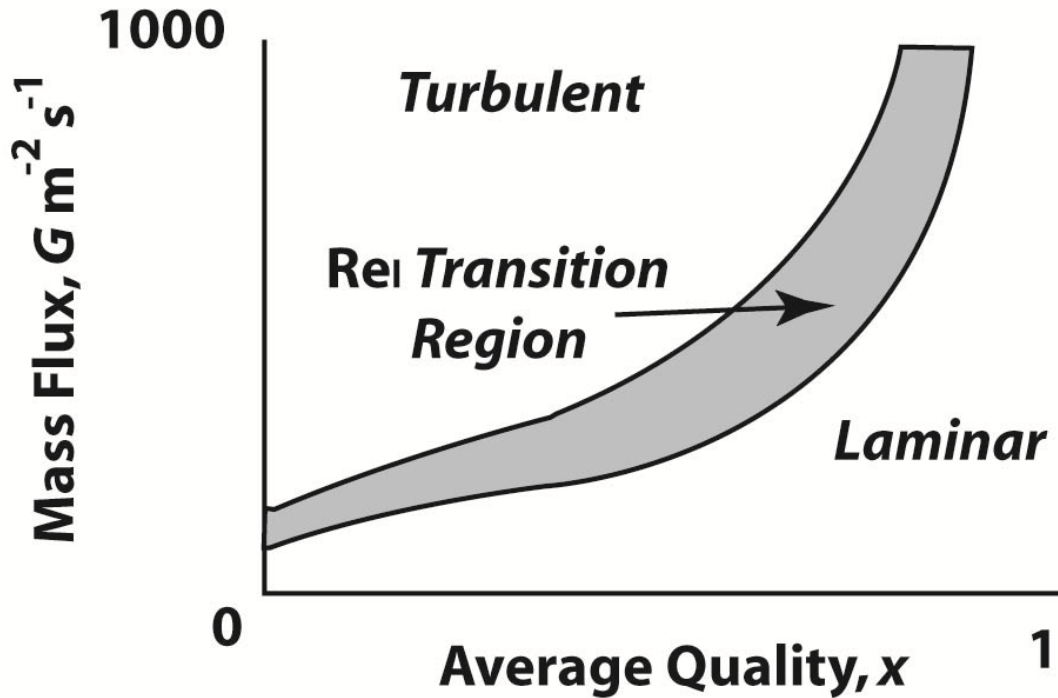


Figure 7.8: Typical Transition Region For Interpolation Between Laminar and Turbulent Liquid Reynolds Number Values

Table 7.3: Empirical Constants for Predicting Pressure Drop During Annular and Wavy Flow with Laminar and Turbulent Liquid Phases

Annular	
Laminar	$\frac{f_i}{f_1} = 0.0007 \cdot X^{0.48} \cdot Re_1^{0.91} \cdot \left(\frac{Ca_1}{1-\alpha}\right)^{-0.258} \left(\frac{\rho_l}{\rho_v}\right)^{0.1}$
Turbulent	$\frac{f_i}{f_1} = 1.72 \cdot X^{0.43} \cdot Re_1^{-0.164} \cdot \left(\frac{Ca_1}{1-\alpha}\right)^{0.07} \left(\frac{\rho_l}{\rho_v}\right)^{0.5}$
Wavy	
Laminar	$\frac{f_i}{f_1} = 0.0001 \cdot X^{0.477} \cdot Re_1^{1.057} \cdot Fr_{mod}^{0.064} \left(\frac{\rho_l}{\rho_v}\right)^{0.6717}$
Turbulent	$\frac{f_i}{f_1} = 1.634 \cdot X^{0.49} \cdot Re_1^{-0.2} \cdot Fr_{mod}^{-0.039} \left(\frac{\rho_l}{\rho_v}\right)^{0.614}$

laminar and turbulent liquid Reynolds number values. This approach allows for a smooth transition between predicted laminar and turbulent pressure drop. A summary of the regression constants for annular and wavy flow is shown in Table 7.3.

7.2.2 Intermittent Regime

The pressure drop in the intermittent regime is modeled using an approach based on previous work by Fukano *et al.* (1989), Garimella *et al.* (2002), and Chung and Kawaji (2004), where the two-phase flow is divided into two distinct regions. The regions consist of a film/bubble and liquid slug region as presented in Figure 7.9. Both regions are assumed to be axi-symmetric. Vapor bubble symmetry was always observed in the 0.508 and 1.00 mm diameter tube data; however, some of the 3.00 mm diameter tube data exhibit some stratification of the bubbles due to the increased importance of gravity on liquid-vapor distribution at such diameters.

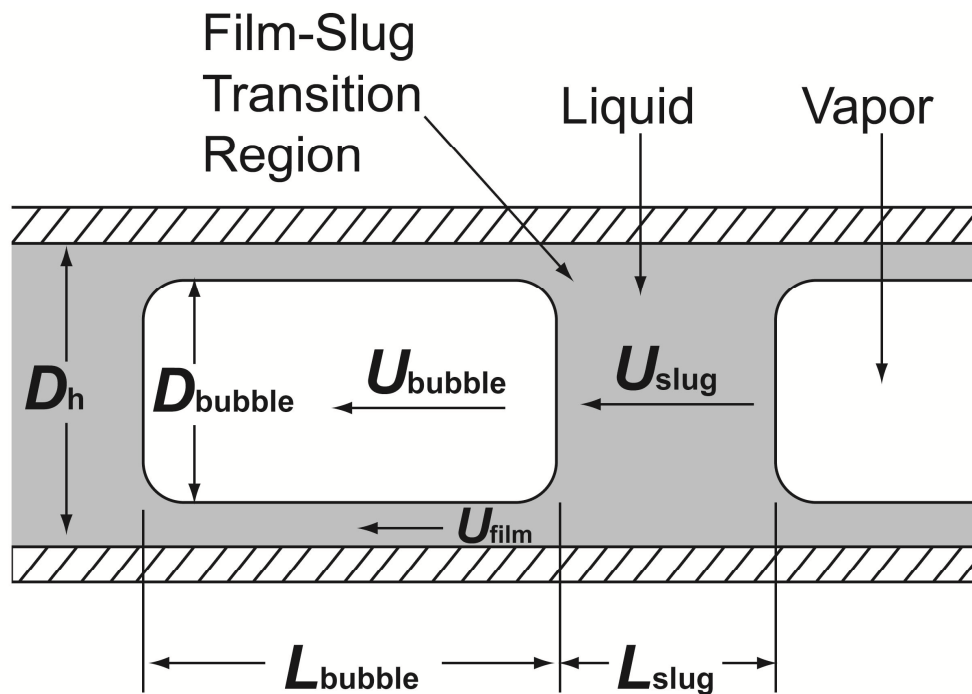


Figure 7.9: Schematic of Unit Cell During Intermittent Flow (Garimella *et al.*, 2002)

The pressure drop is modeled for a unit cell consisting of a single vapor bubble and liquid slug. The total pressure drop within a unit cell is due to the sum of the pressure drop in the film-vapor bubble region, $(dP/dz)_{f/b}$, the liquid slug, $(dP/dz)_{slug}$, and the transitions between the film/bubble and slug regions, ΔP_{tran} . Thus, it accounts for the acceleration of the liquid as it flows around the bubble and deceleration as it flows from the bubble region to the liquid slug region downstream. The average pressure drop per unit cell can be predicted by:

$$\left(\frac{dP}{dz}\right)_f = \left(\frac{dP}{dz}\right)_{f/b} \frac{L_{bubble}}{L_{UC}} + \left(\frac{dP}{dz}\right)_{slug} \frac{L_{slug}}{L_{UC}} + \Delta P_{tran} \frac{1}{L_{UC}} \quad (7.26)$$

The details of the intermittent regime model are presented in Appendix D and a summary of the equations and methodology is presented below. In the pressure drop experiments conducted in the present study, only four out of all the data points were predicted by the Nema (2007) flow regime map to be in the intermittent regime. The other observed intermittent data points from the present study were predicted to be in either the intermittent-annular or intermittent-discrete wave flow regimes. It was found that using a model specific to the intermittent flow regime for predicting pressure drop instead of using the annular/wavy flow model described above yields a small improvement in accuracy in predicting the data from the present study in the intermittent and transitional regimes. Thus, applying only the annular and wavy flow model to all the data from the present study results in an AAD and AD of 12.7% and 1.3%, respectively, and predicts 85.5% of the data within 25%. When applying the intermittent model in combination with the annular and wavy flow model, the AAD and AD are 12.5% and -0.9%, respectively, with 86.9% of the data predicted within 25%. Given the fact that the intermittent flow model could only be validated with four data points, it was deemed that adequate confirmation of its modeling of intermittent phenomena had not been achieved in this study. In addition, the marginal improvement in the overall predictions did not

warrant the added complexity of using the intermittent flow model. If additional pressure drop data in the intermittent flow regime are obtained for such operating conditions and geometries by future researchers, the model outlined here can serve as a starting point, and can be refined and validated further.

A summary of the equations for this preliminary intermittent pressure drop model is shown in Table 7.4. First, the unit cell parameters are obtained using Equations D.4, D.7, D.12 and D.16-D.18. The pressure drops in each region of the unit cell can then be calculated using Equations D.2 and D.13. The solutions to the interface velocity (Equation D.12) and the film/bubble pressure gradient (Equation D.13) are obtained iteratively. The pressure loss from the transitions around the vapor bubble is calculated using Equation D.14, and the overall pressure gradient for a unit cell is predicted using Equation 7.26.

7.2.3 Summary of Predictions

The pressure drops predicted using the models described above are compared with the measured values in Figure 7.10 categorized by tube diameter and in Figure 7.11 categorized by flow regime. Predicted and measured pressure drops for all data points are also shown in Figure 7.12 as a function of quality and mass flux for the different tubes and saturation conditions investigated in this study. The model is able to predict values and trends of the pressure drop for each tube diameter and saturation temperature well, with 85.5% of the data predicted within $\pm 25\%$ with an AAD of 12.7%. The R^2 value of the model predictions to the data from the present study is 98.4%. A summary of the deviations for the different tube diameters is displayed in Table 7.5, while the deviations categorized by saturation temperature are shown in Table 7.6. In addition, the predictive capabilities for each flow regime are shown in Table 7.7. Agreement between

Table 7.4: Summary of Equations for Predicting Pressure Drop in the Intermittent Flow Regime

Unit Cell Parameters	
Bubble Diameter	
$R_{\text{bubble}} = \sqrt{\alpha_{\text{bubble}}} R_{\text{tube}}$	
Where α_{bubble} is predicting using Equations 7.16 and 7.17 with x_{tran} from	D.16
$X_{\text{slug}} = 0.3521 = \left(\frac{\rho_v}{\rho_l}\right)^{0.5} \left(\frac{\mu_l}{\mu_v}\right)^{0.1} \left(\frac{1-x_{\text{tran}}}{x_{\text{tran}}}\right)^{0.9}$	
Unit Cell Length	
$\frac{L_{\text{UC}}}{D} = 0.19 \cdot Bo^{-0.3353} \cdot Re_{\text{slug}}^{0.418}$	D.18
Vapor Bubble Length	
$\alpha = \left(\frac{L_{\text{bubble}}}{L_{\text{UC}}}\right) \left(\frac{R_{\text{bubble}}}{R_{\text{tube}}}\right)^2$	D.17
Slug Velocity	
$U_{\text{slug}} = \frac{j_1}{1-\alpha}$	D.4
Bubble Velocity	
$U_{\text{bubble}} = 2.4 \cdot Bo^{-0.132} \cdot Re_l^{-0.105} \cdot j$	D.7
Interface Velocity	
$U_{\text{interface}} = -\left(\frac{dP}{dz}\right)_{\text{fb}} \left(R_{\text{tube}}^2 - R_{\text{bubble}}^2\right) / 4\mu_l$	D.12
$U_{\text{film}} = U_{\text{interface}} / 2$	
Pressure Loss Components	
Pressure Gradient in Liquid Slug	
$\left(\frac{dP}{dz}\right)_{\text{slug}} = f_{\text{slug}} \frac{1}{2} \rho_l U_{\text{slug}}^2 D^{-1}$	D.2
<p>f_{slug} is calculated using the Churchill (1977) correlation (Equation 7.20) where $Re = Re_{\text{slug}} = \rho_l U_{\text{slug}} \mu_l^{-1}$</p>	
Pressure Gradient in Film/Bubble Region	
$\left(\frac{dP}{dz}\right)_{\text{fb}} = f_{\text{film}} \frac{\rho_v (U_{\text{bubble}} - U_{\text{interface}})^2}{4R_{\text{bubble}}}$	D.13
<p>f_{film} is calculated using the Churchill (1977) correlation (Equation 7.20) where $Re = Re_{\text{film}} = \rho_l U_{\text{film}} (D - D_{\text{bubble}}) \mu_l^{-1}$.</p>	
Transitional Pressure Loss	
$\Delta P_{\text{tran}} = \rho_l \left[1 - \left(\frac{R_{\text{bubble}}}{R_{\text{tube}}}\right)^2\right] (U_{\text{bubble}} - U_{\text{film}})(U_{\text{slug}} - U_{\text{film}})$	D.14
Pressure Drop Per Unit Cell	
$\left(\frac{dP}{dz}\right)_f = \left(\frac{dP}{dz}\right)_{\text{fb}} \frac{L_{\text{bubble}}}{L_{\text{UC}}} + \left(\frac{dP}{dz}\right)_{\text{slug}} \frac{L_{\text{slug}}}{L_{\text{UC}}} + \Delta P_{\text{tran}} \frac{1}{L_{\text{UC}}}$	7.26

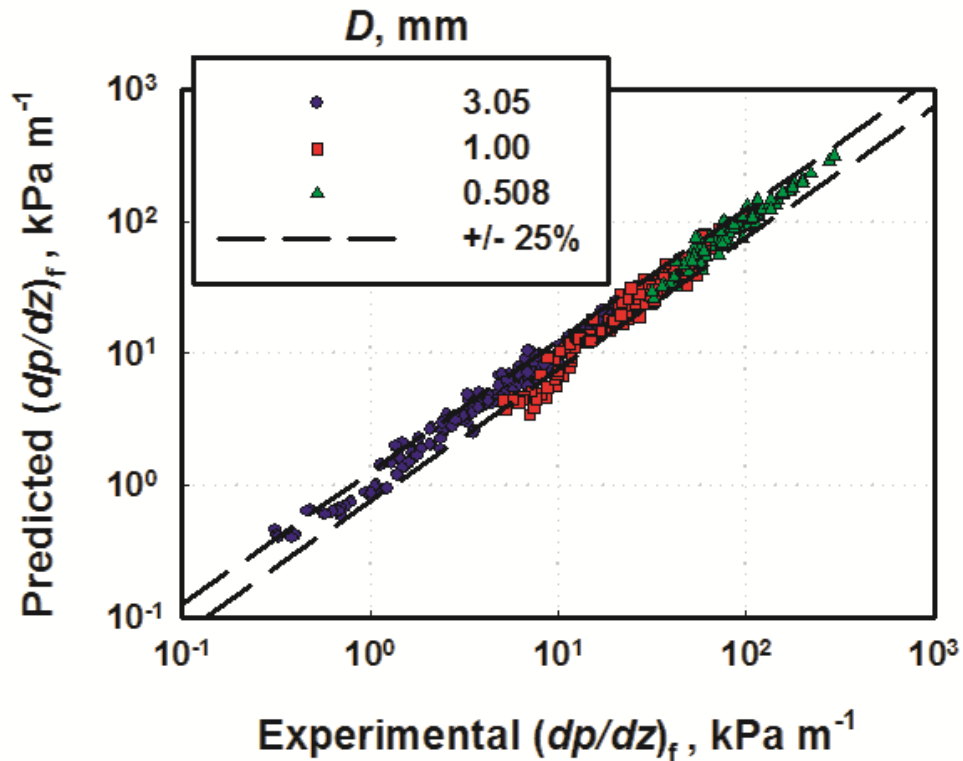


Figure 7.10: Frictional Pressure Gradient Predictions Categorized by Tube Diameter

the predictions and the data is best for the smallest tube diameter ($D = 0.508$ mm) where the flow is mostly predicted to be annular, and pressure drop is the greatest. The agreement with mist, annular and disperse wave flow regimes is very good with each resulting in an AAD of 11.4, 11.8, and 11.3%, respectively. The agreement in the discrete wave, discrete wave-intermittent, and intermittent flow regime is lower. There were very few data points predicted by the Nema flow map in the intermittent flow regime (4 data points.) The discrete wave (45 data points) and discrete wave-intermittent transition (16 data points) regimes were typically encountered at low qualities and low mass fluxes during large diameter tube ($D = 3.05$ mm) experiments. In these ranges, experimental uncertainty was the highest. Despite over-predicting much of the data in this region, it can be observed in Figure 7.12 that most of the predicted values fall within

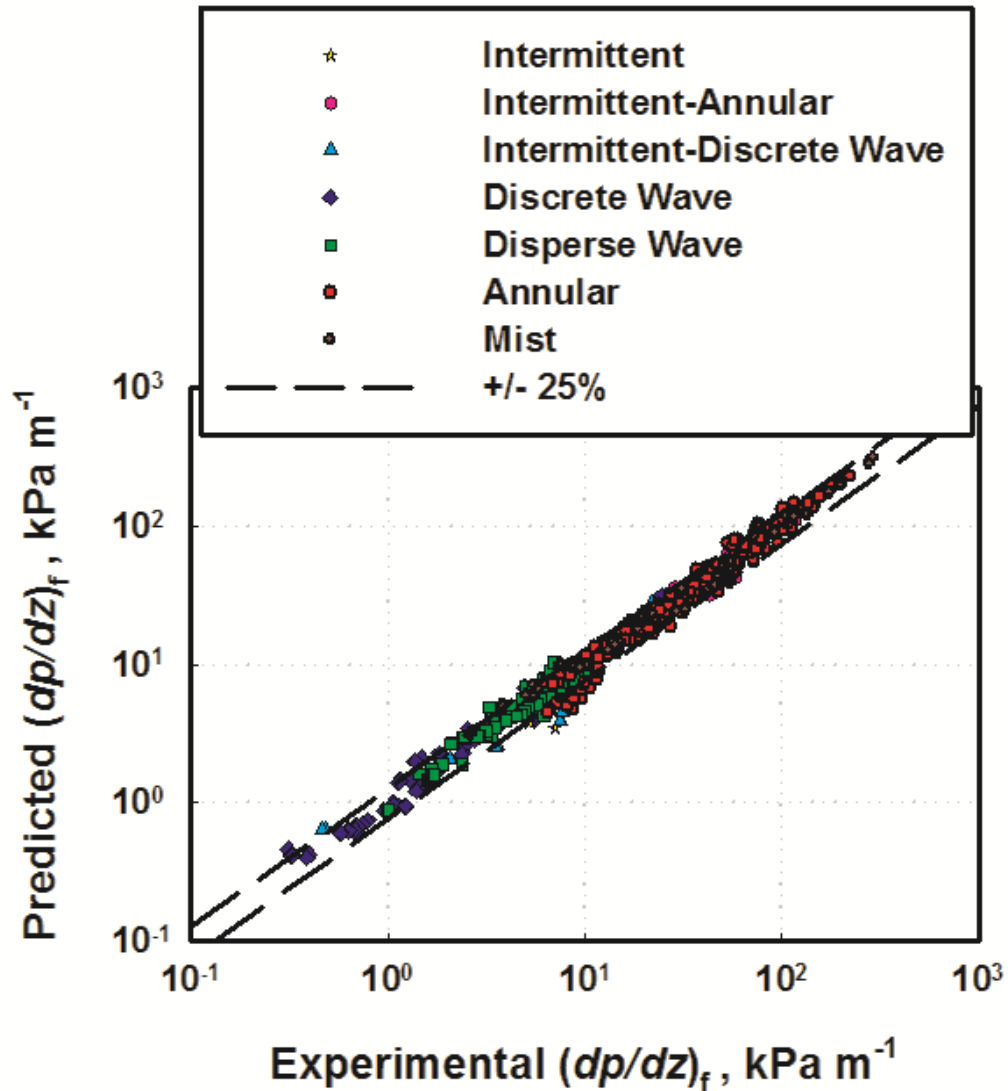
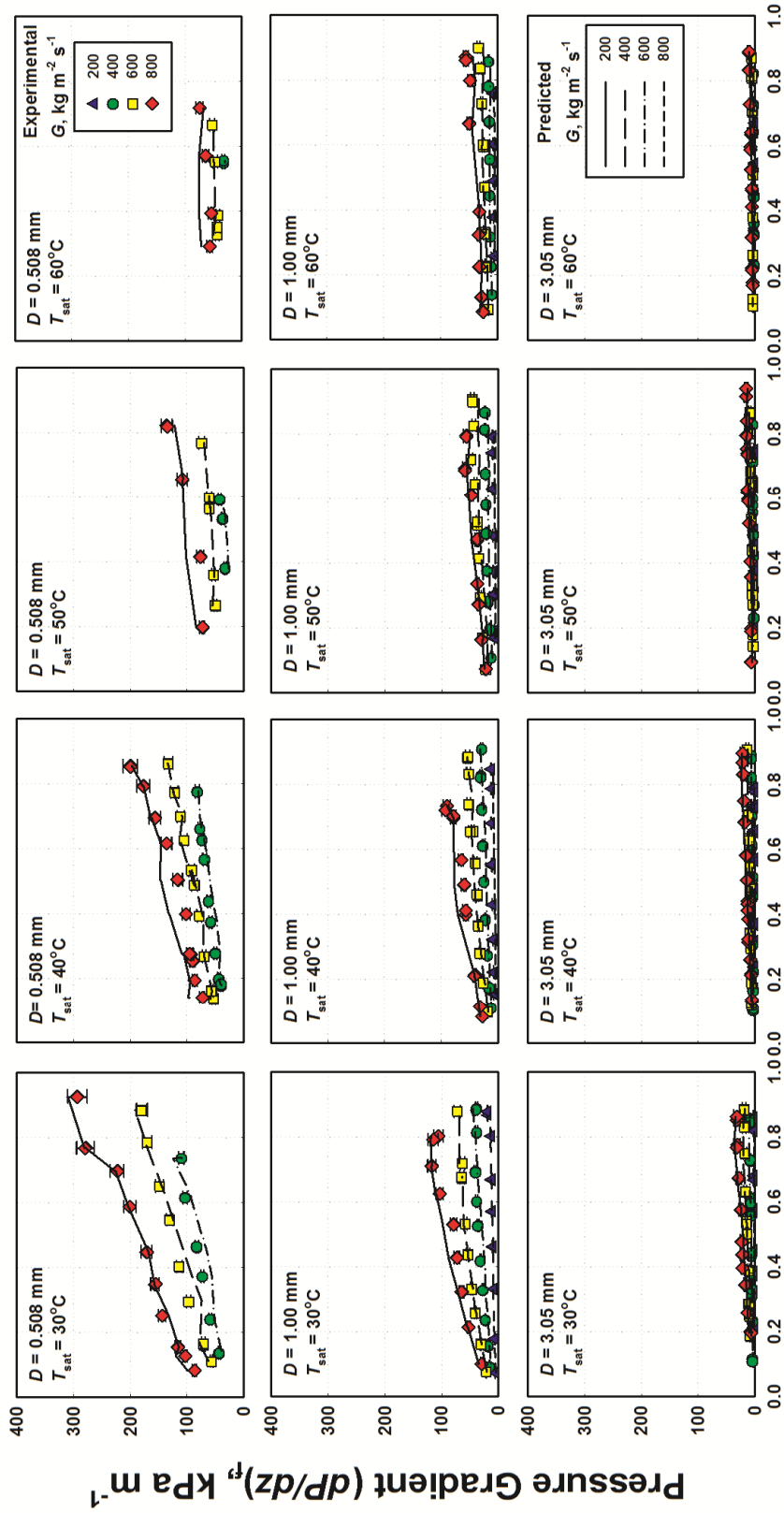


Figure 7.11: Frictional Pressure Gradient Predictions Categorized by Flow Regime

the experimental uncertainty. There are several discontinuities and slope changes in the model lines plotted in Figure 7.12. These discontinuities and slope changes are in part due to deviations in the actual mass flux for the particular data point from the nominal value, and not because of changes in any fundamental mechanisms for pressure drop. A representative example of such deviations from the nominal values can be seen for the case when the nominal condition is $T_{\text{sat}} = 30^\circ\text{C}$, $D = 0.508 \text{ mm}$ and $G = 800 \text{ kg m}^{-2} \text{ s}^{-1}$. For this case, at $x = 0.69$, the mass flux is $G = 780 \text{ kg m}^{-2} \text{ s}^{-1}$, while at $x = 0.76$, $G = 821$



Average Quality, x
Figure 7.12: Frictional Pressure Drop for 0.508, 1.00, and 3.05 mm Test Sections

Table 7.5: Pressure Drop Model Predictions by Tube Diameter

<i>D</i> (mm)	AAD %	AD %	Data < 25% Deviation
3.05	11.7	3.8	89.7
1.00	15.5	-8.3	77.6
0.508	10.0	0.9	90.8
Overall	12.7	1.3	85.5

Table 7.6: Pressure Drop Model Predictions by Saturation Temperature

<i>T_{sat}</i> (°C)	AAD %	AD %	Data < 25% Deviation
30	11.6	-1.4	92.2
40	12.7	-1.1	84.3
50	14.8	-3.3	77.5
60	11.9	0.9	87.5

Table 7.7: Pressure Drop Model Predictions by Flow Regime

Regime	AAD %	AD %	Data < 25% Deviation
Intermittent	28.4	28.4	50.0
Annular-Intermittent	13.9	4.2	89.5
Discrete-Intermittent	19.7	5.7	53.3
Discrete Wave	14.8	1.4	86.4
Disperse Wave	11.3	3.2	87.9
Annular Film	11.8	-2.8	86.2
Mist	11.4	2.3	92.2

kg m⁻² s⁻¹, resulting in a sharp local increase in predicted and measured pressure drops. The 0.508 mm diameter tube has the largest pressure drop, which can influence the experimental mass flux that is achieved for a given nominal mass flux. Therefore, these types of variations are observed more frequently for data at this tube diameter and at high mass fluxes.

Application of the annular flow model to the transition region results in reasonable agreement (Table 7.7.) The agreement in the annular-intermittent transition region is good with an AAD of 13.9% and 89.5% of the data being predicted within 25%. Agreement is not as good for the discrete wave-intermittent transition regime (Table 7.7), which is due to the high experimental uncertainties.

Trends predicted by the pressure drop model are shown in Figure 7.13. The top plot demonstrates the effects of mass flux and quality on predicted pressure drop. As quality and mass flux increase, the predicted pressure drop increases. However, there is a discontinuity observed at each mass flux. This is due to the discontinuity in predicted Martinelli Parameter, where the liquid phase transitions from laminar to turbulent flow. As the mass flux decreases, this transition occurs at lower qualities where more liquid inventory is needed to achieve turbulent flow in the liquid phase.

The effects of saturation temperature are shown in the center plot in Figure 7.13. As the saturation temperature increases, the predicted pressure drop decreases. As previously discussed, the density ratio approaches 1 as saturation temperature is increased. This decreasing difference in phase velocities results in a decrease in interfacial shear. As saturation temperature is increased, the liquid density and viscosity decrease. The decrease in these properties results in a larger liquid Reynolds number at a given mass flux and quality. This causes the discontinuity associated with the Martinelli Parameter to occur at increasing qualities for increasing saturation temperatures.

The influence of tube diameter on predicted pressure drop is displayed in the bottom plot in Figure 7.13. As expected, pressure drop increases with decreasing tube diameter.

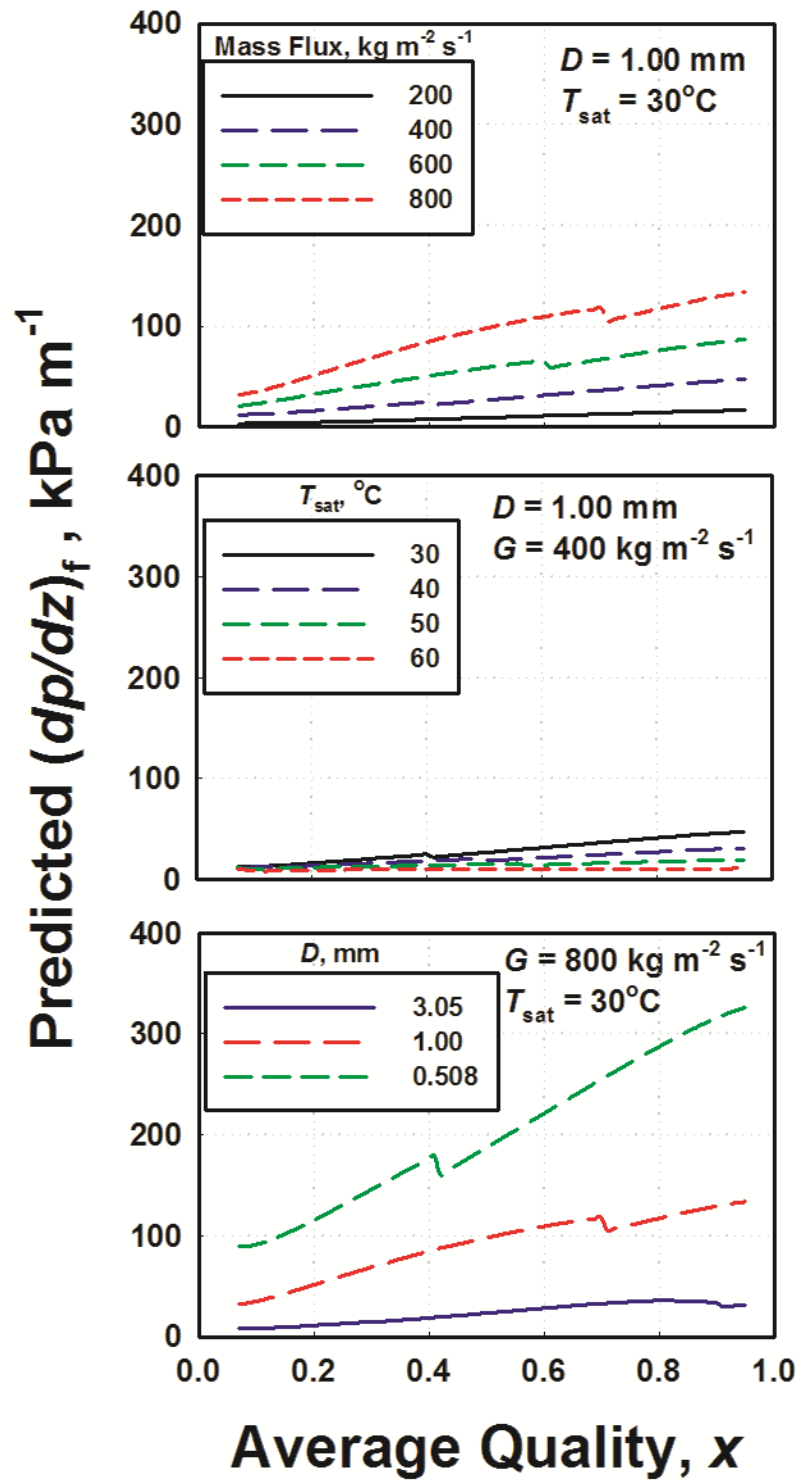


Figure 7.13: Illustration of Pressure Drop Model Trends

7.3 Heat Transfer Model

This section details the heat transfer model developed for microchannel condensation based on the experiments conducted in this study. A majority of the experimental data (65%) are predicted to be in the annular regime with the remaining data being predicted to be in the wavy flow regime. There were no data points in the intermittent regime based on the Nema (2007) flow regime map. The annular flow model is presented first, followed by the wavy flow model and then the comparison of the predictions from the model with the measured heat transfer coefficients.

The model was first developed using the R404A data from this study, and is subsequently used to predict ammonia (NH_3) condensation data obtained by Fronk and Garimella (2012). In addition, this model, developed for circular tubes based on data from the present study was modified using condensation heat transfer coefficients measured by Fronk and Garimella (2010) in rectangular geometries to extend the range of applicability of the model.

7.3.1 Annular Model

The annular flow model is based on the two-phase multiplier approach of Thome *et al.* (2003). In this approach, the focus is on the annular film characteristics instead of the bulk liquid flow. The model of Thome *et al.* (2003) was adapted from previous flow boiling work for refrigerants reported by Kattan *et al.* (1998b). In a similar manner, the Nusselt number for the present study can be written based on the film thickness, δ , instead of the tube diameter. The film thickness is assumed uniform around the entire tube. The film Nusselt number depends on the liquid Reynolds and Prandtl numbers, analogous to single phase flow, coupled with a two-phase multiplier, ϕ .

$$Nu = \frac{h_{\text{ann}} \delta}{k_1} = A \cdot \text{Re}_1^n \cdot \text{Pr}_1^m \cdot \phi \quad (7.27)$$

where the liquid Reynolds number is defined as $\text{Re}_1 = (1-x) \cdot G \cdot D / [\mu_1 \cdot (1+\alpha^{0.5})]$, and the Prandtl number is defined as $\text{Pr}_1 = c_{p,1} \cdot \mu_1 / k_1$. The film thickness is deduced using the void fraction model from the present study described above (Equations 7.16-17.)

$$\delta = \frac{1}{2}(D - D_i) = \frac{D}{2}(1 - \sqrt{\alpha}) \quad (7.28)$$

The film thickness is assumed to be uniform and smooth but it was observed that there are significant disturbances throughout the condensation process resulting in a dynamic film thickness. Thome *et al.* (2003) used the two-phase multiplier to account for the increase in heat transfer area, and reduction in film thickness, as a result of the vapor-liquid interface being roughened by the difference in phase velocities and liquid properties. Therefore, in the present study, it is assumed that the two-phase multiplier depends on the difference in phase velocities.

$$\phi = \left[1 + \left(\frac{U_v}{U_l} \right)^b \right] = \left[1 + \left(\left[\frac{x}{1-x} \right] \cdot \left[\frac{\rho_l}{\rho_v} \right] \cdot \left[\frac{1-\alpha}{\alpha} \right] \right)^b \right] \quad (7.29)$$

The average phase velocities are displayed in more convenient terms to show the influence of the respective parameters on the two-phase multiplier. The first two terms, the quality and density ratio, are similar to what Andresen (2007) used for his annular flow model. The product of these terms accounts for the effect of reduced pressure. For example, as the reduced pressure is increased, the difference in phase velocities decreases because the liquid and vapor densities approach each other. This results in a decrease in interfacial disturbances, and therefore a decrease in heat transfer.

A regression analysis was conducted to obtain the empirical constants for the Nusselt number correlation. Exponents n and m were assumed to be 0.8 and 0.4. Although $m = 0.4$ should be used for heating in the Dittus and Boelter (1930) equation, previous researchers Dobson and Chato (1998) and Shah (1979) recommend its use for condensation. The regression analysis yielded the empirical constants $A = 0.0049$ and $b = 0.69$. The resulting Nusselt number equation becomes:

$$Nu = \frac{h_{\text{ann}} \delta}{k_1} = 0.0049 \text{Re}_1^{0.8} \cdot \text{Pr}_1^{0.4} \left[1 + \left(\frac{U_v}{U_1} \right)^{0.69} \right] \quad (7.30)$$

The constant b , is very similar to that predicted by Thome *et al.* (2003) which was 0.72. Although other properties, e.g., surface tension, are expected to influence the interface, they do not appear explicitly in this equation. However, surface tension is used implicitly through its use in the expression for void fraction, α .

7.3.2 Annular Condensation in Noncircular Geometries

Several different microchannel shapes are employed for heat exchanger design. In an effort to increase the applicability of the microchannel heat transfer model developed here, an attempt was made to extend its applicability to account for different channel shapes.

In square channels, surface tension pulls liquid into the corners resulting in a locally thin film along much of the channel wetted perimeter. At low qualities, there is a large amount of liquid present, and the film thickness is predicted reasonably well using the hydraulic diameter and Equation 7.28. As quality increases, the liquid inventory decreases and a more substantial portion of the liquid volume is pulled to the corners. This results in an increased thinning along a large portion of the rectangular walls, with a

film thickness significantly lower than that predicted by Equation 7.28. Wang and Rose (2006) investigated this behavior in square geometries computationally. An example of the film profile for condensing R134a in square channels from their study is shown in Figure 7.14.

The thinning of the liquid film becomes significant for qualities, $x > 0.6$, as observed by Wang and Rose (2006). This effect is shown in the film thickness plots from their work in Figure 7.14, starting from the upper left plot where $x = 0.98$, to the lower left plot where $x = 0.60$. The thinning of the film thickness results in a decreased thermal resistance, increasing heat transfer coefficients. With this understanding as the basis, the film thickness, δ , in Equation 7.30 can be adjusted to account for this thinning effect. The effective film thickness, δ_{eff} , is a function of surface tension, phase densities, and quality. To account for these influences, an effective film thickness equation was developed using the Bond number, $\text{Bo} = (\rho_1 - \rho_v) \cdot g \cdot D^2 / \sigma$, and the ratio of phase velocities.

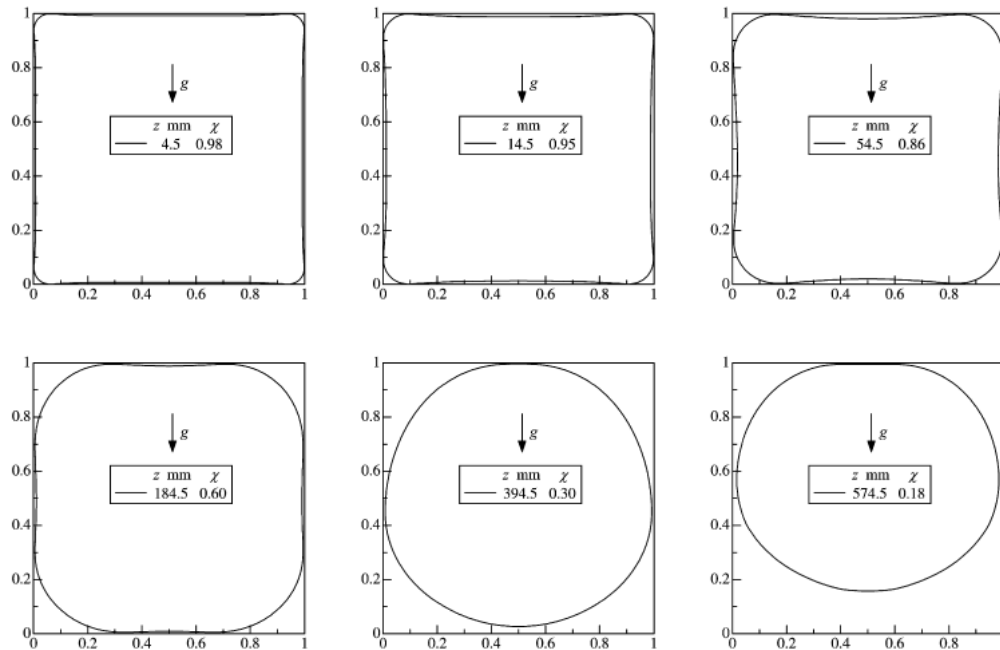


Figure 7.14: Film Profile for Condensing R134a in 1 mm Square Channels from the Computational Study of Wang and Rose (2006)

$$\frac{\delta_{\text{eff}}}{\delta} = 1 - A \cdot Bo^b \cdot \left(\frac{U_v}{U_1} \right)^c \quad (7.31)$$

All experiments in the present study were conducted on circular tubes. To determine the empirical constants for Equation 7.31, a regression analysis was conducted on condensing carbon dioxide data through rectangular microchannels presented by Fronk and Garimella (2010). This yielded empirical constants $A = 0.025$, $b = -0.471$ and $c = 1.1$, resulting in the following effective film thickness equation:

$$\frac{\delta_{\text{eff}}}{\delta} = 1 - 0.025 \cdot Bo^{-0.47} \cdot \left(\frac{U_v}{U_1} \right)^{1.1} \quad (7.32)$$

The effective film thickness, δ_{eff} , approaches δ , as quality decreases and thins as quality increases. As surface tension increases, the thinning increases as predicted. The effective film thickness correlation should only be applied to rectangular channels.

7.3.3 Wavy Flow Model

Heat transfer in the wavy flow regime is typically addressed based on two regions, the liquid film on the upper portion of the tube, and the lower stratified pool portion. A cross-sectional schematic of the wavy flow regime is displayed in Figure 7.15.

The overall wavy flow Nusselt number can be predicted as a sum of the film and pool components.

$$Nu_{\text{wavy}} = \frac{\theta}{2\pi} Nu_{\text{film}} + \left(1 - \frac{\theta}{2\pi} \right) Nu_{\text{pool}} \quad (7.33)$$

The wetted perimeter in contact with the liquid pool and film condensate is determined using the angle, θ , which is predicted using the void fraction model from the present study.

$$(1-\alpha) = \left(1 - \frac{\theta}{2\pi}\right) - \frac{1}{2\pi} \sin(2\pi - \theta) \quad (7.34)$$

The film and pool contributions are determined using the approach presented by Andresen (2007). The film condensation analysis was derived analytically assuming no shear at the vapor liquid interface. The derivation yields the following film Nusselt number.

$$Nu_{\text{film}} = \left(\frac{1.93}{\theta}\right) \left(Ra \left[\frac{1}{Ja_1} + 1\right]\right)^{1/4} \quad (7.35)$$

where

$$Ra = \frac{D^3 g \rho_l (\rho_l - \rho_v) c_{p,l}}{\mu_l k_l} \quad (7.36)$$

$$Ja_1 = \frac{c_{p,l} (T_{\text{sat}} - T_{\text{inner wall}})}{i_{lv}} \quad (7.37)$$

The contribution of the liquid pool is approximated using a two-phase multiplier applied to a single-phase turbulent flow correlation. The approach is similar to that of Andresen (2007), Cavallini *et al.* (2002) and Dobson and Chato (1998) with the only difference

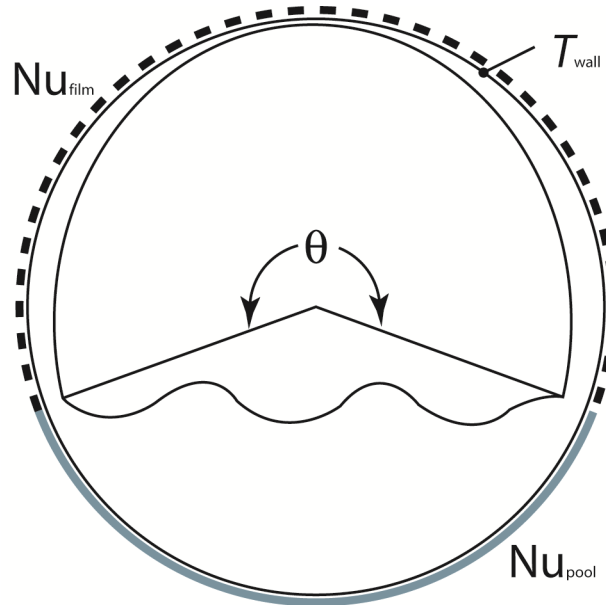


Figure 7.15: Cross-Sectional Schematic of the Wavy Flow Regime

being the two-phase multiplier. The two-phase multiplier presented by Andresen (2007) is used here.

$$Nu_{\text{pool}} = A \cdot \text{Re}_1^{0.8} \text{Pr}_1^{0.4} \left[1 + \left(\frac{x}{1-x} \right)^b \left(\frac{\rho_l}{\rho_v} \right)^c \right] \quad (7.38)$$

where the liquid Reynolds number is defined as $\text{Re}_1 = (1-x) \cdot G \cdot D / \mu_l$, and the Prandtl number is defined as $\text{Pr}_1 = c_{p,l} \cdot \mu_l / k_l$. Regression analysis on the wavy flow regime data from the present study yielded the empirical constants to be $A = 0.0066$, $b = 0.74$, and $c = 1.5$. Inserting Equations 7.55 and 7.38 into Equation 7.33 results in the overall wavy flow regime Nusselt number model.

$$Nu_{\text{wavy}} = \frac{h_{\text{wavy}} D}{k_1} = \left(\frac{1.93}{2\pi} \right) \left(Ra \left[\frac{1}{Ja_1} + 1 \right] \right)^{1/4} + 0.0066 \cdot \text{Re}_1^{0.8} \text{Pr}_1^{0.4} \left[1 + \left(\frac{x}{1-x} \right)^{0.74} \left(\frac{\rho_l}{\rho_v} \right)^{1.51} \right] \left(1 - \frac{\theta}{2\pi} \right) \quad (7.39)$$

7.3.4 Summary of Predictions

The heat transfer model predicts 94% of the data from the present study within 25%, with an AAD of 11.4%. The comparison of predicted versus experimental heat transfer coefficients is presented in Figure 7.16 categorized by tube diameter and in Figure 7.17 categorized by flow regime. A summary of deviations categorized according to tube diameter and saturation temperature is presented in Tables 7.8 and 7.9, respectively.

The predicted and measured heat transfer coefficients are plotted versus quality and mass flux for each tube diameter and saturation temperature under consideration in Figure 7.18. The model is able to predict the trends in the data for each tube diameter and with saturation temperature well. In Figure 7.18, there are some discontinuities and slope changes in the model prediction line that are explained by differences in the nominal

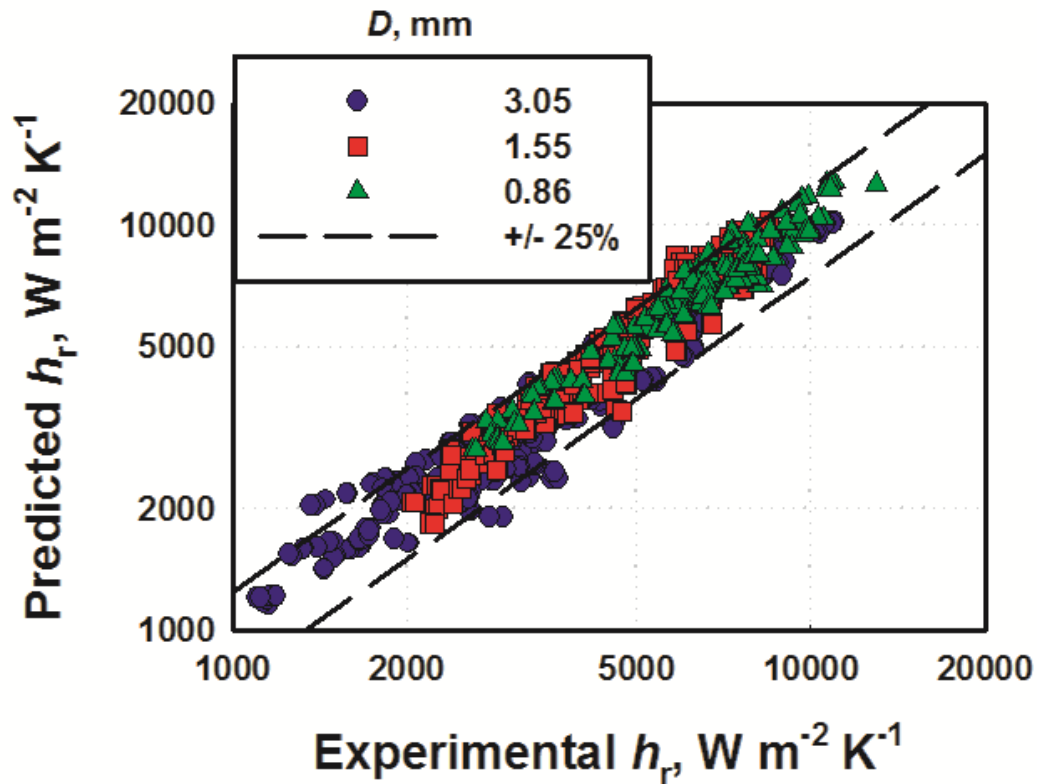


Figure 7.16: Heat Transfer Coefficient Predictions for R404A by Tube Diameter

operating conditions. For example, at $T_{\text{sat}} = 40^\circ\text{C}$, $G = 800 \text{ kg m}^{-2} \text{ s}^{-1}$, there are a few data points ($x = 0.43$, and $x = 0.52$) where the heat transfer coefficient values and predictions are much lower than those adjacent data points. In these cases, the mass flux for the experiment was $G = 775 \text{ kg m}^{-2} \text{ s}^{-1}$ for $x = 0.43$ and $G = 785 \text{ kg m}^{-2} \text{ s}^{-1}$ for $x = 0.52$, while the adjacent point at $x = 0.65$ is at a mass flux of $G = 804 \text{ kg m}^{-2} \text{ s}^{-1}$. Overall, the model slightly over predicts the measured heat transfer coefficients (AD = 4.6%), with the largest discrepancies at the highest mass fluxes. The R^2 of the model for heat transfer data from the present study is 93%. The experimental uncertainty at high mass fluxes is the highest, which may explain the lower degree of agreement in this region. The model predicts the trend of increasing heat transfer coefficient with decreasing tube diameter well. Similarly, the trends in increasing saturation temperature are captured by the model.

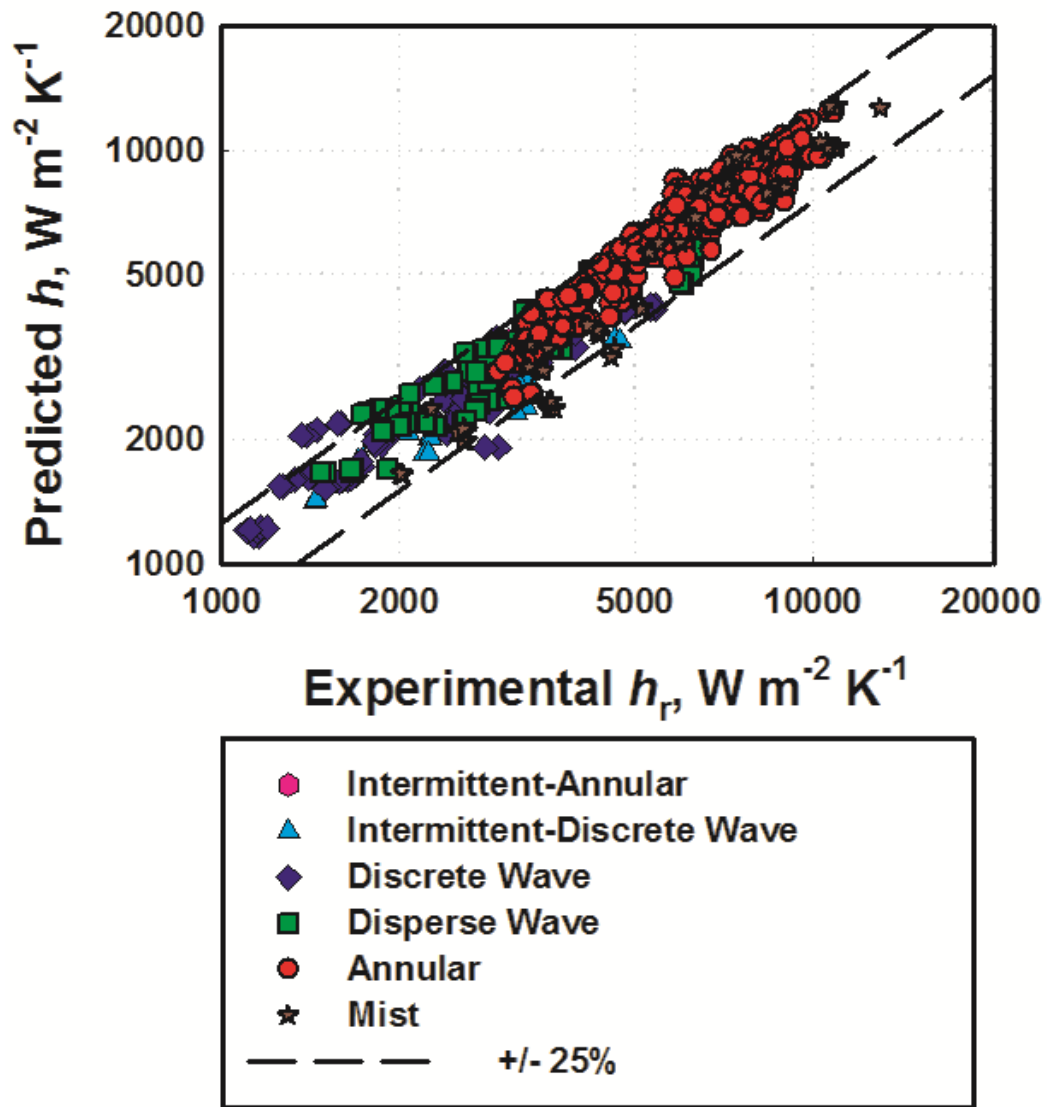


Figure 7.17: Heat Transfer Coefficient Predictions for R404A by Flow Regime

To evaluate the range of applicability of the model, its predictions were compared to data obtained for different fluids. Fronk and Garimella (2012) investigated condensing Ammonia (NH_3) in a round, microchannel tube ($D = 1.435$ mm) at reduced pressures ranging from $0.1 < p_r < 0.23$ and mass fluxes of 75 and 150 $kg m^{-2} s^{-1}$. The Nema (2007) flow regime map predicts all of the data from these operating conditions in the annular and

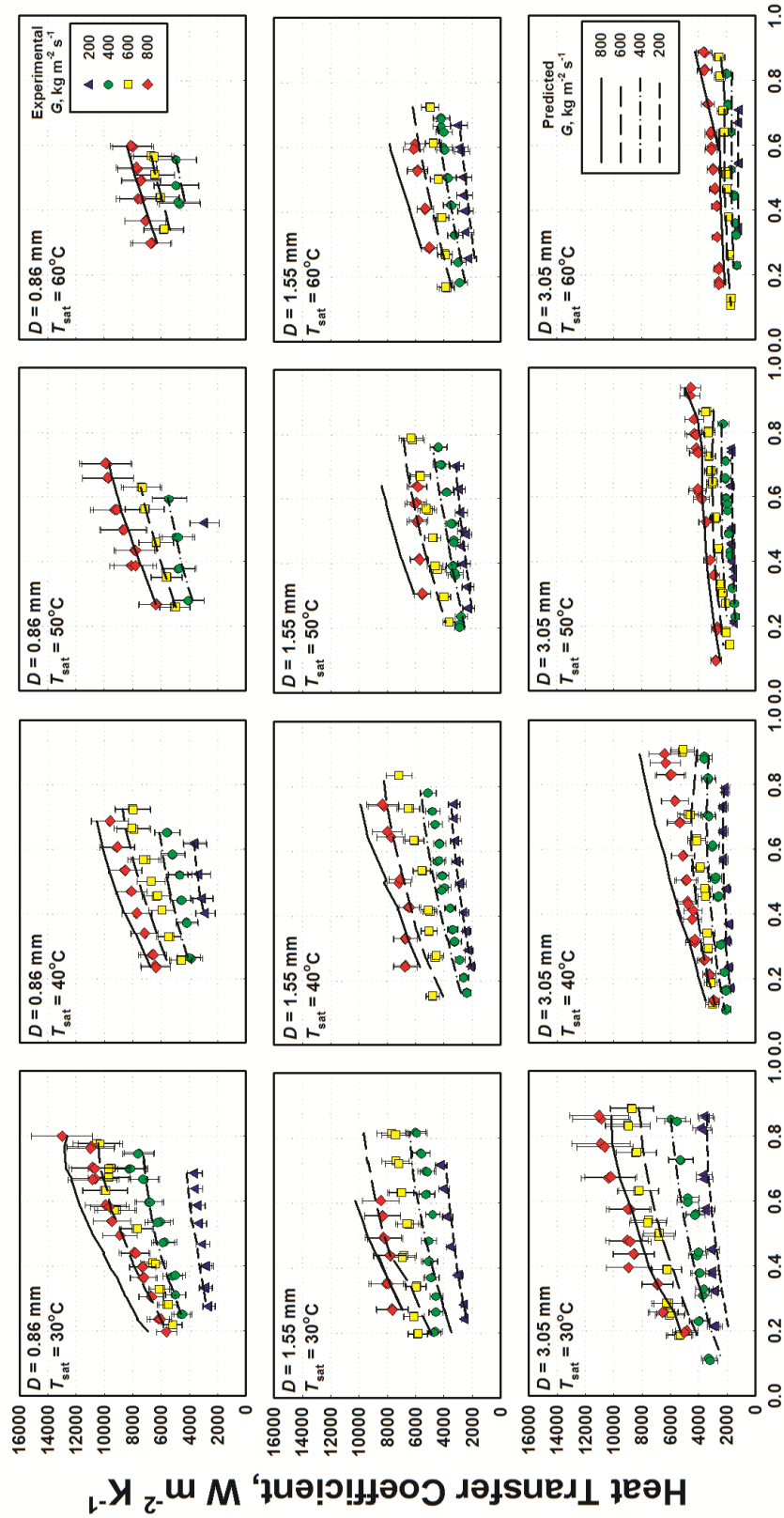


Figure 7.18: Measured and Predicted Heat Transfer Coefficient, for $D = 0.86$, 1.55 , and 3.05 mm Average Quality, x

annular-intermittent flow regime. Overall, there is good agreement between the heat transfer coefficients predicted by the annular flow heat transfer model from the present study and their data with an AAD of 13.6%, with 84.8% of the data predicted within 25%. The R^2 value from the model developed in this study and their data is 85.3%. A comparison of the present model and the data of Fronk and Garimella (2012) is shown in Figure 7.19 and summarized in Tables 7.8 and 7.9. The results are also categorized by flow regime in Table 7.10. The model slightly over-predicts their heat transfer coefficients with an AD = 10.0% at the lowest reduced pressure ($p_r = 0.10$), and slightly under-predicts their heat transfer coefficients with an AD = -16.0% at the highest reduced pressure ($p_r = 0.23$.) Despite the drastically different properties of R404A and NH_3 , and mass fluxes almost an order of magnitude smaller than those of this study, the agreement of their data with the present model is significantly better than with the models from the literature with which Fronk and Garimella (2012) compared their data. They found the best agreement of their data to be with the models of Bandhauer *et al.* (2006) and Dobson and Chato (1998), both with an AAD of 28%.

Table 7.8: Heat Transfer Model Predictions by Tube Diameter

Fluid	D_h (mm)	AAD %	AD %	Data < 25% Deviation
R404A	3.05	11.7	0.2	94.0
	1.55	12.5	8.0	91.3
	0.860	9.6	7.5	95.8
	Overall	11.4	4.6	93.6
NH_3	1.435	13.6	-4.6	84.8
CO_2	0.160	10.4	-8.0	100.0
	0.150	11.3	4.7	97.7
	0.133	11.2	7.3	90.4
	0.100	8.9	-2.3	100.0
	Overall	10.5	0.5	97.0
All		11.4	2.3	93.4

Table 7.9: Heat Transfer Model Predictions by Saturation Temperature

Fluid	T_{sat} (°C)	p_r	AAD %	AD %	Data < 25% Deviation
R404A	30	0.38	11.9	4.1	94.0
	40	0.49	11.9	8.7	95.7
	50	0.62	11.1	5.3	90.5
	60	0.77	9.6	-0.2	97.3
NH ₃	30	0.10	11.5	10.0	89.5
	40	0.14	10.8	-1.1	97.3
	50	0.18	15.2	-11.4	74.4
	60	0.23	16.9	-16.0	78.4
CO ₂	15	0.69	8.9	0.4	100.0
	20	0.78	9.1	-2.7	100.0
	25	0.87	13.2	3.8	91.4

Table 7.10: Heat Transfer Model Predictions by Flow Regime

Fluid	Regime	AAD %	AD %	Data < 25% Deviation
R404A	Intermittent	/	/	/
	Annular-Intermittent	8.5	8.5	100.0
	Discrete Wave-Intermittent	11.7	-6.2	86.4
	Discrete Wave	10.6	1.9	95.0
	Disperse Wave	10.9	4.7	97.5
	Annular	11.5	7.5	93.2
	Mist	14.8	-3.5	83.0
NH ₃	Intermittent	18.6	-16.4	65.0
	Annular-Intermittent	13.9	10.0	87.0
	Annular	12.6	-5.6	88.0
	Mist	/	/	/
CO ₂	Intermittent	2.7	2.7	100
	Annular-Intermittent	8.7	-0.5	98.0
	Annular	11.3	0.9	96.6
	Mist	/	/	/

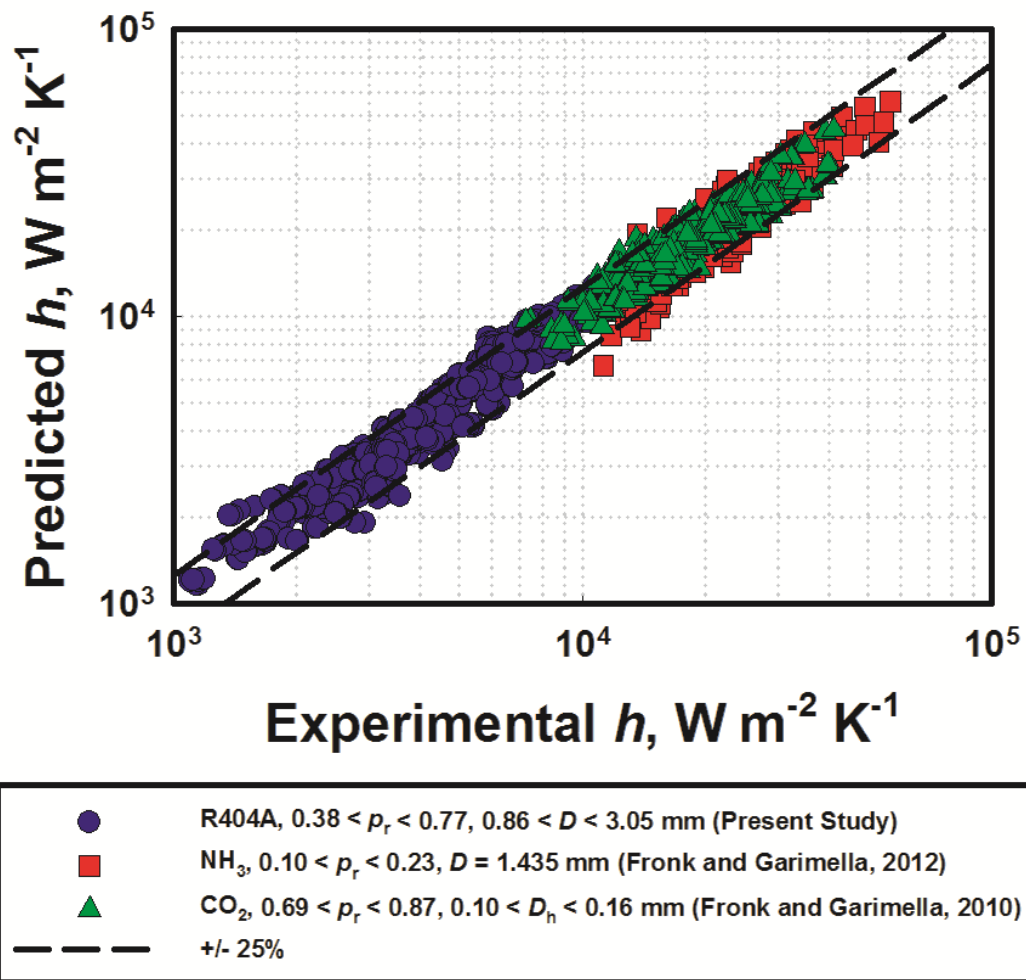


Figure 7.19: Heat Transfer Coefficient Predictions for R404A, NH₃ (Fronk and Garimella, 2012), and CO₂ (Fronk and Garimella, 2010)

The present model adapted for rectangular geometries was also used to predict the data from Fronk and Garimella (2010) for condensing CO₂ in rectangular channels with hydraulic diameters ranging from $100 \leq D_h \leq 160$ μm , reduced pressures from $0.69 \leq p_r \leq 0.87$, and mass fluxes from $400 \leq G \leq 800$ $\text{kg m}^{-2} \text{s}^{-1}$.

Agreement with the data is excellent, with 97% of data being predicted within 25% and an AAD of 10.5%. The R^2 value of the model developed from this study and their data is 86.7%. A comparison of predicted versus experimental heat transfer coefficients of

Fronk and Garimella (2010, 2012) for CO₂ and NH₃ is shown in Figure 7.19. A summary of the results is presented for varying hydraulic diameter and saturation temperature in Tables 7.8 and 7.9, respectively. The model is able to capture the effect of decreasing hydraulic diameter. Similarly, the heat transfer model predicts changes in saturation temperature well.

Trends in the heat transfer coefficients predicted by the present model are shown in Figure 7.20. The top plot demonstrates the effects of mass flux and quality on predicted heat transfer coefficient. As expected, heat transfer coefficients increase with increasing mass flux and quality. The model predicts a decrease in heat transfer coefficient with increasing saturation temperature, as was seen in the experiments. In the annular flow regime, this decrease is a result of decreased interfacial shear. In the wavy flow regime, the conductivity and latent heat decrease with increasing saturation temperature, resulting in a decrease in heat transfer coefficient. The effect of tube diameter on predicted heat transfer coefficient is demonstrated in the lower plot and follows expected trends. A comparison of model predictions for varying fluids is presented in Figure 7.21. For the same tube diameter and mass flux, the predicted heat transfer coefficient for R404A ($T_{\text{sat}} = 30^{\circ}\text{C}$, $p_r = 0.38$), NH₃ ($T_{\text{sat}} = 30^{\circ}\text{C}$, $p_r = 0.10$), and CO₂ ($T_{\text{sat}} = 18^{\circ}\text{C}$, $p_r = 0.75$) are plotted for the entire condensation process. The heat transfer coefficient of NH₃ is significantly higher than that of R404A and CO₂. This demonstrates the superior transport properties of NH₃ compared to those of R404A. Heat transfer coefficient predictions for R404A and CO₂ are similar with CO₂ heat transfer coefficients being slightly higher than those of R404A. For example, at $x = 0.90$, the predicted heat transfer coefficient for R404A is $4549 \text{ W m}^{-2} \text{ K}^{-1}$ while for CO₂, the heat transfer coefficient is $4927 \text{ W m}^{-2} \text{ K}^{-1}$. The reduced pressure of R404A is about half of CO₂ in this case, which counteracts the poorer thermophysical properties of R404A compared to those of CO₂.

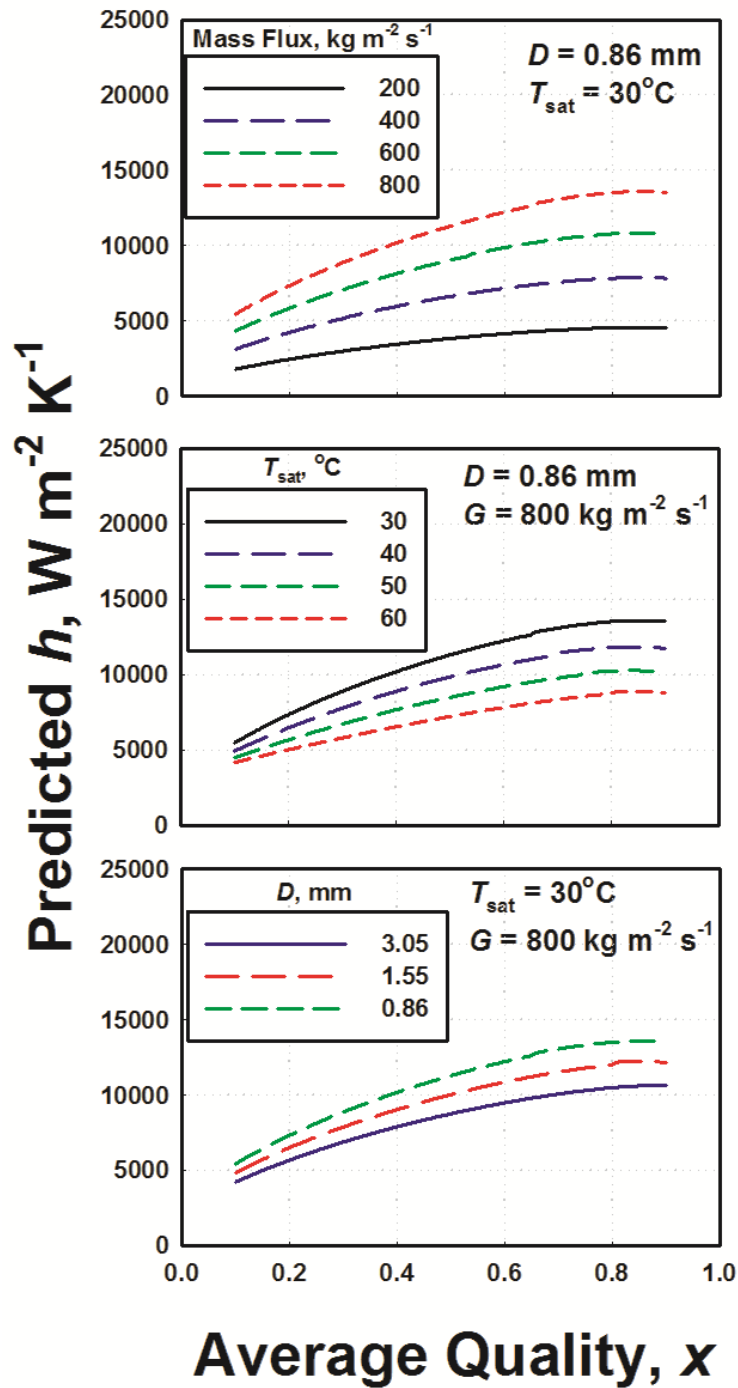


Figure 7.20: Illustration of Heat Transfer Model Trends

Overall, the model developed here was in good agreement with data from the present study, and on microchannel condensation for three different fluids; R404A, NH_3 , and CO_2 from Fronk and Garimella (2010, 2012). The model predicts 93.4% of data from

the present study and from Fronk and Garimella (2010, 2012) within 25% with an AAD of 11.4%. The circular tube model was developed solely from R404A data from this work and was found to predict NH₃ data from Fronk and Garimella (2012) well. To account for the varying film thickness along the channel perimeter in rectangular geometries, an effective film thickness model for rectangular channels was developed and fit to the CO₂ data of Fronk and Garimella (2010) with very good agreement.

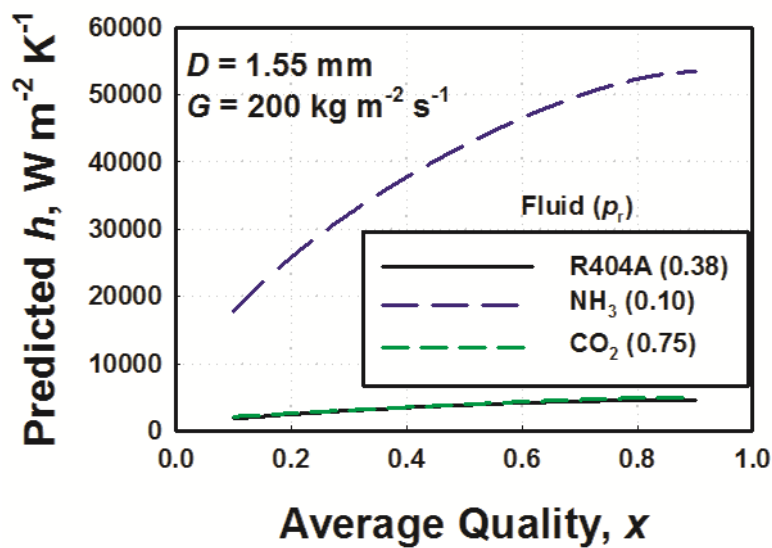


Figure 7.21: Prediction of Heat Transfer Model for R404A, NH₃, and CO₂

CHAPTER 8: CONCLUSIONS AND RECOMMENDATIONS

A comprehensive investigation of flow regimes, void fraction, pressure drop, and heat transfer for condensation through microchannels was conducted. Experiments were conducted on refrigerant R404A throughout the entire condensation range at varying mass fluxes ($200 \leq G \leq 800 \text{ kg m}^{-2} \text{ s}^{-1}$) and saturation temperatures from 30 to 60°C. At these saturation temperatures, condensation occurs over a wide range of mid-to-high reduced pressures ($0.38 \leq p_r \leq 0.77$.) High speed video recordings of the condensation process at high pressures were obtained in three tube diameters, $D = 0.508, 1.00, \text{ and } 3.00$ mm. Four major flow regimes were observed (annular, stratified, intermittent, and dispersed) and the observed flow transitions were found to agree well with the Nema (2007) flow regime map. An image analysis program was developed to measure void fraction from the high-speed video data. The void fraction data agreed well with the Baroczy (1965) correlation, but a new model based on physical insights from the present study was developed. This model agreed well with the data from the present study (AAD = 10.3%, AD = 0.2%), predicting 92% of the data within 25%. The model also predicted void fraction data obtained for condensing R134a reasonably well (Winkler *et al.*, 2012), AAD = 15%, AD = -4%.) Also, the model predicted the trends with respect to tube diameter and saturation temperature well, and converges to the homogeneous model as the reduced pressure approaches unity.

The void fraction model and the Nema (2007) flow regime map were used as the building blocks for pressure drop and heat transfer models. A multi-regime pressure drop correlation was developed from pressure drop data on 0.508, 1.00, and 3.05 mm diameter tubes. The intermittent regime model developed using the approach used by Garimella *et al.* (2002). However, only four pressure drop data points from the present study were in the intermittent regime, thus not providing adequate validation for the model. In addition, the improvement in overall model predictions offered by including the

intermittent model was not substantial enough to warrant the added complexity. If additional data are available in the intermittent regime in the future, this model can be used as a starting point and refined further based on those data. The void fraction model was used to obtain the vapor-liquid interfacial perimeter for the wavy and annular pressure drop model. For wavy flow, gravitation forces were assumed to dampen waves, resulting in a smooth vapor-liquid interface. For annular flow, surface tension forces were assumed to exert a dampening influence on interfacial waves. Therefore, the Froude and capillary numbers were used to model the interfacial friction factors for wavy and annular flows, respectively. A linear interpolation between the interfacial friction factors in these regimes was suggested for the transition region. The model agreed well with the measured pressure drop data with an AAD and AD of 12.7 and 1.3%, respectively. It predicts 85.5% of the data within 25%.

A multi-regime heat transfer model was also developed based on data for condensing R404A through 0.86, 1.55, and 3.05 mm diameter tubes. The wavy flow model was developed based on the approach of Andresen (2007). The void fraction model developed here was used to determine the area of the wetted perimeter in contact with the gravity driven film condensate and the convective liquid pool. The annular flow model was developed based on the two-phase multiplier approach of Thome *et al.* (2003) using the film thickness as the characteristic length. The liquid film thickness was deduced from the void fraction model developed in this study. The model agreed well with the data, predicting 93.6% within 25%, with an AAD and AD of 11.4% and 4.6%, respectively. The annular flow heat transfer model was also able to predict the data of Fronk and Garimella (2012) for condensation of NH_3 at low reduced pressures ($0.10 \leq p_r \leq 0.23$) through a circular 1.435 mm diameter tube, with an AAD and AD of 13.5% and -4.6%, respectively. It predicted 84.7% of the data within 25%. Based on observations from the literature, the annular model was further extended to rectangular microchannel

geometries. For this, the characteristic film thickness was adjusted to account for the thinning of the film condensate in rectangular geometries at high qualities. The resulting extended model for rectangular geometries was compared to condensing CO₂ data of Fronk and Garimella (2010) in tubes with varying hydraulic diameters from 100 to 160 μm. Agreement with their data was very good, predicting 97% of the data within 25%, with an AAD and AD of 10.5 and 0.5%, respectively.

The findings and correlations developed from this work make an important contribution to the understanding of condensation over a wide range of pressures, mass fluxes and microchannel diameters. This increased understanding will yield more accurate and efficient condenser designs, and yield better estimates of fluid inventories in two-phase systems. In addition, the image analysis tool will result in accurate local and bulk measurements of void fraction and vapor bubble parameters in future investigations of two-phase flow and phase change phenomena.

Recommendations for Future work

This investigation has led to an increased understanding of condensation in microchannels over a wide range of operating conditions. However, there are still several key issues that require further investigation.

- The intermittent flow pressure drop model was not fully validated in the present study. To assist in obtaining a better understanding of this regime, additional measurements of intermittent flow during condensation are required. Measurements of bubble/slug size and length variations and distributions are some of the parameters that would help achieve this enhanced understanding. Because intermittent flows often occur in small diameter channels at low qualities, and mass fluxes, measurements of pressure drop and heat transfer

coefficients in this regime are particularly challenging, and will perhaps require different methods than those that were employed in the present study.

- Optical visualization of flow parameters such as film thickness becomes increasingly challenging at hydraulic diameters < 0.5 mm. In addition, in disperse flows, interface tracking through direct optical flow visualization is not possible. In such cases, measurement of secondary parameters such as electrical capacitance/impedance to deduce these flow parameters could be employed with increased accuracies.
- Microchannel heat exchangers often use channels with noncircular geometries. Visualization of condensing flows in such noncircular geometries, especially for $D_h < 1$ mm, are needed to further validate and refine flow regime maps such as those by Nema (2007). Such studies will also provide insights into the film thinning in surface tension driven flows in channels with sharp corners, and the associated increase in heat transfer coefficients.
- The present study focused on understanding condensation in single, circular tubes. Multi-port microchannel designs may experience flow maldistribution. An example of maldistribution is shown in Figure 8.1. Maldistribution can significantly influence the local flow regimes and void fractions, and in turn, the local pressure drop and heat transfer. A better understanding of the effects and causes of maldistribution, and development of methods to minimize it or mitigate its effects will lead to better, more compact and efficient phase-change heat transfer devices.
- In the present study, high uncertainties in measured heat transfer coefficients were observed at high mass fluxes, high qualities, low reduced pressures, and small tube diameters. Under these conditions, refrigerant heat transfer coefficients are expected to be large and ensuring that the refrigerant resistance is the largest can be challenging. Future work should focus on alternative methods for measuring

such high heat transfer coefficients across small temperature differences on the order of 0.1 K during condensation in microchannels.

- Similar investigations of void fraction, pressure drop, and heat transfer should be conducted on alternative condensing fluids, including zeotropic mixtures, which will increasingly gain importance as working fluids, and will present additional challenges through species transport and mass transfer resistances in one or both phases.

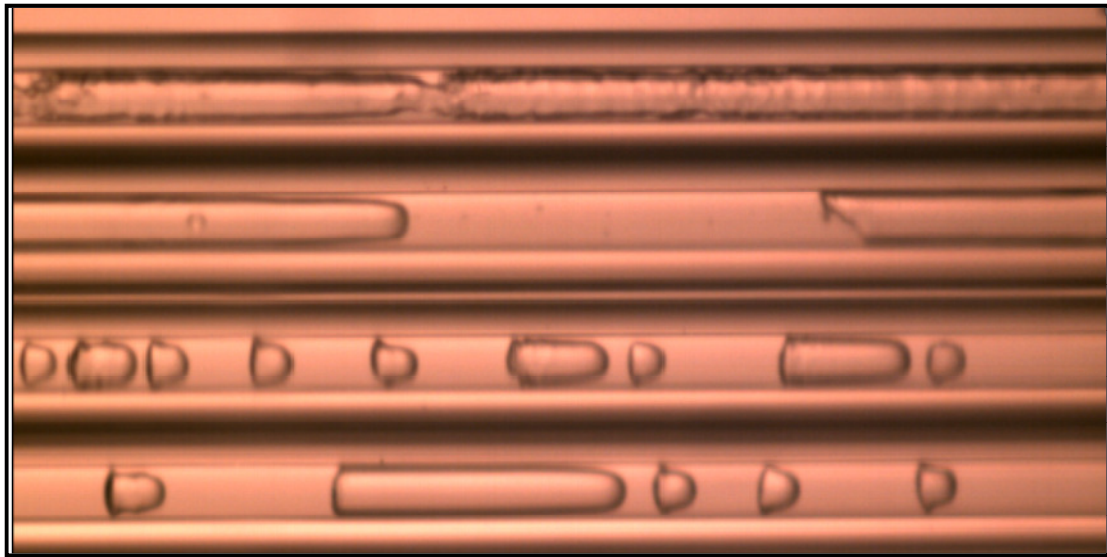


Figure 8.1: Observed Flow Maldistribution in Condensing R404A Through 1.00 mm Diameter Tubes

APPENDIX A - UNCERTAINTY PROPAGATION

Uncertainty propagation analyses were conducted using the Engineering Equation Solver platform. A sample calculation for uncertainty in heat transfer and pressure drop measurements is presented here following the examples presented in Chapter 4 and in more detail in Appendix B.1 and B.2. The measured values for the representative data point presented here can be found in Tables 4.1-4.3. The representative data point presented here is for $D = 3.05 \text{ mm}$, $T_{\text{sat}} = 31.15^\circ\text{C}$, $G = 806 \text{ kg m}^{-2} \text{ s}^{-1}$, and $x_{r,\text{test,avg}} = 0.85$.

A.1. LARGE TUBE TEST FACILITY HEAT DUTY UNCERTAINTY

The heat duty in the test section is measured using the thermal amplification technique and requires heat duties from the secondary heat exchanger, \dot{Q}_{sec} , heat losses to the ambient, $\dot{Q}_{\text{loss, ambient}}$, and heat additions from the pump, \dot{Q}_{pump} (Equation 4.16.) Heat loss and pump addition uncertainties are conservatively assumed to be $\pm 50\%$ of calculated values. The uncertainty in the measured heat duty in the secondary heat exchanger is a function of temperature and pressure measurements used to determine the inlet and outlet enthalpies, and the mass flow rate of the coolant. The resulting uncertainty in the secondary heat exchanger is:

$$\left(U_{\dot{Q}_{\text{sec}}} \right)^2 = \left(\frac{\partial \dot{Q}_{\text{sec}}}{\partial \dot{m}_{\text{sec}}} U_{\dot{m}_{\text{sec}}} \right)^2 + \left(\frac{\partial \dot{Q}_{\text{sec}}}{\partial i_{w,\text{sec,in}}} U_{i_{w,\text{sec,in}}} \right)^2 + \left(\frac{\partial \dot{Q}_{\text{sec}}}{\partial i_{w,\text{sec,out}}} U_{i_{w,\text{sec,out}}} \right)^2 \quad (\text{A.1})$$

Differentiating for the respective terms results in:

$$\left(U_{\dot{Q}_{\text{sec}}} \right)^2 = \left(\Delta i_{w,\text{sec}} \cdot U_{\dot{m}_{\text{sec}}} \right)^2 + \left(\dot{m}_{\text{sec}} \cdot U_{i_{w,\text{sec,in}}} \right)^2 + \left(\dot{m}_{\text{sec}} \cdot U_{i_{w,\text{sec,out}}} \right)^2 \quad (\text{A.2})$$

where

$$\left(U_{i_{w,\text{sec,in}}} \right)^2 = \left(\frac{\partial i_{w,\text{sec,in}}}{\partial T_{w,\text{sec,in}}} U_{T_{w,\text{sec,in}}} \right)^2 = \left(c_p U_{T_{w,\text{sec,in}}} \right)^2 \quad (\text{A.3})$$

$$\left(U_{i_{w,\text{sec,out}}} \right)^2 = \left(\frac{\partial i_{w,\text{sec,out}}}{\partial T_{w,\text{sec,out}}} U_{T_{w,\text{sec,out}}} \right)^2 = \left(c_p U_{T_{w,\text{sec,out}}} \right)^2 \quad (\text{A.4})$$

The uncertainty in the mass flow rate arises from the uncertainty (0.15% of the measured value) in the measured flow rate from the Coriolis flow meter, $U_{\dot{m}_{sec}} = 1.957 \times 10^{-5} \text{ kg/s}$.

The uncertainty in the measured enthalpies is:

$$U_{i_{w,sec,in}} = U_{i_{w,sec,out}} = (4.19 \text{ kJ/kg-K})(0.25 \text{ K}) = 1.05 \text{ kJ/kg}$$

Substituting the calculated values into Equation A.2 results in an uncertainty in the measured secondary heat duty of:

$$U_{\dot{Q}_{sec}} = \sqrt{(47.45 \text{ kJ/kg} \cdot 1.96 \times 10^{-5} \text{ kg/s})^2 + 2(3.9 \times 10^{-3} \text{ kg/s} \cdot 1.05 \text{ kJ/kg})^2} = 5.87 \text{ W}$$

This uncertainty in measured secondary heat duty is 3.2% of the measured value ($\dot{Q}_{sec} = 185.8 \text{ W}$.) The uncertainty in measured test section heat duty is deduced from Equation 4.16 and is:

$$\left(U_{\dot{Q}_{test}} \right)^2 = \left(\frac{\partial \dot{Q}_{test}}{\partial \dot{Q}_{sec}} U_{\dot{Q}_{sec}} \right)^2 + \left(\frac{\partial \dot{Q}_{test}}{\partial \dot{Q}_{loss,ambient}} U_{\dot{Q}_{loss,ambient}} \right)^2 + \left(\frac{\partial \dot{Q}_{test}}{\partial \dot{Q}_{pump}} U_{\dot{Q}_{pump}} \right)^2 \quad (\text{A.5})$$

Differentiating for the respective terms results in:

$$\left(U_{\dot{Q}_{test}} \right)^2 = \left(U_{\dot{Q}_{sec}} \right)^2 + \left(U_{\dot{Q}_{loss,ambient}} \right)^2 + \left(U_{\dot{Q}_{pump}} \right)^2 \quad (\text{A.6})$$

Substituting the result of Equation A.2, and assessing a conservative 50% for the calculated pump addition and heat losses, the resulting uncertainty in test section heat duty is:

$$U_{\dot{Q}_{test}} = \sqrt{(5.87 \text{ W})^2 + (1.62 \text{ W})^2 + (11 \text{ W})^2} = 12.58 \text{ W}$$

This uncertainty in test section heat duty is 7.8% of the measured value ($\dot{Q}_{test} = 160.5 \text{ W}$.)

The pump heat addition in this example is the biggest contributor to uncertainty and is about 6.8%. The ambient heat losses in this case are low (1%) due to the low saturation temperature.

A.2. UA

To determine the uncertainty in measured heat transfer coefficient, the uncertainty in UA is required. The UA is calculated using Equation 4.19 and is a function of test section heat duty and test section LMTD. Thus, the uncertainty in UA is:

$$(U_{UA})^2 = \left(\frac{\partial UA}{\partial \dot{Q}_{\text{test}}} U_{\dot{Q}_{\text{test}}} \right)^2 + \left(\frac{\partial UA}{\partial \text{LMTD}} U_{\text{LMTD}} \right)^2 \quad (\text{A.7})$$

Differentiating for the respective terms results in:

$$(U_{UA})^2 = \left(\frac{1}{\text{LMTD}} U_{\dot{Q}_{\text{test}}} \right)^2 + \left(\frac{-\dot{Q}_{\text{test}}}{\text{LMTD}^2} U_{\text{LMTD}} \right)^2 \quad (\text{A.8})$$

The uncertainty in test section heat duty was calculated in Appendix A.1, while the uncertainty in LMTD is a function of the measured coolant and refrigerant temperatures. Equation 4.20 describes the calculation of the LMTD, the corresponding uncertainty is given by:

$$(U_{\text{LMTD}})^2 = \left(\frac{\partial \text{LMTD}}{\partial T_{\text{ref},\text{in}}} U_{T_{\text{ref}}} \right)^2 + \left(\frac{\partial \text{LMTD}}{\partial T_{\text{ref},\text{out}}} U_{T_{\text{ref}}} \right)^2 + \left(\frac{\partial \text{LMTD}}{\partial T_{\text{w,pri,test,in}}} U_T \right)^2 + \left(\frac{\partial \text{LMTD}}{\partial T_{\text{w,pri,test,out}}} U_T \right)^2 \quad (\text{A.9})$$

Differentiating for the respective terms results in the following terms:

$$\begin{aligned} \frac{\partial \text{LMTD}}{\partial T_{\text{ref},\text{in}}} &= \frac{1}{\ln(\Delta T_1 / \Delta T_2)} - \frac{\Delta T_1 - \Delta T_2}{[\ln(\Delta T_1 / \Delta T_2)]^2} \frac{1}{\Delta T_1} = 0.575 \\ \frac{\partial \text{LMTD}}{\partial T_{\text{ref},\text{out}}} &= -\frac{1}{\ln(\Delta T_1 / \Delta T_2)} + \frac{\Delta T_1 - \Delta T_2}{[\ln(\Delta T_1 / \Delta T_2)]^2} \frac{1}{\Delta T_2} = 0.4388 \\ \frac{\partial \text{LMTD}}{\partial T_{\text{w,pri,test,in}}} &= \frac{1}{\ln(\Delta T_1 / \Delta T_2)} - \frac{\Delta T_1 - \Delta T_2}{[\ln(\Delta T_1 / \Delta T_2)]^2} \frac{1}{\Delta T_2} = -0.4388 \\ \frac{\partial \text{LMTD}}{\partial T_{\text{w,pri,test,out}}} &= -\frac{1}{\ln(\Delta T_1 / \Delta T_2)} + \frac{\Delta T_1 - \Delta T_2}{[\ln(\Delta T_1 / \Delta T_2)]^2} \frac{1}{\Delta T_1} = -0.575 \end{aligned} \quad (\text{A.10})$$

The uncertainty in measured coolant temperatures is $U_T = 0.25^\circ\text{C}$ and the uncertainty in measured refrigerant temperature is a function of measured pressure. The uncertainty in measured refrigerant temperature is:

$$U_T(P) = \frac{\partial T}{\partial P} U_P \quad (\text{A.11})$$

Approximating the differential results in:

$$\frac{\partial T}{\partial P} = \frac{T[P+U_P] - T[P-U_P]}{2U_P} \quad (\text{A.12})$$

The uncertainty in measured pressure, U_P , is 0.075% of the range (0.2586 kPa); therefore, the resulting uncertainty in measured refrigerant temperature is:

$$U_T(P) = \left(\frac{303.7 - 303.7 \text{ K}}{2(0.2586 \text{ kPa})} \right) (0.2586 \text{ kPa}) = 0.1 \text{ K}$$

Substituting the respective values into Equation A.9, the resulting uncertainty in LMTD is:

$$U_{\text{LMTD}} = \sqrt{(0.575 \cdot 0.1)^2 + (0.439 \cdot 0.1)^2 + (-0.575 \cdot 0.25)^2 + (-0.439 \cdot 0.25)^2} = 0.189 \text{ K}$$

This uncertainty in UA is calculated using Equation A.8:

$$U_{UA} = \sqrt{\left(0.1 \frac{1}{\text{K}} (12.58\text{W})\right)^2 + \left(-1.35 \frac{\text{W}}{\text{K}^2} (0.189\text{K})\right)^2} = 1.183 \frac{\text{W}}{\text{K}}$$

This uncertainty in UA is 8% of the measured value (14.8 W K⁻¹.)

A.3. HEAT TRANSFER COEFFICIENT

The condensation heat transfer coefficient is deduced from Equation 4.28. The uncertainties in measured heat transfer area, wall thermal resistance, and heat transfer in the reducer and tee are neglected. The resulting uncertainty is a function of uncertainties in calculated UA and coolant side heat transfer coefficient.

$$(U_{h_r})^2 = \left(\frac{\partial h_r}{\partial UA} U_{UA} \right)^2 + \left(\frac{\partial h_r}{\partial h_w} U_{h_w} \right)^2 \quad (\text{A.13})$$

Differentiating for the respective terms results in the following terms:

$$\begin{aligned} \frac{\partial h_r}{\partial UA} &= \frac{1}{A_{\text{ref}}} \frac{1}{(UA)^2} \frac{1}{(1/UA - 1/h_w A_w - R_{\text{wall}})^2} = 1188 \text{ m}^{-2} \\ \frac{\partial h_r}{\partial h_w} &= -\frac{A_w}{A_{\text{ref}}} \frac{1}{(h_w A_w)^2} \frac{1}{(1/UA - 1/h_w A_w - R_{\text{wall}})^2} = -0.4339 \end{aligned} \quad (\text{A.14})$$

An uncertainty of 25% is assessed for the calculated water side heat transfer coefficient and the uncertainty in UA was deduced in Appendix A.2. The resulting uncertainty in heat transfer coefficient is calculated using Equation A.13.

$$U_{h_r} = \sqrt{(1188 \text{ m}^{-2} \cdot 1.183 \text{ W/K})^2 + (-0.43 \cdot 3419 \text{ W/m}^2\text{-K})^2} = 2027 \text{ W/m}^2\text{-K}$$

This uncertainty in the measured heat transfer coefficient is 18.3% of the measured value ($h_r = 10884 \text{ W/m}^2\text{-K}$.)

A.4. FRICTIONAL PRESSURE DROP

The frictional pressure drop is deduced from the measured pressure drop, inlet contractions and outlet expansions, and the deceleration of the two-phase flow during condensation (Equation 4.30.) The expansion, contraction and deceleration terms are calculated values and an uncertainty of 50% is assessed to these components. The uncertainty in frictional pressure drop is:

$$\begin{aligned} (U_{\Delta P_f})^2 &= \left(\frac{\partial \Delta P_f}{\partial \Delta P_{\text{measured}}} U_{\Delta P_{\text{measured}}} \right)^2 + \left(\frac{\partial \Delta P_f}{\partial \Delta P_{\text{deceleration}}} U_{\Delta P_{\text{deceleration}}} \right)^2 \\ &+ \left(\frac{\partial \Delta P_f}{\partial \Delta P_{\text{contraction}}} U_{\Delta P_{\text{contraction}}} \right)^2 + \left(\frac{\partial \Delta P_f}{\partial \Delta P_{\text{expansion}}} U_{\Delta P_{\text{expansion}}} \right)^2 \end{aligned} \quad (\text{A.15})$$

Differentiating for the respective terms results in the following terms:

$$\left(U_{\Delta P_f}\right)^2 = \left(U_{\Delta P_{\text{measured}}}\right)^2 + \left(U_{\Delta P_{\text{deceleration}}}\right)^2 + \left(U_{\Delta P_{\text{contraction}}}\right)^2 + \left(U_{\Delta P_{\text{expansion}}}\right)^2 \quad (\text{A.16})$$

The uncertainty in measured pressure drop is obtained from the pressure transducer (0.075% of the range) and is $U_{\Delta P_{\text{measured}}} = 46.54 \text{ Pa}$. The resulting uncertainty in frictional pressure drop from Equation A.16 is:

$$U_{\Delta P_f} = \sqrt{(46.54 \text{ Pa})^2 + (965.5 \text{ Pa})^2 + (2366 \text{ Pa})^2 + (804 \text{ Pa})^2} = 2679 \text{ Pa}$$

This uncertainty in the frictional pressure drop is 18.5% of the measured value ($\Delta P_f = 14465 \text{ Pa}$.) A significant portion of the uncertainty comes from the inlet and outlet losses of the test section. The predicted contraction uncertainty is 16% of the frictional pressure drop, the expansion uncertainty is 5.5% of the frictional pressure drop, and the deceleration is 6.7% of the frictional pressure drop.

A.5. SMALL TUBE TEST FACILITY HEAT DUTY

The uncertainty in heat transfer coefficient and pressure drop in the small tube test facility follows the same approach as presented in Appendices A.1 to A.4. The only difference in formulation is in the prediction of test section heat duty. The test section heat duty in the small tube test facility is deduced using Equation 4.42 and is a function in the difference in thermodynamic states at the inlet and outlet of the pre- and post-heaters, the heat addition of the heaters and the heat losses through the system. The uncertainty in test section heat duty is:

$$\begin{aligned} \left(U_{\dot{Q}_{\text{test}}}\right)^2 = & \left(\frac{\partial \dot{Q}_{\text{test}}}{\partial \dot{m}_r} U_{\dot{m}_r}\right)^2 + \left(\frac{\partial \dot{Q}_{\text{test}}}{\partial i_{r, \text{pre-heat,in}}} U_{i_{r, \text{pre-heat,in}}}\right)^2 + \left(\frac{\partial \dot{Q}_{\text{test}}}{\partial i_{r, \text{post-heat,out}}} U_{i_{r, \text{post-heat,out}}}\right)^2 \\ & + \left(\frac{\partial \dot{Q}_{\text{pre-heater}}}{\partial \dot{Q}_{\text{pre-heater}}} U_{\dot{Q}_{\text{pre-heater}}}\right)^2 + \left(\frac{\partial \dot{Q}_{\text{test}}}{\partial \dot{Q}_{\text{post-heater}}} U_{\dot{Q}_{\text{post-heater}}}\right)^2 + \left(\frac{\partial \dot{Q}_{\text{test}}}{\partial \dot{Q}_{\text{loss,ambient}}} U_{\dot{Q}_{\text{loss,ambient}}}\right)^2 \end{aligned} \quad (\text{A.17})$$

Differentiating for the respective terms results in the following terms:

$$\begin{aligned} \left(U_{\dot{Q}_{test}} \right)^2 &= \left(\Delta i_{pre-to-post} \cdot U_{\dot{m}_r} \right)^2 + \left(\dot{m}_r \cdot U_{i_{r, pre-heat, in}} \right)^2 + \left(\dot{m}_r \cdot U_{i_{r, post-heat, out}} \right)^2 \\ &+ \left(U_{\dot{Q}_{pre-heater}} \right)^2 + \left(U_{\dot{Q}_{post-heater}} \right)^2 + \left(U_{\dot{Q}_{loss, ambient}} \right)^2 \end{aligned} \quad (A.18)$$

The uncertainty in ambient heat losses is assumed to be 50% of the calculated value. The uncertainties in measured refrigerant flow rate (0.10% of reading) and heater inputs (0.2% of reading) are determined based on vendor specifications for the respective equipment and instrumentation. The uncertainty in the measured enthalpies is deduced from the pressure and temperature measurements and the refrigerant property functions.

The resulting uncertainty in measured heat duty calculated by Equation A.18 is:

$$U_{\dot{Q}_{test}} = \sqrt{\left(161 \cdot 1.125 \times 10^{-6} \right)^2 + \left(1.125 \times 10^{-3} \cdot 0.3782 \right)^2 + \left(1.125 \times 10^{-3} \cdot 0.335 \right)^2 + (0.295)^2 + (0.1474)^2 + (0.931)^2} = 1.154 \text{ W}$$

This uncertainty in the test section heat duty is 3.0% of the measured value ($\dot{Q}_{test} = 38.15 \text{ W}$.)

APPENDIX B - SAMPLE DATA POINT CALCULATIONS

Appendix B.1 – Sample Test Calculation for $D = 3.05$ (mm)

Primary Loop	
$T_{w, \text{test, in}}$ ($^{\circ}\text{C}$)	20.19
$T_{w, \text{test, out}}$ ($^{\circ}\text{C}$)	20.38
$\dot{V}_{w, \text{prim}}$ (m^3/s)	1.269×10^{-4}
Secondary Loop	
$T_{w, \text{sec, in}}$ ($^{\circ}\text{C}$)	7.25
$T_{w, \text{sec, out}}$ ($^{\circ}\text{C}$)	18.57
$\dot{m}_{w, \text{sec}}$ (kg/s)	3.92×10^{-3}
Pre-Condenser	
$T_{w, \text{pre, in}}$ ($^{\circ}\text{C}$)	9.23
$T_{w, \text{pre, out}}$ ($^{\circ}\text{C}$)	46.42
$\dot{V}_{w, \text{pre}}$ (m^3/s)	3.16×10^{-6}
Post-Condenser	
$T_{w, \text{post, in}}$ ($^{\circ}\text{C}$)	5.6
$T_{w, \text{post, out}}$ ($^{\circ}\text{C}$)	14.5
$\dot{V}_{w, \text{post}}$ (m^3/s)	1.83×10^{-5}

Refrigerant Loop	
$P_{r, \text{pre, in}}$ (kPa)	1475
$P_{r, \text{test, in}}$ (kPa)	1471
$P_{r, \text{test, out}}$ (kPa)	1449
$P_{r, \text{post, out}}$ (kPa)	1449
$\Delta P_{r, \text{test}}$ (kPa)	15.66
$T_{r, \text{pre, in}}$ ($^{\circ}\text{C}$)	98.93
$T_{r, \text{pre, in, sat}}$ ($^{\circ}\text{C}$)	31.55
$\Delta T_{\text{sup, pre}}$ ($^{\circ}\text{C}$)	67.38
$T_{r, \text{pre, out}}$ ($^{\circ}\text{C}$)	32.99
$T_{r, \text{test, in}}$ ($^{\circ}\text{C}$)	31.45
$T_{r, \text{test, in, sat}}$ ($^{\circ}\text{C}$)	31.40
$\text{Error}_{r, \text{test, in}}$ ($^{\circ}\text{C}$)	0.05
$T_{r, \text{test, out}}$ ($^{\circ}\text{C}$)	30.85
$T_{r, \text{test, out, sat}}$ ($^{\circ}\text{C}$)	30.95
$\text{Error}_{r, \text{test, out}}$ ($^{\circ}\text{C}$)	0.1
$T_{r, \text{post, in}}$ ($^{\circ}\text{C}$)	30.77
$T_{r, \text{post, out}}$ ($^{\circ}\text{C}$)	20.75
$T_{r, \text{post, out, sat}}$ ($^{\circ}\text{C}$)	30.46
$\Delta T_{\text{sub, post}}$ ($^{\circ}\text{C}$)	9.71
\dot{m}_r (kg/s)	0.005881

Data Point	
p_r	0.3926
P_{critical} (kPa)	3729
G ($\text{kg}/\text{m}^2\text{-s}$)	806
$x_{r, \text{test, avg}}$	0.85
Date of Experiment	16 Sep 2010
Run of Experiment	55
Assumed Variables	
P_w (kPa)	275.8
P_{ambient} (kPa)	101.0
ϵ_{ins}	0.85

Heat Transfer Calculations – 16 September 2010 – Run 55		
Inputs	Equations	Results
Heat Losses in Pre-Condenser (Shell-and-Tube)		
$D_{pre, o, s} = 38.1 \text{ mm}$ $D_{pre, i, s} = 34.8 \text{ mm}$ $D_{pre, ins, s} = 100 \text{ mm}$ $k_{pre, s} = 14.9 \text{ W/m-K}$ $k_{ins} = 0.043 \text{ W/m-K}$ $L_{pre, s} = 460 \text{ mm}$ $\epsilon_{ins} = 0.85$ $\sigma =$ $5.67 \times 10^{-8} \text{ W m}^{-2} \text{ K}^{-4}$ $T_{ambient} = 24.72 \text{ }^\circ\text{C}$ $P_{ambient} = 101 \text{ kPa}$ $g = 9.81 \text{ m/s}^2$ $T_{w, pre, in} = 9.23 \text{ }^\circ\text{C}$ $T_{w, pre, out} = 46.42 \text{ }^\circ\text{C}$	$R_{wall} = \frac{\ln\left(\frac{D_{pre, o, s}}{D_{pre, i, s}}\right)}{2\pi k_{pre, s} L_{pre, s}}$	$R_{wall} =$ $2.104 \times 10^{-3} \text{ K/W}$
	$R_{ins} = \frac{\ln\left(\frac{D_{pre, ins, s}}{D_{pre, o, s}}\right)}{2\pi k_{ins} L_{pre, s}}$	$R_{ins} = 7.764 \text{ K/W}$
	$R_{radiation} = \frac{1}{\epsilon_{ins} \pi D_{pre, ins, s} L_{pre, s} \sigma (T_{ins}^2 + T_{ambient}^2) (T_{ins} + T_{ambient})}$	$R_{radiation} = 1.356 \text{ K/W}$ $T_{ins} = 25.09 \text{ }^\circ\text{C}$
	$T_{avg} = (T_{ins} + T_{ambient}) / 2$	$T_{avg} = 24.9 \text{ }^\circ\text{C}$
	$Pr_{air}, \nu_{air}, \rho_{air}, k_{air}, \beta_{air} = f(T_{avg}, P_{ambient})$	$Pr_{air} = 0.71$ $\nu_{air} =$ $1.56 \times 10^{-5} \text{ m}^2/\text{s}$ $\rho_{air} = 1.188 \text{ kg/m}^3$ $k_{air} = 0.026 \text{ W/m-K}$ $\beta_{air} = 3.4 \times 10^{-3} \text{ 1/K}$
	<p>By assuming a negligible convective resistance in cooling lines:</p> $T_{inner\ wall} = (T_{w, pre, in} + T_{w, pre, out}) / 2$	$T_{inner\ wall} = 27.83 \text{ }^\circ\text{C}$
	$Ra = \frac{g \beta_{air} (T_{ins} - T_{ambient}) D_{pre, ins, s}^3}{\nu_{air} \alpha_{air}}$	$Ra = 35152$
	$Nu = \frac{h_{nat. conv.} D_{ins}}{k_{air}} = \left[0.60 + \frac{0.387 Ra^{1/6}}{\left(1 + \left(\frac{0.559}{Pr_{air}} \right)^{9/16} \right)^{8/27}} \right]^2$ (Churchill and Chu, 1975)	$Nu = 5.94$ $h_{nat. conv.} =$ $1.559 \text{ W/m}^2\text{-K}$

Heat Transfer Calculations – 16 September 2010 – Run 55		
Inputs	Equations	Results
	$R_{\text{nat. conv.}} = \frac{1}{h_{\text{nat. conv.}} \pi D_{\text{ins}} L_{\text{pre, s}}}$	$R_{\text{nat. conv.}} = 4.438 \text{ K/W}$
	$\dot{Q}_{\text{loss, pre}} = \frac{(T_{\text{inner wall}} - T_{\text{ambient}})}{R_{\text{wall}} + R_{\text{ins}} + \left(\frac{R_{\text{nat. conv.}} \cdot R_{\text{radiation}}}{R_{\text{nat. conv.}} + R_{\text{radiation}}} \right)}$	$\dot{Q}_{\text{loss, pre}} = 0.353 \text{ W}$
Heat Losses in Post-Condenser (Shell-and-Tube)		
$D_{\text{post, o, s}} = 38.1 \text{ mm}$ $D_{\text{post, i, s}} = 34.8 \text{ mm}$ $D_{\text{post, ins, s}} = 100 \text{ mm}$ $k_{\text{post, s}} = 14.9 \text{ W/m-K}$	$R_{\text{wall}} = \frac{\ln \left(\frac{D_{\text{post, o, s}}}{D_{\text{post, i, s}}} \right)}{2\pi k_{\text{post, s}} L_{\text{post, s}}}$	$R_{\text{wall}} = 4.7 \times 10^{-3} \text{ K/W}$
$k_{\text{ins}} = 0.043 \text{ W/m-K}$ $L_{\text{post, s}} = 206 \text{ mm}$ $\epsilon_{\text{ins}} = 0.85$ $\sigma =$	$R_{\text{ins}} = \frac{\ln \left(\frac{D_{\text{post, ins, s}}}{D_{\text{post, o, s}}} \right)}{2\pi k_{\text{ins}} L_{\text{post, s}}}$	$R_{\text{ins}} = 17.34 \text{ K/W}$
$5.67 \times 10^{-8} \text{ W m}^{-2} \text{K}^{-4}$ $T_{\text{ambient}} = 24.72^\circ \text{C}$ $P_{\text{ambient}} = 101 \text{ kPa}$ $g = 9.81 \text{ m/s}^2$ $T_{\text{w, post, in}} = 5.6^\circ \text{C}$ $T_{\text{w, post, out}} = 14.51^\circ \text{C}$	$R_{\text{radiation}} = \frac{1}{\epsilon_{\text{ins}} \pi D_{\text{post, ins, s}} L_{\text{post, s}} \sigma (T_{\text{ins}}^2 + T_{\text{ambient}}^2) (T_{\text{ins}} + T_{\text{ambient}})}$	$R_{\text{radiation}} = 3.06 \text{ K/W}$ $T_{\text{ins}} = 23.13^\circ \text{C}$
	$T_{\text{avg}} = (T_{\text{ins}} + T_{\text{ambient}}) / 2$	$T_{\text{avg}} = 23.93^\circ \text{C}$
	$\text{Pr}_{\text{air}}, \nu_{\text{air}}, \rho_{\text{air}}, k_{\text{air}}, \beta_{\text{air}} = f(T_{\text{avg}}, P_{\text{ambient}})$	$\text{Pr}_{\text{air}} = 0.71$ $\nu_{\text{air}} = 1.56 \times 10^{-5} \text{ m}^2/\text{s}$ $\rho_{\text{air}} = 1.188 \text{ kg/m}^3$ $k_{\text{air}} = 0.026 \text{ W/m-K}$ $\beta_{\text{air}} = 3.4 \times 10^{-3} \text{ 1/K}$
	By assuming a negligible convective resistance in cooling lines: $T_{\text{inner wall}} = (T_{\text{w, post, in}} + T_{\text{w, post, out}}) / 2$	$T_{\text{inner wall}} = 10.1^\circ \text{C}$
	$Ra = \frac{g \beta_{\text{air}} (T_{\text{ins}} - T_{\text{ambient}}) D_{\text{post, ins, s}}^3}{\nu_{\text{air}} \alpha_{\text{air}}}$	$Ra = 152513$

Heat Transfer Calculations – 16 September 2010 – Run 55

Inputs	Equations	Results
	$Nu = \frac{h_{\text{nat. conv.}} D_{\text{ins}}}{k_{\text{air}}} = \left(0.60 + \frac{0.387 Ra^{1/6}}{\left(1 + \left(\frac{0.559}{Pr_{\text{air}}} \right)^{9/16} \right)^{8/27}} \right)^2$ <p>(Churchill and Chu, 1975)</p>	$Nu = 8.689$ $h_{\text{nat. conv.}} = 2.279 \text{ W/m}^2\text{-K}$
	$R_{\text{nat. conv.}} = \frac{1}{h_{\text{nat. conv.}} \pi D_{\text{ins}} L_{\text{pre, s}}}$	$R_{\text{nat. conv.}} = 6.781 \text{ K/W}$
	$\dot{Q}_{\text{loss, post}} = \frac{(T_{\text{inner wall}} - T_{\text{ambient}})}{R_{\text{wall}} + R_{\text{ins}} + \left(\frac{R_{\text{nat. conv.}} R_{\text{radiation}}}{R_{\text{nat. conv.}} + R_{\text{radiation}}} \right)}$	$\dot{Q}_{\text{loss, post}} = -0.75 \text{ W}$ (implies heat gain)

Heat Losses in Refrigerant Tubing from Pre-Condenser Outlet to Test Section Inlet

$D_{\text{tube, r, i}} = 10.2 \text{ mm}$ $D_{\text{tube, r, o}} = 12.7 \text{ mm}$ $D_{\text{r, ins}} = 100 \text{ mm}$ $k_{\text{tube, r}} = 15.5 \text{ W/m-K}$ $k_{\text{ins}} = 0.043 \text{ W/m-K}$ $L_{\text{r, pre-to-test}} = 1016 \text{ mm}$	$R_{\text{wall}} = \frac{\ln \left(\frac{D_{\text{tube, r, o}}}{D_{\text{tube, r, i}}} \right)}{2\pi k_{\text{tube, r}} L_{\text{r, pre-to-test}}}$	$R_{\text{wall}} = 2.22 \times 10^{-3} \text{ K/W}$
$\epsilon_{\text{ins}} = 0.85$ $\sigma = 5.67 \times 10^{-8} \text{ W m}^{-2}\text{K}^{-4}$ $T_{\text{ambient}} = 24.72 \text{ }^\circ\text{C}$ $P_{\text{ambient}} = 101 \text{ kPa}$ $g = 9.81 \text{ m/s}^2$ $T_{\text{r, pre, out}} = 31.49 \text{ }^\circ\text{C}$ $T_{\text{r, test, in}} = 32.99 \text{ }^\circ\text{C}$	$R_{\text{ins}} = \frac{\ln \left(\frac{D_{\text{r, ins}}}{D_{\text{tube, r, o}}} \right)}{2\pi k_{\text{ins}} L_{\text{r, pre-to-test}}}$	$R_{\text{ins}} = 7.52 \text{ K/W}$
	$R_{\text{radiation}} = \frac{1}{\epsilon_{\text{ins}} \pi D_{\text{r, ins}} L_{\text{r, pre-to-test}} \sigma (T_{\text{ins}}^2 + T_{\text{ambient}}^2) (T_{\text{ins}} + T_{\text{ambient}})}$	$R_{\text{radiation}} = 0.6135 \text{ K/W}$ $T_{\text{ins}} = 25.19 \text{ }^\circ\text{C}$
	$T_{\text{avg}} = (T_{\text{ins}} + T_{\text{ambient}}) / 2$	$T_{\text{avg}} = 24.72 \text{ }^\circ\text{C}$
	$Pr_{\text{air}}, \nu_{\text{air}}, \rho_{\text{air}}, k_{\text{air}}, \beta_{\text{air}} = f(T_{\text{avg}}, P_{\text{ambient}})$	$Pr_{\text{air}} = 0.71$ $\nu_{\text{air}} = 1.56 \times 10^{-5} \text{ m}^2/\text{s}$ $\rho_{\text{air}} = 1.188 \text{ kg/m}^3$ $k_{\text{air}} = 0.026 \text{ W/m-K}$ $\beta_{\text{air}} = 3.4 \times 10^{-3} \text{ 1/K}$

Heat Transfer Calculations – 16 September 2010 – Run 55

Inputs	Equations	Results
	By assuming a negligible convective resistance in tubing: $T_{\text{inner wall}} = (T_{r, \text{pre, out}} + T_{r, \text{test, in}}) / 2$	$T_{\text{inner wall}} = 32.74^\circ\text{C}$
	$Ra = \frac{g \beta_{\text{air}} (T_{\text{ins}} - T_{\text{ambient}}) D_{r, \text{ins}}^3}{\nu_{\text{air}} \alpha_{\text{air}}}$	$Ra = 44670$
	$Nu = \frac{h_{\text{nat. conv.}} D_{\text{ins}}}{k_{\text{air}}} = \left(0.60 + \frac{0.387 Ra^{1/6}}{\left(1 + \left(\frac{0.559}{Pr_{\text{air}}} \right)^{9/16} \right)^{8/27}} \right)^2$ (Churchill and Chu, 1975)	$Nu = 6.316$ $h_{\text{nat. conv.}} = 1.657 \text{ W/m}^2\text{-K}$
	$R_{\text{nat. conv.}} = \frac{1}{h_{\text{nat. conv.}} \pi D_{\text{ins}} L_{r, \text{pre-to-test}}}$	$R_{\text{nat. conv.}} = 1.89 \text{ K/W}$
	$\dot{Q}_{\text{loss, pre-to-test}} = \frac{(T_{\text{inner wall}} - T_{\text{ambient}})}{R_{\text{wall}} + R_{\text{ins}} + \left(\frac{R_{\text{nat. conv.}} R_{\text{radiation}}}{R_{\text{nat. conv.}} + R_{\text{radiation}}} \right)}$	$\dot{Q}_{\text{loss, pre-to-test}} = 1.005 \text{ W}$
Heat Losses in Refrigerant Tubing from Test Section Outlet to Post-Condenser Inlet		
$D_{\text{tube, r, i}} = 10.2 \text{ mm}$ $D_{\text{tube, r, o}} = 12.7 \text{ mm}$ $D_{r, \text{ins}} = 100 \text{ mm}$ $k_{\text{tube, r}} = 15.5 \text{ W/m-K}$ $k_{\text{ins}} = 0.043 \text{ W/m-K}$ $L_{r, \text{test-to-post}} = 1016 \text{ mm}$ $\epsilon_{\text{ins}} = 0.85$ $\sigma = 5.67 \times 10^{-8} \text{ W m}^{-2}\text{K}^{-4}$ $T_{\text{ambient}} = 24.72^\circ\text{C}$ $P_{\text{ambient}} = 101 \text{ kPa}$	$R_{\text{wall}} = \frac{\ln \left(\frac{D_{\text{tube, r, o}}}{D_{\text{tube, r, i}}} \right)}{2\pi k_{\text{tube, r}} L_{r, \text{test-to-post}}}$	$R_{\text{wall}} = 2.2 \times 10^{-3} \text{ K/W}$
	$R_{\text{ins}} = \frac{\ln \left(\frac{D_{r, \text{ins}}}{D_{\text{tube, r, o}}} \right)}{2\pi k_{\text{ins}} L_{r, \text{test-to-post}}}$	$R_{\text{ins}} = 7.518 \text{ K/W}$
	$R_{\text{radiation}} = \frac{1}{\epsilon_{\text{ins}} \pi D_{r, \text{ins}} L_{r, \text{test-to-post}} \sigma (T_{\text{ins}}^2 + T_{\text{ambient}}^2) (T_{\text{ins}} + T_{\text{ambient}})}$	$R_{\text{radiation}} = 0.614 \text{ K/W}$ $T_{\text{ins}} = 25.08^\circ\text{C}$
	$T_{\text{avg}} = (T_{\text{ins}} + T_{\text{ambient}}) / 2$	$T_{\text{avg}} = 24.9^\circ\text{C}$

Heat Transfer Calculations – 16 September 2010 – Run 55		
Inputs	Equations	Results
$g = 9.81 \text{ m/s}^2$ $T_{r, \text{ test, out}} = 30.89^\circ \text{C}$ $T_{r, \text{ post, in}} = 30.77^\circ \text{C}$	$\text{Pr}_{\text{air}}, \nu_{\text{air}}, \rho_{\text{air}}, k_{\text{air}}, \beta_{\text{air}} = f(T_{\text{avg}}, P_{\text{ambient}})$	$\text{Pr}_{\text{air}} = 0.71$ $\nu_{\text{air}} = 1.56 \times 10^{-5} \text{ m}^2/\text{s}$ $\rho_{\text{air}} = 1.188 \text{ kg/m}^3$ $k_{\text{air}} = 0.025 \text{ W/m-K}$ $\beta_{\text{air}} = 3.4 \times 10^{-3} \text{ 1/K}$
	By assuming a negligible convective resistance in tubing: $T_{\text{inner wall}} = (T_{r, \text{ test, out}} + T_{r, \text{ pre, in}}) / 2$	$T_{\text{inner wall}} = 30.83^\circ \text{C}$
	$Ra = \frac{g \beta_{\text{air}} (T_{\text{ins}} - T_{\text{ambient}}) D_{r, \text{ ins}}^3}{\nu_{\text{air}} \alpha_{\text{air}}}$	$Ra = 34546$
	$Nu = \frac{h_{\text{nat. conv.}} D_{\text{ins}}}{k_{\text{air}}} = \left(0.60 + \frac{0.387 Ra^{1/6}}{\left(1 + \left(\frac{0.559}{\text{Pr}_{\text{air}}} \right)^{9/16} \right)^{8/27}} \right)^2$	$Nu = 5.92$ $h_{\text{nat. conv.}} = 1.55 \text{ W/m}^2\text{-K}$
	(Churchill and Chu, 1975)	
	$R_{\text{nat. conv.}} = \frac{1}{h_{\text{nat. conv.}} \pi D_{\text{ins}} L_{r, \text{ test-to-post}}}$	$R_{\text{nat. conv.}} = 2.018 \text{ K/W}$
	$\dot{Q}_{\text{loss, test-to-post}} = \frac{(T_{\text{inner wall}} - T_{\text{ambient}})}{R_{\text{wall}} + R_{\text{ins}} + \left(\frac{R_{\text{nat. conv.}} R_{\text{radiation}}}{R_{\text{nat. conv.}} + R_{\text{radiation}}} \right)}$	$\dot{Q}_{\text{loss, test-to-post}} = 0.76 \text{ W}$
Heat Losses In Secondary Heat Exchanger (Shell-and-Tube)		
$D_{\text{sec, o}} = 25.4 \text{ mm}$ $D_{\text{sec, i}} = 22.9 \text{ mm}$ $D_{\text{sec, ins}} = 100 \text{ mm}$ $k_{\text{sec}} = 14.9 \text{ W/m-K}$	$R_{\text{wall}} = \frac{\ln \left(\frac{D_{\text{sec, o}}}{D_{\text{sec, i}}} \right)}{2\pi k_{\text{sec}} L_{\text{sec}}}$	$R_{\text{wall}} = 6.4 \times 10^{-3} \text{ K/W}$
$k_{\text{ins}} = 0.043 \text{ W/m-K}$ $L_{\text{sec}} = 173 \text{ mm}$ $\epsilon_{\text{ins}} = 0.85$	$R_{\text{ins}} = \frac{\ln \left(\frac{D_{\text{sec, ins}}}{D_{\text{sec, o}}} \right)}{2\pi k_{\text{ins}} L_{\text{sec}}}$	$R_{\text{ins}} = 29.32 \text{ K/W}$

Heat Transfer Calculations – 16 September 2010 – Run 55		
Inputs	Equations	Results
$\sigma = 5.67 \times 10^{-8} \text{ W m}^{-2} \text{ K}^{-4}$ $T_{\text{ambient}} = 24.72^\circ \text{ C}$ $P_{\text{ambient}} = 101 \text{ kPa}$ $g = 9.81 \text{ m/s}^2$ $T_{\text{w, sec, out}} = 18.57^\circ \text{ C}$ $T_{\text{w, sec, out}} = 7.25^\circ \text{ C}$	$R_{\text{radiation}} = \frac{1}{\varepsilon_{\text{ins}} \pi D_{\text{sec, ins}} L_{\text{sec}} \sigma (T_{\text{ins}}^2 + T_{\text{ambient}}^2) (T_{\text{ins}} + T_{\text{ambient}})}$	$R_{\text{radiation}} = 3.629 \text{ K/W}$ $T_{\text{ins}} = 23.76^\circ \text{ C}$
	$T_{\text{avg}} = (T_{\text{ins}} + T_{\text{ambient}}) / 2$	$T_{\text{avg}} = 24.24^\circ \text{ C}$
	$\text{Pr}_{\text{air}}, \nu_{\text{air}}, \rho_{\text{air}}, k_{\text{air}}, \beta_{\text{air}} = f(T_{\text{avg}}, P_{\text{ambient}})$	$\text{Pr}_{\text{air}} = 0.71$ $\nu_{\text{air}} = 1.56 \times 10^{-5} \text{ m}^2/\text{s}$ $\rho_{\text{air}} = 1.188 \text{ kg/m}^3$ $k_{\text{air}} = 0.026 \text{ W/m-K}$ $\beta_{\text{air}} = 3.4 \times 10^{-3} \text{ 1/K}$
	By assuming a negligible convective resistance in tubing: $T_{\text{inner wall}} = (T_{\text{r, test, out}} + T_{\text{r, pre, in}}) / 2$	$T_{\text{inner wall}} = 12.91^\circ \text{ C}$
	$Ra = \frac{g \beta_{\text{air}} (T_{\text{ins}} - T_{\text{ambient}}) D_{\text{sec, ins}}^3}{\nu_{\text{air}} \alpha_{\text{air}}}$	$Ra = 92451$
	$Nu = \frac{h_{\text{nat. conv.}} D_{\text{ins}}}{k_{\text{air}}} = \left(0.60 + \frac{0.387 Ra^{1/6}}{\left(1 + \left(\frac{0.559}{\text{Pr}_{\text{air}}} \right)^{9/16} \right)^{8/27}} \right)^2$ (Churchill and Chu, 1975)	$Nu = 7.617$ $h_{\text{nat. conv.}} = 1.998 \text{ W/m}^2\text{-K}$
	$R_{\text{nat. conv.}} = \frac{1}{h_{\text{nat. conv.}} \pi D_{\text{ins}} L_{\text{sec}}}$	$R_{\text{nat. conv.}} = 9.211 \text{ K/W}$
$\dot{Q}_{\text{loss, sec}} = \frac{(T_{\text{inner wall}} - T_{\text{ambient}})}{R_{\text{wall}} + R_{\text{ins}} + \left(\frac{R_{\text{nat. conv.}} R_{\text{radiation}}}{R_{\text{nat. conv.}} + R_{\text{radiation}}} \right)}$	$\dot{Q}_{\text{loss, sec}} = -0.37 \text{ W}$ (implies heat gain)	
Heat Losses In Primary Loop		
$D_{\text{tube, r, i}} = 10.2 \text{ mm}$ $D_{\text{tube, r, o}} = 12.7 \text{ mm}$ $D_{\text{r, ins}} = 76 \text{ mm}$	$R_{\text{wall}} = \frac{\ln \left(\frac{D_{\text{tube, r, o}}}{D_{\text{tube, r, i}}} \right)}{2\pi k_{\text{tube, r}} L_{\text{prim. equiv.}}}$	$R_{\text{wall}} = 3.452 \times 10^{-4} \text{ K/W}$

Heat Transfer Calculations – 16 September 2010 – Run 55

Inputs	Equations	Results
$k_{\text{tube, r}} = 15.3 \text{ W/m-K}$ $k_{\text{ins}} = 0.043 \text{ W/m-K}$ $L_{\text{prim. equiv.}} = 4.548 \text{ m}$ $\epsilon_{\text{ins}} = 0.85$ $\sigma = 5.67 \times 10^{-8} \text{ W m}^{-2} \text{K}^{-4}$ $T_{\text{ambient}} = 24.72^\circ \text{C}$ $P_{\text{ambient}} = 101 \text{ kPa}$ $g = 9.81 \text{ m/s}^2$ $T_{\text{w, test, in}} = 20.19^\circ \text{C}$ $T_{\text{w, test, out}} = 20.38^\circ \text{C}$	$R_{\text{ins}} = \frac{\ln\left(\frac{D_{\text{r, ins}}}{D_{\text{tube, r, o}}}\right)}{2\pi k_{\text{ins}} L_{\text{prim. equiv.}}}$	$R_{\text{ins}} = 1.456 \text{ K/W}$
	$R_{\text{radiation}} = \frac{1}{\epsilon_{\text{ins}} \pi D_{\text{sec, ins}} L_{\text{sec}} \sigma (T_{\text{ins}}^2 + T_{\text{ambient}}^2) (T_{\text{ins}} + T_{\text{ambient}})}$	$R_{\text{radiation}} = 0.1811 \text{ K/W}$ $T_{\text{ins}} = 24.43^\circ \text{C}$
	$T_{\text{avg}} = (T_{\text{ins}} + T_{\text{ambient}}) / 2$	$T_{\text{avg}} = 24.53^\circ \text{C}$
	$\text{Pr}_{\text{air}}, \nu_{\text{air}}, \rho_{\text{air}}, k_{\text{air}}, \beta_{\text{air}} = f(T_{\text{avg}}, P_{\text{ambient}})$	$\text{Pr}_{\text{air}} = 0.71$ $\nu_{\text{air}} = 1.56 \times 10^{-5} \text{ m}^2/\text{s}$ $\rho_{\text{air}} = 1.188 \text{ kg/m}^3$ $k_{\text{air}} = 0.026 \text{ W/m-K}$ $\beta_{\text{air}} = 3.4 \times 10^{-3} \text{ 1/K}$
	<p>By assuming a negligible convective resistance in tubing:</p> $T_{\text{inner wall}} = (T_{\text{w, test, out}} + T_{\text{w, test, in}}) / 2$	$T_{\text{inner wall}} = 20.29^\circ \text{C}$
	$Ra = \frac{g \beta_{\text{air}} (T_{\text{ins}} - T_{\text{ambient}}) D_{\text{r, ins}}^3}{\nu_{\text{air}} \alpha_{\text{air}}}$	$Ra = 15956$
	$Nu = \frac{h_{\text{nat. conv.}} D_{\text{ins}}}{k_{\text{air}}} = \left(0.60 + \frac{0.387 Ra^{1/6}}{\left(1 + \left(\frac{0.559}{\text{Pr}_{\text{air}}} \right)^{9/16} \right)^{8/27}} \right)^2$ <p>(Churchill and Chu, 1975)</p>	$Nu = 4.891$ $h_{\text{nat. conv.}} = 1.69 \text{ W/m}^2 \text{-K}$
	$R_{\text{nat. conv.}} = \frac{1}{h_{\text{nat. conv.}} \pi D_{\text{ins}} L_{\text{prim. equiv.}}}$	$R_{\text{nat. conv.}} = 0.5456 \text{ K/W}$
	$\dot{Q}_{\text{loss, prim}} = \frac{(T_{\text{inner wall}} - T_{\text{ambient}})}{R_{\text{wall}} + R_{\text{ins}} + \left(\frac{R_{\text{nat. conv.}} R_{\text{radiation}}}{R_{\text{nat. conv.}} + R_{\text{radiation}}} \right)}$	$\dot{Q}_{\text{loss, prim}} = -2.785 \text{ W}$
Water Heat Transfer Coefficient in Test Section Annulus		
$T_{\text{w, test, in}} = 20.19^\circ \text{C}$	$T_{\text{w, test, avg}} = (T_{\text{w, test, out}} + T_{\text{w, test, in}}) / 2$	$T_{\text{w, test, avg}} = 20.29^\circ \text{C}$

Heat Transfer Calculations – 16 September 2010 – Run 55

Inputs	Equations	Results
$T_{w, \text{test, out}} = 20.38^\circ\text{C}$ $P_w = 275.8 \text{ kPa}$ $D_{\text{annulus, i}} = 10.2 \text{ mm}$ $D_{\text{test, o}} = 6.35 \text{ mm}$ $\dot{V}_{w, \text{prim}} = 1.269 \times 10^{-4} \text{ (m}^3/\text{s)}$	$\text{Pr}_w, \nu_w, \rho_w, k_w = f(T_{w, \text{test, avg}}, P_w)$	$\text{Pr}_w = 6.945$ $\nu_w = 9.96 \times 10^{-7} \text{ m}^2/\text{s}$ $\rho_w = 998.2 \text{ kg/m}^3$ $k_w = 0.599 \text{ W/m-K}$
	$A_{\text{annulus}} = (\pi/4)(D_{\text{annulus, i}}^2 - D_{\text{test, o}}^2)$	$A_{\text{annulus}} = 5.02 \times 10^{-5} \text{ m}^2$
	$V_{\text{annulus}} = \frac{\dot{V}_{w, \text{prim}}}{A_{\text{annulus}}}$	$V_{\text{annulus}} = 2.537 \text{ m/s}$
	$D_{\text{hydraulic}} = D_{\text{annulus, i}} - D_{\text{test, o}}$	$D_{\text{hydraulic}} = 3.85 \text{ mm}$
	$\text{Re}_{\text{annulus}} = \frac{V_{\text{annulus}} D_{\text{hydraulic}}}{\nu_{w, \text{prim}}}$	$\text{Re}_{\text{annulus}} = 9801$
	$r^* = D_{\text{test, o}} / D_{\text{annulus, i}}$	$r^* = 0.6225$
	$Nu_{\text{turbulent}} = 0.25 \text{Re}_{\text{annulus}}^{0.78} \text{Pr}_w^{0.48} (r^*)^{0.14}$ (Garimella and Christensen, 1995)	$Nu_{\text{turbulent}} = 87.9$
	$h_{\text{annulus}} = \frac{Nu_{\text{turbulent}} k_w}{D_{\text{hydraulic}}}$	$h_{\text{annulus}} = 13677 \text{ W/m}^2\text{K}^1$
Heat Losses in Test Section		
$h_{\text{annulus}} = 13677 \text{ W/m}^2\text{K}^1$ $L_{\text{annulus}} = 152.4 \text{ mm}$ $D_{\text{annulus, i}} = 10.2 \text{ mm}$ $D_{\text{annulus, o}} = 12.7 \text{ mm}$ $D_{\text{test, ins}} = 100 \text{ mm}$ $k_{\text{annulus}} = 14.9 \text{ W/m-K}$ $k_{\text{ins}} = 0.043 \text{ W/m-K}$ $\epsilon_{\text{ins}} = 0.85$ $\sigma = 5.67 \times 10^{-8} \text{ W m}^{-2}\text{K}^{-4}$ $T_{\text{ambient}} = 24.72^\circ\text{C}$ $P_{\text{ambient}} = 101 \text{ kPa}$	$R_{\text{annulus, o}} = \frac{1}{h_{\text{annulus}} \pi D_{\text{annulus, i}} L_{\text{annulus}}}$	$R_{\text{annulus, o}} = 1.5 \times 10^{-2} \text{ K/W}$
	$R_{\text{wall}} = \frac{\ln\left(\frac{D_{\text{annulus, o}}}{D_{\text{annulus, i}}}\right)}{2\pi k_{\text{annulus}} L_{\text{annulus}}}$	$R_{\text{wall}} = 1.54 \times 10^{-2} \text{ K/W}$
	$R_{\text{ins}} = \frac{\ln\left(\frac{D_{\text{test, ins}}}{D_{\text{annulus, o}}}\right)}{2\pi k_{\text{ins}} L_{\text{annulus}}}$	$R_{\text{ins}} = 50.12 \text{ K/W}$
	$R_{\text{radiation}} = \frac{1}{\epsilon_{\text{ins}} \pi D_{\text{test, ins}} L_{\text{annulus}} \sigma (T_{\text{ins}}^2 + T_{\text{ambient}}^2) (T_{\text{ins}} + T_{\text{ambient}})}$	$R_{\text{radiation}} = 4.105 \text{ K/W}$ $T_{\text{ins}} = 24.45^\circ\text{C}$
	$T_{\text{avg}} = (T_{\text{ins}} + T_{\text{ambient}}) / 2$	$T_{\text{avg}} = 24.59^\circ\text{C}$

Heat Transfer Calculations – 16 September 2010 – Run 55		
Inputs	Equations	Results
$g = 9.81 \text{ m/s}^2$ $T_{w, \text{ test, in}} = 20.19^\circ \text{C}$ $T_{w, \text{ test, out}} = 20.38^\circ \text{C}$	$\text{Pr}_{\text{air}}, \nu_{\text{air}}, \rho_{\text{air}}, k_{\text{air}}, \beta_{\text{air}} = f(T_{\text{avg}}, P_{\text{ambient}})$	$\text{Pr}_{\text{air}} = 0.71$ $\nu_{\text{air}} = 1.56 \times 10^{-5} \text{ m}^2/\text{s}$ $\rho_{\text{air}} = 1.188 \text{ kg/m}^3$ $k_{\text{air}} = 0.026 \text{ W/m-K}$ $\beta_{\text{air}} = 3.4 \times 10^{-3} \text{ 1/K}$
	$T_{w, \text{ test, avg}} = (T_{w, \text{ test, out}} + T_{w, \text{ test, in}}) / 2$	$T_{w, \text{ test, avg}} = 20.29^\circ \text{C}$
	$Ra = \frac{g \beta_{\text{air}} (T_{\text{ins}} - T_{\text{ambient}}) D_{r, \text{ ins}}^3}{\nu_{\text{air}} \alpha_{\text{air}}}$	$Ra = 25586$
	$Nu = \frac{h_{\text{nat. conv.}} D_{\text{ins}}}{k_{\text{air}}} = \left(0.60 + \frac{0.387 Ra^{1/6}}{\left(1 + \left(\frac{0.559}{\text{Pr}_{\text{air}}} \right)^{9/16} \right)^{8/27}} \right)^2$	$Nu = 5.492$ $h_{\text{nat. conv.}} = 1.44 \text{ W/m}^2\text{-K}$
	(Churchill and Chu, 1975)	
	$R_{\text{nat. conv.}} = \frac{1}{h_{\text{nat. conv.}} \pi D_{\text{test, ins}} L_{\text{annulus}}}$	$R_{\text{nat. conv.}} = 14.51 \text{ K/W}$
	$\dot{Q}_{\text{loss, test}} = \frac{(T_{\text{inner wall}} - T_{\text{ambient}})}{R_{\text{annulus, o}} + R_{\text{wall}} + R_{\text{ins}} + \left(\frac{R_{\text{nat. conv.}} R_{\text{radiation}}}{R_{\text{nat. conv.}} + R_{\text{radiation}}} \right)}$	$\dot{Q}_{\text{loss, test}} = -0.08 \text{ W}$ (implies heat gain)
Average Test Section Quality		
$P_w = 275.8 \text{ kPa}$	$i_{w, \text{ pre, in}} = f(T_{w, \text{ pre, in}}, P_w)$	$i_{w, \text{ pre, in}} = 39.03 \text{ kJ/kg}$
$T_{w, \text{ pre, in}} = 9.23^\circ \text{C}$	$i_{w, \text{ pre, out}} = f(T_{w, \text{ pre, out}}, P_w)$	$i_{w, \text{ pre, out}} = 194.6 \text{ kJ/kg}$
$T_{w, \text{ pre, out}} = 46.42^\circ \text{C}$	$\rho_{w, \text{ pre, in}} = f(T_{w, \text{ pre, in}}, P_w)$	$\rho_{w, \text{ pre, in}} = 999.4 \text{ kg/m}^3$
$\dot{V}_{w, \text{ pre}} = 3.2 \times 10^{-6} \text{ m}^3/\text{s}$	$\dot{m}_{w, \text{ pre}} = \rho_{w, \text{ pre, in}} \dot{V}_{w, \text{ pre}}$	$\dot{m}_{w, \text{ pre}} = 3.16 \times 10^{-3} \text{ kg/s}$
$\dot{Q}_{\text{loss, pre}} = 0.353 \text{ W}$	$\dot{Q}_{\text{pre}} = \dot{m}_{w, \text{ pre}} (i_{w, \text{ pre, out}} - i_{w, \text{ pre, in}}) + \dot{Q}_{\text{loss, pre}}$	$\dot{Q}_{\text{pre}} = 0.492 \text{ kW}$
$T_{r, \text{ pre, in}} = 98.93^\circ \text{C}$	$T_{r, \text{ pre, in, sat}} = f(P_{r, \text{ pre, in}}, x = 1)$	$T_{r, \text{ pre, in, sat}} = 31.55^\circ \text{C}$
$P_{r, \text{ pre, in}} = 1475 \text{ kPa}$	$\Delta T_{\text{sup, pre}} = T_{r, \text{ pre, in}} - T_{r, \text{ pre, in, sat}}$	$\Delta T_{\text{sup, pre}} = 67.38 \text{ K}$
$\dot{m}_r = 5.881 \times 10^{-3} \text{ kg/s}$	$i_{r, \text{ pre, in}} = f(T_{r, \text{ pre, in}}, P_{r, \text{ pre, in}})$	$i_{r, \text{ pre, in}} = 453.6 \text{ kJ/kg}$

Heat Transfer Calculations – 16 September 2010 – Run 55

Inputs	Equations	Results
$\dot{Q}_{\text{loss, pre-to-test}} = 1.005 \text{ W}$ $P_{r, \text{test, in}} = 1471 \text{ kPa}$	$i_{r, \text{pre, out}} = \left(i_{r, \text{pre, in}} - \frac{\dot{Q}_{\text{pre}}}{\dot{m}_r} \right)$	$i_{r, \text{pre, out}} = 370 \text{ kJ/kg}$
$T_{w, \text{post, in}} = 5.6^\circ \text{C}$ $T_{w, \text{post, out}} = 14.5^\circ \text{C}$	$i_{r, \text{test, in}} = \left(i_{r, \text{pre, out}} - \frac{\dot{Q}_{\text{loss, pre-to-test}}}{\dot{m}_r} \right)$	$i_{r, \text{test, in}} = 369.8 \text{ kJ/kg}$
$\dot{V}_{w, \text{post}} = 1.8 \times 10^{-5} \text{ m}^3/\text{s}$	$x_{r, \text{test, in}} = f(i_{r, \text{test, in}}, P_{r, \text{test, in}})$	$x_{r, \text{test, in}} = 0.9456$
$\dot{Q}_{\text{loss, post}} = -0.754 \text{ W}$ $T_{r, \text{post, out}} = 20.75^\circ \text{C}$	$i_{w, \text{post, in}} = f(T_{w, \text{post, in}}, P_w)$	$i_{w, \text{post, in}} = 23.83 \text{ kJ/kg}$
$P_{r, \text{post, out}} = 1449 \text{ kPa}$	$i_{w, \text{post, out}} = f(T_{w, \text{post, out}}, P_w)$	$i_{w, \text{post, out}} = 61.13 \text{ kJ/kg}$
$\dot{Q}_{\text{loss, test-to-post}} = 0.765 \text{ W}$ $P_{r, \text{test, out}} = 1449 \text{ kPa}$	$\rho_{w, \text{post, in}} = f(T_{w, \text{post, in}}, P_w)$	$\rho_{w, \text{post, in}} = 1000 \text{ kg/m}^3$
$T_{r, \text{pre, in, sat}} = 31.55^\circ \text{C}$	$\dot{m}_{w, \text{post}} = \rho_{w, \text{post, in}} \dot{V}_{w, \text{post}}$	$\dot{m}_{w, \text{post}} = 0.0183 \text{ kg/s}$
$T_{r, \text{post, out, sat}} = 30.45^\circ \text{C}$	$\dot{Q}_{\text{post}} = \dot{m}_{w, \text{post}} (i_{w, \text{post, out}} - i_{w, \text{post, in}}) + \dot{Q}_{\text{loss, post}}$	$\dot{Q}_{\text{post}} = 0.683 \text{ kW}$
	$T_{r, \text{post, out, sat}} = f(P_{r, \text{post, out}}, x = 0)$	$T_{r, \text{post, out, sat}} = 30.45^\circ \text{C}$
	$\Delta T_{\text{sub, post}} = T_{r, \text{post, out}} - T_{r, \text{post, out, sat}}$	$\Delta T_{\text{sub, post}} = 9.71^\circ \text{C}$
	$i_{r, \text{post, out}} = f(T_{r, \text{post, out}}, P_{r, \text{post, out}})$	$i_{r, \text{post, out}} = 228.3 \text{ kJ/kg}$
	$i_{r, \text{post, in}} = \left(i_{r, \text{post, out}} + \frac{\dot{Q}_{\text{post}}}{\dot{m}_r} \right)$	$i_{r, \text{post, in}} = 344.4 \text{ kJ/kg}$
	$i_{r, \text{test, out}} = \left(i_{r, \text{post, in}} + \frac{\dot{Q}_{\text{loss, test-to-post}}}{\dot{m}_r} \right)$	$i_{r, \text{test, out}} = 344.5 \text{ kJ/kg}$
	$x_{r, \text{test, out}} = f(P_{r, \text{test, out}}, i_{r, \text{test, out}})$	$x_{r, \text{test, out}} = 0.7588$
	$x_{\text{test, avg}} = (x_{\text{test, in}} + x_{\text{test, out}}) / 2$	$x_{\text{test, avg}} = 0.8522$
Refrigerant Heat Transfer Coefficient		
$T_{w, \text{sec, out}} = 18.57^\circ \text{C}$	$i_{w, \text{sec, o}} = f(T_{w, \text{sec, out}}, P_w)$	$i_{w, \text{sec, o}} = 78.2 \times 10^3 \text{ J/kg}$
$T_{w, \text{sec, in}} = 7.25^\circ \text{C}$	$i_{w, \text{sec, i}} = f(T_{w, \text{sec, in}}, P_w)$	$i_{w, \text{sec, i}} = 30.7 \times 10^3 \text{ J/kg}$
$P_w = 275.8 \text{ kPa}$	$\dot{Q}_{\text{sec}} = \dot{m}_{w, \text{sec}} (i_{w, \text{sec, o}} - i_{w, \text{sec, i}})$	$\dot{Q}_{\text{sec}} = 185.8 \text{ W}$
$\dot{m}_{w, \text{sec}} = 3.92 \times 10^{-3} \text{ kg/s}$	$\dot{Q}_{\text{loss, ambient}} = \dot{Q}_{\text{loss, test}} + \dot{Q}_{\text{loss, prim}} + \dot{Q}_{\text{loss, sec}}$	$\dot{Q}_{\text{loss, ambient}} = -3.24 \text{ W}$
$\dot{Q}_{\text{loss, test}} = -0.08 \text{ W}$	$\dot{Q}_{\text{pump}} = 9.0397 \dot{V}_{w, \text{prim, gpm}}^2 + 0.1304 \dot{V}_{w, \text{prim, gpm}}^3 + 0.4034 \dot{V}_{w, \text{prim, gpm}}^3$	$\dot{Q}_{\text{pump}} = 22 \text{ W}$

Heat Transfer Calculations – 16 September 2010 – Run 55

Inputs	Equations	Results
$\dot{Q}_{\text{loss, prim}} = -2.79 \text{ W}$	$\dot{Q}_{\text{test}} = \dot{Q}_{\text{sec}} + \dot{Q}_{\text{loss, ambient}} - \dot{Q}_{\text{pump}}$	$\dot{Q}_{\text{test}} = 160.5 \text{ W}$
$\dot{Q}_{\text{loss, sec}} = -0.37 \text{ W}$	$T_{r, \text{test, in, sat}} = f(P_{r, \text{test, in}}, i_{r, \text{test, in}})$	$T_{r, \text{test, in, sat}} = 31.55^\circ\text{C}$
$\dot{V}_{w, \text{prim, gpm}} = 2.012 \text{ gpm}$	$\text{Error}_{r, \text{test, in}} = T_{r, \text{test, in}} - T_{r, \text{test, in, sat}}$	$\text{Error}_{r, \text{test, in}} = 0.06^\circ\text{C}$
$i_{r, \text{test, in}} = 369.8 \text{ kJ/kg}$	$T_{r, \text{test, out, sat}} = f(P_{r, \text{test, out}}, i_{r, \text{test, out}})$	$T_{r, \text{test, out, sat}} = 30.85^\circ\text{C}$
$P_{r, \text{test, in}} = 1471 \text{ kPa}$	$\text{Error}_{r, \text{test, out}} = T_{r, \text{test, out}} - T_{r, \text{test, out, sat}}$	$\text{Error}_{r, \text{test, out}} = 0.04^\circ\text{C}$
$i_{r, \text{test, out}} = 344.5 \text{ kJ/kg}$	$\text{LMTD} = \frac{(T_{r, \text{test, in}} - T_{w, \text{test, out}}) - (T_{r, \text{test, out}} - T_{w, \text{test, in}})}{\ln \left[\frac{(T_{r, \text{test, in}} - T_{w, \text{test, out}})}{(T_{r, \text{test, out}} - T_{w, \text{test, in}})} \right]}$	$\text{LMTD} = 10.87^\circ\text{C}$
$P_{r, \text{test, out}} = 1449 \text{ kPa}$	$UA = \dot{Q}_{\text{test}} / (\text{LMTD})$	$UA = 14.77 \text{ W/K}$
$T_{r, \text{test, in}} = 31.5^\circ\text{C}$	$R_{\text{wall}} = \frac{\ln \left(\frac{D_{\text{test, o}}}{D_{\text{test, i}}} \right)}{2\pi k_{\text{test}} (L_{\text{annulus}} + 2 \cdot (L_{\text{reducer}} + L_{\text{tee}}))}$	$R_{\text{wall}} = 1.31 \times 10^{-3} \text{ K/W}$
$T_{r, \text{test, out}} = 30.8^\circ\text{C}$	$R_{\text{annulus, i}} = \frac{1}{h_{\text{annulus}} \pi D_{\text{test, o}} L_{\text{annulus}}}$	$R_{\text{annulus, i}} = 2.4 \times 10^{-2} \text{ K/W}$
$k_{\text{test}} = 398.3 \text{ W/m-K}$	$T_{w, \text{test, avg}} = (T_{w, \text{test, out}} + T_{w, \text{test, in}}) / 2$	$T_{w, \text{test, avg}} = 20.29^\circ\text{C}$
$T_{w, \text{test, in}} = 20.19^\circ\text{C}$	$\text{Pr}_w, \nu_w, \rho_w, k_w = f(T_{w, \text{test, avg}}, P_w)$	$\text{Pr}_w = 6.945$ $\nu_w = 9.96 \times 10^{-7} \text{ m}^2/\text{s}$ $\rho_w = 998.2 \text{ kg/m}^3$ $k_w = 0.599 \text{ W/m-K}$
$T_{w, \text{test, out}} = 20.38^\circ\text{C}$	$\frac{Ra}{L^3} = \frac{g \beta_w (T_{\text{wall, o}} - T_{w, \text{test, avg}})}{\nu_w \alpha_w}$	$\frac{Ra}{L^3} = 5.5 \times 10^{10} \text{ m}^{-3}$
$h_{\text{annulus}} = 13677 \text{ W/m}^2\text{K}^1$	$Ra_{\text{reducer}}^* = \frac{[\ln(D_{\text{reducer}}/D_{\text{test, o}})]^4}{(D_{\text{test, o}}^{-3/5} + D_{\text{reducer}}^{-3/5})^5} \left(\frac{Ra}{L^3} \right)$ (Incorpera and DeWitt, 1996)	$Ra_{\text{reducer}}^* = 14.96$
$D_{\text{test, i}} = 3.048 \text{ mm}$	$Ra_{\text{tee}}^* = \frac{[\ln(D_{\text{tee}}/D_{\text{test, o}})]^4}{(D_{\text{test, o}}^{-3/5} + D_{\text{tee}}^{-3/5})^5} \left(\frac{Ra}{L^3} \right)$ (Incorpera and DeWitt, 1996)	$Ra_{\text{tee}}^* = 52.04$
$D_{\text{test, o}} = 6.35 \text{ mm}$	for: $100 \leq Ra_{\text{reducer}}^* \leq 10^7$ $k_{\text{effective, reducer}} = (k_w) \cdot 0.386 \left(\frac{\text{Pr}_w}{0.861 + \text{Pr}_w} \right)^{1/4} (Ra_{\text{reducer}}^*)^{1/4}$ (Irvine and Hartnett, 1975)	
$L_{\text{annulus}} = 152.4 \text{ mm}$		
$L_{\text{reducer}} = 22.86 \text{ mm}$		
$L_{\text{tee}} = 13.21 \text{ mm}$		
$D_{\text{reducer}} = 9.25 \text{ mm}$		
$D_{\text{tee}} = 10.41 \text{ mm}$		
$x_{\text{test, avg}} = 0.8522$		

Heat Transfer Calculations – 16 September 2010 – Run 55

Inputs	Equations	Results
	for: $Ra_{reducer}^* \leq 100$ $k_{effective, reducer} = k_w$ (Irvine and Hartnett, 1975)	$k_{effective, reducer} =$ 0.599 W/m-K
	for: $100 \leq Ra_{tee}^* \leq 10^7$ $k_{effective, tee} = (k_w) \cdot 0.386 \left(\frac{Pr_w}{0.861 + Pr_w} \right)^{1/4} (Ra_{tee}^*)^{1/4}$ for: $Ra_{tee}^* \leq 100$ $k_{effective, reducer} = k_w$ (Irvine and Hartnett, 1975)	$k_{effective, tee} =$ 0.599 W/m-K
	$R_{reducer} = \frac{\ln \left(\frac{D_{reducer}}{D_{test, o}} \right)}{2\pi k_{effective, reducer} L_{reducer}}$	$R_{reducer} = 4.37 \text{ K/W}$
	$R_{tee} = \frac{\ln \left(\frac{D_{tee}}{D_{test, o}} \right)}{2\pi k_{effective, tee} L_{tee}}$	$R_{tee} = 9.94 \text{ K/W}$
	$R_{conv, equiv.}^{-1} = R_{annulus, i}^{-1} + 2(R_{tee}^{-1} + R_{reducer}^{-1})$	$R_{conv, equiv.} = 0.024 \text{ K/W}$
	$h_r = \left[(UA)^{-1} - R_{wall} - R_{conv, equiv.} \right]^{-1} \cdot \left[\pi D_{test, i} (L_{annulus} + 2(L_{reducer} + L_{tee})) \right]^{-1}$	$h_r = 10884 \text{ W/m}^2\text{-K}$
	$R_r = \frac{1}{h_r \pi D_{test, i} (L_{annulus} + 2(L_{reducer} + L_{tee}))}$	$R_r = 0.0427 \text{ K/W}$
	$R_{ratio} = \frac{R_r}{R_{wall} + R_{conv, equiv.}}$	$R_{ratio} = 1.711$
	$\dot{Q}_{test} = \frac{((T_{r, test, in, sat} - T_{r, test, out, sat})/2 - T_{wall, o})}{R_r + R_{wall}}$	$T_{wall, o} = 24.09^\circ\text{C}$
	$\dot{Q}_{reducer} = 2 \cdot \frac{(T_{wall, o} - T_{w, test, avg})}{R_{reducer}}$	$\dot{Q}_{reducer} = 1.739 \text{ W}$
	$\dot{Q}_{tee} = 2 \cdot \frac{(T_{wall, o} - T_{w, test, avg})}{R_{tee}}$	$\dot{Q}_{tee} = 0.765 \text{ W}$
	$\dot{Q}_{annulus} = \frac{(T_{wall, o} - T_{w, test, avg})}{R_{annulus, i}}$	$\dot{Q}_{annulus} = 158.1 \text{ W}$
	$P_{r, test, avg} = (P_{r, test, in} + P_{r, test, out})/2$	$P_{r, test, avg} = 1460 \text{ kPa}$

Heat Transfer Calculations – 16 September 2010 – Run 55

Inputs	Equations	Results
	$i_{r, fg} = f(P_{r, test, avg}, x_{r, test, avg})$	$i_{r, fg} = 132.86 \text{ kJ/kg}$
	$\Delta x = \frac{\dot{Q}_{test}}{\dot{m}_r i_{r, fg}}$	$\Delta x = 0.2054$

Pressure Drop Calculations – 16 September 2010 – Run 55		
Inputs	Equations	Results
$D_{tee} = 6.35$ mm $D_{contraction} = 4.57$ mm	$A_{ratio, 1} = \frac{A_{contraction}}{A_{tee}} = \left(\frac{D_{contraction}}{D_{tee}} \right)^2$	$A_{ratio, 1} = 0.6834$
$D_{test, i} = 3.048$ mm $\dot{m}_r = 5.881 \times 10^{-3}$ kg/s	$A_{ratio, 2} = \frac{A_{test}}{A_{contraction}} = \left(\frac{D_{test}}{D_{contraction}} \right)^2$	$A_{ratio, 2} = 0.444$
$x_{r, test, in} = 0.9456$	$G = \frac{\dot{m}_r}{A_{test}} = \frac{\dot{m}_r}{0.25 \cdot \pi \cdot D_{test, i}^2}$	$G = 806$ kg/m ² - s
$P_{r, test, in} = 1471$ kPa $x_{r, test, out} = 0.7588$	$G_{contraction} = G \cdot A_{ratio, 2}$	$G_{contraction} = 354$ kg/m ² - s
$P_{r, test, out} = 1449$ kPa $B = 0.25$	$G_{tee} = G \cdot A_{ratio, 1} \cdot A_{ratio, 2}$	$G_{tee} = 156$ kg/m ² - s
$\Delta P_{measured} = 15.658$ kPa $L_{test} = 0.4572$ m	$C_{C, 1} = \frac{1}{0.639 [1 - (A_{ratio, 1})]^{1/2} + 1}$ (Chisholm, 1983)	$C_{C, 1} = 0.6774$
	$C_{C, 2} = \frac{1}{0.639 [1 - (A_{ratio, 2})]^{1/2} + 1}$ (Chisholm, 1983)	$C_{C, 2} = 0.6928$
	$(\rho_1, \mu_1)_{in} = f(x_{r, test, in}, P_{r, test, in})$	$\rho_{1, in} = 1014$ kg/m ³ $\mu_{1, in} = 1.2 \times 10^{-4}$ kg/m-s
	$(\rho_v, \mu_v)_{in} = f(x_{r, test, in}, P_{r, test, in})$	$\rho_{v, in} = 79.07$ kg/m ³ $\mu_{v, in} = 1.5 \times 10^{-5}$ kg/m-s
	$(\rho_1, \mu_1)_{out} = f(x_{r, test, out}, P_{r, test, out})$	$\rho_{1, out} = 1017$ kg/m ³ $\mu_{1, out} = 1.2 \times 10^{-4}$ kg/m-s
	$(\rho_v, \mu_v)_{out} = f(x_{r, test, out}, P_{r, test, out})$	$\rho_{v, out} = 77.7$ kg/m ³ $\mu_{v, out} = 1.5 \times 10^{-5}$ kg/m-s
	$\psi_H = 1 + \left(\frac{\rho_{1, in}}{\rho_{v, in}} - 1 \right) x_{r, test, in}$ (Hewitt, 1994)	$\psi_H = 12.2$

Pressure Drop Calculations – 16 September 2010 – Run 55

Inputs	Equations	Results
	$\Delta P_{\text{contraction}, 1} = \frac{G_{\text{contraction}}^2}{2\rho_{1, \text{in}}} \left(1 - A_{\text{ratio}, 1}^2 + \left(\frac{1}{C_{C, 1}} - 1 \right)^2 \right) \psi_H$ <p>(Hewitt, 1994)</p>	$\Delta P_{\text{contraction}, 1} = 0.715 \text{ kPa}$
	$\Delta P_{\text{contraction}, 2} = \frac{G^2}{2\rho_{1, \text{in}}} \left(1 - A_{\text{ratio}, 2}^2 + \left(\frac{1}{C_{C, 2}} - 1 \right)^2 \right) \psi_H$ <p>(Hewitt, 1994)</p>	$\Delta P_{\text{contraction}, 2} = 4.02 \text{ kPa}$
	$\Delta P_{\text{contraction}} = \Delta P_{\text{contraction}, 1} + \Delta P_{\text{contraction}, 2}$	$\Delta P_{\text{contraction}} = 4.73 \text{ kPa}$ (30% of $\Delta P_{\text{measured}}$)
	$\psi_S = 1 + \left(\frac{\rho_{1, \text{out}}}{\rho_{v, \text{out}}} - 1 \right) \left[Bx_{r, \text{test}, \text{out}} (1 - x_{r, \text{test}, \text{out}}) + x_{r, \text{test}, \text{out}}^2 \right]$ <p>(Chisholm, 1983)</p>	$\psi_S = 8.51$
	$\Delta P_{\text{expansion}, 2} = \frac{G^2 A_{\text{ratio}, 2} (1 - A_{\text{ratio}, 2}) \psi_S}{\rho_{1, \text{out}}}$ <p>(Hewitt, 1994)</p>	$\Delta P_{\text{expansion}, 2} = 1.34 \text{ kPa}$
	$\Delta P_{\text{expansion}, 1} = \frac{G_{\text{contraction}}^2 A_{\text{ratio}, 1} (1 - A_{\text{ratio}, 1}) \psi_S}{\rho_{1, \text{out}}}$ <p>(Hewitt, 1994)</p>	$\Delta P_{\text{expansion}, 1} = 0.268 \text{ kPa}$
	$\Delta P_{\text{expansion}} = \Delta P_{\text{expansion}, 1} + \Delta P_{\text{expansion}, 2}$	$\Delta P_{\text{expansion}} = 1.61 \text{ kPa}$ (10% of $\Delta P_{\text{measured}}$)
	$\alpha_{r, \text{test}, \text{in}} = \left[1 + \left(\frac{1 - x_{r, \text{test}, \text{in}}}{x_{r, \text{test}, \text{in}}} \right)^{0.74} \left(\frac{\rho_{v, \text{in}}}{\rho_{1, \text{in}}} \right)^{0.65} \left(\frac{\mu_{1, \text{in}}}{\mu_{v, \text{in}}} \right)^{0.13} \right]^{-1}$ <p>(Baroczy, 1965)</p>	$\alpha_{r, \text{test}, \text{in}} = 0.9708$
	$\alpha_{r, \text{test}, \text{out}} = \left[1 + \left(\frac{1 - x_{r, \text{test}, \text{out}}}{x_{r, \text{test}, \text{out}}} \right)^{0.74} \left(\frac{\rho_{v, \text{out}}}{\rho_{1, \text{out}}} \right)^{0.65} \left(\frac{\mu_{1, \text{out}}}{\mu_{v, \text{out}}} \right)^{0.13} \right]^{-1}$ <p>(Baroczy, 1965)</p>	$\alpha_{r, \text{test}, \text{out}} = 0.9377$

Pressure Drop Calculations – 16 September 2010 – Run 55

Inputs	Equations	Results
	$ \Delta P_{\text{deceleration}} = \left G^2 \left[\frac{x^2}{\rho_{v, \text{out}} \alpha} + \frac{(1-x)^2}{\rho_{l, \text{out}} (1-\alpha)} \right]_{\substack{\alpha=\alpha_{r, \text{test, out}} \\ x=x_{r, \text{test, out}}}} - G^2 \left[\frac{x^2}{\rho_{v, \text{in}} \alpha} + \frac{(1-x)^2}{\rho_{l, \text{in}} (1-\alpha)} \right]_{\substack{\alpha=\alpha_{r, \text{test, in}} \\ x=x_{r, \text{test, in}}}} \right $ <p>(Carey, 1992)</p>	$ \Delta P_{\text{deceleration}} = 1.92 \text{ kPa}$ <p>(12% of $\Delta P_{\text{measured}}$)</p>
	$\Delta P_{\text{measured}} = \Delta P_f - \Delta P_{\text{deceleration}} + \Delta P_{\text{contraction}} - \Delta P_{\text{expansion}}$	$\Delta P_f = 14.46 \text{ kPa}$ <p>(92% of $\Delta P_{\text{measured}}$)</p>
	$\nabla P_f = \frac{\Delta P_f}{L_{\text{test}}}$	$\nabla P_f = 31.62 \text{ kPa/m}$

Appendix B.2 – Sample Test Calculation for $D = 1.55$ (mm)

Primary Loop	
$T_{w, \text{test, in}}$ ($^{\circ}\text{C}$)	32.4
$T_{w, \text{test, out}}$ ($^{\circ}\text{C}$)	32.8
$\dot{V}_{w, \text{prim}}$ (m^3/s)	3.68×10^{-5}
Pre-Heater	
$\dot{Q}_{\text{pre-heat}}$ (W)	147.4
Post-Heater	
$\dot{Q}_{\text{post-heat}}$ (W)	73.7

Refrigerant Loop	
$P_{r, \text{pre-heat, in}}$ (kPa)	1810
$P_{r, \text{test, in}}$ (kPa)	1810
$P_{r, \text{test, out}}$ (kPa)	1780
$P_{r, \text{post-heat, out}}$ (kPa)	1778
$\Delta P_{r, \text{test}}$ (kPa)	29.50
$T_{r, \text{pre-heat, in}}$ ($^{\circ}\text{C}$)	23.8
$T_{r, \text{pre-heat, in, sat}}$ ($^{\circ}\text{C}$)	39.9
$\Delta T_{\text{sub pre}}$ ($^{\circ}\text{C}$)	16.1
$T_{r, \text{test, in}}$ ($^{\circ}\text{C}$)	39.6
$T_{r, \text{test, in, sat}}$ ($^{\circ}\text{C}$)	39.85
$Error_{r, \text{test, in}}$ ($^{\circ}\text{C}$)	0.25
$T_{r, \text{test, out}}$ ($^{\circ}\text{C}$)	39.5
$T_{r, \text{test, out, sat}}$ ($^{\circ}\text{C}$)	39.84
$Error_{r, \text{test, out}}$ ($^{\circ}\text{C}$)	0.34
$T_{r, \text{post-heat, out}}$ ($^{\circ}\text{C}$)	51.0
$T_{r, \text{post-heat, out, sat}}$ ($^{\circ}\text{C}$)	39.84
$\Delta T_{\text{sub, post}}$ ($^{\circ}\text{C}$)	11.16
\dot{m}_r (kg/s)	1.125×10^{-3}

Data Point	
p_r	0.4855
P_{critical} (kPa)	3729
G ($\text{kg}/\text{m}^2\text{-s}$)	597
$x_{r, \text{test, avg}}$	0.7323
Date of Experiment	14 June 2011
Run of Experiment	120
Assumed Variables	
P_w (kPa)	275.8
P_{ambient} (kPa)	101.0
ϵ_{ins}	0.85

Heat Transfer Calculations – 14 June 2011 – Run 120		
Inputs	Equations	Results
Heat Losses in Pre-Heater		
$D_{\text{pre-heat, o}} = 15.24 \text{ mm}$ $D_{\text{pre-heat, i}} = 10.16 \text{ mm}$ $D_{\text{pre-heat, ins}} = 25.4 \text{ mm}$ $k_{\text{pre-heater assembly}} = 15.3 \text{ W/m-K}$ $k_{\text{ins}} = 0.043 \text{ W/m-K}$ $L_{\text{heater, equiv.}} = 95 \text{ mm}$ $\epsilon_{\text{ins}} = 0.85$ $\sigma = 5.67 \times 10^{-8} \text{ W m}^{-2} \text{K}^{-4}$ $T_{\text{ambient}} = 23^\circ \text{C}$ $P_{\text{ambient}} = 101 \text{ kPa}$ $g = 9.81 \text{ m/s}^2$ $T_{\text{r, pre-heat, in}} = 23.8^\circ \text{C}$ $T_{\text{r, test, in}} = 39.8^\circ \text{C}$	$R_{\text{wall}} = \frac{\ln\left(\frac{D_{\text{pre-heat, o}}}{D_{\text{pre-heat, i}}}\right)}{2\pi k_{\text{pre-heater assembly}} L_{\text{heater, equiv.}}}$	$R_{\text{wall}} = 4.4 \times 10^{-2} \text{ K/W}$
	$R_{\text{ins}} = \frac{\ln\left(\frac{D_{\text{pre-heat, ins}}}{D_{\text{pre-heat, o}}}\right)}{2\pi k_{\text{ins}} L_{\text{heater, equiv.}}}$	$R_{\text{ins}} = 7.764 \text{ K/W}$
	$R_{\text{radiation}} = \frac{1}{\epsilon_{\text{ins}} \pi D_{\text{pre-heat, ins}} L_{\text{heater, equiv.}} \sigma (T_{\text{ins}}^2 + T_{\text{ambient}}^2) (T_{\text{ins}} + T_{\text{ambient}})}$	$R_{\text{radiation}} = 25.86 \text{ K/W}$ $T_{\text{ins}} = 23.78^\circ \text{C}$
	$T_{\text{avg}} = (T_{\text{ins}} + T_{\text{ambient}}) / 2$	$T_{\text{avg}} = 24.85^\circ \text{C}$
	$\text{Pr}_{\text{air}}, \nu_{\text{air}}, \rho_{\text{air}}, k_{\text{air}}, \beta_{\text{air}} = f(T_{\text{avg}}, P_{\text{ambient}})$	$\text{Pr}_{\text{air}} = 0.71$ $\nu_{\text{air}} = 1.54 \times 10^{-5} \text{ m}^2/\text{s}$ $\rho_{\text{air}} = 1.188 \text{ kg/m}^3$ $k_{\text{air}} = 0.026 \text{ W/m-K}$ $\beta_{\text{air}} = 3.4 \times 10^{-3} \text{ 1/K}$
	<p>By assuming a negligible convective resistance in cooling lines:</p> $T_{\text{inner wall}} = (T_{\text{r, pre-heat, in}} + T_{\text{r, test, in}}) / 2$	$T_{\text{inner wall}} = 31.79^\circ \text{C}$
	$Ra = \frac{g \beta_{\text{air}} (T_{\text{ins}} - T_{\text{ambient}}) D_{\text{pre-heat, ins}}^3}{\nu_{\text{air}} \alpha_{\text{air}}}$	$Ra = 5982$
	$Nu = \frac{h_{\text{nat. conv.}} D_{\text{ins}}}{k_{\text{air}}} = \left[0.60 + \frac{0.387 Ra^{1/6}}{\left(1 + \left(\frac{0.559}{\text{Pr}_{\text{air}}} \right)^{9/16} \right)^{8/27}} \right]^2$ <p>(Churchill and Chu, 1975)</p>	$Nu = 3.875$ $h_{\text{nat. conv.}} = 3.98 \text{ W/m}^2\text{-K}$

Heat Transfer Calculations – 14 June 2011 – Run 120		
Inputs	Equations	Results
	$R_{\text{nat. conv.}} = \frac{1}{h_{\text{nat. conv.}} \pi D_{\text{pre-heat, ins}} L_{\text{heater, equiv.}}}$	$R_{\text{nat. conv.}} = 33.13 \text{ K/W}$
	$\dot{Q}_{\text{loss, pre-heater}} = \frac{(T_{\text{inner wall}} - T_{\text{ambient}})}{R_{\text{wall}} + R_{\text{ins}} + \left(\frac{R_{\text{nat. conv.}} R_{\text{radiation}}}{R_{\text{nat. conv.}} + R_{\text{radiation}}} \right)}$	$\dot{Q}_{\text{loss, pre-heater}} = 0.255 \text{ W}$
Heat Losses in Post-Heater		
$D_{\text{post-heat, o}} = 15.24 \text{ mm}$ $D_{\text{post-heat, i}} = 10.16 \text{ mm}$ $D_{\text{post-heat, ins}} = 25.4 \text{ mm}$	$R_{\text{wall}} = \frac{\ln \left(\frac{D_{\text{post-heat, o}}}{D_{\text{post-heat, i}}} \right)}{2\pi k_{\text{post-heat}} L_{\text{heater, equiv.}}}$	$R_{\text{wall}} = 4.7 \times 10^{-3} \text{ K/W}$
$k_{\text{post-heat}} = 15.3 \text{ W/m-K}$ $k_{\text{ins}} = 0.043 \text{ W/m-K}$ $L_{\text{heater, equiv.}} = 95 \text{ mm}$	$R_{\text{ins}} = \frac{\ln \left(\frac{D_{\text{post-heat, ins}}}{D_{\text{post-heat, o}}} \right)}{2\pi k_{\text{ins}} L_{\text{heater, equiv.}}}$	$R_{\text{ins}} = 17.34 \text{ K/W}$
$\epsilon_{\text{ins}} = 0.85$ $\sigma = 5.67 \times 10^{-8} \text{ W m}^{-2} \text{ K}^{-4}$ $T_{\text{ambient}} = 23.0^\circ \text{C}$	$R_{\text{radiation}} = \frac{1}{\epsilon_{\text{ins}} \pi D_{\text{post-heat, ins}} L_{\text{heater, equiv.}} \sigma (T_{\text{ins}}^2 + T_{\text{ambient}}^2) (T_{\text{ins}} + T_{\text{ambient}})}$	$R_{\text{radiation}} = 25.2 \text{ K/W}$ $T_{\text{ins}} = 31.82^\circ \text{C}$
$P_{\text{ambient}} = 101 \text{ kPa}$ $g = 9.81 \text{ m/s}^2$	$T_{\text{avg}} = (T_{\text{ins}} + T_{\text{ambient}}) / 2$	$T_{\text{avg}} = 27.41^\circ \text{C}$
$T_{\text{r, test, out}} = 39.69^\circ \text{C}$ $T_{\text{r, post-heat, out}} = 50.95^\circ \text{C}$	$\text{Pr}_{\text{air}}, \nu_{\text{air}}, \rho_{\text{air}}, k_{\text{air}}, \beta_{\text{air}} = f(T_{\text{avg}}, P_{\text{ambient}})$	$\text{Pr}_{\text{air}} = 0.71$ $\nu_{\text{air}} = 1.54 \times 10^{-5} \text{ m}^2/\text{s}$ $\rho_{\text{air}} = 1.188 \text{ kg/m}^3$ $k_{\text{air}} = 0.026 \text{ W/m-K}$ $\beta_{\text{air}} = 3.4 \times 10^{-3} \text{ 1/K}$
	By assuming a negligible convective resistance in cooling lines: $T_{\text{inner wall}} = (T_{\text{r, test, out}} + T_{\text{r, post-heat, out}}) / 2$	$T_{\text{inner wall}} = 45.32^\circ \text{C}$
	$Ra = \frac{g \beta_{\text{air}} (T_{\text{ins}} - T_{\text{ambient}}) D_{\text{post-heat, ins}}^3}{\nu_{\text{air}} \alpha_{\text{air}}}$	$Ra = 14238$

Heat Transfer Calculations – 14 June 2011 – Run 120

Inputs	Equations	Results
	$Nu = \frac{h_{\text{nat. conv.}} D_{\text{ins}}}{k_{\text{air}}} = \left(0.60 + \frac{0.387 Ra^{1/6}}{\left(1 + \left(\frac{0.559}{Pr_{\text{air}}} \right)^{9/16} \right)^{8/27}} \right)^2$ <p>(Churchill and Chu, 1975)</p>	$Nu = 4.758$ $h_{\text{nat. conv.}} =$ $4.89 \text{ W/m}^2\text{-K}$
	$R_{\text{nat. conv.}} = \frac{1}{h_{\text{nat. conv.}} \pi D_{\text{ins}} L_{\text{heater, equiv.}}}$	$R_{\text{nat. conv.}} = 26.99 \text{ K/W}$
	$\dot{Q}_{\text{loss, post-heat}} = \frac{(T_{\text{inner wall}} - T_{\text{ambient}})}{R_{\text{wall}} + R_{\text{ins}} + \left(\frac{R_{\text{nat. conv.}} R_{\text{radiation}}}{R_{\text{nat. conv.}} + R_{\text{radiation}}} \right)}$	$\dot{Q}_{\text{loss, post-heat}} = 0.677 \text{ W}$

Heat Losses in Tee from Pre-Heater Outlet to Test Section Inlet

$D_{\text{tee, i}} = 3.175 \text{ mm}$ $D_{\text{tee, o}} = 9.525 \text{ mm}$ $D_{\text{tee, ins}} = 25.4 \text{ mm}$ $k_{\text{tee}} = 15.3 \text{ W/m-K}$ $k_{\text{ins}} = 0.043 \text{ W/m-K}$ $L_{\text{tee, equiv}} = 79.9 \text{ mm}$ $\epsilon_{\text{ins}} = 0.85$ $\sigma =$ $5.67 \times 10^{-8} \text{ W m}^{-2} \text{ K}^{-4}$ $T_{\text{ambient}} = 23.0^\circ \text{C}$ $P_{\text{ambient}} = 101 \text{ kPa}$ $g = 9.81 \text{ m/s}^2$ $T_{\text{r, test, in}} = 39.8^\circ \text{C}$	$R_{\text{wall}} = \frac{\ln \left(\frac{D_{\text{tee, o}}}{D_{\text{tee, i}}} \right)}{2\pi k_{\text{tee}} L_{\text{tee, equiv.}}}$	$R_{\text{wall}} = 0.143 \text{ K/W}$
	$R_{\text{ins}} = \frac{\ln \left(\frac{D_{\text{tee, ins}}}{D_{\text{tee, o}}} \right)}{2\pi k_{\text{ins}} L_{\text{tee, equiv.}}}$	$R_{\text{ins}} = 45.45 \text{ K/W}$
	$R_{\text{radiation}} = \frac{1}{\epsilon_{\text{ins}} \pi D_{\text{tee, ins}} L_{\text{tee, equiv.}} \sigma (T_{\text{ins}}^2 + T_{\text{ambient}}^2) (T_{\text{ins}} + T_{\text{ambient}})}$	$R_{\text{radiation}} = 30.62 \text{ K/W}$ $T_{\text{ins}} = 27.54^\circ \text{C}$
	$T_{\text{avg}} = (T_{\text{ins}} + T_{\text{ambient}}) / 2$	$T_{\text{avg}} = 25.27^\circ \text{C}$
	$Pr_{\text{air}}, \nu_{\text{air}}, \rho_{\text{air}}, k_{\text{air}}, \beta_{\text{air}} = f(T_{\text{avg}}, P_{\text{ambient}})$	$Pr_{\text{air}} = 0.71$ $\nu_{\text{air}} = 1.54 \times 10^{-5} \text{ m}^2/\text{s}$ $\rho_{\text{air}} = 1.188 \text{ kg/m}^3$ $k_{\text{air}} = 0.026 \text{ W/m-K}$ $\beta_{\text{air}} = 3.4 \times 10^{-3} \text{ 1/K}$

Heat Transfer Calculations – 14 June 2011 – Run 120

Inputs	Equations	Results
	By assuming a negligible convective resistance in tubing: $T_{\text{inner wall}} = T_{r, \text{test, in}}$	$T_{\text{inner wall}} = 39.8^\circ\text{C}$
	$Ra = \frac{g \beta_{\text{air}} (T_{\text{ins}} - T_{\text{ambient}}) D_{\text{tee, ins}}^3}{\nu_{\text{air}} \alpha_{\text{air}}}$	$Ra = 7329$
	$Nu = \frac{h_{\text{nat. conv.}} D_{\text{ins}}}{k_{\text{air}}} = \left(0.60 + \frac{0.387 Ra^{1/6}}{\left(1 + \left(\frac{0.559}{Pr_{\text{air}}} \right)^{9/16} \right)^{8/27}} \right)^2$ (Churchill and Chu, 1975)	$Nu = 4.063$ $h_{\text{nat. conv.}} = 4.17 \text{ W/m}^2\text{-K}$
	$R_{\text{nat. conv.}} = \frac{1}{h_{\text{nat. conv.}} \pi D_{\text{ins}} L_{\text{tee, equiv.}}}$	$R_{\text{nat. conv.}} = 37.58 \text{ K/W}$
	$\dot{Q}_{\text{loss, tee, in}} = \frac{(T_{\text{inner wall}} - T_{\text{ambient}})}{R_{\text{wall}} + R_{\text{ins}} + \left(\frac{R_{\text{nat. conv.}} R_{\text{radiation}}}{R_{\text{nat. conv.}} + R_{\text{radiation}}} \right)}$	$\dot{Q}_{\text{loss, tee, in}} = 0.269 \text{ W}$

Heat Losses in Tee from Test Section Outlet to Post-Heater Inlet

$D_{\text{tee, i}} = 3.175 \text{ mm}$ $D_{\text{tee, o}} = 9.525 \text{ mm}$ $D_{\text{tee, ins}} = 25.4 \text{ mm}$ $k_{\text{tee}} = 15.3 \text{ W/m-K}$ $k_{\text{ins}} = 0.043 \text{ W/m-K}$ $L_{\text{tee, equiv.}} = 79.9 \text{ mm}$ $\epsilon_{\text{ins}} = 0.85$ $\sigma =$ $5.67 \times 10^{-8} \text{ W m}^{-2}\text{K}^{-4}$ $T_{\text{ambient}} = 23.0^\circ\text{C}$ $P_{\text{ambient}} = 101 \text{ kPa}$ $g = 9.81 \text{ m/s}^2$	$R_{\text{wall}} = \frac{\ln \left(\frac{D_{\text{tee, o}}}{D_{\text{tee, i}}} \right)}{2\pi k_{\text{tee}} L_{\text{tee, equiv.}}}$	$R_{\text{wall}} = 0.1431 \text{ K/W}$
	$R_{\text{ins}} = \frac{\ln \left(\frac{D_{\text{tee, ins}}}{D_{\text{tee, o}}} \right)}{2\pi k_{\text{ins}} L_{\text{tee, equiv.}}}$	$R_{\text{ins}} = 45.45 \text{ K/W}$
	$R_{\text{radiation}} = \frac{1}{\epsilon_{\text{ins}} \pi D_{\text{tee, ins}} L_{\text{tee, equiv.}} \sigma (T_{\text{ins}}^2 + T_{\text{ambient}}^2) (T_{\text{ins}} + T_{\text{ambient}})}$	$R_{\text{radiation}} = 30.62 \text{ K/W}$ $T_{\text{ins}} = 27.51^\circ\text{C}$
	$T_{\text{avg}} = (T_{\text{ins}} + T_{\text{ambient}}) / 2$	$T_{\text{avg}} = 25.25^\circ\text{C}$

Heat Transfer Calculations – 14 June 2011 – Run 120		
Inputs	Equations	Results
$T_{r, \text{ test, out}} = 39.69^\circ\text{C}$	$\text{Pr}_{\text{air}}, \nu_{\text{air}}, \rho_{\text{air}}, k_{\text{air}}, \beta_{\text{air}} = f(T_{\text{avg}}, P_{\text{ambient}})$	$\text{Pr}_{\text{air}} = 0.71$ $\nu_{\text{air}} = 1.54 \times 10^{-5} \text{ m}^2/\text{s}$ $\rho_{\text{air}} = 1.188 \text{ kg/m}^3$ $k_{\text{air}} = 0.026 \text{ W/m-K}$ $\beta_{\text{air}} = 3.4 \times 10^{-3} \text{ 1/K}$
	By assuming a negligible convective resistance in tubing: $T_{\text{inner wall}} = T_{r, \text{ test, out}}$	$T_{\text{inner wall}} = 39.69^\circ\text{C}$
	$Ra = \frac{g \beta_{\text{air}} (T_{\text{ins}} - T_{\text{ambient}}) D_{\text{tee, ins}}^3}{\nu_{\text{air}} \alpha_{\text{air}}}$	$Ra = 7284$
	$Nu = \frac{h_{\text{nat. conv.}} D_{\text{ins}}}{k_{\text{air}}} = \left(0.60 + \frac{0.387 Ra^{1/6}}{\left(1 + \left(\frac{0.559}{\text{Pr}_{\text{air}}} \right)^{9/16} \right)^{8/27}} \right)^2$	$Nu = 4.057$ $h_{\text{nat. conv.}} = 4.17 \text{ W/m}^2\text{-K}$
	(Churchill and Chu, 1975)	
	$R_{\text{nat. conv.}} = \frac{1}{h_{\text{nat. conv.}} \pi D_{\text{ins}} L_{\text{tee, equiv.}}}$	$R_{\text{nat. conv.}} = 37.64 \text{ K/W}$
$\dot{Q}_{\text{loss, tee, out}} = \frac{(T_{\text{inner wall}} - T_{\text{ambient}})}{R_{\text{wall}} + R_{\text{ins}} + \left(\frac{R_{\text{nat. conv.}} R_{\text{radiation}}}{R_{\text{nat. conv.}} + R_{\text{radiation}}} \right)}$	$\dot{Q}_{\text{loss, tee, out}} = 0.27 \text{ W}$	
Heat Losses In Tubing From Tees to Heat Transfer Test Section		
$D_{\text{tube, o}} = 3.175 \text{ mm}$ $D_{\text{tube, i}} = 1.549 \text{ mm}$ $D_{\text{tube, ins}} = 25.4 \text{ mm}$ $k_{\text{tube}} = 398.3 \text{ W/m-K}$	$R_{\text{wall}} = \frac{\ln \left(\frac{D_{\text{tube, o}}}{D_{\text{tube, i}}} \right)}{2\pi k_{\text{tube}} L_{\text{tee-to-test}}}$	$R_{\text{wall}} = 2.87 \times 10^{-3} \text{ K/W}$
$k_{\text{ins}} = 0.043 \text{ W/m-K}$ $L_{\text{tee-to-test}} = 99.8 \text{ mm}$ $\epsilon_{\text{ins}} = 0.85$	$R_{\text{ins}} = \frac{\ln \left(\frac{D_{\text{tube, ins}}}{D_{\text{tube, o}}} \right)}{2\pi k_{\text{ins}} L_{\text{tee-to-test}}}$	$R_{\text{ins}} = 77.12 \text{ K/W}$

Heat Transfer Calculations – 14 June 2011 – Run 120		
Inputs	Equations	Results
$\sigma = 5.67 \times 10^{-8} \text{ W m}^{-2} \text{ K}^{-4}$ $T_{\text{ambient}} = 23.0^\circ \text{ C}$ $P_{\text{ambient}} = 101 \text{ kPa}$ $g = 9.81 \text{ m/s}^2$ $T_{\text{r, test, in}} = 39.8^\circ \text{ C}$ $T_{\text{r, test, out}} = 39.7^\circ \text{ C}$	$R_{\text{radiation}} = \frac{1}{\epsilon_{\text{ins}} \pi D_{\text{tube, ins}} L_{\text{tee-to-test}} \sigma (T_{\text{ins}}^2 + T_{\text{ambient}}^2) (T_{\text{ins}} + T_{\text{ambient}})}$	$R_{\text{radiation}} = 24.75 \text{ K/W}$ $T_{\text{ins}} = 25.6^\circ \text{ C}$
	$T_{\text{avg}} = (T_{\text{ins}} + T_{\text{ambient}}) / 2$	$T_{\text{avg}} = 24.31^\circ \text{ C}$
	$\text{Pr}_{\text{air}}, \nu_{\text{air}}, \rho_{\text{air}}, k_{\text{air}}, \beta_{\text{air}} = f(T_{\text{avg}}, P_{\text{ambient}})$	$\text{Pr}_{\text{air}} = 0.71$ $\nu_{\text{air}} = 1.54 \times 10^{-5} \text{ m}^2/\text{s}$ $\rho_{\text{air}} = 1.188 \text{ kg/m}^3$ $k_{\text{air}} = 0.026 \text{ W/m-K}$ $\beta_{\text{air}} = 3.4 \times 10^{-3} \text{ 1/K}$
	<p>By assuming a negligible convective resistance in tubing:</p> $T_{\text{inner wall}} = (T_{\text{r, test, in}} + T_{\text{r, test, out}}) / 2$	$T_{\text{inner wall}} = 39.74^\circ \text{ C}$
	$Ra = \frac{g \beta_{\text{air}} (T_{\text{ins}} - T_{\text{ambient}}) D_{\text{tube, ins}}^3}{\nu_{\text{air}} \alpha_{\text{air}}}$	$Ra = 4242$
	$Nu = \frac{h_{\text{nat. conv.}} D_{\text{ins}}}{k_{\text{air}}} = \left(0.60 + \frac{0.387 Ra^{1/6}}{\left(1 + \left(\frac{0.559}{\text{Pr}_{\text{air}}} \right)^{9/16} \right)^{8/27}} \right)^2$ (Churchill and Chu, 1975)	$Nu = 3.581$ $h_{\text{nat. conv.}} = 3.68 \text{ W/m}^2 \text{-K}$
	$R_{\text{nat. conv.}} = \frac{1}{h_{\text{nat. conv.}} \pi D_{\text{ins}} L_{\text{sec}}}$	$R_{\text{nat. conv.}} = 34.13 \text{ K/W}$
$\dot{Q}_{\text{loss, tee-to-test}} = \frac{(T_{\text{inner wall}} - T_{\text{ambient}})}{R_{\text{wall}} + R_{\text{ins}} + \left(\frac{R_{\text{nat. conv.}} R_{\text{radiation}}}{R_{\text{nat. conv.}} + R_{\text{radiation}}} \right)}$	$\dot{Q}_{\text{loss, tee-to-test}} = 0.183 \text{ W}$	
Water Heat Transfer Coefficient in Test Section Annulus		
$T_{\text{w, test, in}} = 32.4^\circ \text{ C}$ $T_{\text{w, test, out}} = 32.8^\circ \text{ C}$	$T_{\text{w, test, avg}} = (T_{\text{w, test, out}} + T_{\text{w, test, in}}) / 2$	$T_{\text{w, test, avg}} = 32.59^\circ \text{ C}$

Heat Transfer Calculations – 14 June 2011 – Run 120		
Inputs	Equations	Results
$P_w = 275.8 \text{ kPa}$ $D_{\text{annulus}, i} = 4.57 \text{ mm}$ $D_{\text{test}, o} = 3.175 \text{ mm}$ $\dot{V}_{w, \text{prim}} =$ $3.68 \times 10^{-5} \text{ m}^3/\text{s}$	$\text{Pr}_w, \nu_w, \rho_w, k_w = f(T_{w, \text{test}, \text{avg}}, P_w)$	$\text{Pr}_w = 5.093$ $\nu_w = 7.59 \times 10^{-7} \text{ m}^2/\text{s}$ $\rho_w = 994.9 \text{ kg/m}^3$ $k_w = 0.620 \text{ W/m-K}$
	$A_{\text{annulus}} = (\pi/4)(D_{\text{annulus}, i}^2 - D_{\text{test}, o}^2)$	$A_{\text{annulus}} = 8.49 \times 10^{-6} \text{ m}^2$
	$V_{\text{annulus}} = \frac{\dot{V}_{w, \text{prim}}}{A_{\text{annulus}}}$	$V_{\text{annulus}} = 4.33 \text{ m/s}$
	$D_{\text{hydraulic}} = D_{\text{annulus}, i} - D_{\text{test}, o}$	$D_{\text{hydraulic}} = 1.395 \text{ mm}$
	$\text{Re}_{\text{annulus}} = \frac{V_{\text{annulus}} D_{\text{hydraulic}}}{\nu_{w, \text{prim}}}$	$\text{Re}_{\text{annulus}} = 7963$
	$r^* = D_{\text{test}, o} / D_{\text{annulus}, i}$	$r^* = 0.6947$
	$\text{Nu}_{\text{turbulent}} = 0.25 \text{Re}_{\text{annulus}}^{0.78} \text{Pr}_w^{0.48} (r^*)^{0.14}$ (Garimella and Christensen, 1995)	$\text{Nu}_{\text{turbulent}} = 63.43$
	$h_{\text{annulus}} = \frac{\text{Nu}_{\text{turbulent}} k_w}{D_{\text{hydraulic}}}$	$h_{\text{annulus}} = 28177 \text{ W/m}^2\text{-K}$
Heat Losses in Test Section		
$h_{\text{annulus}} = 28177 \text{ W/m}^2\text{-K}$ $L_{\text{annulus}} = 145 \text{ mm}$ $D_{\text{annulus}, i} = 4.57 \text{ mm}$ $D_{\text{annulus}, o} = 6.35 \text{ mm}$ $D_{\text{test}, \text{ins}} = 25.4 \text{ mm}$ $k_{\text{annulus}} = 15.3 \text{ W/m-K}$ $k_{\text{ins}} = 0.043 \text{ W/m-K}$ $\epsilon_{\text{ins}} = 0.85$ $\sigma =$ $5.67 \times 10^{-8} \text{ W m}^{-2}\text{K}^{-4}$ $T_{\text{ambient}} = 23.0^\circ\text{C}$ $P_{\text{ambient}} = 101 \text{ kPa}$ $g = 9.81 \text{ m/s}^2$ $T_{w, \text{test}, \text{in}} = 20.19^\circ\text{C}$	$R_{\text{annulus}, o} = \frac{1}{h_{\text{annulus}} \pi D_{\text{annulus}, i} L_{\text{annulus}}}$	$R_{\text{annulus}, o} = 1.7 \times 10^{-2} \text{ K/W}$
	$R_{\text{wall}} = \frac{\ln\left(\frac{D_{\text{annulus}, o}}{D_{\text{annulus}, i}}\right)}{2\pi k_{\text{annulus}} L_{\text{annulus}}}$	$R_{\text{wall}} = 2.36 \times 10^{-2} \text{ K/W}$
	$R_{\text{ins}} = \frac{\ln\left(\frac{D_{\text{test}, \text{ins}}}{D_{\text{annulus}, o}}\right)}{2\pi k_{\text{ins}} L_{\text{annulus}}}$	$R_{\text{ins}} = 35.39 \text{ K/W}$
	$R_{\text{radiation}} = \frac{1}{\epsilon_{\text{ins}} \pi D_{\text{test}, \text{ins}} L_{\text{annulus}} \sigma (T_{\text{ins}}^2 + T_{\text{ambient}}^2) (T_{\text{ins}} + T_{\text{ambient}})}$	$R_{\text{radiation}} = 17.08 \text{ K/W}$ $T_{\text{ins}} = 25.13^\circ\text{C}$
	$T_{\text{avg}} = (T_{\text{ins}} + T_{\text{ambient}}) / 2$	$T_{\text{avg}} = 24.06^\circ\text{C}$

Heat Transfer Calculations – 14 June 2011 – Run 120		
Inputs	Equations	Results
$T_{w, \text{ test, out}} = 20.38^\circ\text{C}$	$\text{Pr}_{\text{air}}, \nu_{\text{air}}, \rho_{\text{air}}, k_{\text{air}}, \beta_{\text{air}} = f(T_{\text{avg}}, P_{\text{ambient}})$	$\text{Pr}_{\text{air}} = 0.71$ $\nu_{\text{air}} = 1.55 \times 10^{-5} \text{ m}^2/\text{s}$ $\rho_{\text{air}} = 1.188 \text{ kg/m}^3$ $k_{\text{air}} = 0.026 \text{ W/m-K}$ $\beta_{\text{air}} = 3.4 \times 10^{-3} \text{ 1/K}$
	$T_{w, \text{ test, avg}} = (T_{w, \text{ test, out}} + T_{w, \text{ test, in}}) / 2$	$T_{w, \text{ test, avg}} = 20.29^\circ\text{C}$
	$Ra = \frac{g \beta_{\text{air}} (T_{\text{ins}} - T_{\text{ambient}}) D_{\text{test, ins}}^3}{\nu_{\text{air}} \alpha_{\text{air}}}$	$Ra = 3379$
	$Nu = \frac{h_{\text{nat. conv.}} D_{\text{ins}}}{k_{\text{air}}} = \left(0.60 + \frac{0.387 Ra^{1/6}}{\left(1 + \left(\frac{0.559}{\text{Pr}_{\text{air}}} \right)^{9/16} \right)^{8/27}} \right)^2$	$Nu = 3.401$ $h_{\text{nat. conv.}} = 3.51 \text{ W/m}^2\text{-K}$
	(Churchill and Chu, 1975)	
	$R_{\text{nat. conv.}} = \frac{1}{h_{\text{nat. conv.}} \pi D_{\text{test, ins}} L_{\text{annulus}}}$	$R_{\text{nat. conv.}} = 24.66 \text{ K/W}$
$\dot{Q}_{\text{loss, test}} = \frac{(T_{\text{inner wall}} - T_{\text{ambient}})}{R_{\text{annulus, o}} + R_{\text{wall}} + R_{\text{ins}} + \left(\frac{R_{\text{nat. conv.}} R_{\text{radiation}}}{R_{\text{nat. conv.}} + R_{\text{radiation}}} \right)}$	$\dot{Q}_{\text{loss, test, ann}} = 0.211 \text{ W}$	
Average Test Section Quality		
$\dot{Q}_{\text{pre-heat}} = 147.4 \text{ W}$ $\dot{Q}_{\text{loss, pre-heat}} = 0.353 \text{ W}$ $T_{r, \text{ pre-heat, in}} = 23.8^\circ\text{C}$ $P_{r, \text{ pre-heat, in}} = 1810 \text{ kPa}$ $P_{r, \text{ test, in}} = 1810 \text{ kPa}$ $\dot{Q}_{\text{loss, pre-heat}} = 0.26 \text{ W}$ $\dot{Q}_{\text{loss, tee, in}} = 0.27 \text{ W}$ $\dot{m}_r = 1.125 \times 10^{-3} \text{ kg/s}$ $\dot{Q}_{\text{loss, post-heat}} = 0.677 \text{ W}$	$T_{r, \text{ pre-heat, in, sat}} = f(P_{r, \text{ pre-heat, in}}, x = 0)$	$T_{r, \text{ pre-heat, in, sat}} = 39.85^\circ\text{C}$
	$\Delta T_{\text{sub, pre}} = T_{r, \text{ pre-heat, in, sat}} - T_{r, \text{ pre-heat, in}}$	$\Delta T_{\text{sub, pre}} = 16.05 \text{ K}$
	$i_{r, \text{ pre-heat, in}} = f(T_{r, \text{ pre-heat, in}}, P_{r, \text{ pre-heat, in}})$	$i_{r, \text{ pre-heat, in}} = 232.7 \text{ kJ/kg}$
	$i_{r, \text{ test, in}} = \left(i_{r, \text{ pre-heat, in}} + \frac{\dot{Q}_{\text{pre-heat}} - \dot{Q}_{\text{loss, pre-heat}} - \dot{Q}_{\text{loss, tee, in}}}{\dot{m}_r} \right)$	$i_{r, \text{ test, in}} = 363.4 \text{ kJ/kg}$
	$x_{r, \text{ test, in}} = f(i_{r, \text{ test, in}}, P_{r, \text{ test, in}})$	$x_{r, \text{ test, in}} = 0.872$
	$T_{r, \text{ post-heat, out, sat}} = f(P_{r, \text{ post-heat, out}}, x = 1)$	$T_{r, \text{ post-heat, out, sat}} = 39.84^\circ\text{C}$
	$\Delta T_{\text{sup, post}} = T_{r, \text{ post-heat, out}} - T_{r, \text{ post-heat, out, sat}}$	$\Delta T_{\text{sup, post}} = 9.71^\circ\text{C}$

Heat Transfer Calculations – 14 June 2011 – Run 120		
Inputs	Equations	Results
$\dot{Q}_{\text{loss, tee, out}} = 0.2671 \text{ W}$ $T_{\text{r, post-heat, out}} = 51.0 \text{ }^\circ\text{C}$ $P_{\text{r, post-heat, out}} = 1778 \text{ kPa}$ $P_{\text{r, test, out}} = 1780 \text{ kPa}$	$i_{\text{r, post-heat, out}} = f(T_{\text{r, post-heat, out}}, P_{\text{r, post-heat, out}})$	$i_{\text{r, post-heat, out}} = 394.7 \text{ kJ/kg}$
	$i_{\text{r, test, out}} =$ $\left(i_{\text{r, post-heat, out}} - \frac{\dot{Q}_{\text{post-heater}} - \dot{Q}_{\text{loss, post-heat}} - \dot{Q}_{\text{loss, tee, out}}}{\dot{m}_{\text{r}}} \right)$	$i_{\text{r, test, out}} = 329.4 \text{ kJ/kg}$
	$x_{\text{r, test, out}} = f(P_{\text{r, test, out}}, i_{\text{r, test, out}})$	$x_{\text{r, test, out}} = 0.5925$
	$x_{\text{test, avg}} = (x_{\text{test, in}} + x_{\text{test, out}}) / 2$	$x_{\text{test, avg}} = 0.7328$
Refrigerant Heat Transfer Coefficient		
$P_{\text{w}} = 275.8 \text{ kPa}$ $\dot{Q}_{\text{loss, test, ann}} = 0.211 \text{ W}$ $\dot{Q}_{\text{loss, tee-to-test}} = 0.183 \text{ W}$ $\dot{Q}_{\text{loss, pre-heat}} = 0.255 \text{ W}$ $\dot{Q}_{\text{loss, post-heat}} = 0.677 \text{ W}$ $\dot{Q}_{\text{loss, tee, in}} = 0.269 \text{ W}$ $\dot{Q}_{\text{loss, tee, out}} = 0.267 \text{ W}$ $i_{\text{r, test, in}} = 363.4 \text{ kJ/kg}$ $P_{\text{r, test, in}} = 1810 \text{ kPa}$ $i_{\text{r, test, out}} = 329.4 \text{ kJ/kg}$ $P_{\text{r, test, out}} = 1780 \text{ kPa}$ $T_{\text{r, test, in}} = 39.6 \text{ }^\circ\text{C}$ $T_{\text{r, test, out}} = 39.5 \text{ }^\circ\text{C}$ $k_{\text{test}} = 398.3 \text{ W/m-K}$ $T_{\text{w, test, in}} = 32.39 \text{ }^\circ\text{C}$ $T_{\text{w, test, out}} = 32.8 \text{ }^\circ\text{C}$ $P_{\text{w}} = 275.8 \text{ kPa}$ $h_{\text{annulus}} = 28177 \text{ W/m}^2\text{K}^1$ $D_{\text{test, i}} = 1.549 \text{ mm}$ $D_{\text{test, o}} = 3.175 \text{ mm}$ $L_{\text{annulus}} = 145 \text{ mm}$	$\dot{Q}_{\text{loss, ambient}} = \dot{Q}_{\text{loss, test, ann}} + \dot{Q}_{\text{loss, tee-to-test}} + \dot{Q}_{\text{loss, pre-heat}} + \dot{Q}_{\text{loss, post-heat}} + \dot{Q}_{\text{loss, tee, in}} + \dot{Q}_{\text{loss, tee, out}}$	$\dot{Q}_{\text{loss, ambient}} = 1.86 \text{ W}$
	$\dot{Q}_{\text{test}} = \dot{m}_{\text{r}} (i_{\text{r, post-heat, out}} - i_{\text{r, pre-heat, in}}) - \dot{Q}_{\text{pre-heater}} - \dot{Q}_{\text{post-heater}} + \dot{Q}_{\text{loss, ambient}}$	$\dot{Q}_{\text{test}} = 38.15 \text{ W}$
	$T_{\text{r, test, in, sat}} = f(P_{\text{r, test, in}}, i_{\text{r, test, in}})$	$T_{\text{r, test, in, sat}} = 39.85 \text{ }^\circ\text{C}$
	$Error_{\text{r, test, in}} = T_{\text{r, test, in}} - T_{\text{r, test, in, sat}}$	$Error_{\text{r, test, in}} = 0.25 \text{ }^\circ\text{C}$
	$T_{\text{r, test, out, sat}} = f(P_{\text{r, test, out}}, i_{\text{r, test, out}})$	$T_{\text{r, test, out, sat}} = 39.84 \text{ }^\circ\text{C}$
	$Error_{\text{r, test, out}} = T_{\text{r, test, out}} - T_{\text{r, test, out, sat}}$	$Error_{\text{r, test, out}} = 0.34 \text{ }^\circ\text{C}$
	$LMTD = \frac{(T_{\text{r, test, in}} - T_{\text{w, test, out}}) - (T_{\text{r, test, out}} - T_{\text{w, test, in}})}{\ln \left[\frac{(T_{\text{r, test, in}} - T_{\text{w, test, out}})}{(T_{\text{r, test, out}} - T_{\text{w, test, in}})} \right]}$	$LMTD = 7.15 \text{ }^\circ\text{C}$
	$UA = \dot{Q}_{\text{test}} / (LMTD)$	$UA = 5.336 \text{ W/K}$
	$R_{\text{wall}} = \frac{\ln \left(\frac{D_{\text{test, o}}}{D_{\text{test, i}}} \right)}{2\pi k_{\text{test}} (L_{\text{annulus}} + 2 \cdot (L_{\text{reducer}} + L_{\text{tee}}))}$	$R_{\text{wall}} = 1.40 \times 10^{-3} \text{ K/W}$
	$R_{\text{annulus, i}} = \frac{1}{h_{\text{annulus}} \pi D_{\text{test, o}} L_{\text{annulus}}}$	$R_{\text{annulus, i}} = 2.45 \times 10^{-2} \text{ K/W}$
	$T_{\text{w, test, avg}} = (T_{\text{w, test, out}} + T_{\text{w, test, in}}) / 2$	$T_{\text{w, test, avg}} = 32.59 \text{ }^\circ\text{C}$
	$Pr_{\text{w}}, \nu_{\text{w}}, \rho_{\text{w}}, k_{\text{w}} = f(T_{\text{w, test, avg}}, P_{\text{w}})$	$Pr_{\text{w}} = 5.093$ $\nu_{\text{w}} = 7.59 \times 10^{-7} \text{ m}^2/\text{s}$ $\rho_{\text{w}} = 998.2 \text{ kg/m}^3$ $k_{\text{w}} = 0.6197 \text{ W/m-K}$

Heat Transfer Calculations – 14 June 2011 – Run 120

Inputs	Equations	Results
$L_{\text{reducer}} = 18.5 \text{ mm}$ $L_{\text{tee}} = 11.5 \text{ mm}$ $D_{\text{reducer}} = 4.57 \text{ mm}$ $D_{\text{tee}} = 4.8 \text{ mm}$ $x_{\text{test, avg}} = 0.7323$	$\frac{Ra}{L^3} = \frac{g\beta_w (T_{\text{wall, o}} - T_{w, \text{test, avg}})}{\nu_w \alpha_w}$	$\frac{Ra}{L^3} = 3.26 \times 10^{10} \text{ m}^{-3}$
	$Ra_{\text{reducer}}^* = \frac{[\ln(D_{\text{reducer}}/D_{\text{test, o}})]^4}{(D_{\text{test, o}}^{-3/5} + D_{\text{reducer}}^{-3/5})^5} \left(\frac{Ra}{L^3}\right)$ <p>(Incorpera and DeWitt, 1996)</p>	$Ra_{\text{reducer}}^* = 5.06$
	$Ra_{\text{tee}}^* = \frac{[\ln(D_{\text{tee}}/D_{\text{test, o}})]^4}{(D_{\text{test, o}}^{-3/5} + D_{\text{tee}}^{-3/5})^5} \left(\frac{Ra}{L^3}\right)$	$Ra_{\text{tee}}^* = 4.85 \times 10^{-7}$
	<p>for: $100 \leq Ra_{\text{reducer}}^* \leq 10^7$</p> $k_{\text{effective, reducer}} = (k_w) \cdot 0.386 \left(\frac{Pr_w}{0.861 + Pr_w}\right)^{1/4} (Ra_{\text{reducer}}^*)^{1/4}$ <p>(Incorpera and DeWitt, 1996)</p>	
	<p>for: $Ra_{\text{reducer}}^* \leq 100$</p> $k_{\text{effective, reducer}} = k_w$ <p>(Irvine and Hartnett, 1975)</p>	$k_{\text{effective, reducer}} = 0.620 \text{ W/m-K}$
	<p>for: $100 \leq Ra_{\text{tee}}^* \leq 10^7$</p> $k_{\text{effective, tee}} = (k_w) \cdot 0.386 \left(\frac{Pr_w}{0.861 + Pr_w}\right)^{1/4} (Ra_{\text{tee}}^*)^{1/4}$ <p>for: $Ra_{\text{tee}}^* \leq 100$</p> $k_{\text{effective, reducer}} = k_w$ <p>(Irvine and Hartnett, 1975)</p>	$k_{\text{effective, tee}} = 0.620 \text{ W/m-K}$
	$R_{\text{reducer}} = \frac{\ln\left(\frac{D_{\text{reducer}}}{D_{\text{test, o}}}\right)}{2\pi k_{\text{effective, reducer}} L_{\text{reducer}}}$	$R_{\text{reducer}} = 5.056 \text{ K/W}$
	$R_{\text{tee}} = \frac{\ln\left(\frac{D_{\text{tee}}}{D_{\text{test, o}}}\right)}{2\pi k_{\text{effective, tee}} L_{\text{tee}}}$	$R_{\text{tee}} = 9.23 \text{ K/W}$
	$R_{\text{conv, equiv.}}^{-1} = R_{\text{annulus, i}}^{-1} + 2(R_{\text{tee}}^{-1} + R_{\text{reducer}}^{-1})$	$R_{\text{conv, equiv.}} = 0.024 \text{ K/W}$
	$h_t = \left[(UA)^{-1} - R_{\text{wall}} - R_{\text{conv, equiv.}} \right]^{-1} \cdot \left[\pi D_{\text{test, i}} (L_{\text{annulus}} + 2(L_{\text{reducer}} + L_{\text{tee}})) \right]^{-1}$	$h_t = 6194 \text{ W/m}^2\text{-K}$

Heat Transfer Calculations – 14 June 2011 – Run 120

Inputs	Equations	Results
	$R_r = \frac{1}{h_r \pi D_{\text{test}, i} (L_{\text{annulus}} + 2(L_{\text{reducer}} + L_{\text{tee}}))}$	$R_r = 0.1618 \text{ K/W}$
	$R_{\text{ratio}} = \frac{R_r}{R_{\text{wall}} + R_{\text{conv. equiv.}}}$	$R_{\text{ratio}} = 6.328$
	$\dot{Q}_{\text{test}} = \frac{((T_{r, \text{test}, \text{in}, \text{sat}} - T_{r, \text{test}, \text{out}, \text{sat}})/2 - T_{\text{wall}, o})}{R_r + R_{\text{wall}}}$	$T_{\text{wall}, o} = 33.51^\circ\text{C}$
	$\dot{Q}_{\text{reducer}} = 2 \cdot \frac{(T_{\text{wall}, o} - T_{w, \text{test}, \text{avg}})}{R_{\text{reducer}}}$	$\dot{Q}_{\text{reducer}} = 0.3652 \text{ W}$
	$\dot{Q}_{\text{tee}} = 2 \cdot \frac{(T_{\text{wall}, o} - T_{w, \text{test}, \text{avg}})}{R_{\text{tee}}}$	$\dot{Q}_{\text{tee}} = 0.2001 \text{ W}$
	$\dot{Q}_{\text{annulus}} = \frac{(T_{\text{wall}, o} - T_{w, \text{test}, \text{avg}})}{R_{\text{annulus}, i}}$	$\dot{Q}_{\text{annulus}} = 37.63 \text{ W}$
	$P_{r, \text{test}, \text{avg}} = (P_{r, \text{test}, \text{in}} + P_{r, \text{test}, \text{out}})/2$	$P_{r, \text{test}, \text{avg}} = 1795 \text{ kPa}$
	$i_{r, \text{fg}} = f(P_{r, \text{test}, \text{avg}}, x_{r, \text{test}, \text{avg}})$	$i_{r, \text{fg}} = 120.65 \text{ kJ/kg}$
	$\Delta x = \frac{\dot{Q}_{\text{test}}}{\dot{m}_r i_{r, \text{fg}}}$	$\Delta x = 0.2812$

Pressure Drop Calculations – 14 June 2011 – Run 120		
Inputs	Equations	Results
$D_{tee} = 4.8 \text{ mm}$ $D_{contraction} = 3.175 \text{ mm}$ $D_{test, i} = 1.549 \text{ mm}$ $\dot{m}_r = 1.125 \times 10^{-3} \text{ kg/s}$ $x_{r, test, in} = 0.8721$ $P_{r, test, in} = 1810 \text{ kPa}$ $x_{r, test, out} = 0.5925$ $P_{r, test, out} = 1780 \text{ kPa}$ $B = 0.25$ $\Delta P_{measured} = 29.497 \text{ kPa}$ $L_{test} = 0.3048 \text{ m}$	$A_{ratio, 1} = \frac{A_{contraction}}{A_{tee}} = \left(\frac{D_{contraction}}{D_{tee}} \right)^2$	$A_{ratio, 1} = 0.4375$
	$A_{ratio, 2} = \frac{A_{test}}{A_{contraction}} = \left(\frac{D_{test}}{D_{contraction}} \right)^2$	$A_{ratio, 2} = 0.238$
	$G = \frac{\dot{m}_r}{A_{test}} = \frac{\dot{m}_r}{0.25 \cdot \pi \cdot D_{test, i}^2}$	$G = 596.8 \text{ kg/m}^2 \cdot \text{s}$
	$G_{contraction} = G \cdot A_{ratio, 2}$	$G_{contraction} = 142 \text{ kg/m}^2 \cdot \text{s}$
	$G_{tee} = G \cdot A_{ratio, 1} \cdot A_{ratio, 2}$	$G_{tee} = 62 \text{ kg/m}^2 \cdot \text{s}$
	$C_{C, 1} = \frac{1}{0.639 [1 - (A_{ratio, 1})]^{1/2} + 1}$ (Chisholm, 1983)	$C_{C, 1} = 0.676$
	$C_{C, 2} = \frac{1}{0.639 [1 - (A_{ratio, 2})]^{1/2} + 1}$ (Chisholm, 1983)	$C_{C, 2} = 0.6419$
	$(\rho_1, \mu_1)_{in} = f(x_{r, test, in}, P_{r, test, in})$	$\rho_{1, in} = 967 \text{ kg/m}^3$ $\mu_{1, in} = 1.05 \times 10^{-4} \text{ kg/m-s}$
	$(\rho_v, \mu_v)_{in} = f(x_{r, test, in}, P_{r, test, in})$	$\rho_{v, in} = 101.2 \text{ kg/m}^3$ $\mu_{v, in} = 1.6 \times 10^{-5} \text{ kg/m-s}$
	$(\rho_1, \mu_1)_{out} = f(x_{r, test, out}, P_{r, test, out})$	$\rho_{1, out} = 967 \text{ kg/m}^3$ $\mu_{1, out} = 1.05 \times 10^{-4} \text{ kg/m-s}$
	$(\rho_v, \mu_v)_{out} = f(x_{r, test, out}, P_{r, test, out})$	$\rho_{v, out} = 101.2 \text{ kg/m}^3$ $\mu_{v, out} = 1.6 \times 10^{-5} \text{ kg/m-s}$
$\psi_H = 1 + \left(\frac{\rho_{1, in}}{\rho_{v, in}} - 1 \right) x_{r, test, in}$ (Hewitt, 1994)	$\psi_H = 8.465$	

Pressure Drop Calculations – 14 June 2011 – Run 120

Inputs	Equations	Results
	$\Delta P_{\text{contraction}, 1} = \frac{G_{\text{contraction}}^2}{2\rho_{l, \text{in}}} \left(1 - A_{\text{ratio}, 1}^2 + \left(\frac{1}{C_{C, 1}} \right)^2 \right) \psi_H$ <p>(Hewitt, 1994)</p>	$\Delta P_{\text{contraction}, 1} = 1.618 \text{ kPa}$
	$\Delta P_{\text{contraction}, 2} = \frac{G^2}{2\rho_{l, \text{in}}} \left(1 - A_{\text{ratio}, 2}^2 + \left(\frac{1}{C_{C, 2}} \right)^2 \right) \psi_H$ <p>(Hewitt, 1994)</p>	$\Delta P_{\text{contraction}, 2} = 1.955 \text{ kPa}$
	$\Delta P_{\text{contraction}} = \Delta P_{\text{contraction}, 1} + \Delta P_{\text{contraction}, 2}$	$\Delta P_{\text{contraction}} = 3.54 \text{ kPa}$ (12% of $\Delta P_{\text{measured}}$)
	$\psi_S = 1 + \left(\frac{\rho_{l, \text{out}}}{\rho_{v, \text{out}}} - 1 \right) \left[Bx_{r, \text{test}, \text{out}} (1 - x_{r, \text{test}, \text{out}}) + x_{r, \text{test}, \text{out}}^2 \right]$ <p>(Chisholm, 1983)</p>	$\psi_S = 4.521$
	$\Delta P_{\text{expansion}, 2} = \frac{G^2 A_{\text{ratio}, 2} (1 - A_{\text{ratio}, 2}) \psi_S}{\rho_{l, \text{out}}}$ <p>(Hewitt, 1994)</p>	$\Delta P_{\text{expansion}, 2} = 0.302 \text{ kPa}$
	$\Delta P_{\text{expansion}, 1} = \frac{G_{\text{contraction}}^2 A_{\text{ratio}, 1} (1 - A_{\text{ratio}, 1}) \psi_S}{\rho_{l, \text{out}}}$ <p>(Hewitt, 1994)</p>	$\Delta P_{\text{expansion}, 1} = 0.410 \text{ kPa}$
	$\Delta P_{\text{expansion}} = \Delta P_{\text{expansion}, 1} + \Delta P_{\text{expansion}, 2}$	$\Delta P_{\text{expansion}} = 0.711 \text{ kPa}$ (2.4% of $\Delta P_{\text{measured}}$)
	$\alpha_{r, \text{test}, \text{in}} = \left[1 + \left(\frac{1 - x_{r, \text{test}, \text{in}}}{x_{r, \text{test}, \text{in}}} \right)^{0.74} \left(\frac{\rho_{v, \text{in}}}{\rho_{l, \text{in}}} \right)^{0.65} \left(\frac{\mu_{l, \text{in}}}{\mu_{v, \text{in}}} \right)^{0.13} \right]^{-1}$ <p>(Baroczy, 1965)</p>	$\alpha_{r, \text{test}, \text{in}} = 0.934$
	$\alpha_{r, \text{test}, \text{out}} = \left[1 + \left(\frac{1 - x_{r, \text{test}, \text{out}}}{x_{r, \text{test}, \text{out}}} \right)^{0.74} \left(\frac{\rho_{v, \text{out}}}{\rho_{l, \text{out}}} \right)^{0.65} \left(\frac{\mu_{l, \text{out}}}{\mu_{v, \text{out}}} \right)^{0.13} \right]^{-1}$ <p>(Baroczy, 1965)</p>	$\alpha_{r, \text{test}, \text{out}} = 0.8175$

Pressure Drop Calculations – 14 June 2011 – Run 120

Inputs	Equations	Results
	$ \Delta P_{\text{deceleration}} = \left G^2 \left[\frac{x^2}{\rho_{v, \text{out}} \alpha} + \frac{(1-x)^2}{\rho_{l, \text{out}} (1-\alpha)} \right]_{\substack{\alpha=\alpha_{r, \text{test, out}} \\ x=x_{r, \text{test, out}}} } - G^2 \left[\frac{x^2}{\rho_{v, \text{in}} \alpha} + \frac{(1-x)^2}{\rho_{l, \text{in}} (1-\alpha)} \right]_{\substack{\alpha=\alpha_{r, \text{test, in}} \\ x=x_{r, \text{test, in}}} } \right $ <p>(Carey, 1992)</p>	$ \Delta P_{\text{deceleration}} = 1.11 \text{ kPa}$ (3.7% of $\Delta P_{\text{measured}}$)
	$\Delta P_{\text{measured}} = \Delta P_f - \Delta P_{\text{deceleration}} + \Delta P_{\text{contraction}} - \Delta P_{\text{expansion}}$	$\Delta P_f = 27.75 \text{ kPa}$ (94% of $\Delta P_{\text{measured}}$)
	$\nabla P_f = \frac{\Delta P_f}{L_{\text{test}}}$	$\nabla P_f = 91.04 \text{ kPa/m}$

APPENDIX C - PRIMARY LOOP PUMP HEAT ADDITION CALCULATION

The pump heat addition is required to determine the test section heat duty (Equation 4.16.) Andresen (2007) investigated the pump heat additions in the large tube test facility by the coolant circulation pump (Micromotion 5000-750, S/N 365623.) A comparison between the ideal pump work and the actual work obtained from the pump curves required to achieve the primary coolant flow rate was used to determine a pump efficiency. It was assumed that all of the inefficiencies resulted in heat additions to the coolant lines. From this, Andresen developed a curve fit for determining pump heat addition based on the volumetric flow of the primary coolant. The approach used by Andersen is detailed below.

The pump efficiency was defined as the ratio of ideal work required to maintain a given coolant flow rate and the actual shaft work.

$$\eta = \frac{\dot{W}_{\text{ideal}}}{\dot{W}_{\text{shaft}}} \quad (\text{C.1})$$

Assuming all the inefficiencies result in heat dissipation into the coolant:

$$\frac{\dot{Q}_{\text{pump}}}{\dot{W}_{\text{shaft}}} = 1 - \eta \quad (\text{C.2})$$

The shaft work was obtained by fitting the pump speed and torque curves provided by the vendor to the following expressions.

$$\tau (\text{Nm}) = \frac{0.8}{700} \Delta P_{\text{prim}} (\text{kPa}) + 0.1 \quad (\text{C.3})$$

$$\omega (\text{rpm}) = 860 \cdot \dot{V} (\text{gpm}) + 300 \cdot \frac{\Delta P_{\text{prim}} (\text{kPa})}{220} \quad (\text{C.4})$$

The pump shaft work is then calculated by:

$$\dot{W}_{\text{shaft}} = \tau \omega \quad (\text{C.5})$$

and the ideal work is calculated as:

$$\dot{W}_{\text{ideal}} = \Delta P_{\text{prim}} \cdot \dot{V}_{\text{w, rpim}} \quad (\text{C.6})$$

Pressure drop data from the primary loop and Equations C.3 and C.4 were used to develop a cubic fit for pump heat additions. The regression analysis by Andresen (2007) yielded the following correlation for the 3.05 mm test section set-up.

$$\dot{Q}_{\text{pump}} = (9.0397)\dot{V}_{\text{w, prim, gpm}} + (0.1304)\dot{V}_{\text{w, prim, gpm}}^2 + (0.4034)\dot{V}_{\text{w, prim, gpm}}^3 \quad (\text{C.7})$$

APPENDIX D - INTERMITTENT PRESSURE DROP MODEL

D.1 Intermittent Regime

As discussed in Section 7.2.2, the pressure drop in the intermittent regime is modeled using an approach based on previous work by Fukano *et al.* (1989), Garimella *et al.* (2002), and Chung and Kawaji (2004), where the two-phase flow is divided into two distinct regions. The regions consist of a film/bubble and liquid slug region as presented in Figure D.1. The relevant velocities and dimensions are provided in the schematic to guide in the model development.

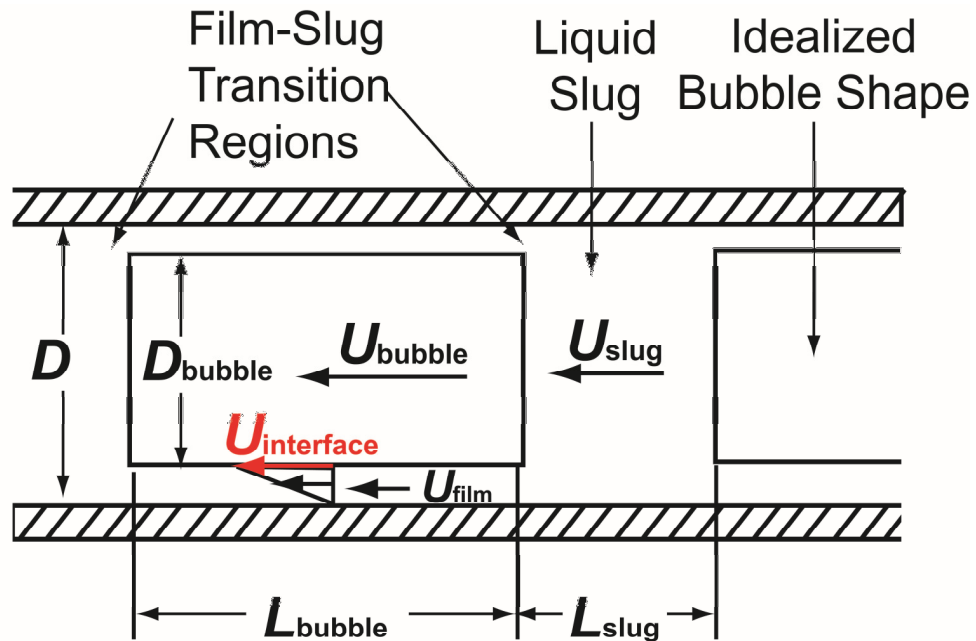


Figure D.1: Schematic of Idealized Unit Cell During Intermittent Flow with Relevant Dimensions, Adapted from Garimella *et al.* (2002)

The pressure drop is modeled for a unit cell consisting of a single vapor bubble and liquid slug. The total pressure drop within a unit cell is due to the sum of the pressure drop in the film-vapor bubble region, $(dP/dz)_{f/b}$, the liquid slug, $(dP/dz)_{slug}$, and the transitions between the film/bubble and slug regions, ΔP_{tran} . Thus, it accounts for the acceleration of the liquid as it flows around the bubble and deceleration as it flows from the bubble

region to the liquid slug region downstream. The average pressure drop per unit cell can be predicted by:

$$\left(\frac{dp}{dx}\right)_{fr} = \left(\frac{dp}{dx}\right)_{fb} \frac{L_{bubble}}{L_{UC}} + \left(\frac{dp}{dx}\right)_{slug} \frac{L_{slug}}{L_{UC}} + \Delta P_{tran} \frac{1}{L_{UC}} \quad (D.1)$$

To predict the average frictional pressure drop, the individual pressure drops and lengths of these bubble and slug regions are required. The frictional pressure drop in the liquid slug is approximated by the single-phase pressure drop equation.

$$\left(\frac{dp}{dx}\right)_{slug} = f_{slug} \frac{1}{2} \rho_l U_{slug}^2 D^{-1} \quad (D.2)$$

Where U_{slug} is the slug velocity and f_{slug} can be predicted using the Churchill (1977) friction factor and slug Reynolds number, $Re_{slug} = \rho_l U_{slug} D \mu_l^{-1}$. The Churchill (1977) friction factor is based on the Reynolds number and surface roughness, ϵ .

$$f = 8 \cdot \left[\left((8/Re)^{12} + \left(\left(2.457 \cdot \ln \left(\frac{1}{(7/Re)^{0.9} + 0.27 \cdot (\epsilon/D)} \right) \right)^{16} + (37530/Re)^{16} \right)^{-1.5} \right)^{1/12} \right] \quad (D.3)$$

The slug velocity is approximated in the same manner as Chung and Kawaji (2004).

$$U_{slug} = \frac{j_l}{1-\alpha} \quad (D.4)$$

To determine the pressure drop in the film-bubble region, the vapor bubble velocity and interfacial velocity are needed. In previous studies, the vapor bubble velocity was approximated based on the superficial velocity. For example, Garimella *et al.* (2002) evaluated the vapor bubble velocity using the model developed by Dukler and Hubbard (1975) but found that this resulted in a value ranging from $1.18j$ to $1.24j$. They approximated the vapor bubble velocity by $U_{bubble} = 1.2j$. In this study, the vapor bubble velocity is directly measured and can be used.

Fukano and Kariyasaki (1993) compared their air-water data in capillary tubes ($D = 1, 2.4$ and 4.9 mm) and found that there was an influence of tube diameter, which they associated with surface tension, on the vapor bubble velocities. They found an almost linear dependence between the volumetric flux j and their measured bubble velocities for air-water data for each tube.

$$U_{bubb} = C_K j^{1.05} \quad (D.5)$$

For each tube diameter, they empirically derived the constant C_K , which increased with decreasing tube diameter. They also observed that in smaller tube diameters, the distribution of the vapor became axi-symmetric as compared to the stratified nature of the vapor bubbles in larger tubes. In some of the larger diameter tube data, the vapor bubble velocity was actually less than that of the volumetric flux. They attributed this to the large vapor bubbles stratifying in the large diameter tubes and "sticking" to the tube surface. These two key observations were also seen in the present study. Therefore, Equation D.5 is used as the basis for predicting the measured vapor bubble velocity from the present study.

The vapor bubble velocity for all intermittent for $D = 0.508, 1.00,$ and 3.00 mm were obtained from the high-speed video frame analysis in the present study. Whenever a vapor bubble appeared during the analysis, the velocity was measured until the vapor bubble exited the field of view and an average of all of the measured velocities for that individual vapor bubble was calculated. Typically, at least five measurements of the velocity of a vapor bubble were taken. For many of the analyses, several vapor bubbles were present throughout the 500 frames analyzed. The number of vapor bubbles for each frame range from 2 to 52. For each analysis conducted at a specific operating condition, all of the vapor bubble velocity averages are averaged. This overall average of all the

vapor bubbles is the representative value for vapor bubble velocity for a specific operating condition. These vapor bubble velocities are compared to the volumetric flux in Figure D.2. Average vapor bubble velocity follows a similar trend to that observed by Fukano and Kariyasaki (1993) with respect to diameter. This is can be observed by comparing the 3.00 and 0.508 mm diameter tube data. The 3.00 mm diameter data are in general less than 20% of the volumetric flux, while the 0.508 mm data are close to 20% greater. The vapor bubble velocities for 3.00 mm diameter tube data are typically less than the total volumetric flux. This may be because the top portion of the vapor bubble is slowed down by the thin film, while a major portion of the liquid flows underneath in the stratified fluid region pulling the vapor bubble in the direction of the flow. Therefore, it is clear that there is an influence of tube diameter on the parameter C_K from Equation D.5. As a result, a correlation for vapor bubble velocity was developed for data from the present study as follows.

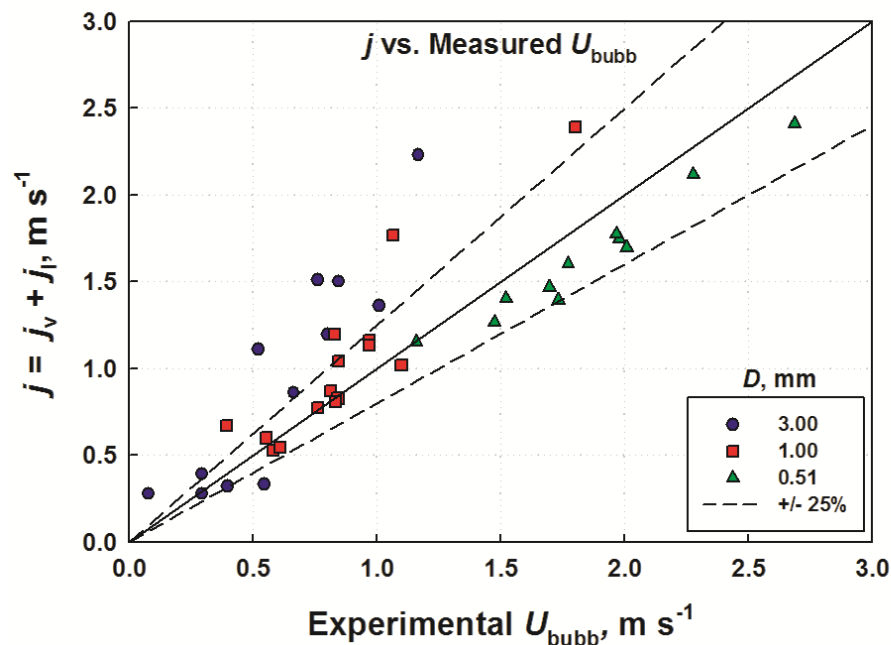


Figure D.2: Plot of Measured Vapor Bubble Velocity, U_{bubble} , as Compared to Volumetric Flux, j

The relative importance of surface tension to gravitational forces changes in the range of tube diameters examined in this study. This is observed visually with stratification occurring during condensation in the 3.00 mm tubes during intermittent and stratified-annular flow, but not being seen in the 1.00 mm and 0.508 mm diameter tube data. The Bond number expresses the ratio of surface tension to gravitational forces, and can be used to differentiate between the C_K values for the different tube diameters. A comparison of Bond number versus measured vapor bubble velocity is shown in Figure D.3 for all intermittent flow data from the present study.

For each tube diameter, there is a variation in Bond number as a result of property variations for each saturation temperature under consideration. For example, at $T_{\text{sat}} = 60^\circ\text{C}$, $D = 3.00$ mm, the Bond number is over 60 while for $T_{\text{sat}} = 30^\circ\text{C}$, $D = 3.00$ mm, the Bond number is about 25. The variation in Bond number due to fluid properties is lower at smaller diameters, because the diameter contribution dominates. The relative effects of

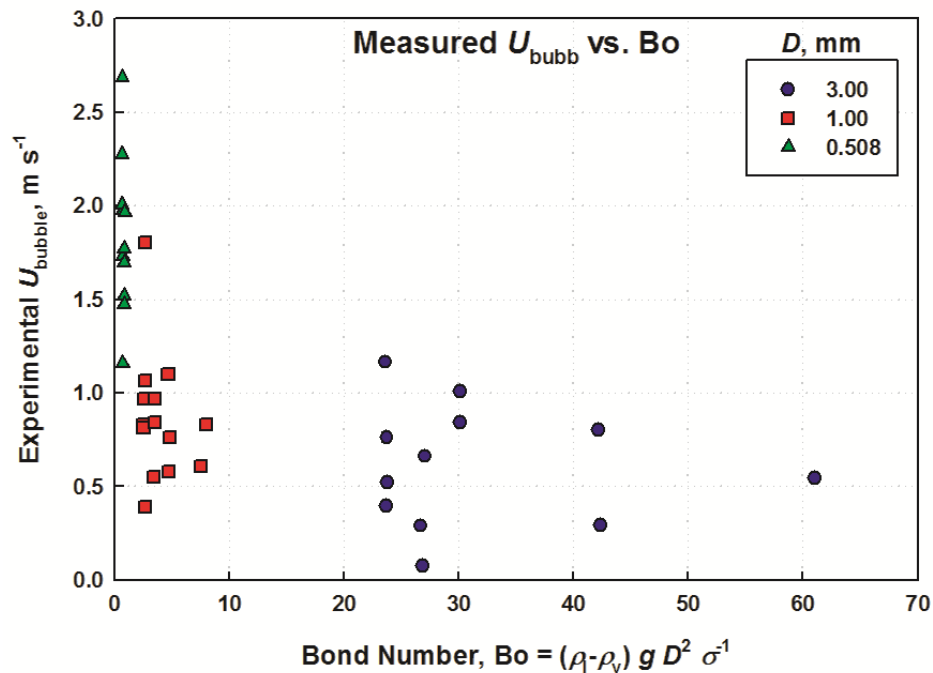


Figure D.3: Bond Number Versus U_{bubble}

these forces are important in determining the local vapor-liquid distribution within the tube where a vapor bubble is present. As Bond number decreases, the vapor bubble becomes axi-symmetric, resulting in a thin film of constant thickness surrounding the bubble. As Bond number increases, the vapor bubble becomes stratified with unequal film thickness axially, and in general resulting in longer, slower moving vapor bubbles.

In the case of small tube diameter data ($D = 1.00, 0.508$ mm) where the vapor bubble is axi-symmetric, the vapor bubble must “push” the liquid slug out of the center of the tube and along the edges of the vapor bubble. The “pushing” requires an inertial displacement of the liquid slug while the thin film induces a viscous drag along the bubble edges. A series of photographs and a schematic of the vapor bubble and liquid slug interactions are shown in Figure D.4. The vapor bubble in this case is traveling faster than the liquid slug. The tail of the liquid slug is shed around the nose of the vapor bubble into the liquid film. If the slug and vapor lengths are stable, an equal portion of liquid enters the slug from the liquid film at the tail end of the vapor bubble. Similarly, in the large tube, the lower stratified liquid “pulls” on the vapor bubble and is opposed by viscous forces in the thin film coating the top surface of the bubble and the momentum loss in the displacement of the liquid slug. A series of photographs and a schematic of the vapor bubble and liquid slug interactions in the 3.00 mm diameter tube are shown in Figure D.5. The stratification of the vapor bubble in the large tube is evident and the tail of the vapor bubble exhibits a more gradual shape. In both cases, the motion of the bubble in the liquid phase can be thought of as being similar to that of an object in submerged flow. Drag coefficients for such scenarios are dependent on the fluid Reynolds number. The liquid Reynolds number dependence can be seen in the vapor bubble velocity data as shown in Figure D.6.

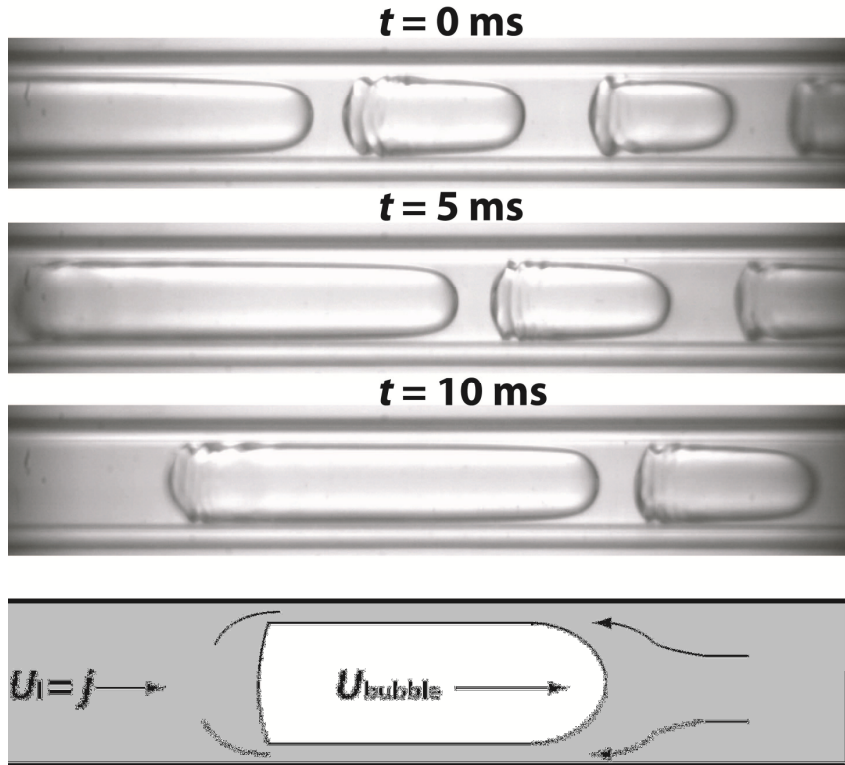


Figure D.4: Photographs and Schematic of Vapor Bubble and Liquid Slug Interactions in the Small Diameter Tubes ($D = 0.508, 1.00$ mm)

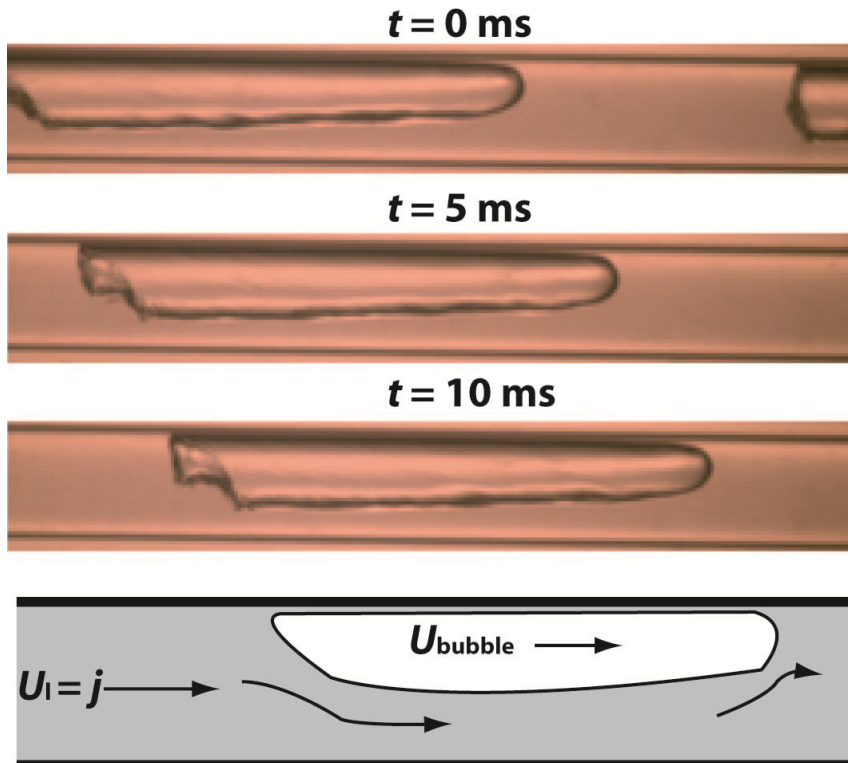


Figure D.5: Photographs and Schematic of Vapor Bubble and Liquid Slug Interactions for the Large Diameter Tube ($D = 3.00$ mm)

There are distinct, almost linear, trends in the measured bubble velocity as a function of the liquid Reynolds number, as would be expected with the idealization of the vapor bubble as an object submerged in a fluid flow. This diameter influence can be related to the Bond number, leading to the following expression for vapor bubble velocity as a function of the total volumetric flux. Therefore, C_K (Equation D.5) can be modeled with a dependence on the Bond number and liquid Reynolds number.

$$U_{bubb} = a \cdot \underbrace{Bo^b \cdot Re_l^c}_{C_K} \cdot j \quad (D.6)$$

This formulation accounts for the relative influence of surface tension and gravitational forces, and the drag between the bubble and the liquid. A regression analysis was conducted to determine the best fit for the empirical constants in Equation D.6.

$$U_{bubb} = 2.4 \cdot Bo^{-0.132} \cdot Re_l^{-0.105} \cdot j \quad (D.7)$$

The AAD and AD for all measured bubble velocities was 13.8 and 2.8% respectively.

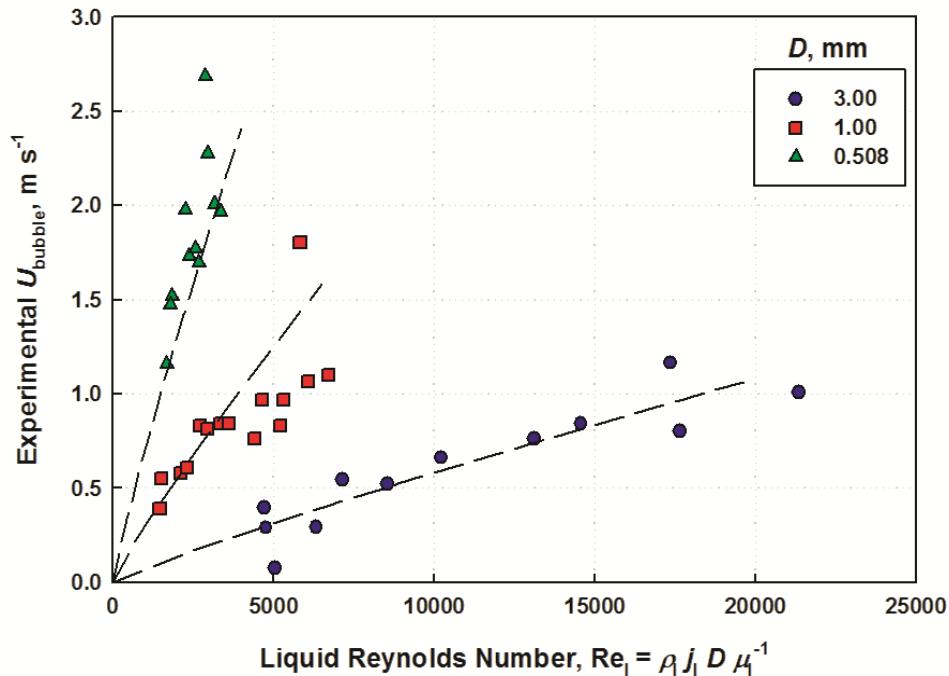


Figure D.6: Liquid Reynolds Number Versus Measured U_{bubble}

Liquid Reynolds numbers ranged from $1464 < Re_1 < 21367$, while Bond numbers ranged from $0.67 < Bo < 61.01$.

It was not possible to measure film or interface velocities from the high speed video data; therefore, an analytical solution is required to approximate the pressure drop in the film/bubble region. The interfacial velocity, $U_{interface}$, can be deduced based on a shear balance at the interface as presented by Garimella *et al.* (2002) as follows:

$$\tau_{interface} = \mu_l \left(\frac{du_{film}}{dr} \right)_{r=R_{bubble}} = \tau_{bubble} (r = R_{bubble}) \quad (D.8)$$

Assuming that the vapor bubble is driven solely by the pressure gradient, the shear stress in the vapor bubble can be predicted by:

$$\tau_{bubble} (r = R_{bubble}) = -\frac{R_{bubble}}{2} \left(\frac{dp}{dx} \right)_{f/b} \quad (D.9)$$

The velocity profile in the liquid film can be modeled as combined Couette-Poiseuille flow through an annulus. The resulting velocity profile and shear stress is:

$$u_{film}(r) = \frac{-\left(\frac{dp}{dx}\right)_{f/b}}{4\mu_l} \left[R_{tube}^2 - r^2 - (R_{tube}^2 - R_{bubble}^2) \frac{\ln(R_{tube}/r)}{\ln(R_{tube}/R_{bubble})} \right] + U_{interface} \frac{\ln(R_{tube}/r)}{\ln(R_{tube}/R_{bubble})} \quad (D.10)$$

$$\tau_{interface} = \frac{-\left(\frac{dp}{dx}\right)_{f/b}}{4} \left[-2R_{bubble} - (R_{tube}^2 - R_{bubble}^2) \frac{R_{tube}/R_{bubble}}{\ln(R_{tube}/R_{bubble})} \right] + U_{interface} \mu_l \frac{R_{tube}/R_{bubble}}{\ln(R_{tube}/R_{bubble})} \quad (D.11)$$

Setting Equation D.9 and D.10 equal and solving for interfacial velocity yields:

$$U_{interface} = \frac{-\left(\frac{dp}{dx}\right)_{f/b}}{4\mu_l} (R_{tube}^2 - R_{bubble}^2) \quad (D.12)$$

The average film velocity will be half of the interfacial velocity for laminar flow, $U_{film} = U_{interface}/2$. The frictional pressure drop per unit length along the length of the vapor bubble can be deduced by:

$$\left(\frac{dp}{dx}\right)_{f/b} = f_{film} \frac{\rho_v (U_{bubble} - U_{interface})^2}{4R_{bubble}} \quad (D.13)$$

The film friction factor, f_{film} , is calculated by the Churchill (1977) friction factor (Equation D.3) with the film Reynolds number, $Re_{film} = \rho_l U_{film} (D - D_{bubble}) \mu_l^{-1}$. The interfacial velocity, $U_{interface}$, and vapor bubble-film frictional pressure drop, $(dP/dz)_{f/b}$, have to be deduced iteratively. All vapor bubble conditions but one ($Re_{bubble} = 1571$) in this study were turbulent, with vapor bubble Reynolds numbers ranging from $2269 < Re_{bubble} < 10717$ while all liquid films were found to be laminar with $18.5 < Re_{film} < 848.6$.

The model for the pressure drop during the transition of liquid from the slug to the film region and the transition from the film to the liquid slug downstream is based on the work of Dukler and Hubbard (1975) similar to the approach of Garimella *et al.* (2002). They hypothesized that the difference in velocities in the liquid film and slug result in a significant mixing region at the tail end of the vapor bubble resulting in significant pressure losses and a flat bubble tail. Upstream of the bubble, the vapor overtakes the liquid slug and liquid is shed uniformly from the faster moving liquid slug to the slower moving liquid film surrounding the vapor bubble. They developed the following equation for transitional pressure loss based on these considerations.

$$\Delta P_{tran} = \rho_l \left[1 - \left(\frac{R_{bubble}}{R_{tube}} \right)^2 \right] (U_{bubble} - U_{film})(U_{slug} - U_{film}) \quad (D.14)$$

The first three terms represents the amount of mass gained in the liquid slug from the film and the last term is related to the relative velocity between the slug and film regions.

A relation for vapor bubble radius, R_{bubble} , and unit cell component lengths, L_{UC} , L_{bubble} , L_{slug} , is needed to provide closure to the pressure drop model. Garimella *et al.* (2002) found that the ratio of bubble diameter to tube diameter varied from 0.899 to 0.911 and estimated the ratio as 0.9 for simplicity. Chung and Kawaji (2004) also approximated bubble radius as 90% of the tube radius. The bubble diameter in most cases was observed to be smaller than this for the data in the present study. The diameter observed in the present study was not appreciably influenced by mass flux or quality, but only by fluid properties. Once the flow begins to transition to intermittent flow, vapor bubbles form with a set bubble diameter, which did not change appreciably as quality decreases. Therefore, determining the bubble diameter at the onset of intermittent flow can define the bubble diameter throughout the rest of the condensation process until bubble flow/dispersed flow is achieved. For the analysis, the vapor bubble is approximated as having a circular cross section, with the local void fraction of the vapor bubble, α_{bubble} used to approximate the bubble radius. The local void fraction can be calculated using the void fraction model developed in the previous section (Equation 7.16 and 7.17) using a transition quality, x_{tran} . The transition quality is predicted based on the minimum amount of liquid required for the intermittent regime to exist (Barnea *et al.*, 1983) which corresponds to a Martinelli parameter of $X_{slug} = 0.3521$. The transitional quality, x_{tran} , can be deduced by evaluating the Martinelli parameter for the slug:

$$X_{slug} = 0.3521 = \left(\frac{\rho_v}{\rho_l} \right)^{0.5} \left(\frac{\mu_l}{\mu_v} \right)^{0.1} \left(\frac{1 - x_{tran}}{x_{tran}} \right)^{0.9} \quad (D.15)$$

The local void fraction, α_{bubble} , can be evaluated using Equations 7.16 and 7.17 with the transitional quality, x_{tran} to predict the vapor bubble radius.

$$R_{\text{bubble}} = \sqrt{\alpha_{\text{bubble}}} R_{\text{tube}} \quad (\text{D.16})$$

The bulk void fraction, α , and vapor bubble radius, R_{bubble} , can be used to deduce the ratio of vapor bubble length, L_{bubble} , to the unit cell length, L_{UC} based on a simple cylindrical geometry idealization.

$$\alpha = \left(\frac{L_{\text{bubble}}}{L_{\text{UC}}} \right) \left(\frac{R_{\text{bubble}}}{R_{\text{tube}}} \right)^2 \quad (\text{D.17})$$

The frictional components of Equation D.1 can be predicted; however, the length of a unit cell is required to predict the effects of the transitional component. The prediction of unit cell length, L_{UC} , is predicted empirically based on the approach of Garimella *et al.* (2002).

$$\frac{L_{\text{UC}}}{D_h} = A \cdot Bo^b \cdot Re_{\text{slug}}^c \quad (\text{D.18})$$

A regression analysis was conducted using the pressure drop data to determine the best fit for these parameters. Predicting the unit cell length using measured frequencies from the high speed video data was attempted, but due to the stochastic nature of the process, it was not possible to correlate the measured values accurately. Therefore, pressure drop data from the present study were used instead of slug frequency data. This is similar to the approach used by Garimella *et al.* (2002). The empirical constants were found to be $A = 0.19$, $b = -0.3353$, and $c = 0.418$. The length of the unit cell, L_{UC} , and vapor bubble ratio for Equation D.17 are used to determine the lengths of each component and provide the remaining values for the intermittent pressure drop model.

D.2 Transition Region

The transition region from Intermittent to Annular or Wavy Flow is predicted using a linear interpolation between the pressure drop models predicted at the two transition conditions. The transition conditions are predicted using the vapor Weber number. Nema (2007) found that the transition from intermittent flow to intermittent-annular or intermittent-wavy occurred in the range of $6 < We_v < 35$. The beginning of the transition region is predicted at $We_v = We_{tran,cvc} = 35$, and the transition to intermittent flow is predicted at $We_v = We_{tran,int} = 6$. Figure D.7 shows the general range over which the transition region typically occurs. The pressure drop within this region is then predicted by:

$$\left(\frac{dp}{dz}\right)_f = \left(\frac{We_{tran,cvc} - We_v}{We_{tran,cvc} - We_{tran,int}}\right)\left(\frac{dp}{dz}\right)_{f,int,tran} + \left(\frac{We_v - We_{tran,int}}{We_{tran,cvc} - We_{tran,int}}\right)\left(\frac{dp}{dz}\right)_{f,cvc,tran} \quad (D.19)$$

The pressure drop $(dP/dz)_{f,int,tran}$ is calculated using Equation D.1 for $We_{tran,int}$ and $(dP/dz)_{f,cvc,tran}$ is calculated using Equation 7.21 for $We_{tran,cvc}$.

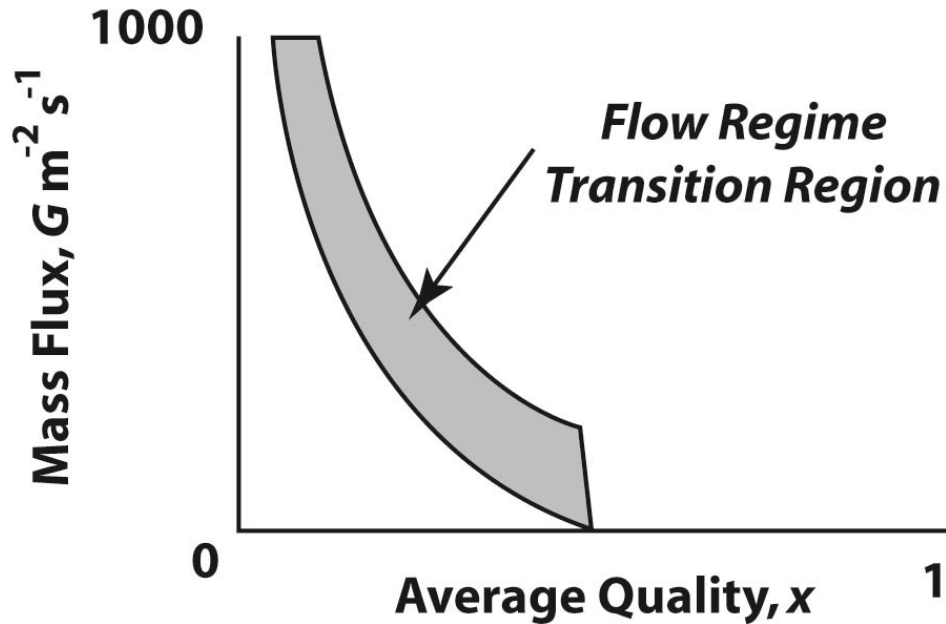


Figure D.7: Typical Transition Region for Interpolation Between Intermittent and Annular or Wavy Flow

D.3 Summary

The pressure drops predicted using the intermittent and transition region model described in Appendix D compared with the measured values are summarized for each flow regime in Table D.1. The agreement in the intermittent, annular-intermittent, and discrete wave-intermittent regimes is better compared to that achieved using only the annular or wavy flow regime models, respectively. However, when comparing the overall statistics of the two models, using the annular and wavy flow model presented in Chapter 7 results in an AAD and AD of 12.7% and 1.3%, respectively, and 85.5% of the data are predicted within 25%. The model presented here in Appendix D predicts the entire data set with an AAD and AD of 12.5% and -0.9%, respectively, and predicts 86.9% of the data within 25%. Therefore, the additional accuracy of the intermittent model does not warrant the added complexity for predicting pressure drop for the data in the present study. More intermittent flow regime data are needed for validation and refinement of the model.

Table D.1: Pressure Drop Model Predictions by Flow Regime

Regime	AAD %	AD %	Data < 25% Deviation
Intermittent	17.5	2.5	75.0
Annular-Intermittent	9.8	-0.5	100.0
Discrete-Intermittent	21.3	4.1	76.7
Discrete Wave	14.8	1.4	86.4
Disperse Wave	11.3	3.2	87.9
Annular Film	11.8	-2.8	86.2
Mist	11.4	2.3	92.2
Total	12.5	-0.9	86.9

APPENDIX E - VOID FRACTION MODEL

Data Point	
$P_{r, \text{test}}$ (kPa)	1884
P_{critical} (kPa)	3729
P_r	0.505
G (kg/m ² -s)	804
$x_{r, \text{test, avg}}$	0.19
$T_{r, \text{sat}}$ (°C)	41.23
Exp. Date	4 Aug 11
Exp. Run	91
$\alpha_{\text{exper.}}$ (-)	0.4989
$\nabla P_{\text{exper.}}$ (kPa/m)	85.97
D (mm)	0.5083
Fluid	R404A

Condensation Void Fraction Model		
Inputs	Equations	Results
Variables and Properties		
$D = 0.5083 \text{ mm}$ $P_{r, \text{test}} = 1884 \text{ kPa}$ $G = 804 \text{ kg/m}^2\text{-s}$ $x_{r, \text{test, avg}} = 0.19$ $T_{r, \text{sat}} = 41.23^\circ\text{C}$	$\rho_1, \mu_1 = f(x_{r, \text{avg}}, P_{r, \text{test}})$	$\rho_1 = 957 \text{ kg/m}^3$ $\mu_1 = 1.02 \times 10^{-4} \text{ kg/m-s}$
	$\rho_v, \mu_v = f(x_{r, \text{avg}}, P_{r, \text{test}})$	$\rho_v = 105 \text{ kg/m}^3$ $\mu_v = 1.60 \times 10^{-5} \text{ kg/m-s}$
	$\sigma = f(P_{r, \text{test}})$	$\sigma = 2.37 \times 10^{-3} \text{ N/m}$
	$Re_1 = \frac{(1-x)GD}{\mu_1}$	$Re_1 = 3237$
	$Re_v = \frac{xGD}{\mu_v}$	$Re_v = 4880$
	$Ca_1 = \frac{\mu_1(1-x)G}{\rho_1\sigma}$	$Ca_1 = 0.0293$
	$j_1 = \frac{(1-x)G}{\rho_1}$	$j_1 = 0.682 \text{ m/s}$
	$j_v = \frac{xG}{\rho_v}$	$j_v = 1.71 \text{ m/s}$
	$j = j_1 + j_v$	$j = 2.39 \text{ m/s}$
	$\beta = \frac{j_v}{j_1 + j_v}$	$\beta = 0.7145$
Martinelli Parameter Calculation		
$D = 0.5083 \text{ mm}$ $G = 804 \text{ kg/m}^2\text{-s}$ $x_{r, \text{test, avg}} = 0.19$ $\rho_1 = 957 \text{ kg/m}^3$ $\rho_v = 105 \text{ kg/m}^3$ $Re_1 = 3237$ $Re_v = 4880$	if : $Re < 2000$ $n = 1$ $B = 16$ if : $Re \geq 2000$ $n = 0.25$ $B = 0.079$	$n_1 = 0.25$ $B_1 = 0.079$ $n_v = 0.25$ $B_v = 0.079$
	$f = B \cdot Re^n$	$f_1 = 0.0105$ $f_v = 0.0095$
	$(dP/dz)_{v,1} = \frac{2 \cdot f_{v,1} \cdot j_{v,1}^2}{\rho_{v,1} D}$	$(dP/dz)_v = 4187 \text{ Pa/m}$ $(dP/dz)_1 = 9093 \text{ Pa/m}$

Condensation Void Fraction Model		
Inputs	Equations	Results
	$X = \left[\frac{(dP/dz)_l}{(dP/dz)_v} \right]^{1/2}$	$X = 1.474$
Drift Flux Calculation		
$X = 1.474$ $\rho_l = 957 \text{ kg/m}^3$ $\rho_v = 105 \text{ kg/m}^3$ $Ca_1 = 0.0293$ $j = 2.39 \text{ m/s}$ $\beta = 0.7145$	$\bar{V}_{vj} = 0.3355 \cdot X^{0.2492} \cdot Ca_1^{0.1535} \cdot \left(\sqrt{\frac{\rho_l}{\rho_v}} - 1 \right)^{0.809} \cdot j$	$\bar{V}_{vj} = 0.811 \text{ m/s}$
	$\alpha = \frac{\beta}{1 + \bar{V}_{vj}/j}$	$\alpha = 0.4953$
	$Error = \frac{\alpha_{exp} - \alpha}{\alpha_{exp}}$	$Error = 1\%$

APPENDIX F - CONDENSATION HEAT TRANSFER AND PRESSURE DROP MODELS

Annular Data Point	
$P_{r, test}$ (kPa)	1460
$P_{critical}$ (kPa)	3729
p_r	0.393
G (kg/m ² -s)	806
$x_{r, test, avg}$	0.85
$T_{r, sat}$ (°C)	31.16
T_{wall} (°C)	24.3
Exp. Date	16 Sep 10
Exp. Run	55
h_{exp} (W/m ² -K)	10882
$(dP/dz)_{exp}$ (kPa/m)	31.63
D (mm)	3.048
Fluid	R404A

Wavy Data Point	
$P_{r, test}$ (kPa)	1421
$P_{critical}$ (kPa)	3729
p_r	0.381
G (kg/m ² -s)	200.4
$x_{r, test, avg}$	0.3254
$T_{r, sat}$ (°C)	29.92
T_{wall} (°C)	23.1
Exp. Date	18 Sep 10
Exp. Run	13
h_{exp} (W/m ² -K)	2793
$(dP/dz)_{exp}$ (kPa/m)	1.401
D (mm)	3.048
Fluid	R404A

Annular - Rect. Data Point (Fronk and Garimella, 2010)	
$P_{r, test}$ (kPa)	6460
$P_{critical}$ (kPa)	7378
p_r	0.876
G (kg/m ² -s)	392.8
$x_{r, test, avg}$	0.72
$T_{r, sat}$ (°C)	25.17
T_{wall} (°C)	NA
Exp. Date	NA
Exp. Run	NA
h_{exp} (W/m ² -K)	14867
$(dP/dz)_{exp}$ (kPa/m)	NA
D (mm)	0.160
Fluid	CO ₂

Intermittent Data Point	
$P_{r, test}$ (kPa)	1418
$P_{critical}$ (kPa)	3729
p_r	0.38
G (kg/m ² -s)	213
$x_{r, test, avg}$	0.1762
$T_{r, sat}$ (°C)	29.92
T_{wall} (°C)	NA
Exp. Date	14 July 11
Exp. Run	155
h_{exp} (W/m ² -K)	NA
$(dP/dz)_{exp}$ (kPa/m)	5.95
D (mm)	1.0
Fluid	R404A

Condensation Pressure Drop and Heat Transfer Models		
Inputs	Equations	Results
Variables and Properties - Annular		
$P_{r, \text{test}} = 1460 \text{ kPa}$ $G = 806 \text{ kg/m}^2\text{-s}$ $x_{r, \text{test, avg}} = 0.85$ $T_{r, \text{sat}} = 31.2 \text{ }^\circ\text{C}$ $D = 3.048 \text{ mm}$	$\rho_1, \mu_1, Pr_1, c_{p,1}, k_1, i_{fg} = f(x_{r, \text{avg}}, P_{r, \text{test}})$	$\rho_1 = 1013 \text{ kg/m}^3$ $\mu_1 = 1.18 \times 10^{-4} \text{ kg/m-s}$ $Pr_1 = 3.03$ $c_{p,1} = 1.603 \text{ kJ/kg-K}$ $k_1 = 0.0624 \text{ W/m-K}$ $i_{fg} = 132.6 \text{ kJ/kg}$
	$\rho_v, \mu_v = f(x_{r, \text{avg}}, P_{r, \text{test}})$	$\rho_v = 78.22 \text{ kg/m}^3$ $\mu_v = 1.50 \times 10^{-5} \text{ kg/m-s}$
	$\sigma = f(P_{r, \text{test}})$	$\sigma = 3.37 \times 10^{-3} \text{ N/m}$
	$Re_1 = \frac{(1-x)G \cdot D}{\mu_1}$	$Re_1 = 3081$
	$Re_v = \frac{x \cdot G \cdot D}{\mu_v}$	$Re_v = 139935$
	$Ca_1 = \frac{\mu_1(1-x)G}{\rho_1 \cdot \sigma}$	$Ca_1 = 0.00411$
	$We_v = \frac{(x \cdot G)^2 D}{\rho_v \cdot \sigma}$	$We_v = 5450$
	$Fr_{\text{mod}} = \frac{G \cdot x}{\sqrt{D \cdot g \cdot \rho_v (\rho_1 - \rho_v)}}$	$Fr_{\text{mod}} = 14.69$
	$j_1 = \frac{(1-x)G}{\rho_1}$	$j_1 = 0.118 \text{ m/s}$
	$j_v = \frac{xG}{\rho_v}$	$j_v = 8.78 \text{ m/s}$

Condensation Pressure Drop and Heat Transfer Models		
Inputs	Equations	Results
	$j = j_1 + j_v$	$j = 8.90 \text{ m/s}$
	$\beta = \frac{j_v}{j_1 + j_v}$	$\beta = 0.9868$
	$X = \left[\frac{(dP/dz)_1}{(dP/dz)_v} \right]^{1/2}$	$X = 0.07763$
	$\bar{V}_{vj} = 0.3355 \cdot X^{0.2492} \cdot C a_1^{0.1535} \cdot \left(\sqrt{\frac{\rho_1}{\rho_v}} - 1 \right)^{0.809} \cdot j$	$\bar{V}_{vj} = 1.471 \text{ m/s}$
	$\alpha = \frac{\beta}{1 + \bar{V}_{vj}/j}$	$\alpha = 0.85$
	$U_1 = \frac{j_1}{1 - \alpha}$	$U_1 = 0.7672 \text{ m/s}$
	$U_v = \frac{j_v}{\alpha}$	$U_v = 10.37 \text{ m/s}$
	$Re_{1\alpha} = \frac{(1-x)GD}{\mu_1(1+\alpha^{0.5})}$	$Re_{1\alpha} = 1605$
	$f_{1v} = 8 \cdot \left[\frac{\left(\frac{8}{Re_{1v}} \right)^{12} + \left(2.457 \cdot \ln \left(\frac{1}{\left(\frac{7}{Re_{1v}} \right)^{0.9} + 0.27 \cdot (\epsilon/D)} \right) \right)^{16} + (37530 / Re_{1v})^{16}}{\left(\left(\frac{8}{Re_{1v}} \right)^{12} + \left(2.457 \cdot \ln \left(\frac{1}{\left(\frac{7}{Re_{1v}} \right)^{0.9} + 0.27 \cdot (\epsilon/D)} \right) \right)^{16} + (37530 / Re_{1v})^{16} \right)^{-1.5}} \right]^{1/12}$	$f_1 = 0.0399$

Condensation Pressure Drop and Heat Transfer Models		
Inputs	Equations	Results
Pressure Drop Model - Annular		
$X = 0.07763$ $Re_{l\alpha} = 1605$ $Ca_1 = 0.00411$ $\alpha = 0.85$ $\rho_l = 1013 \text{ kg/m}^3$ $\rho_v = 78.22 \text{ kg/m}^3$ $f_l = 0.0399$ $D = 3.048 \text{ mm}$ $j_v = 8.78 \text{ m/s}$ $\left(\frac{dP}{dz}\right)_{exp} =$ 31.63 kPa/m	$f_i = A \cdot X^a \cdot Re_{l\alpha}^b \cdot \left(\frac{Ca_1}{1-\alpha}\right)^c \cdot \left(\frac{\rho_l}{\rho_v}\right)^d \cdot f_l$ <p>for : $Re_{l\alpha} < 2000$ $A = 0.0007, a = 0.481, b = 0.9115$ $c = -0.2582, d = 0.1007$</p>	$f_i = 0.02248$
	$\left(\frac{dP}{dz}\right)_f = \frac{1}{2} f_i \cdot \rho_v \cdot j_v^2 \cdot \alpha^{-2.5} \cdot D^{-1}$	$\left(\frac{dP}{dz}\right)_f = 33.7 \text{ kPa/m}$
	$Error = \frac{\left(\frac{dP}{dz}\right)_{f,exp} - \left(\frac{dP}{dz}\right)_f}{\left(\frac{dP}{dz}\right)_{f,exp}}$	$Error = 6.5\%$
Heat Transfer Model - Annular		
$\alpha = 0.85$ $D = 3.048 \text{ mm}$ $Re_{l\alpha} = 1605$ $Pr_l = 3.03$ $k_l = 0.0624 \text{ W/m-K}$ $U_l = 0.7672 \text{ m/s}$ $U_v = 10.37 \text{ m/s}$ $h_{exp} = 10882 \text{ W/m}^2\text{-K}$	$\delta = \frac{D}{2} (1 - \sqrt{\alpha})$	$\delta = 1.216 \times 10^{-4} \text{ m}$
	$Nu = 0.0049 Re_{l\alpha}^{0.8} Pr_l^{0.4} \left[1 + \left(\frac{U_v}{U_l}\right)^{0.6933} \right]$	$Nu = 19.82$
	$h = \frac{Nu \cdot k_l}{\delta}$	$h = 10169 \text{ W/m}^2\text{-K}$
	$Error = \frac{h_{exp} - h}{h_{exp}}$	$Error = 6.6\%$
Variables and Properties - Wavy		
$P_{r, test} = 1421 \text{ kPa}$ $G = 200 \text{ kg/m}^2\text{-s}$ $x_{r, test, avg} = 0.3254$ $T_{r, sat} = 29.92^\circ \text{C}$ $D = 3.048 \text{ mm}$	$\rho_l, \mu_l, Pr_l, c_{p,l}, k_l, i_{fg} = f(x_{r, avg}, P_{r, test})$	$\rho_l = 1020 \text{ kg/m}^3$ $\mu_l = 1.20 \times 10^{-4} \text{ kg/m-s}$ $Pr_l = 3.03$ $c_{p,l} = 1.589 \text{ kJ/kg-K}$ $k_l = 0.0628 \text{ W/m-K}$ $i_{fg} = 134.2 \text{ kJ/kg}$

Condensation Pressure Drop and Heat Transfer Models		
Inputs	Equations	Results
	$\rho_v, \mu_v = f(x_{r, \text{avg}}, P_{r, \text{test}})$	$\rho_v = 75.43 \text{ kg/m}^3$ $\mu_v = 1.49 \times 10^{-5} \text{ kg/m-s}$
	$\sigma = f(P_{r, \text{test}})$	$\sigma = 3.50 \times 10^{-3} \text{ N/m}$
	$Re_1 = \frac{(1-x)G \cdot D}{\mu_1}$	$Re_1 = 3438$
	$Re_v = \frac{x \cdot G \cdot D}{\mu_v}$	$Re_v = 13313$
	$Ca_1 = \frac{\mu_1(1-x)G}{\rho_1 \cdot \sigma}$	$Ca_1 = 0.00454$
	$We_v = \frac{(x \cdot G)^2 D}{\rho_v \cdot \sigma}$	$We_v = 49.1$
	$Fr_{\text{mod}} = \frac{G \cdot x}{\sqrt{D \cdot g \cdot \rho_v (\rho_1 - \rho_v)}}$	$Fr_{\text{mod}} = 1.413$
	$j_1 = \frac{(1-x)G}{\rho_1}$	$j_1 = 0.133 \text{ m/s}$
	$j_v = \frac{xG}{\rho_v}$	$j_v = 0.865 \text{ m/s}$
	$j = j_1 + j_v$	$j = 0.997 \text{ m/s}$
	$\beta = \frac{j_v}{j_1 + j_v}$	$\beta = 0.8671$
	$X = \left[\frac{(dP/dz)_1}{(dP/dz)_v} \right]^{1/2}$	$X = 0.6683$
	$\bar{V}_{vj} = 0.3355 \cdot X^{0.2492} \cdot Ca_1^{0.1535} \cdot \left(\sqrt{\frac{\rho_1}{\rho_v}} - 1 \right)^{0.809} \cdot j$	$\bar{V}_{vj} = 0.2932 \text{ m/s}$
	$\alpha = \frac{\beta}{1 + \bar{V}_{vj}/j}$	$\alpha = 0.67$
	$U_1 = \frac{j_1}{1 - \alpha}$	$U_1 = 0.4018 \text{ m/s}$
	$U_v = \frac{j_v}{\alpha}$	$U_v = 1.29 \text{ m/s}$
	$Re_{1\alpha} = \frac{(1-x)GD}{\mu_1(1 + \alpha^{0.5})}$	$Re_{1\alpha} = 1890$

Condensation Pressure Drop and Heat Transfer Models		
Inputs	Equations	Results
	$f_{lv} = 8 \cdot \left[\left(\frac{8}{Re_{lv}} \right)^{12} + \left(\left(2.457 \cdot \ln \left(\frac{1}{(7/Re_{lv})^{0.9} + 0.27 \cdot (\epsilon/D)} \right) \right)^{16} \right)^{-1.5} + (37530/Re_{lv})^{16} \right]^{1/12}$	$f_l = 0.03385$
Pressure Drop Model - Wavy		
$X = 0.6683$ $Re_{l\alpha} = 1890$ $Fr_{mod} = 1.413$ $\alpha = 0.67$ $\rho_l = 1020 \text{ kg/m}^3$ $\rho_v = 75.43 \text{ kg/m}^3$ $f_l = 0.03385$ $D = 3.048 \text{ mm}$ $j_v = 0.865 \text{ m/s}$ $\left(\frac{dP}{dz} \right)_{exp} = 1.401 \text{ kPa/m}$	$f_i = A \cdot X^a \cdot Re_{l\alpha}^b \cdot Fr_{mod}^c \left(\frac{\rho_l}{\rho_v} \right)^d \cdot f_l$ for : $Re_{l\alpha} < 2000$ $A = 0.0001, a = 0.4773, b = 1.0566$ $c = 0.064, d = 0.6717$	$f_i = 0.04758$
	$\left(\frac{dP}{dz} \right)_f = \frac{1}{2} f_i \cdot \rho_v \cdot j_v^2 \cdot \alpha^{-2.5} \cdot D^{-1}$	$\left(\frac{dP}{dz} \right)_f = 1.197 \text{ kPa/m}$
	$Error = \frac{\left(\frac{dP}{dz} \right)_{f,exp} - \left(\frac{dP}{dz} \right)_f}{\left(\frac{dP}{dz} \right)_{f,exp}}$	$Error = 14.6\%$
Heat Transfer Model - Wavy		
$\alpha = 0.67$ $D = 3.048 \text{ mm}$ $Re_l = 3438$ $\rho_l = 1020 \text{ kg/m}^3$ $Pr_l = 3.03$ $c_{p,l} = 1.589 \text{ kJ/kg-K}$ $k_l = 0.0628 \text{ W/m-K}$ $i_{fg} = 134.2 \text{ kJ/kg}$ $\rho_v = 75.43 \text{ kg/m}^3$ $T_{r,sat} = 29.92 \text{ }^\circ\text{C}$ $T_{inner\ wall} = 23.1 \text{ }^\circ\text{C}$ $h_{exp} = 10882 \text{ W/m}^2\text{-K}$ $x_{r, test, avg} = 0.3254$	$(1-\alpha) = \left(1 - \frac{\theta}{2\pi} \right) - \frac{1}{2\pi} \sin(2\pi - \theta)$	$\theta = 3.689$
	$Ja_1 = \frac{c_{p,l} (T_{sat} - T_{inner\ wall})}{i_{fg}}$	$Ja_1 = 0.08124$
	$Ra = \frac{D^3 g \rho_l (\rho_l - \rho_v) c_{p,l}}{\mu_l k_l}$	$Ra = 5.65 \times 10^7$
	$Nu_{wavy} = \left(\frac{1.93}{2\pi} \right) (Ra [Ja_1^{-1} + 1])^{0.25} + 0.00666 Re_l^{0.8} Pr_l^{0.4} \left[1 + \left(\frac{x}{1-x} \right)^{0.7375} \left(\frac{\rho_l}{\rho_v} \right)^{0.7375} \right] \left(1 - \frac{\theta}{2\pi} \right)$	$Nu_{wavy} = 139.4$
	$h_{wavy} = \frac{Nu_{wavy} k_l}{D}$	$h_{wavy} = 2872 \text{ W/m}^2\text{-K}$
	$Error = \frac{h_{exp} - h_{wavy}}{h_{exp}}$	$Error = 2.8\%$

Condensation Pressure Drop and Heat Transfer Models		
Inputs	Equations	Results
Variables and Properties - Annular - Rectangular Geometry		
$P_{r, \text{test}} = 6460 \text{ kPa}$ $G = 393 \text{ kg/m}^2\text{-s}$ $x_{r, \text{test, avg}} = 0.72$ $T_{r, \text{sat}} = 25.2 \text{ }^\circ\text{C}$ $D_h = 0.160 \text{ mm}$	$\rho_1, \mu_1, Pr_1, c_{p,1}, k_1, i_{fg} = f(x_{r, \text{avg}}, P_{r, \text{test}})$	$\rho_1 = 707.9 \text{ kg/m}^3$ $\mu_1 = 5.67 \times 10^{-5} \text{ kg/m-s}$ $Pr_1 = 4.80$ $c_{p,1} = 5.994 \text{ kJ/kg-K}$ $k_1 = 0.0709 \text{ W/m-K}$ $i_{fg} = 118.4 \text{ kJ/kg}$
	$\rho_v, \mu_v = f(x_{r, \text{avg}}, P_{r, \text{test}})$	$\rho_v = 244.7 \text{ kg/m}^3$ $\mu_v = 2.02 \times 10^{-5} \text{ kg/m-s}$
	$\sigma = f(P_{r, \text{test}})$	$\sigma = 5.39 \times 10^{-4} \text{ N/m}$
	$Re_1 = \frac{(1-x)G \cdot D}{\mu_1}$	$Re_1 = 310.4$
	$Re_v = \frac{x \cdot G \cdot D}{\mu_v}$	$Re_v = 2241$
	$Ca_1 = \frac{\mu_1(1-x)G}{\rho_1 \cdot \sigma}$	$Ca_1 = 0.0164$
	$We_v = \frac{(x \cdot G)^2 D}{\rho_v \cdot \sigma}$	$We_v = 97.1$
	$Fr_{\text{mod}} = \frac{G \cdot x}{\sqrt{D \cdot g \cdot \rho_v (\rho_1 - \rho_v)}}$	$Fr_{\text{mod}} = 21.2$
	$j_1 = \frac{(1-x)G}{\rho_1}$	$j_1 = 0.155 \text{ m/s}$
	$j_v = \frac{xG}{\rho_v}$	$j_v = 1.16 \text{ m/s}$
	$j = j_1 + j_v$	$j = 1.31 \text{ m/s}$
	$\beta = \frac{j_v}{j_1 + j_v}$	$\beta = 0.882$
	$X = \left[\frac{(dP/dz)_1}{(dP/dz)_v} \right]^{1/2}$	$X = 0.4844$

Condensation Pressure Drop and Heat Transfer Models		
Inputs	Equations	Results
	$\bar{V}_{vj} = 0.3355 \cdot X^{0.2492} \cdot C a_1^{0.1535} \cdot \left(\sqrt{\frac{\rho_1}{\rho_v}} - 1 \right)^{0.809} \cdot j$	$\bar{V}_{vj} = 0.1465 \text{ m/s}$
	$\alpha = \frac{\beta}{1 + \bar{V}_{vj}/j}$	$\alpha = 0.793$
	$U_1 = \frac{j_1}{1 - \alpha}$	$U_1 = 0.7503 \text{ m/s}$
	$U_v = \frac{j_v}{\alpha}$	$U_v = 1.458 \text{ m/s}$
	$Re_{1\alpha} = \frac{(1-x)GD}{\mu_1(1+\alpha^{0.5})}$	$Re_{1\alpha} = 164.2$
	$Bo = \frac{(\rho_1 - \rho_v) g D^2}{\sigma}$	$Bo = 0.2159$
Heat Transfer Model - Annular - Rectangular Geometry		
$\alpha = 0.793$ $D = 0.160 \text{ mm}$ $Bo = 0.2159$ $Re_{1\alpha} = 164.2$ $Pr_1 = 4.8$ $k_1 = 0.07087 \text{ W/m-K}$ $U_1 = 0.7503 \text{ m/s}$ $U_v = 1.458 \text{ m/s}$ $h_{exp} = 14867 \text{ W/m}^2\text{-K}$	$\delta = \frac{D}{2} (1 - \sqrt{\alpha})$	$\delta = 8.764 \times 10^{-6} \text{ m}$
	$\delta_{eff} = \left(1 - 0.0247 \cdot Bo^{-0.4706} \cdot \left(\frac{U_v}{U_1} \right)^{1.0998} \right)$	$\delta_{eff} = 7.839 \times 10^{-6} \text{ m}$
	$Nu = 0.0049 Re_{1\alpha}^{0.8} Pr_1^{0.4} \left[1 + \left(\frac{U_v}{U_1} \right)^{0.6933} \right]$	$Nu = 1.403$
	$h = \frac{Nu \cdot k_1}{\delta_{eff}}$	$h = 12687 \text{ W/m}^2\text{-K}$
	$Error = \frac{h_{exp} - h}{h_{exp}}$	$Error = 14.7\%$
Variables and Properties - Intermittent		
$P_{r, test} = 1418 \text{ kPa}$ $G = 213 \text{ kg/m}^2\text{-s}$ $x_{r, test, avg} = 0.1762$ $T_{r, sat} = 29.92^\circ\text{C}$ $D = 1.0 \text{ mm}$	$\rho_1, \mu_1, Pr_1, c_{p,1}, k_1, i_{fg} = f(x_{r, avg}, P_{r, test})$	$\rho_1 = 1020 \text{ kg/m}^3$ $\mu_1 = 1.20 \times 10^{-4} \text{ kg/m-s}$ $Pr_1 = 3.03$ $c_{p,1} = 1.589 \text{ kJ/kg-K}$ $k_1 = 0.0628 \text{ W/m-K}$ $i_{fg} = 134.2 \text{ kJ/kg}$
	$\rho_v, \mu_v = f(x_{r, avg}, P_{r, test})$	$\rho_v = 75.43 \text{ kg/m}^3$ $\mu_v = 1.49 \times 10^{-5} \text{ kg/m-s}$
	$\sigma = f(P_{r, test})$	$\sigma = 3.5 \times 10^{-3} \text{ N/m}$

Condensation Pressure Drop and Heat Transfer Models		
Inputs	Equations	Results
	$Re_1 = \frac{(1-x)G \cdot D}{\mu_1}$	$Re_1 = 1466$
	$Re_v = \frac{x \cdot G \cdot D}{\mu_v}$	$Re_v = 2531$
	$Ca_1 = \frac{\mu_1(1-x)G}{\rho_1 \cdot \sigma}$	$Ca_1 = 0.00590$
	$We_v = \frac{(x \cdot G)^2 D}{\rho_v \cdot \sigma}$	$We_v = 5.35$
	$j_1 = \frac{(1-x)G}{\rho_1}$	$j_1 = 0.172 \text{ m/s}$
	$j_v = \frac{xG}{\rho_v}$	$j_v = 0.498 \text{ m/s}$
	$j = j_1 + j_v$	$j = 0.671 \text{ m/s}$
	$\beta = \frac{j_v}{j_1 + j_v}$	$\beta = 0.743$
	$X = \left[\frac{(dP/dz)_1}{(dP/dz)_v} \right]^{1/2}$	$X = 1.259$
	$\bar{V}_{vj} = 0.3355 \cdot X^{0.2492} \cdot Ca_1^{0.1535} \cdot \left(\sqrt{\frac{\rho_1}{\rho_v}} - 1 \right)^{0.809} \cdot j$	$\bar{V}_{vj} = 0.3734 \text{ m/s}$
	$\alpha = \frac{\beta}{1 + \bar{V}_{vj}/j}$	$\alpha = 0.547$
	$U_1 = \frac{j_1}{1 - \alpha}$	$U_1 = 0.3804 \text{ m/s}$
	$U_v = \frac{j_v}{\alpha}$	$U_v = 0.911 \text{ m/s}$
	$Bo = \frac{(\rho_1 - \rho_v) g D^2}{\sigma}$	$Bo = 2.646$
Pressure Gradient in Liquid Slug		
$U_1 = 0.3804 \text{ m/s}$ $D = 1.0 \text{ mm}$ $\rho_1 = 1020 \text{ kg/m}^3$	$U_{slug} = U_1 = \frac{j_1}{1 - \alpha}$	$U_{slug} = 0.3804 \text{ m/s}$
	$Re_{slug} = \frac{\rho_1 \cdot U_1 \cdot D}{\mu_1}$	$Re_{slug} = 3236$

Condensation Pressure Drop and Heat Transfer Models

Inputs	Equations	Results
$\mu_1 = 1.20 \times 10^{-4} \text{ kg/m-s}$	$f_{\text{slug}} = 8 \cdot \left[\left(\frac{8}{Re_{\text{slug}}} \right)^{12} + \left(\frac{2.457 \cdot \ln \left(\frac{1}{(7/Re_{\text{slug}})^{0.9} + 0.27 \cdot (\epsilon/D)} \right)}{\left((37530/Re_{\text{slug}})^{16} \right)} \right)^{16} \right]^{-1.5}$	$f_{\text{slug}} = 0.04303$
	$\left(\frac{dP}{dz} \right)_{\text{slug}} = \frac{1}{2} f_{\text{slug}} \cdot \rho_1 \cdot U_{\text{slug}}^2 \cdot D^{-1}$	$\left(\frac{dP}{dz} \right)_{\text{slug}} = 3174 \text{ Pa/m}$

Pressure Gradient in Vapor Bubble/Liquid Film

$Bo = 2.646$ $Re_1 = 1466$ $j = 0.671 \text{ m/s}$ $\rho_1 = 1020 \text{ kg/m}^3$ $\mu_1 = 1.20 \times 10^{-4} \text{ kg/m-s}$ $\rho_v = 75.43 \text{ kg/m}^3$ $\mu_v = 1.49 \times 10^{-5} \text{ kg/m-s}$ $D = 1.0 \text{ mm}$ $R_{\text{tube}} = 0.5 \text{ mm}$	$U_{\text{bubb}} = 2.394 Bo^{-0.1316} Re_1^{-0.1045} j$	$U_{\text{bubb}} = 0.6594 \text{ m/s}$	
	$X_{\text{slug}} = 0.3521 = \left(\frac{\rho_v}{\rho_1} \right)^{0.5} \left(\frac{\mu_1}{\mu_v} \right)^{0.1} \left(\frac{1-x_{\text{tran}}}{x_{\text{tran}}} \right)^{0.9}$	$x_{\text{tran}} = 0.4863$	
	$Ca_{1, \text{bubble}} = \frac{\mu_l (1-x_{\text{tran}}) G}{\rho_1 \cdot \sigma}$	$Ca_{1, \text{bubble}} = 0.00368$	
	$X_{\text{bubble}} = \left[\frac{\left(\frac{dP}{dz} \right)_l}{\left(\frac{dP}{dz} \right)_v} \right]_{x_{\text{tran}}}^{1/2}$	$X_{\text{bubble}} = 0.4089$	
	$j_{\text{bubble}} = \frac{x_{\text{tran}} G}{\rho_v} + \frac{(1-x_{\text{tran}}) G}{\rho_1}$	$j_{\text{bubble}} = 1.483 \text{ m/s}$	
	$\bar{V}_{\text{vj, bubble}} = 0.3355 \cdot X_{\text{bubble}}^{0.2492} \cdot Ca_{1, \text{bubble}}^{0.1535} \cdot \left(\sqrt{\frac{\rho_1}{\rho_v}} - 1 \right)^{0.809} \cdot j_{\text{bubble}}$	$\bar{V}_{\text{vj, bubble}} = 0.3734 \text{ m/s}$	
	$\alpha_{\text{bubble}} = \frac{\beta}{1 + \bar{V}_{\text{vj, bubble}} / j_{\text{bubble}}}$	$\alpha_{\text{bubble}} = 0.7409$	
	$R_{\text{bubble}} = \sqrt{\alpha_{\text{bubble}}} \frac{D}{2}$	$R_{\text{bubble}} = 0.43 \text{ mm}$	
	Solve Iteratively		
	$U_{\text{film}} = U_{\text{interface}} / 2$	$U_{\text{film}} = 0.0371 \text{ m/s}$	
$Re_{\text{bubble}} = \frac{\rho_v \cdot (U_{\text{bubble}} - U_{\text{interface}}) \cdot 2R_{\text{bubble}}}{\mu_v}$	$Re_{\text{bubble}} = 2560$		

Condensation Pressure Drop and Heat Transfer Models		
Inputs	Equations	Results
	$f_{\text{bubble}} = 8 \cdot \left[\left(\frac{8}{Re_{\text{bubble}}} \right)^{12} + \left(\left(2.457 \cdot \ln \left(\frac{1}{(7/Re_{\text{bubble}})^{0.9} + 0.27 \cdot (\epsilon/2R_{\text{bubble}})} \right) \right) \right)^{16} + (37530/Re_{\text{bubble}})^6 \right]^{-1.5}$	$f_{\text{film}} = 0.03658$
	$U_{\text{interface}} = \frac{(dP/dz)_{f/b}}{4\mu_1} (R_{\text{tube}}^2 - R_{\text{bubble}}^2)$	$U_{\text{interface}} = 0.0742 \text{ m/s}$
	$(dP/dz)_{f/b} = f_{\text{bubble}} \frac{\rho_v (U_{\text{bubble}} - U_{\text{interface}})}{4R_{\text{bubble}}}$	$(dP/dz)_{f/b} = 549 \text{ Pa/m}$
Transitional Pressure Drop		
$R_{\text{bubble}} = 0.4304 \text{ mm}$ $R_{\text{tube}} = 0.5 \text{ mm}$ $U_{\text{film}} = 0.0371 \text{ m/s}$ $U_{\text{bubb}} = 0.6594 \text{ m/s}$ $U_{\text{slug}} = 0.3804 \text{ m/s}$ $\rho_1 = 1020 \text{ kg/m}^3$	$\Delta P_{\text{tran}} = \rho_1 \left[1 - \left(\frac{R_{\text{bubble}}}{R_{\text{tube}}} \right)^2 \right] \cdot (U_{\text{bubble}} - U_{\text{film}}) (U_{\text{slug}} - U_{\text{film}})$ <p>(Dukler and Hubbard, 1975)</p>	$\Delta P_{\text{tran}} = 28.22 \text{ Pa}$
Overall Pressure Gradient		
$Bo = 2.646$ $Re_{\text{slug}} = 3236$ $\alpha = 0.793$ $R_{\text{bubble}} = 0.4304 \text{ mm}$	$\frac{L_{\text{UC}}}{D} = 0.19 \cdot Bo^{-0.3353} \cdot Re_{\text{slug}}^{0.418}$	$L_{\text{UC}} = 6.14 \text{ mm}$
	$\alpha = \left(\frac{L_{\text{bubble}}}{L_{\text{UC}}} \right) \left(\frac{R_{\text{bubble}}}{R_{\text{tube}}} \right)^2$	$L_{\text{bubble}} = 4.54 \text{ mm}$
	$L_{\text{UC}} = L_{\text{bubble}} + L_{\text{slug}}$	$L_{\text{slug}} = 1.61 \text{ mm}$
$R_{\text{tube}} = 0.5 \text{ mm}$ $\left(\frac{dP}{dz} \right)_{\text{slug}} = 3174 \text{ Pa/m}$ $\left(\frac{dP}{dz} \right)_{f/b} = 549 \text{ Pa/m}$ $\Delta P_{\text{tran}} = 28.22 \text{ Pa}$	$\left(\frac{dP}{dz} \right)_f = \left(\frac{dP}{dz} \right)_{f/b} \frac{L_{\text{bubble}}}{L_{\text{UC}}} + \left(\frac{dP}{dz} \right)_{\text{slug}} \frac{L_{\text{slug}}}{L_{\text{UC}}} + \Delta P_{\text{tran}} \frac{1}{L_{\text{UC}}}$	$(dP/dz)_f = 5831 \text{ Pa/m}$
	$\text{Error} = \frac{(dP/dz)_{f,\text{exp}} - (dP/dz)_f}{(dP/dz)_{f,\text{exp}}}$	$\text{Error} = 2\%$

REFERENCES

- Akers, W.W., Deans, H.A., Crosser, O.K., 1959. Condensation Heat Transfer within Horizontal Tubes. Chemical Engineering Progress Symposium Series 55 (29), 171-176.
- Andresen, U.C., 2007. Supercritical Gas Cooling and Near-Critical-Pressure Condensation of Refrigerant Blends In Microchannels, Mechanical Engineering. Georgia Institute of Technology, Atlanta.
- Armand, A.A., 1946. The Resistance During the Movement of a Two-Phase System in Horizontal Pipes. *Izv. Vses. Teplotekh. Inst.* 1, 16–23 (AERE-Lib/Trans 828).
- Baird, J.R., Fletcher, D.F., Haynes, B.S., 2003. Local condensation heat transfer rates in fine passages. *International Journal of Heat and Mass Transfer* 46 (23), 4453-4466.
- Baker, O., 1954. Simultaneous Flow of Oil and Gas. *Oil and Gas Journal* 53, 185-195.
- Bandhauer, T.M., 2002. Heat transfer in microchannel geometries during condensation of R-134a, Mechanical Engineering. Iowa State University, Ames, Iowa, p. 224.
- Bandhauer, T.M., Agarwal, A., Garimella, S., 2006. Measurement and Modeling of Condensation Heat Transfer Coefficients in Circular Microchannels. *Journal of Heat Transfer* 128 (10), 1050-1059.
- Barnea, D., Luninski, Y., Taitel, Y., 1983. Flow Pattern in Horizontal and Vertical Two Phase Flow in Small Diameter Pipes. 61 (5), 617.
- Baroczy, C.J., 1965. Correlation of Liquid Fraction in Two-Phase Flow with Applications to Liquid Metals. Chemical Engineering Progress Symposium Series 61 (57), 179-191.
- Baroczy, C.J., 1966. Systematic correlation for two-phase pressure drop. Chemical Engineering Progress Symposium Series 62 (64), 232-249.
- Blasius, H., 1908. Grenzschichten in Fluessigkeiten mit kleiner Reibung. *Zeitschrift fuer Mathematik und Physik* 56, 1-37.
- Breber, 1980. Prediction of Horizontal Tubeside Condensation of Pure Components Using Flow Regime Criteria. *Journal of Heat Transfer* 102 (3), 471-476.
- Butterworth, D., 1975. A Comparison of some Void-Fraction Relationships for Co-Current Gas-Liquid Flow. *International Journal of Multiphase Flow* 1 (6), 845-850.
- Canière, H., Joen, C.T., Willockx, A., Paepe, M.D., Christians, M., Rooyen, E.v., Liebenberg, L., Meyer, J.P., 2007. Horizontal two-phase flow characterization for small diameter tubes with a capacitance sensor. *Measurement Science and Technology* 18 (9), 2898.

Carey, V.P., 1992. Liquid-Vapor Phase-Change Phenomena : An Introduction to the Thermophysics of Vaporization and Condensation Processes in Heat Transfer Equipment. Hemisphere Pub. Corp., Washington, D.C.

Cavallini, A., Bortolin, S., Del Col, D., Matkovic, M., Rossetto, L., 2011. Condensation Heat Transfer and Pressure Losses of High- and Low-Pressure Refrigerants Flowing in a Single Circular Minichannel. *Heat Transfer Engineering* 32 (2), 90-98.

Cavallini, A., Censi, G., Col, D.D., Doretti, L., Longo, G.A., Rossetto, L., 2002. Condensation of Halogenated Refrigerants Inside Smooth Tubes. *HVAC&R Research* 8 (4).

Cavallini, A., Col, D.D., Doretti, L., Matkovic, M., Rossetto, L., Zilio, C., Censi, G., 2006a. Condensation in Horizontal Smooth Tubes: A New Heat Transfer Model for Heat Exchanger Design. *Heat Transfer Engineering* 27 (8), 31-38.

Cavallini, A., Del Col, D., Doretti, L., Matkovic, M., Rossetto, L., Zilio, C., 2005. A Model for Condensation Inside Minichannels, Proceedings of HT05 National Heat Transfer Conference. ASME, San Francisco.

Cavallini, A., Doretti, L., Matkovic, M., Rossetto, L., 2006b. Update on Condensation Heat Transfer and Pressure Drop inside Minichannels. *Heat Transfer Engineering* 27 (4), 74-87.

Cavallini, A., Zecchin, R., 1974. Dimensionless Correlation for Heat Transfer in Forced Convection Condensation, Proceedings of the 5th International Heat Transfer Conference, JSME, pp. 309-313.

Chexal, B., Lellouche, G., Horowitz, J., Healzer, J., 1992. A Void Fraction Correlation for Generalized Applications. *Progress in Nuclear Energy* 27 (4), 255-295.

Chisholm, D., 1967. A Theoretical Basis for the Lockhart-Martinelli Correlation for Two-Phase Flow. *International Journal of Heat and Mass Transfer* 10 (12), 1767-1778.

Chisholm, D., 1973a. Pressure Gradients Due to Friction During the Flow of Evaporating Two-Phase Mixtures in Smooth Tubes and Channels. *International Journal of Heat and Mass Transfer* 16, 347-358.

Chisholm, D., 1973b. Void Fraction during Two-Phase Flow. *Journal of Mechanical Engineering Science* 15 (3), 235-236.

Chisholm, D., 1983. Two-Phase Flow in Pipelines and Heat Exchangers. G. Godwin in Association with the Institution of Chemical Engineers, London ; New York.

Chung, P.M.Y., Kawaji, M., 2004. The effect of channel diameter on adiabatic two-phase flow characteristics in microchannels. *International Journal of Multiphase Flow* 30 (7-8), 735-761.

Chung, P.M.Y., Kawaji, M., Kawahara, A., Shibata, Y., 2004. Two-Phase Flow through Square and Circular Microchannels - Effects of Channel Geometry. *Journal of Fluids Engineering, Transactions of the ASME* 126 (4), 546-552.

Churchill, S.W., Chu, H.H.S., 1975. Correlating equations for laminar and turbulent free convection from a vertical plate. *International Journal of Heat and Mass Transfer* 18 (11), 1323-1329.

Coleman, J.W., Garimella, S., 1999. Characterization of Two-Phase Flow Patterns in Small Diameter Round and Rectangular Tubes. *International Journal of Heat and Mass Transfer* 42 (15), 2869-2881.

Coleman, J.W., Garimella, S., 2000a. Two-Phase Flow Regime Transitions in Microchannel Tubes: The Effect of Hydraulic Diameter. *American Society of Mechanical Engineers, Heat Transfer Division, (Publication) HTD* 366, 71-83.

Coleman, J.W., Garimella, S., 2000b. Visualization of Refrigerant Two-Phase Flow during Condensation, 34th National Heat Transfer Conference, paper NHTC2000-12115, Pittsburgh, Pennsylvania.

Coleman, J.W., Garimella, S., 2003. Two-Phase Flow Regimes in Round, Square and Rectangular Tubes during Condensation of Refrigerant R 134a. *International Journal of Refrigeration* 26 (1), 117-128.

Crawford, T., Weisman, J., 1984. Two-phase (vapor-liquid) flow pattern transitions in ducts of non-circular cross-section and under diabatic conditions. *International Journal of Multiphase Flow* 10 (3), 385-391.

Damianides, C., Westwater, J.W., 1988. Two phase flow patterns in a compact heat exchanger and in small tubes, *Proceedings of Second U.K. National Conference on Heat Transfer, Glasgow, Scotland*, pp. 1257-1268.

Dobson, M.K., Chato, J.C., 1998. Condensation in Smooth Horizontal Tubes. *Journal of Heat Transfer, Transactions ASME* 120 (1), 193.

Dukler, A.E., Hubbard, M.G., 1975. A Model for Gas-Liquid Slug Flow in Horizontal and Near Horizontal Tubes. *Industrial and Engineering Chemistry, Fundamentals* 14 (4), 337-347.

El Hajal, J., Thome, J.R., Cavallini, A., 2003. Condensation in Horizontal Tubes, Part 1: Two-Phase Flow Pattern Map. *International Journal of Heat and Mass Transfer* 46 (18), 3349-3363.

Friedel, L., 1979. Improved Friction Pressure Drop Correlation for Horizontal and Vertical Two Phase Flow. *3R International* 18(7), 485-491.

Fukano, T., Kariyasaki, A., 1993. Characteristics of Gas-Liquid Two-Phase Flow in a Capillary Tube. *Nuclear Engineering and Design* 141 (1-2), 59-68.

Fukano, T., Kariyasaki, A., Kagawa, M., 1989. Flow Patterns and Pressure Drop in Isothermal Gas-Liquid Concurrent Flow in a Horizontal Capillary Tube, Proceedings of the 1989 ANS National Heat Transfer Conference, Philadelphia, Pennsylvania, pp. 153-161.

Garimella, S., Agarwal, A., Coleman, J.W., 2003a. Two-Phase Pressure Drops in the Annular Flow Regime in Circular Microchannels, 21st IIR International Congress of Refrigeration. International Institute of Refrigeration, Washington, DC.

Garimella, S., Agarwal, A., Killion, J.D., 2005. Condensation Pressure Drop in Circular Microchannels. Heat Transfer Engineering 26 (3), 28.

Garimella, S., Bandhauer, T.M., 2001. Measurement of Condensation Heat Transfer Coefficients in Microchannel Tubes, 3 ed. American Society of Mechanical Engineers, New York, NY, United States, p. 243.

Garimella, S., Killion, J.D., Coleman, J.W., 2002. Experimentally Validated Model for Two-Phase Pressure Drop in the Intermittent Flow Regime for Circular Microchannels. Journal of Fluids Engineering, Transactions of the ASME 124 (1), 205-214.

Garimella, S., Killion, J.D., Coleman, J.W., 2003b. An Experimentally Validated Model for Two-Phase Pressure Drop in the Intermittent Flow Regime for Noncircular Microchannels. Journal of Fluids Engineering, Transactions of the ASME 125 (5), 887-894.

Graham, D.M., Newell, T.A., Chato, J.C., 1998. Experimental Investigation of Void Fraction during Refrigerant Condensation. Air Conditioning and Refrigeration Center, University of Illinois, Urbana-Champaign, IL.

Griffith, P., Lee, K.S., 1964. Stability of Annulus of Liquid in Tube. Transactions of the ASME--Journal of Basic Engineering 86, 666-668.

Hewitt, G.F., G. L. Shires and T. R. Bott, 1994. Process Heat Transfer. CRC Press LLC.

Isbin, H.S., Rodriguez, H.A., Larson, H.C., Pattie, B.D., 1959. Void Fractions in Two-Phase Flow. AIChE Journal 5 (4), 427-432.

Ishii, M., 1977. One-Dimensional Drift-Flux Model and Constitutive Equations for Relative Motion between Phases in Various Two-Phase Flow Regimes, ANL Report ANL-77-47.

Ishii, M., Chawla, T.C., Zuber, N., 1976. Constitutive Equation for Vapor Drift Velocity in Two-Phase Annular Flow. AIChE Journal 22 (2), 283.

Jassim, E., Newell, T., Chato, J., 2007. Probabilistic determination of two-phase flow regimes in horizontal tubes utilizing an automated image recognition technique. Experiments in Fluids 42 (4), 563-573.

Jassim, E.W., Newell, T.A., 2006. Prediction of two-phase pressure drop and void fraction in microchannels using probabilistic flow regime mapping. *International Journal of Heat and Mass Transfer* 49 (15-16), 2446-2457.

Jassim, E.W., Newell, T.A., Chato, J.C., 2008a. Prediction of refrigerant void fraction in horizontal tubes using probabilistic flow regime maps. *Experimental Thermal and Fluid Science* 32 (5), 1141-1155.

Jassim, E.W., Newell, T.A., Chato, J.C., 2008b. Prediction of two-phase condensation in horizontal tubes using probabilistic flow regime maps. *International Journal of Heat and Mass Transfer* 51 (3-4), 485-496.

Jeffreys, H., 1926. On the Formation of Water Waves by Wind. *Proc. Royal Soc. A* (107), 189.

Jiang, Y., 2004. Quasi Single-Phase and Condensation Heat Transfer and Pressure Drop of Refrigerant R404 at Supercritical and near Critical Pressures, *Mechanical Engineering*. Iowa State University, Ames.

Kattan, N., Thome, J.R., Favrat, D., 1998a. Flow Boiling in Horizontal Tubes: Part 1--- Development of a Diabatic Two-Phase Flow Pattern Map. *Journal of Heat Transfer* 120 (1), 140-147.

Kattan, N., Thome, J.R., Favrat, D., 1998b. Flow Boiling in Horizontal Tubes: Part 3--- Development of a New Heat Transfer Model Based on Flow Pattern. *Journal of Heat Transfer* 120 (1), 156-165.

Kawahara, A., Chung, P.M.Y., Kawaji, M., 2002. Investigation of Two-Phase Flow Pattern, Void Fraction and Pressure Drop in a Microchannel. *International Journal of Multiphase Flow* 28 (9), 1411-1435.

Kays, W.M., Leung, E.Y., 1963. Heat transfer in annular passages—hydrodynamically developed turbulent flow with arbitrarily prescribed heat flux. *International Journal of Heat and Mass Transfer* 6 (7), 537-557.

Killion, J.D., Garimella, S., 2004. Pendant Droplet Motion for Absorption on Horizontal Tube Banks. *International Journal of Heat and Mass Transfer* 47 (19-20), 4403-4414.

Klein, S., 2008. Engineering Equation Solver. F Chart Software, Madison, Wisconsin.

Kosky, P.G., Staub, F.W., 1971. Local condensing heat transfer coefficients in the annular flow regime. *AIChE Journal* 17 (5), 1037-1043.

Koyama, S., Lee, J., Yonemoto, R., 2004. An Investigation on Void Fraction of Vapor-Liquid Two-Phase Flow for Smooth and Microfin Tubes with R134a at Adiabatic Condition. *International Journal of Multiphase Flow* 30 (3), 291.

- Lee, H.J., Lee, S.Y., 2001. Pressure drop correlations for two-phase flow within horizontal rectangular channels with small heights. *International Journal of Multiphase Flow* 27 (5), 783-796.
- Lemmon, E.W., McLinden, M.O., Huber, M.L., 2002. Refprop Version, 7.0 Beta Version, NIST Standard Reference Database 23. NIST.
- Lockhart, R.W., Martinelli, R.C., 1949. Proposed Correlation of Data for Isothermal Two-Phase, Two-Component Flow in Pipes. *Chemical Engineering Progress* 45 (1), 39-45.
- Mandhane, J.M., Gregory, G.A., Aziz, K., 1974. A flow pattern map for gas-liquid flow in horizontal pipes. *International Journal of Multiphase Flow* 1 (4), 537.
- Mishima, K., Hibiki, T., 1996a. Quantitative Limits of Thermal and Fluid Phenomena Measurements using the Neutron Attenuation Characteristics of Materials. *Experimental Thermal and Fluid Science* 12 (4), 461-472.
- Mishima, K., Hibiki, T., 1996b. Some Characteristics of Air-Water Two-Phase Flow in Small Diameter Vertical Tubes. *International Journal of Multiphase Flow* 22 (4), 703-712.
- Mitra, B., 2005. Supercritical Gas Cooling and Condensation of Refrigerant R410A at near-Critical Pressures, Mechanical Engineering. Georgia Institute of Technology, Atlanta.
- Moriyama, K., Inoue, A., Ohira, H., 1992. Thermohydraulic characteristics of two-phase flow in extremely narrow channels (frictional pressure drop and void fraction of adiabatic two-component two-phase flow). *Heat Transfer - Japanese Research* 21 (8), 823-837.
- Moser, K.W., Webb, R.L., Na, B., 1998. A New Equivalent Reynolds Number Model for Condensation in Smooth Tubes. *Journal of Heat Transfer* 120 (2), 410-417.
- Nema, G., 2007. Flow Regime Transitions During Condensation in Microchannels, School of Mechanical Engineering. Georgia Institute of Technology, Atlanta, p. 147.
- Niño, V.G., 2002. Characterization of two-phase flow in microchannels, Mechanical Engineering. University of Illinois, Urbana-Champaign, IL.
- Nusselt, W., 1916. Oberflächenkondensation des Wasser dampfes. *Zetschrift des Vereins deutscher Inguenere* 60, 541-575.
- Petukhov, B.S., 1970. Heat Transfer and Friction in Turbulent Pipe Flow with Variable Physical Properties. *Advances in Heat Transfer* 6.
- Rabas, T.J., Arman, B., 2000. Effect of the Exit Condition on the Performance of In-Tube Condensers. *Heat Transfer Engineering* 21 (1), 4-14.

- Rice, C.K., 1987. Effect of Void Fraction Correlation and Heat Flux Assumption on Refrigerant Charge Inventory Predictions, pt 1 ed. ASHRAE, Atlanta, GA, USA, New York, NY, USA, p. 341.
- Rouhani, S.Z., Axelsson, E., 1970. Calculation of Void Volume Fraction in the Subcooled and Quality Boiling regions. *International Journal of Heat and Mass Transfer* 13 (2), 383-393.
- Sadatomi, M., Sato, Y., Saruwatari, S., 1982. Two-Phase Flow in Vertical Noncircular Channels. *International Journal of Multiphase Flow* 8 (6), 641-655.
- Sardesai, R.G., Owen, R.G., Pulling, D.J., 1981. Flow Regimes for Condensation of a Vapour Inside a Horizontal Tube. *Chemical Engineering Science* 36, 1173-1180.
- Scott, D.S., 1963. Properties of Co-Current Gas-Liquid Flow. *Advances in Chemical Engineering* 4.
- Serizawa, A., Feng, Z., Kawara, Z., 2002. Two-Phase Flow in Microchannels. *Experimental Thermal and Fluid Science* 26 (6-7), 703.
- Shah, M.M., 1979. A general correlation for heat transfer during film condensation inside pipes. *International Journal of Heat and Mass Transfer* 22 (4), 547-556.
- Smith, S.L., 1969. Void Fractions in Two-Phase Flow. A Correlation based upon an Equal Velocity Head Model, Proceedings of the Institution of Mechanical Engineers, Thermodynamics and Fluid Mechanics Group, pp. 647-657.
- Soliman, H.M., 1982. On the Annular-to-Wavy Flow Pattern Transition During Condensation Inside Horizontal Tubes. *The Canadian Journal of Chemical Engineering* 60 (4), 475.
- Soliman, H.M., Azer, N.Z., 1971. Flow Patterns During Condensation Inside a Horizontal Tube, ASHRAE Semi-annual Meeting, Philadelphia, PA.
- Steiner, D., 1998. Kapitel Hbb: Strömungssieden gesättigter Flüssigkeiten, VDI-Wärmeatlas, 8th ed. VDI-Gesellschaft Verfahrenstechnik und Chemieingenieurwesen (GVC), Düsseldorf, pp. Hbb1-Hbb35.
- Su, Q., Yu, G.X., Wang, H.S., Rose, J.W., 2009. Microchannel condensation : Correlations and theory. *International Journal of Refrigeration* 32 (6), 1149-1152.
- Sugawara, S., Katsuta, K., Ishihara, I., Muto, T., 1967. Consideration on the pressure loss of two-phase flow in small-diameter tubes. Proc. 4th National Heat Transfer Symp. of Japan, 169-172.
- Suo, M., Griffith, P., 1964. Two-Phase Flow in Capillary Tubes. American Society of Mechanical Engineers—Transactions—Journal of Basic Engineering 86 (3), 576.

- Swagelok, 2003. An Installer's Pocket Guide for Swagelok Tube Fittings, Solon, OH.
- Taitel, Y., Bornea, D., Dukler, A.E., 1980. Modelling flow pattern transitions for steady upward gas-liquid flow in vertical tubes. *AIChE Journal* 26 (3), 345-354.
- Taitel, Y., Dukler, A.E., 1976. Model for Predicting Flow Regime Transitions in Horizontal and Near Horizontal Gas-Liquid Flow. 22 (1), 47.
- Tandon, T.N., Varma, H.K., Gupta, C.P., 1982. A New Flow Regimes Map for Condensation Inside Horizontal Tubes. *Journal of Heat Transfer* 104 (4), 763-768.
- Taylor, B.N., Kuyatt, C.E., 1994. Guidelines for Evaluating and Expressing the Uncertainty of NIST Measurement Results. National Institute of Standards and Technology.
- The MathWorks Inc., 2004a. Matlab Image Processing Toolbox, Ver. 4.2. Matlab Version 7.0.0.19920 Release 14, Natick, MA.
- The MathWorks Inc., 2004b. Matlab Spline Toolbox, Ver. 3.2. Matlab Version 7.0.0.19920 Release 14, Natick, MA.
- The MathWorks Inc., 2004c. Matlab Version 7.0.0.19920 Release 14. <http://www.mathworks.com>, Natick, MA.
- Thome, J.R., El Hajal, J., Cavallini, A., 2003. Condensation in horizontal tubes, part 2: New heat transfer model based on flow regimes. *International Journal of Heat and Mass Transfer* 46 (18), 3365.
- Tran, T.N., Chyu, M.C., Wambsganss, M.W., France, D.M., 2000. Two-phase pressure drop of refrigerants during flow boiling in small channels: an experimental investigation and correlation development. *International Journal of Multiphase Flow* 26 (11), 1739-1754.
- Traviss, D.P., Rohsenow, W.M., 1973. Flow Regimes in Horizontal Two-Phase Flow with Condensation. *ASHRAE Transactions* 79 (n Part 2), 31-39.
- Traviss, D.P., Rohsenow, W.M., Baron, A.B., 1973. Forced-Convection Condensation Inside Tubes: A Heat Transfer Equation for Condenser Design. *ASHRAE Transactions* 79 (1), 157-165.
- Triplett, K.A., Ghiaasiaan, S.M., Abdel-Khalik, S.I., LeMouel, A., McCord, B.N., 1999a. Gas-Liquid Two-Phase Flow in Microchannels. Part II: Void Fraction and Pressure Drop. *International Journal of Multiphase Flow* 25 (3), 395.
- Triplett, K.A., Ghiaasiaan, S.M., Abdel-Khalik, S.I., Sadowski, D.L., 1999b. Gas-Liquid Two-Phase Flow in Microchannels. Part I: Two-Phase Flow Patterns. *International Journal of Multiphase Flow* 25 (3), 377.

- Ungar, E.K., Cornwell, J.D., 1992. Two-phase pressure drop of ammonia in small diameter horizontal tubes. *AIAA* 92, 3891.
- Wallis, G.B., 1969. *One-Dimensional Two-Phase Flow*, New York, McGraw-Hill.
- Wang, C., Chiang, C., Lin, S., 1997. Two-Phase Flow Pattern for R134a Inside a 6.5 mm (0.25 in.) Smooth Tube. *ASHRAE Transactions* 103 (1), 803-812.
- Wang, H.S., Rose, J.W., 2005. A Theory of Film Condensation in Horizontal Noncircular Section Microchannels. *Journal of Heat Transfer* 127 (10), 1096-1105.
- Wang, H.S., Rose, J.W., 2006. Film condensation in horizontal microchannels: Effect of channel shape. *International Journal of Thermal Sciences* 45 (12), 1205-1212.
- Wang, H.S., Rose, J.W., 2011. Theory of heat transfer during condensation in microchannels. *International Journal of Heat and Mass Transfer* 54 (11-12), 2525-2534.
- Webb, R.L., Ermis, K., 2001. Effect of hydraulic diameter on condensation of R-134a in flat, extruded aluminum tubes. *Enhanced Heat Transfer* 8, 77-90.
- Weisman, J., Duncan, D., Gibson, J., Crawford, T., 1979. Effects of fluid properties and pipe diameter on two-phase flow patterns in horizontal lines. *International Journal of Multiphase Flow* 5 (6), 437-462.
- Winkler, J., Killion, J., Garimella, S., 2012. Void fractions for condensing refrigerant flow in small channels. Part II: Void fraction measurement and modeling. *International Journal of Refrigeration* 35 (2), 246-262.
- Yang, C.-Y., Shieh, C.-C., 2001. Flow pattern of air-water and two-phase R-134a in small circular tubes. *International Journal of Multiphase Flow* 27 (7), 1163-1177.
- Yang, C.Y., Webb, R.L., 1997. A Predictive Model for Condensation in Small Hydraulic Diameter Tubes Having Axial Micro-Fins. *Journal of Heat Transfer* 119 (4), 776-782.
- Yashar, D.A., Graham, D.M., Wilson, M.J., Chato, J.C., Kopke, H.R., Newell, T.A., 2001. Investigation of Refrigerant Void Fraction in Horizontal, Microfin Tubes. *HVAC and R Research* 7 (1), 67.
- Zhang, M., Webb, R.L., 2001. Correlation of two-phase friction for refrigerants in small-diameter tubes. *Experimental Thermal and Fluid Science* 25 (3-4), 131-139.
- Zivi, S.M., 1964. Estimation of Steady-State Steam Void-Fraction by Means of the Principle of Minimum Entropy Production. *Journal of Heat Transfer* 86, 247-252.
- Zuber, N., Findlay, J.A., 1965. Average Volumetric Concentration in Two-Phase Flow Systems. *Journal of Heat Transfer* 87, 453-468.